Technische Universität München
Fakultät für Physik
Physics of Energy Conversion and Storage

The role of electrolyte composition in the activity and selectivity of metal and metal oxide electrocatalysts

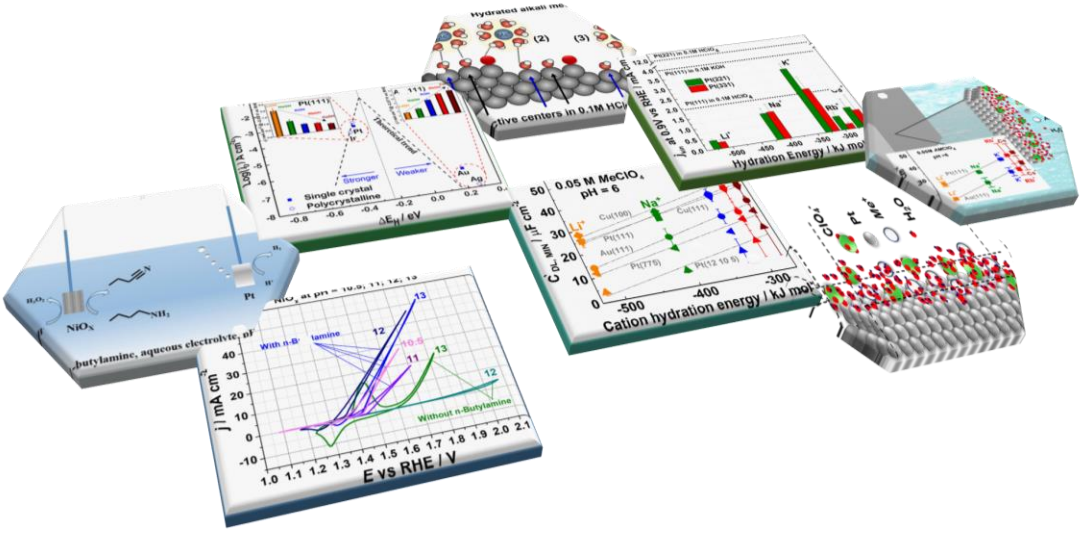

Dissertation

von

Song Xue

Technische Universität München
Fakultät für Physik
Physics of Energy Conversion and Storage

The role of electrolyte composition in the activity and selectivity of metal and metal oxide electrocatalysts

Song Xue

Vollständiger Abdruck der von der Fakultät für Physik der Technischen Universität München zur Erlangung des akademischen Grades eines

Doktors der Naturwissenschaften

genehmigten Dissertation.

Vorsitzender:	Prof. Dr. Martin Zacharias
Prüfer der Dissertation:	1. Prof. Dr. Aliaksandr S. Bandarenka
	2. Prof. Dr. Egill Skulason

Die Dissertation wurde am 23.12.2019 bei der Technischen Universität München eingereicht und durch die Fakultät für Physik am 16.01.2020 angenommen.

Abstract

Electrolytes, which are components of electrocatalytic systems, largely determine their performance. While so-called 'active species', such as intermediates, have been attracting considerable attention as they directly participate in electrocatalytic reactions, the catalytic role of so-called 'spectator species' i.e. electrolyte components, which are not directly involved into the reactions, have largely been ignored. However, recently, several groups found that the activity and selectivity of various electrocatalytic reactions exhibit a strong dependence on the nature of those species. In-depth fundamental understanding of these effects, however, still requires extensive research. In this thesis, the effect of alkali metal cations on the resulting activity was investigated as these cations are generally present in widely used industrially relevant electrolytes. In addition, the impact of *n*-butylammonium (sulfate), one of the novel 'spectator species', was studied in the context of water electrolysis.

Electrocatalytic reactions important for the 'hydrogen economy', namely hydrogen evolution reaction, oxygen reduction reaction, and oxygen evolution reaction, have been selected as model processes in this study. With regard to the hydrogen evolution reaction, the activities of various Pt electrodes appear to be greatly dependent on the type of alkali metal cations present in the electrolytes (the activities decreased in the following order: $Li^+ > Na^+ > K^+ > Rb^+ > Cs^+$). The same trend was observed for the Ir electrodes. The trend for the Au and Ag electrodes, nevertheless, was surprisingly reversed ($Cs^+ > Rb^+ > K^+ > Na^+ > Li^+$). For the oxygen reduction reaction, the performance of Pt electrodes not only depends on the surface structure but also on the type of alkali metal cations in the electrolyte. For the oxygen evolution reaction, adding *n*-butylammonium sulfate enhances dramatically the anodic currents in the case of widely used industrial catalysts. Electrochemical techniques including electrochemical impedance spectroscopy were used to also explore the influence of alkali metal cations on the electric double layer for various model metal electrodes. It was discovered that the local effective concentrations of alkali metal cations near the electrode surface are more than one order of magnitude higher than in the electrolyte bulk (0.05 M solutions were used for this study). It is apparent that the role of alkali metal cations is so far significantly underestimated in the literature.

Acknowledgement

I sincerely thank those who have contributed to this dissertation and supported me during this amazing journey. Without any of them, this research work would not be possible.

First of all, I would like to express my sincere gratitude to my supervisor Prof. Dr. Aliaksandr S. Bandarenka for giving me the opportunity to work in his group. His profound experiences and knowledge have taught me how to conduct research more effectively. His professional suggestions guided me to solve many practical problems in this dissertation. His flexible management gave me a relaxed working environment. Without his constant counselling and support, I could not smoothly finish my PhD.

I would like to thank Prof. Dr. Julia Kunze-Liebhäuser for giving the research opportunity in her group. It was an enjoyable experience. I am also thankful to Andrea Auer for helping me to perform my research in Innsbruck.

My sincere gratitude is reserved for all my colleagues in the ECS group. I would like to thank Dr. Batyr Garlyyev for his constant supports in many projects and great guidance for writing papers. I am also indebted to Dr. Viktor Colic, Sebastian Watzele, Dr. Yunchang Liang and Dr. Marcus Pohl, who led me into this lab and this field. I am grateful to Johannes Fichtner, Dr. Weijin Li, Regina Kluge, Richard Haid, Dr. Daniel Scieszka, Jeongsik Yun, Philipp Marzak, Xing Ding, and Shujin Hou for supporting me both in work and life. I am very appreciative to Siegfried Schreier for maintaining and repairing our experimental setups. I also thank Leon Katzenmeier, Faheem Butt, Paul Scheibenbogen, Jongho Kim, Xiaohan Sun, David McLaughlin, Namitha Rajendran and all the other people who are still or were working in the ECS group.

I also want to thank the China Scholarship Council for financial support and the American Chemical Society, Royal Society of Chemistry, Elsevier and Wiley for permissions to include copyrighted figures as a part of my thesis.

Finally, I want to express special thanks to my parents and sister. I love them so much, and I would not have made it this far without their constant and unconditional support.

CONTENT

1. Introduction

1.1 Electrocatalysis for sustainable energy: potential and challenges

The 'hydrogen economy', as proposed by Bockris[1] in the 1970s, means that hydrogen becomes the main compound to provide energy from a power station to sites where energy is needed. Electricity produced by the power stations from renewable energy sources would be used to perform water electrolysis. Subsequently, hydrogen would be delivered from the distribution stations to homes and factories, where it should be 'reconverted' to electricity using fuel cells, whilst water would be the only by-product.[1] The hydrogen economy thus appears to be a promising solution to associated environmental problems and the energy crisis, which are two of the prominent global issues encountered in the 21st century.[2]

There are two key characteristics of these energy conversion and storage schemes compared to the current systems in operation, namely, environmental-friendliness and improved energy conversion efficiency.[3] Fuel cells are known to produce only water and heat/electricity, without any emission of noxious pollutants or carbon dioxide that often inevitably accompany the burning of fossil fuels.[4] According to the report by Professor Mark Z. Jacobson, an atmospheric expert at Stanford University, airborne pollutants would be dramatically reduced if all cars and trucks started using hydrogen-powered engines, whilst health crises ranging from headaches to heart attacks would be significantly reduced.[5] Of course, the increasingly serious greenhouse effect would be alleviated as well, as the amount of carbon dioxide – one of the main contributors – would be considerably reduced. Therefore, the hydrogen economy-related systems provide a potential way to help human beings resolve various environmental problems.

With regard to sustainable development, energy savings are necessary to meet the considerable increase in energy demand for the coming decades; and the hydrogen economy seems to be one of the key strategies to realise these savings. The energy supply has been growing dramatically in recent decades. For example, in 2017 global energy consumption increased by 2.7 percent, which was double the growth rate in 2016.[6] Therefore, it is widely expected that much more may be needed in the future if

no limitations or enhancements are introduced.[7] The hydrogen economy related schemes have the potential to avoid or at least alleviate this situation. Due to their much higher energy conversion efficiency, fuel cell vehicles have already shown comparable running costs to those of current ones relying on fossil fuels. For example, the Toyota Mirai, a hydrogen fuel cell car produced by Toyota and already commercially available, offers a total running range of 500 kilometres on a full tank, with a running cost 3.5 litres per 100 kilometres (66 American MPG), which is comparable with the average gasoline cars.[8] However, unlike the internal combustion engines owing a relatively mature technology and widely used in daily life, fuel cells still have considerable room to improve[9]. Under laboratory conditions, the energy conversion efficiency of fuel cells can reach 60-80 percent, which is two to three times higher than for the internal combustion engine.[4] What is more, the costs of energy transfer would be much lower if the main form of energy transfer – electricity – would be changed to hydrogen. As early as 1972, Gregory *et al.*[10] indicated that the costs of transferring hydrogen would be lower than of sending electricity by overhead cables when the transport distance is more than 400 kilometres, whilst the cost would then be halved when the distance is more than 1,600 kilometres. The hydrogen economy-related schemes offer unique advantages in numerous commercial sectors in terms of energy savings, such as aircraft and aerospace, chemistry and metallurgy.[10] The maximum total range of aircraft running on liquid hydrogen would increase two- to three-fold for the same weight of fossil fuels; the costs of producing commonly used chemicals, for instance, metal Fe, metal Al, and gaseous NH_3, would be significantly reduced in chemical industry and metallurgy.[1]

To lay the foundations for the hydrogen economy, electrocatalysis related to water electrolysis and fuel cell reactions should be investigated in more detail[12]. As shown in **Figure 1.1**, water electrolysis is the principal mean of transferring renewable and nuclear energies into chemical energy stored as H_2; fuel cells are the main systems for converting the stored chemical energy into electric energy.

However, for the state-of-the-art electrolysers, the obvious drawback is wasting substantial amounts of electrical energy due to the existence of high overpotentials[11]. The same is valid for fuel cells, especially for the reactions taking place at the cathode side of these devices (e.g. oxygen reduction reaction). The efficiency of the electrocatalytic reactions involved in water splitting and fuel cells needs to be

significantly improved.

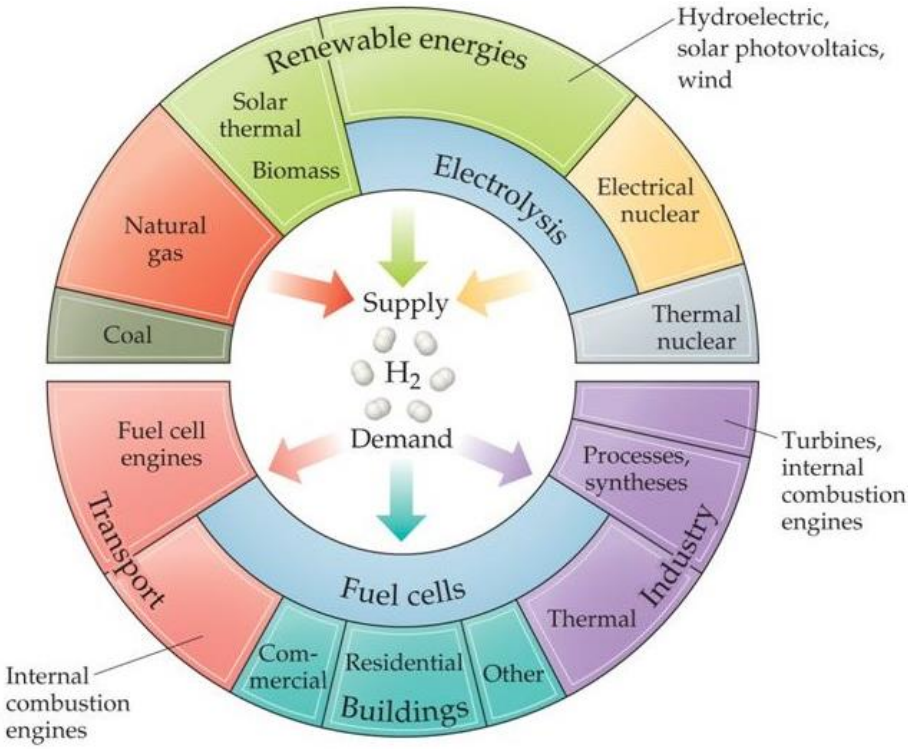

Figure 1.1. The concept of hydrogen economy. Water electrolysers and fuel cells are the principal devices to transfer 'renewable' and 'nuclear' energies into energy stored in chemical bonds of H_2 and *vice versa*. Reprinted with permission from ref.12.

1.2 The role of electrolytes in electrocatalysis

Electrocatalysts accelerate the inner-sphere reactions at the electrode-electrolyte interfaces.[13] Electrocatalysis has been identified as one of the five broad categories of catalytic research widely studied nowadays, along with biocatalysis, homogeneous catalysis, conventional heterogeneous catalysis, and ultra-high vacuum (UHV) surface science.[14] As shown in **Figure 1.2**, the future sustainable energy schemes are expected to rely on electrocatalysis. Moreover, the development of new advanced electrocatalysts is critical to sustainable energy as a whole, not just to the hydrogen economy.

Electrocatalysis, however, is the most complex amongst these five established fields of catalytic research owing to the following reasons:

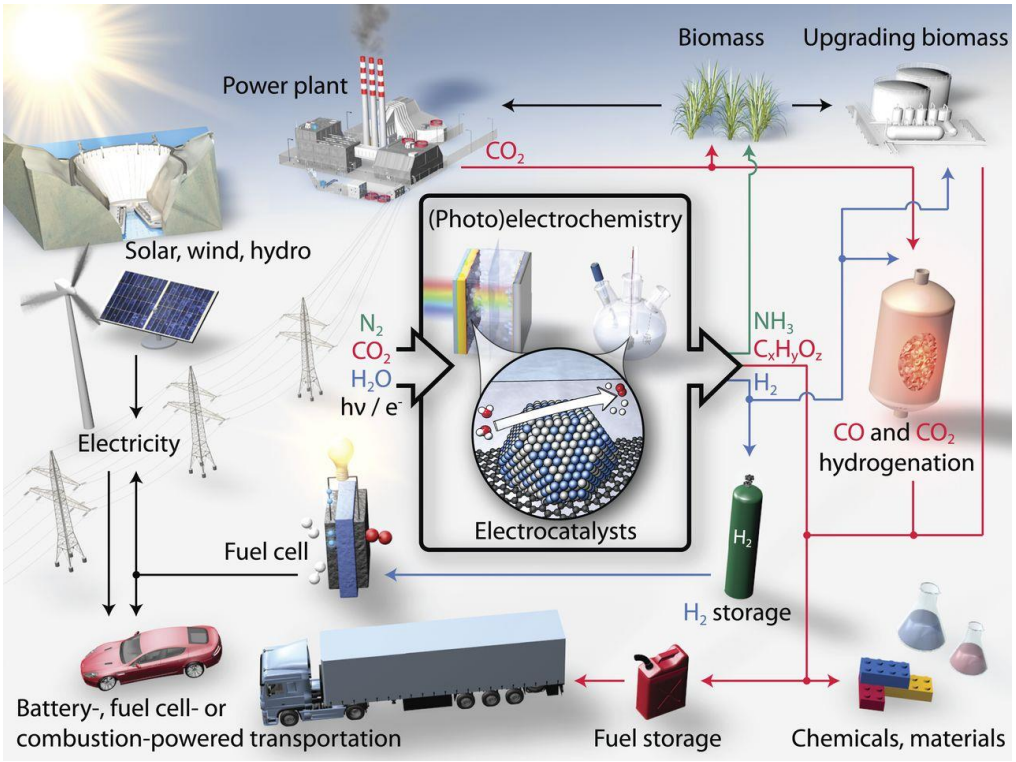

Figure 1.2. Schematic of the role of electrocatalysis in the future of sustainable energy. Reproduced with permission from ref.15.

1. **It involves up to three phases at the interfaces where the reactions occur.** An electrocatalytic reaction can occur at the solid (electrodes)/liquid (electrolytes)/gas (reactants or products) three-phase interface.
2. **The dramatic changes caused by a minor shift in the applied potential.** The structure of the electrical double layer, the Fermi level of electrodes, the free energy of reactants and products, the adsorption energy of ions, and the surface coverage will be significantly changed once the applied potential shifts slightly. Moreover, these changes are often exponential.
3. **Multi-step reactions along with the multiple proton/electron transfers.** Electrocatalytic reactions can involve numerous reaction intermediates and half-reactions. The actual intermediates and half-reactions are highly uncertain and largely depend on various factors in the surrounding environment, such as electrocatalysts, electrolytes, temperature, etc. For instance, carbon dioxide reduction (one of the hot

topics in the area of electrocatalysis nowadays), can have *ca.* 16 different half-reactions[16], because the energetic requirements for the reaction are highly sensitive to the pH value and the number of electrons involved[17] (**Figure 1.3**). Furthermore, for every half-reaction, there are many possibilities for the reaction mechanisms as well[18]. Thus, it is particularly difficult for theoretical investigations to conduct modelling.

4. **Nanosized electrocatalysts.** As it is widely accepted that the best electrocatalysts are likely to all be found at the nanoscale[19,20,21], this creates new challenges for both theoretical and experimental investigations. For theoretical studies, nanometer scale is comparatively too big, which creates considerable uncertainty when building analytical models. In contrast, for experimental research, nano-objects are considered to be too small, because many experimental devices cannot achieve necessary accuracy or resolution and at the same time work in a liquid environment.

Electrocatalytic research, especially for water electrolysis and fuel cells, is currently predominantly focused on optimisation of the working electrodes, such as modifying the electrode surface structure[22,23], searching for new materials[24,25] and changing the surface composition[26,27]. Although these studies have made significant contributions to the development of the field of electrocatalysis, the effect of electrolytes on electrocatalytic reactions should not be overlooked. In fact, the first attempt to investigate the electrolyte effects can be traced back to 1930s[28]. However, the related research attracted much less attention due to the absence of fundamental understandings of such observations. Recently, thanks to the discovered electrolyte-related phenomena, such as pH effects[29], research on electrolytes receives a wider coverage[30,31].

The widely recognised function of electrolytes is (i) to transport ions, (ii) to increase the ionic conductivity of the system and (iii) to provide the required reactants. The function of electrolytes appears simple, yet this is somewhat misleading. Recently, several reports have indicated that ‘spectator species’ have a notable influence on both selectivity and the reaction rates of various electrocatalytic processes.[32,33,34,35,36,37,38,39,40] However, many problems, for example, what the specific impact of each spectator species is and how they affect the overall activity and selectivity, remain up to date unsolved. There is no well-accepted theory fully

explaining the role of electrolytes in changing the electrocatalytic performance; and one of the main goals of this thesis is to contribute to understanding of these effects.

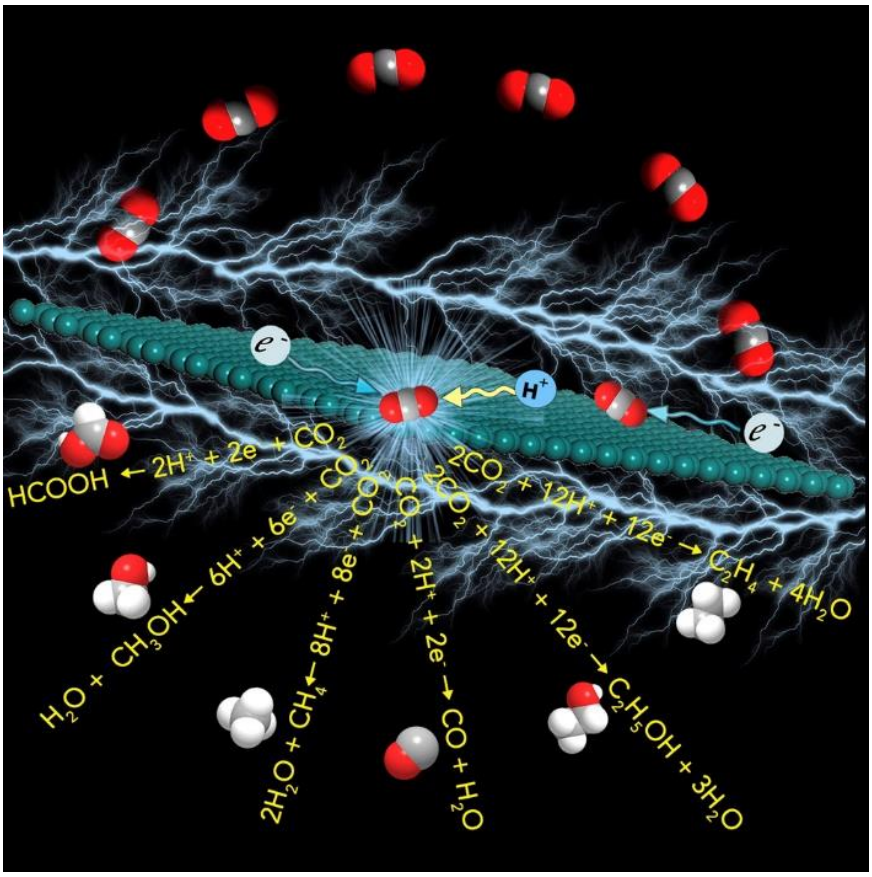

Figure 1.3. Schematic of transformations of carbon dioxide into fuels and chemicals by using electrocatalytic processes. Possible reaction pathways were indicated. Reprinted with permission from ref.16. Copyright 2017, Elsevier.

1.3 Research aims

In this thesis, the influence of alkali metal cations and *n*-butylammonium (sulfate) on the performance of electrocatalytic systems is selected as the study focus. Alkali metal cations were chosen because they are widely used in research and industry and have thus become common components of electrolytes. Determination of how the alkali metal cations influence several necessary energy provision electrocatalytic reactions, such as hydrogen evolution reactions (HER) and oxygen reduction reactions (ORR), will be important for water electrolysers and fuel cells. As it is acknowledged, the high anodic overpotentials still severely hinder a wider commercial application of water electrolysis.[41] It has been reported that the anodic overpotentials were found to be

significantly reduced when *n*-butylammonium sulfate was added into the electrolyte[33]. Here, the effects of *n*-butylammonium sulfate on the electrochemical performance were systematically investigated using industrially relevant electrocatalysts.

It is important to understand why these spectator species have such a great influence, as they do not even directly participate in the reactions. Electrochemical impedance spectroscopy (EIS) was used to study the effect of alkali metal cations on the electrical double layer (EDL) properties, as the structure of EDL largely determines functionality of electrochemical systems.

The structure of the present study is outlined as follows:

In Chapter 2, the key theoretical background used in this thesis (Sabatier principle, electric double layer, and the concept of active sites) will be introduced. Furthermore, the electrocatalytic reactions associated with water electrolysis and fuel cells will be discussed.

In Chapter 3, the used electrochemical set-ups and electrochemical techniques will be introduced.

Chapter 4 is dedicated to the influence of the alkali metal cations on the hydrogen evolution reaction. Two groups of electrodes were chosen based on their location in the so-called 'volcano plots'. One group, which is located on the left side of the volcano plot with stronger hydrogen binding with respect to the optimal value, included Ir(111) and three Pt crystals: Pt(111), Pt(221), and polycrystalline Pt. The other group, which is located on the right side with weaker hydrogen binding energies, consisted of polycrystalline Ag and Au(111). The HER measurements indicated that the activity can be tuned up to a factor of ~4 when changing from LiOH to CsOH.

Chapter 5 deals with the oxygen reduction reaction activity of model stepped single crystals Pt(221) and Pt(331) in different solutions of *Me*OH *(Me*$^+$: Li^+, Na^+, K^+, Rb^+, and Cs^+). It will be shown that the ORR performance of these electrodes strongly depends on both the surface structure of the electrodes and the type of alkali metal cations in the electrolyte.

In Chapter 6, the results of investigation of anodic oxidation reactions for water electrolysis systems are presented for electrolytes containing an 'ionic liquid', namely *n*-butylammonium sulfate. Several widely used industrially relevant catalysts were

chosen, such as cobalt (oxy)hydroxide, nickel (oxy)hydroxide, and nickel-iron (oxy)hydroxide.

In Chapter 7, the effects of the alkali metal cations on the electric double layer will be discussed. These effects were investigated by EIS measurements in 0.05 M *Me*ClO_4 (Me^+: Li^+, Na^+, K^+, Rb^+, Cs^+) electrolytes for six different model electrodes: Pt(111), Au(111), Cu(111), Cu(100), Pt(775) and Pt(12 10 5). Differential electric double layer capacitances of all electrodes have been measured at the potential close to that of zero charge. It will be shown that the above mentioned cations accumulate in the electric double layer region, irrespective of the electrode surface compositions and structures; and the effective concentrations of these cations near the electrode surface are estimated to be almost 80 times higher than their bulk concentrations.

In Chapter 8, conclusions and an outlook are presented.

2. Theoretical part

2.1 The Sabatier principle

The Sabatier principle says that the interaction between a catalyst surface and reaction intermediates should be neither too strong nor too weak.[42] If the interaction is too strong, the products will not desorb from the surface of the catalyst and consequently will prevent it from continuing to catalyze the reaction. In contrast, if the interaction is too weak, the reactants cannot be activated at the surface, and therefore, no reaction will occur. In order to fulfil these requirements, the binding energy between the catalytic surface sites and reactants/intermediates/products should be optimised.

The original Sabatier principle, which can be traced back to 1911[43], is a purely qualitative principle. Following nearly 50 years of development afterwards, a quantification through so-called 'volcano plots' has been established. A combination of the Sabatier principle and the Brønsted catalysis equation, demonstrating the relationship between thermodynamics and kinetics, permits the construction of these volcano plots.[44] The volcano plots were proposed by Balandin[45], among the others, in 1969 in a perspective review and successfully highlighted by Trasatti[43] in 1972 for electrocatalysis. In these plots, a quantity, reflecting the reaction kinetics, is plotted against a property correlated with the stability of the intermediates. The former can be the potential, current or temperature at the beginning or during the reaction; the latter can be the heat of adsorption of a reactant or the formation energy of a product or reaction intermediates. The shape of these plots, resembling a volcano, is usually triangular with a single peak; and the optimally achievable binding energy is located at its apex.

As an example, **Figure 2.1** depicts a volcano plot for the HER on several metal surfaces[46,47,48]. In this plot, the theoretical binding energy of hydrogen on the metal surfaces (ΔE_H) is selected as the x-axis since, according to the reaction mechanism, the intermediates of HER, particularly in acidic electrolytes, are only hydrogen atoms adsorbed on the surface[49,50,51]. In terms of the y-axis, the exchange current density of the HER is used. At low values of ΔE_H, the reaction is slow as it is hindered by the

excessively strong binding of adsorbed hydrogen resulting in a low exchange current density. In contrast, at high values of ΔE_H, the reaction is restricted due to the slow rate of hydrogen adsorption. Therefore, a maximum HER activity should be found at an intermediate value of ΔE_H, with rapid rates of hydrogen desorption as well as hydrogen adsorption.

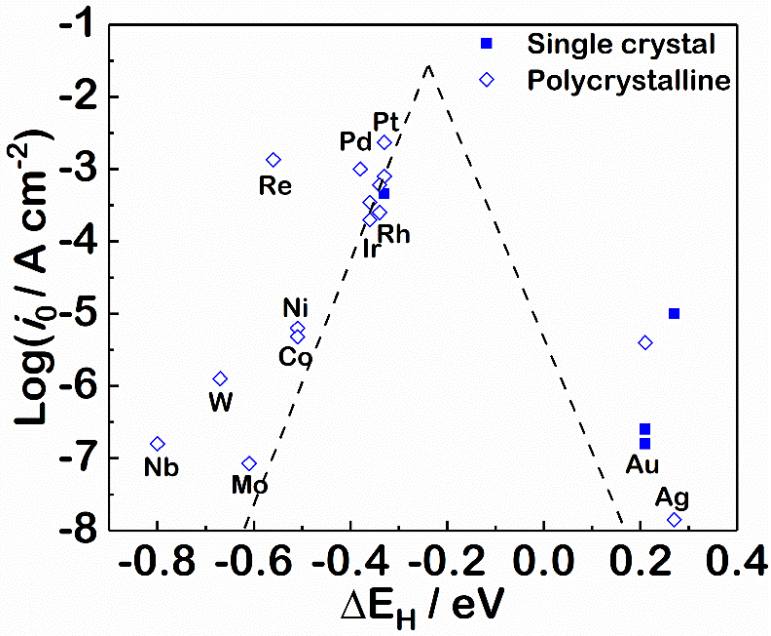

Figure 2.1. A'volcano plot' describing the HER activity trends for different metal surfaces as a function of their theoretical binding energies to the hydrogen reaction intermediates. The theoretical hydrogen binding energies and HER activities are collected from refs 46,52. The catalysts located on the left-hand side exhibit relatively strong binding energies. The ones located on the right-hand side exhibit relatively weak binding energies.

The Sabatier principle, together with its quantification using the 'volcano plots', has proven itself vital in predicting and explaining the catalytic properties as well as guiding new catalyst designs with the help of theoretical calculations such as density functional theory (DFT) calculations[48,53].

2.2 The electrochemical interface and the electric double layer

The electric double layer appears at the surface of an electrode when the electrode is immersed into an electrolyte.[54] The 'electric charges' in the electrode and the 'ionic charges' in the electrolyte rearrange close to the interface when a potential is applied.[54] Specifically in the electrolyte, an excess of ionic charges will form in the vicinity of the

electrode surface; and the structure formed by these oriented dipoles and charged species can be seen as two parallel layers, although the boundaries are rather loose, as shown in **Figure 2.2**. The layer closest to the electrode, which is generally referred to as the ***Helmholtz layer*** or ***Stern layer***, is comprised of solvent molecules and occasionally specifically adsorbed species.[55] The electric centres of the specifically adsorbed ions and the nearest non-specifically adsorbed ions are referred to as the '***inner Helmholtz plane***' (IHP) and the '***outer Helmholtz plane***' (OHP), respectively (**Figure 2.2**). The non-specifically adsorbed ions, driven only by long-range electrostatic forces, form the second layer, generally referred to as the ***diffuse layer***, which extends from the OHP to the bulk electrolyte due to thermal agitation.[56,57]

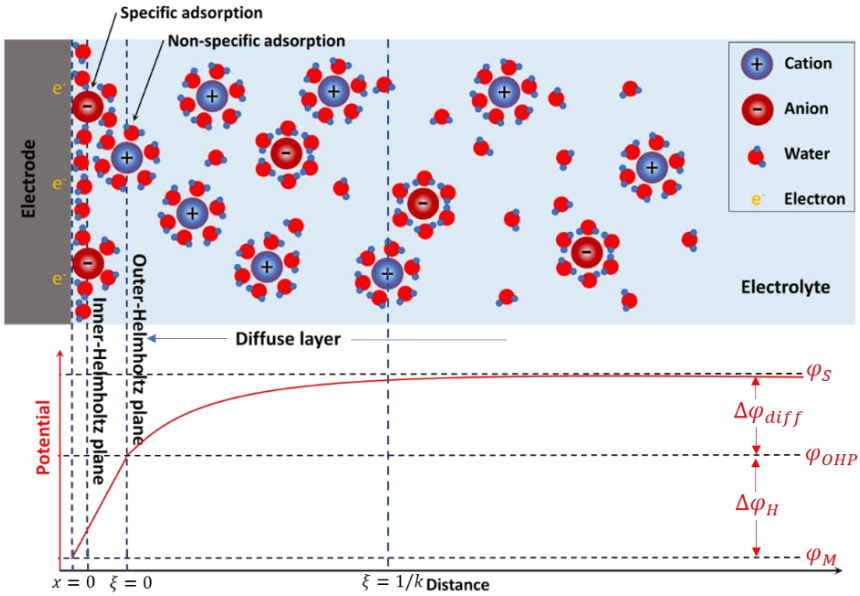

Figure 2.2. Model of the electrical double layer. A negatively charged electrode in an aqueous electrolyte is used as an example. The plot reveals the corresponding potential distribution, in which $\Delta\varphi_H$ and $\Delta\varphi_{diff}$ are potential drops in the Helmholtz layer and the diffuse layer, respectively.

The current understanding of the electric double layer is based on the contributions of several generations of scientists.[58,59,60,61,62,63] In 1853, Helmholtz[58] initially proposed the electric double layer model, in which, one layer is the polarised electrode surface and the other one is the layer of counterions closely adhering to the charged electrode surface. This early model laid the foundations for understanding of the electrochemical interface, although it was not comprehensive as it did not consider the thermal motion that causes ions to leave the layer of counterions. In the first decade of the 20th century, Gouy and Chapman[59,60] considered the effect of thermal motion on the ions near the

surface and introduced a diffuse model of the electrical double layer. In this model, they assumed excess ionic charges distributed as a function of the distance from the electrode surface, ignoring the inner Helmholtz layer. In 1924, Stern proposed the currently most recognised model[61], combining the Helmholtz electric double layer model with the diffuse model. In Stern's representation, some ions follow the proposition from Helmholtz and form an internal Stern layer adhering to the electrode while some form a diffuse layer, as Gouy-Chapman proposed. Since the 1950s, the model was further modified by Grahame, Bockris, Devanathan, and Müller.[62,63]

At present, the well-recognized double layer model is comprised of three regions, namely the inner-Helmholtz plane, the outer-Helmholtz plane, and the diffuse layer (**Figure 2.2**). In the region of $0 \ll x \ll a/2$ (where x is the distance from the electrode surface and a is the diameter of the solvated counter-ion in the electrolyte), a water dipole layer with the so-called specifically adsorbed species, which lose to a certain aspect their solvation shells, is directly attached to the electrode surface and predominantly constitutes the inner-Helmholtz region. The outer-Helmholtz region is comprised of non-specifically adsorbed species which retain their full solvation shell. With regard to $x \gg a/2$, the diffuse layer extends from the outer-Helmholtz plane to the bulk electrolyte.

In the region of $0 \ll x \ll a/2$, namely the Helmholtz region, according to the Poisson equation, the relationship between the space-charge density and the potential can be written as (for a one-dimensional problem):

$$\frac{d^2\varphi(x)}{dx^2} = -\frac{\rho}{\varepsilon_r \varepsilon_0} \tag{2.1}$$

where x is the direction vertical to the electrode surface, $\varphi(x)$ is the corresponding potential and ρ is the space-charge density.

Applying no potential and treating these ions as point charges, we can assume the charge density between the electrode and the Helmholtz plane to approach zero. Hence,

$$\frac{d^2\varphi(x)}{dx^2} = 0 \tag{2.2}$$

Integrating this formula, we can get the following equation

$$\frac{d\varphi(x)}{dx} = Constant \tag{2.3}$$

With the boundary conditions, $x = 0, \varphi(0) = \varphi_M; x = a/2, \varphi(a/2) = \varphi_{OHP};$ the potential is written as

$$\varphi(x) = \varphi_M - \frac{2[\varphi_M - \varphi_{OHP}]x}{a} \tag{2.4}$$

where φ_M is the potential of the electrode, φ_{OHP} the potential at the outer-Helmholtz plane.

The integral capacitance of the interface can be calculated from the following expression

$$C = \frac{\varepsilon_r \varepsilon_0 A}{l} \tag{2.5}$$

where l is the distance separating the plates, A is the surface area of the plates, ε_0 is the vacuum permittivity, and ε_r is the relative permittivity. Based on experimental results, this capacitance should consist of two parts: the water dipole layer and the adsorbed ions. Thus, ignoring the surface area, the capacitance of the Helmholtz layer, C_H, can be given by

$$\begin{aligned} \frac{1}{C_H} &= \frac{1}{C_{dipole}} + \frac{1}{C_{IHP} - C_{OHP}} \\ &= \frac{a_{H_2O}}{\varepsilon_{dipole}\varepsilon_0} + \frac{a_{ion}}{2\varepsilon_{IHP-OHP}\varepsilon_0} \end{aligned} \tag{2.6}$$

where a_{H_2O} and a_{ion} are the diameter of the water molecule and the largest solvated ion, respectively.

Moreover, the capacitance in the Helmholtz region is, in fact, primarily determined by the water molecules, as the effect of the ionic diameter is found to be rather limited. This is essential for the results presented in Chapter 7. It should be noted, however, that this formula does not clearly demonstrate the influence of the electrode materials and the structure of the electrode surface.

In the region of $x \gg a/2$, according to the Gouy-Chapman model, the diffuse region can be described by Boltzmann statistics. In this model, all ions in the electrolyte are

assumed to be point charges and influenced by both electric attraction and thermal motion. To simplify the following discussion, a new variable ξ is used to replace the distance x, where $\xi = x - a/2$. Then, the potential in the diffuse region can be rewritten as:

$$\varphi(x) = \varphi_S - \varphi(\xi) \tag{2.7}$$

where φ_s is the potential of the electrolyte and $\varphi(\xi)$ is the potential at the distance ξ.

According to the linearised Poisson-Boltzmann equation, the relationship between the space-charge density and the potential can be written as:

$$\frac{d^2\varphi(x)}{dx^2} = k^2[\varphi_S - \varphi(\xi)] \tag{2.8}$$

which solves to give

$$\varphi_S - \varphi(\xi) = Constant\ e^{-k\xi} \tag{2.9}$$

Combined with the boundary conditions, $\varphi_S - \varphi(\xi) = \varphi_S - \varphi_{OHP}$ when $\xi = 0$, **Equation (2.9)** thus becomes

$$\begin{aligned} \varphi_S - \varphi(\xi) &= [\varphi_S - \varphi_{OHP}]\, e^{-k\xi} \\ &= \Delta\varphi_{diff} e^{-k\xi} \end{aligned} \tag{2.10}$$

where $\Delta\varphi_{diff}$ is the potential drop across the diffuse region, generally known as ***zeta-potential***. When the distance from the outer Helmholtz layer, ξ, is equal to k^{-1}, the potential drops to a value $1/e$ of $\Delta\varphi_{diff}$. This distance k^{-1} is normally taken as the length of the diffuse layer and referred to as ***Debye-length***.

Based on **Equation (2.5)**, the capacitance of the diffuse layer can be given as:

$$C_{diff} = k\varepsilon_r\varepsilon_0 \tag{2.11}$$

From this formula, it is clear that the capacitance of the diffuse layer is closely associated with the electrolyte.

The whole electric double layer, $0 \ll x \ll k^{-1}$, can be seen as the Helmholtz region and the diffuse layer connected in series.

The potential drop across the whole double layer region, Δφ, can be outlined as:

$$\begin{aligned}\Delta\varphi &= [\varphi_{OHP} - \varphi_M] + [\varphi_S - \varphi_{OHP}]e^{-1} \\ &= \Delta\varphi_H + \frac{\Delta\varphi_{diff}}{e}\end{aligned} \tag{2.12}$$

where $\Delta\varphi_H$ and $\Delta\varphi_{diff}/e$ are the potential drops in the Helmholtz region and the diffuse layer, respectively.

The capacitance of the whole double layer region, C_D, can be summarized as:

$$\begin{aligned}\frac{1}{C_D} &= \frac{1}{C_H} + \frac{1}{C_{diff}} \\ &= \frac{a_{H_2O}}{\varepsilon_{dipole}\varepsilon_0} + \frac{a_{ion}}{2\varepsilon_{IHP-OHP}\varepsilon_0} + \frac{1}{k\varepsilon_r\varepsilon_0}\end{aligned} \tag{2.13}$$

where C_H and C_{diff} are the capacitances of the Helmholtz region and the diffuse layer, respectively.

In concentrated solutions, according to this expression, the capacitance C_D predominantly depends on C_H since C_{diff} is several orders of magnitude higher. In dilute solutions, on the other hand, the capacitance C_{diff} must be taken into account, as k decreases and C_{diff} becomes increasingly significant in this expression for C_D.[56] This rule will exert a significant influence on the experiment design in Chapter 7.

The electric double layer plays an integral role in the functionality of numerous innovative energy systems, ranging from batteries to supercapacitors and from electrolysers to fuel cells. However, further investigation is required as there are still various unsolved questions such as the question of the EDL structure in various systems.[63]

2.3 Catalytic active sites

In electrocatalysis, active sites are an array of sites or a region in the catalyst surface that primarily determine the performance of the catalyst.[56] According to the Sabatier principle, the interaction between reaction intermediates and catalysts should be optimal for the best performance.[42] However, intermediates usually bind differently to various types of sites on the catalyst surface. Thus, the electrocatalytic performance of

different surface sites can vary considerably. This inspired the principle of active sites. Langmuir[64,65] was the first to affirm that, for authentic catalyst surfaces, the assumption that all sites are energetically identical and non-interacting was an unacceptable approximation. Consequently, he proposed the original model to describe the chemisorption of different surface sites. In this model, he assumed that an array of sites would control the activity, and the typical Langmuir adsorption isotherm was obtained. This model provided the first surface science approach in heterogeneous catalysis.[66]

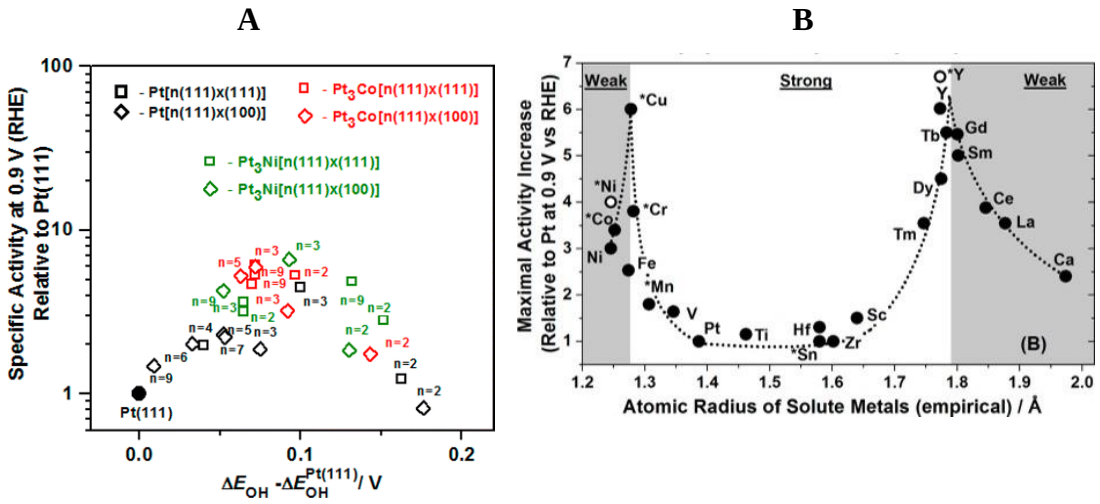

Figure 2.3. The ORR activities of various stepped single crystalline surfaces and metal alloy catalysts. (A) Relative ORR activities of Pt and Pt alloy stepped single crystal electrodes at 0.9 V_{RHE} in 0.1 M $HClO_4$, as compared to Pt(111). Stepped single crystals with different atomic widths of the (111) terraces were characterised. (B) ORR activities of various Pt alloy catalysts at 0.9 V_{RHE} relative to the corresponding Pt catalyst. The activities were plotted against the empirical radius of the solute metal. Graphics are reprinted with permission from ref.67. Copyright 2016, American Chemical Society.

Subsequently, Taylor [68] emphasised the heterogeneity of surface sites and the corresponding effects. Taylor recognised that '…there will be all extremes between the case in which all atoms in the surface are active and that in which relatively few are so active'[68]; and non-equivalent sites can generate different activities due to the local environmental heterogeneity of surface atoms. This heterogeneity originates from both varied coordination numbers of surface atoms and different surface or bulk compositions. Terraces, edges, corners, ledges, vacancies, and kinks on the surface can all cause a variation of coordination numbers of surface atoms.[69] In terms of catalysts with multiple components, it is apparent that the surface composition would differ from that of the bulk catalyst as well as between each crystal facet. This heterogeneity has a

significant effect on the catalyst performance, as has been confirmed by surface science studies[66,70] on samples such as stepped single crystalline surfaces (**Figure 2.3A**) and various metal alloy catalysts (**Figure 2.3B**).

According to the statement of active sites in the Taylor's principle and experimental kinetic measurements, electrochemical reactions are divided into two categories depending on whether a specific surface structure is necessary to promote the reaction.[71]

1. **Structure-sensitive reactions.** For these reactions, the adsorption of the intermediates/reactants and/or the following process predominantly occur on specific sites of the surface. Accordingly, it can be observed that there are always strong interactions between the reaction intermediates and the catalyst surface in this type of reactions.
2. **Structure-insensitive reactions.** In those reactions, all sites on the surface apparently exhibit similar activities. With regard to some of these reactions, the surface even adapts itself to the reaction conditions, as Taylor stated: 'The amount of surface which is catalytically active is determined by the reaction catalysed'.[72,73] In this case, the interactions between intermediates and the catalyst surface are relatively weak.

The present study on active sites is important for deeper fundamental understanding of electrocatalysis and the design of new electrocatalysts. However, in-depth study requires more advanced research techniques, as identification of active centres requires *in-situ* experiments under the working conditions of catalytic systems.[66]

2.4 Electrocatalytic reactions in energy conversion and storage

As discussed in Chapter 1, water electrolysers and fuel cells are the most crucial devices for energy conversion and storage in the hydrogen economy. Water splitting is an efficient method for converting renewable electrical energy into chemical energy; and fuel cells will be the primary devices to release the stored chemical energy in households, for transportation and in industry.[74,75]

Water splitting, usually referred to as water electrolysis, is an electrochemical reaction that decomposes H_2O into O_2 and H_2.[76] It is normally driven by a direct electric current. The corresponding reactions occurring at the cathode and anode are referred to as the hydrogen evolution reaction, HER, and oxygen evolution reaction, OER, respectively.

Fuel cells are typically used for converting the energy stored in hydrogen bonds to electricity.[77] They are one of the most attractive electrochemical cells because of their high theoretical energy density and their environmentally-friendly attributes. In those cells, hydrogen is consumed at the anode by an oxidation reaction referred to as the hydrogen oxidation reaction, HOR, whilst oxygen is reduced at the cathode by the reaction referred to as the oxygen reduction reaction, ORR. During operation, direct current electricity will be produced, as electrons will flow from the anode to the cathode through an external circuit.

In order to comprehend the reactions involved in water electrolysers and fuel cells, some fundamental concepts concerning the reaction kinetics, such as the Butler-Volmer equation, overpotential, and exchange current density, require further clarification.

2.4.1 Reaction kinetics

Generally, ***electrolytes*** are substances that conduct ions. When an electric field, E, is applied, the ions in the electrolyte experience electric field force, F_E:

$$F_E = ze_0E \tag{2.14}$$

where e_0 is the elementary charge, and z is the charge of the ion. The ions in the electrolyte move due to the electric field force, and this motion subsequently leads to an ionic electrical current flowing through the electrolyte.

Electrodes are electronic conductors used for exchanging electrons or ions with the non-metallic aspect, for example, a vacuum or air, an electrolyte or a semiconductor. The electrodes can be metals or semiconductors. The electrodes responsible for transferring electrons from electrolyte species to external circuits are usually referred to as anodes, whilst those responsible for delivering electrons to the electrolyte species are usually referred to as cathodes.

Typical energy conversion or storage systems, such as electrolysers and galvanic cells, are comprised of electrodes and electrolytes. For the electrolyser system, when an electric field is applied, cations migrate towards the cathodes and anions towards the anodes; when the applied potential exceeds a specific value (namely the decomposition potential, φ_0), some cations will receive electrons from the cathodes and become reduced, and some anions will lose electrons at the anodes and become oxidised. This

redox process, driven by a direct current, is referred to as ***electrolysis***. With regard to the galvanic cell, the processes are similar but reversed in relation to the electrolyser.

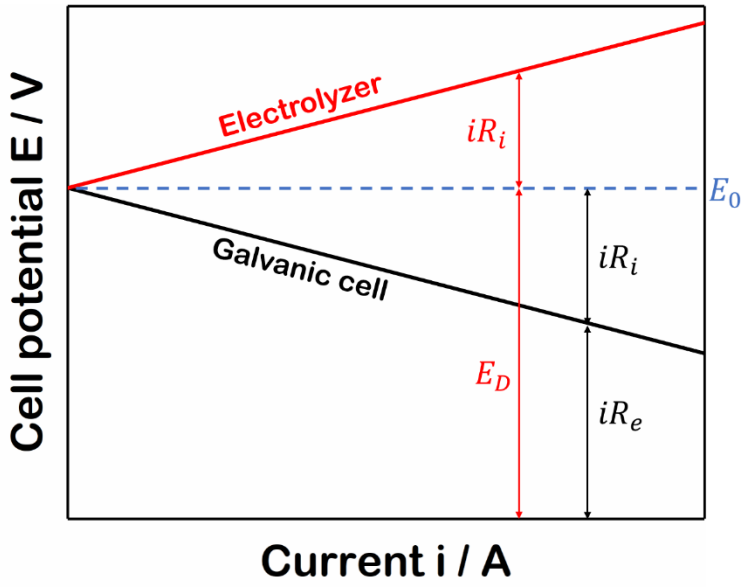

Figure 2.4. Cell potential, E, plotted against load current, i. Red and black lines schematically depict the variation of the potentials for electrolyser systems and galvanic cells, respectively. E_0 is *emf*, E_D - the decomposition potential, R_i - the internal resistance, R_e - the external resistance. When the load current increases, the cell potential will increase in the electrolyser system and decrease in the galvanic cell.

In this work, electrolyser with liquid electrolytes will be explained to describe the relationship between the applied potential and the energy required for driving chemical reactions. As stated, redox reactions in the electrolyser can only occur when the applied potential, φ_c^{elec}, is higher than the decomposition potential, φ_0. At the potential φ_0, the corresponding free energy change, $\Delta_r G$, can be depicted as:

$$\Delta_r G = nF\varphi_0 \qquad (2.15)$$

where n is the number of electrons transferred during the reaction and F is the Faraday constant.

Therefore, the following equations will be established, if the electrolyser is functioning:

$$\text{when} \quad \varphi_c^{elec} > \varphi_0, \quad \text{then,} \quad nF\varphi_c^{elec} - \Delta_r G > 0 \qquad (2.16)$$

In terms of a galvanic cell, if the cell is functioning (namely the cell is discharging), the driving voltage of the external system, φ_c^{galv}, is lower than the electromotive force of the cell, φ_0. Thus, the following equations should be established,

$$\text{when} \quad \varphi_c^{galv} < \varphi_0, \quad \text{then,} \quad nF\varphi_c^{galv} - \Delta_r G < 0 \qquad (2.17)$$

Under standard conditions, i.e. when concentrations are 1 mol dm^{-3} and the pressure is 1 atm, this potential φ_0 is referred to as the ***standard electrode potential***. With regard to the electrolyser system, φ_0 is referred to as the ***decomposition potential*** (E_D).[78] In terms of the galvanic cell, φ_0 is equal to the ***battery electromotive force*** (E_0) / the ***electromotive force of the cell*** (*emf*).[79]

However, due to the internal resistance of electrochemical systems, the measured decomposition potential is higher than its theoretical value; conversely, the observed electromotive force for galvanic cells is always significantly lower (**Figure 2.4**). Moreover, with increasing current, the cell potential increases in the electrolyser system but decreases in the galvanic cell. If only taking the Ohmic drop into consideration, the corresponding relationships between the measured cell potential, E, and the current, i, can be simply indicated in **Equations (2.18)** and **(2.19)** for the electrolyser system and the galvanic cell, respectively (**Figure 2.4**).

$$E = E_D + iR_i \qquad (2.18)$$

$$E = E_0 - iR_i = iR_e \qquad (2.19)$$

where R_i is the internal resistance of electrochemical systems, E_D - the decomposition potential, E_0 - the battery electromotive force, R_e - the external resistance in the electric circuit.[56]

In fact, when a current flows through the cell, causing it to depart from equilibrium, not only will the Ohmic drop affect the cell voltage, but each electrode will display a characteristic current-voltage behaviour; therefore, in general, the measured overall cell voltage will be a combination of both these effects.[56] In **Section 2.4.1.1** and **2.4.1.2**, the system of an electrolyser will be used to discuss the situation of electrochemical equilibrium and non-equilibrium, respectively.

2.4.1.1 Nernst equation

An electrolyser can only operate if the applied potential exceeds the decomposition potential. In order to investigate electrochemical systems, the first step should be to define this potential.

The chemical potential for a component *i* in a mixture, μ_i, is defined as:

$$\mu_i = \mu_i^{0\perp} + RT\, ln\, a_i \tag{2.20}$$

where a_i is the activity of component *i*, $\mu_i^{0\perp}$ is the corresponding chemical potential at unit activity, T - temperature, R - universal gas constant.

Therefore, the total free energy of a mixture of all components can be written as:

$$G = \sum_i n_i \mu_i \tag{2.21}$$

Assuming that a reaction takes place in such a large volume that the fractions of both reactants and products are not considerably changed, the free energy change can be written as

$$\Delta G_r = \sum_i v_i \mu_i \tag{2.22}$$

where v_i is the stoichiometric number of component *i.*

At equilibrium, the free energy change, ΔG_r, must be zero. Thus, the fundamental equation for a chemical reaction at equilibrium can be obtained according to **Equation (2.22)**,

$$\sum_i v_i \mu_i = 0 \tag{2.23}$$

In electrochemical systems, materials of two different phases are brought in contact with each other, namely electrode and electrolyte, resulting in a potential difference, φ. If taking this potential difference φ between electrode and electrolyte into account, the free energy change becomes

$$\Delta G_r = \sum_i v_i(\mu_i + z_i F\varphi) = \sum_i v_i \tilde{\mu}_i \tag{2.24}$$

The introduced $\tilde{\mu}_i$ is defined as the ***electrochemical potential***, and the potential φ is always referred to as the ***Galvani potential***. At the condition of electrochemical equilibrium, the fundamental reaction equilibrium expression (2.23) becomes

$$\sum_i v_i \tilde{\mu}_i = 0 \tag{2.25}$$

Taking the simplest redox reaction as an example, we have

$$S_{Red} \Leftrightarrow S_{Ox} + ne^- \tag{2.26}$$

where S_{Red} and S_{Ox} are termed the reduced and oxidised components in the redox reaction, respectively. When this reaction is at equilibrium, namely that the double layer at the electrode interface and the Galvani potential difference stabilise, according to **Equation (2.25)**, the following relationship can be achieved

$$\tilde{\mu}_{Red} = \tilde{\mu}_{Ox} + n\tilde{\mu}_{e^-} \tag{2.27}$$

Combined with **Equations (2.24)** and **(2.20)**, this equation becomes

$$\mu_{Red}^{0\perp} + RT \ln a_{Red} + nF\varphi_M = \mu_{Ox}^{0\perp} + RT \ln a_{Ox} + nF\varphi_S + n\mu_{e^-}^0 \tag{2.28}$$

Therefore, the Galvani potential difference, $\Delta\varphi$, can be written as

$$\begin{aligned} \Delta\varphi = \varphi_M - \varphi_S &= \frac{\mu_{Ox}^{0\perp} + n\mu_{e^-}^0 - \mu_{Red}^{0\perp}}{nF} + \frac{RT}{nF} ln \frac{a_{Ox}}{a_{Red}} \\ \Delta\varphi &= \Delta\varphi^0 + \frac{RT}{nF} \ln \frac{a_{Ox}}{a_{Red}} \end{aligned} \tag{2.29}$$

where $\Delta\varphi^0$ is the ***standard Galvani potential difference***. In the case that a_{Ox} and a_{Red} are equal, the standard Galvani potential difference is the Galvani potential difference between the electrolyte and the electrode.

For a normal redox reaction on the electrodes as shown in **Equation (2.30)**

$$\sum_{Red} n_{red} S_{Red} \Leftrightarrow \sum_{Ox} n_{Ox} S_{Ox} + ne^- \tag{2.30}$$

Equation (2.28) then becomes

$$\begin{aligned} &\sum_{Red} n_{Red} \left(\mu_{Red}^{0\perp} + RT \ln a_{Red}^{n_{Red}}\right) + nF\varphi_M \\ &\qquad = \sum_{Ox} n_{Ox} \left(\mu_{Ox}^{0\perp} + RT \ln a_{Ox}^{n_{Ox}}\right) + nF\varphi_S + n\mu_{e^-}^0 \end{aligned} \tag{2.31}$$

Therefore, the generalised Nernst equation can be obtained as:

$$E = E^0 + \frac{RT}{nF} \ln \frac{\prod_{Ox} a_{Ox}^{n_{Ox}}}{\prod_{Red} a_{Red}^{n_{Red}}} \tag{2.32}$$

where $\prod_t a_t^{n_t} = a_{S_1}^{n_1} \cdot a_{S_2}^{n_2} \cdot \ldots \cdot a_{S_i}^{n_i}$.

The Nernst equation relates the potential for an electrochemical reaction with the activities of the species participating in the reaction, the standard electrode potential and the temperature at the situation of electrochemical equilibrium.

In addition, according to **Equations (2.28)** and **(2.29)**, defining the absolute value of the potential appears to be impossible. In other words, $\Delta\varphi$ and $\Delta\varphi^0$ are not experimentally measurable. Therefore, an additional electrode with a constant Galvani potential difference is used as a reference point in the electrochemical systems. This electrode is referred to as the ***reference electrode***, and the corresponding system is named the three-electrode system (with a working electrode, reference electrode and counter electrode). A widely accepted reference electrode is the standard hydrogen electrode (SHE) since this electrode can quickly and reproducibly establish its equilibrium potential and maintain this potential well over time.[80] But in fact, the reversible hydrogen electrode (RHE) is the reference electrode used for experimental measurements because the SHE is closely associated with the pH of the electrolyte and defined on the basis of an 'ideal' solution. According to the Nernst equation, the relationship between the potentials versus the RHE and the SHE follows the equation[81]

$$E_{RHE} = E_{SHE} + \ln 10 \cdot \frac{RT}{2F} \log \left[\frac{a_{H_3O^+}^2}{p_{H_2}/p^0} \right] \tag{2.33}$$

Thus, at 25°C and unit H_2 partial pressure ($p_{H_2} = p^0$),

$$E_{RHE} = E_{SHE} + 0.0591 \cdot pH \tag{2.34}$$

As there are many reference electrodes to choose from, e.g., saturated calomel electrode (SCE), mercury-mercurous sulfate electrode (MSE) and mercury-mercury sulfate electrode (MMS), the MMS was chosen as the reference electrode for all the measurements in this research. The potential versus the MMS can be linked to that versus the RHE at room temperature through the following equation

$$E_{RHE} = E_{MMS} + 0.6618 + 0.0591 \cdot pH \tag{2.35}$$

2.4.1.2 Butler-Volmer equation

The Nernst equation describes the situation of the electrochemical system at equilibrium, but what about non-equilibrium states? In other words, based on the Nernst equation, the relationship between the potential of the reaction and activities of chemical species taking part in the reaction is established, but how does the potential influence the electrical current flowing through electrochemical systems when reactions occur on electrodes? Kinetic considerations are given by the Butler-Volmer equation.

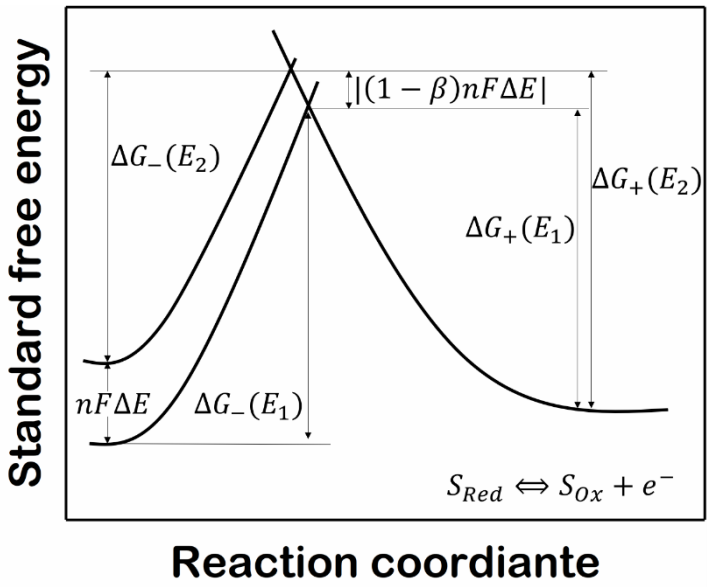

Figure 2.5. Schematic of the free energy change in a redox reaction when one electron is transferred from the electrode. Only parts of the free energy change are reflected in the free energy change of the activated species.

According to the definition, the current density, j, for an electrochemical reaction is given by

$$j = nFv \tag{2.36}$$

where v is the reaction rate, n is the number of electrons participating in the reaction, and F is the Faraday constant.

At the situation near the equilibrium, when the mass transfer-influence is so small that can be disregarded, the reaction rate v is given by

$$v = k \cdot c = k^0 exp(-\frac{\Delta G}{RT}) \cdot c \tag{2.37}$$

where k is the reaction rate constant, c is the concentration of reactants near the electrode surface. For this situation, the reaction rate constant, k, only depends on the free energy change, as given by **Equation (2.37)**; the concentration of reactants, c, is constant.[56]

In the simplest case of redox reactions, i.e. in the case of **Reaction (2.26)** and **Figure 2.5**, the cathodic current density at the potential E_1, $j^-(E_1)$, is

$$j^-(E_1) = -nFv_{Red} = -nFc_{Ox}k_0'^- \, exp\left[-\frac{\Delta G_-(E_1)}{RT}\right] \tag{2.38}$$

where c_{Ox} is the concentration of oxidised species. For the situation near the equilibrium, the transfer of the oxidised species from the bulk to the electrode surface is quick enough to keep the concentration c_{Ox} constant. Besides, the negative sign in this equation accounts for electrons flow from the electrode to the solution.

Only parts of the change in the free energy, caused by the potential change, are reflected in the free energy change of the activated species (**Figure 2.5**). When the electrode potential is changed from E_1 to E_2, there is no change in the free energies of the left part of the **Reaction (2.26)** (also shown in **Figure 2.5**), $\Delta G_+(E)$, which means that not all free energy changes appear for the activated species.[56] For simplicity, an asymmetry factor β is introduced, and according to **Equation (2.16)**, the corresponding free energy changes on the cathode and anode are indicated in the **Equations (2.39)** and **(2.40)**, respectively.

$$\Delta G_-(E_2) = \Delta G_-(E_1) + \beta nF \cdot \Delta E \tag{2.39}$$

$$\Delta G_+(E_2) = \Delta G_+(E_1) - (1-\beta)nF \cdot \Delta E \tag{2.40}$$

Therefore, on alteration of the electrode potential from E_1 to E_2, the current density on the cathode can be written as

$$j^-(E_2) = nFc_{Ox}k_0'^- \, exp\left[-\frac{\Delta G_-(E_1) + \beta nF \cdot \Delta E}{RT}\right] \tag{2.41}$$

As stated in **Section 2.4.1.1**, a reference electrode is needed to measure the electrode

potential. Thus, if taking the potential E_1 as a reference point, i.e., the potential of the reference electrode, the potential change ΔE can be treated as the measured potential, E. Besides, as the reference electrode is independent of factors such as c_{Ox}, the part of $exp[-\Delta G_{-}(E_1)/RT]$ is constant and can be taken into the reaction rate constant, k_0^-. **Equation (2.41)** for the cathodic current density then becomes

$$j^-(E) = -nFc_{Ox}k_0^- \, exp\left[-\frac{\beta nF \cdot E}{RT}\right] \tag{2.42}$$

Similar to the cathodic current density, the anodic current density can be written as:

$$j^+(E) = +nFc_{Red}k_0^+ \, exp\left[+\frac{(1-\beta)nF \cdot E}{RT}\right] \tag{2.43}$$

At the equilibrium potential, E_r, the net current should be zero, which means $j^-(E_r) = j^+(E_r) = j_0$. j_0 is referred to as the ***exchange current density***.

$$j^-(E_r) = -j_0 = -nFc_{Ox}k_0^- \, exp\left[-\frac{\beta nF \cdot E_r}{RT}\right] \tag{2.44}$$

$$j^+(E_r) = +j_0 = +nFc_{Red}k_0^+ \, exp\left[+\frac{(1-\beta)nF \cdot E_r}{RT}\right] \tag{2.45}$$

Therefore, at equilibrium, since **Equation (2.44)** is equal to **Equation (2.45)**, after the rearrangement, the following equation can be written

$$E_r = \frac{RT}{nF}\ln\frac{k_0^-}{k_0^+} + \frac{RT}{nF}\ln\frac{c_{Ox}}{c_{Red}} \tag{2.46}$$

If E^0 is used to replace the first summand, this equation becomes the Nernst equation mentioned in **Section 2.4.1.1**. But it should be noted that this equation is obtained under the condition that the salt in the electrolytes is excessive. Thus, the activity coefficients of the oxidised or reduced species, a, are likely independent of the corresponding concentration, c.

Additionally, the exchange current density, j_0, can be calculated from the **Equations (2.44)** and **(2.45)** by introducing the definition formula of E_r (namely the **Equation (2.46)**),

$$-j_0 = nFk_0^- \ (c_{Red}^{\beta} c_{Ox}^{1-\beta}) exp\left[-\frac{\beta nF \cdot E_0}{RT}\right] \tag{2.47}$$

$$+j_0 = +nFk_0^+ \ (c_{Red}^{\beta} c_{Ox}^{1-\beta}) exp\left[+\frac{(1-\beta)nF \cdot E_0}{RT}\right] \tag{2.48}$$

As the net current is zero, **Equation (2.47)** should be equal to **Equation (2.48)**,

$$nFk_0^- \ exp\left[-\frac{\beta nF \cdot E_0}{RT}\right] = nFk_0^+ \ exp\left[+\frac{(1-\beta)nF \cdot E_0}{RT}\right] \equiv nFk_0 \tag{2.49}$$

therefore,

$$j_0 = nFk_0 \ c_{Red}^{\beta} c_{Ox}^{1-\beta} \tag{2.50}$$

At the situation near the equilibrium, the actual electrode potential, E, should include not only the equilibrium potential, E_r, but also the ***overpotential***, η. Thereby, the overpotential is the difference between the equilibrium potential and the applied potential required to initiate the electrode reactions. The net current is the algebraic sum of the cathodic and anodic current density:

$$j = j^+ + j^- = j_0 \left\{exp\left[\frac{(1-\beta)nF \cdot \eta}{RT}\right] - exp\left[-\frac{\beta nF \cdot \eta}{RT}\right]\right\} \tag{2.51}$$

This is the famous Butler-Volmer equation. But note that this equation is under the condition of relatively low current density; i.e. there is no mass transfer effect. It also does not account for the adsorbate-adsorbate interactions.

At the situation far from the equilibrium, when the mass transfer influence has to be considered, the concentration of the activated species near the electrode surface will differ from the bulk concentration and change with time due to the mass transfer limitations.[82] Therefore, the reaction rate, v, in **Equation (2.37)** should be modified as

$$v = k \cdot c(0,t) = k^0 exp(-\frac{\Delta G}{RT}) \cdot c(0,t) \tag{2.52}$$

The more general expression of the Butler-Volmer equation, applicable to the mass transfer-influenced conditions, can be written as[81]:

$$j = j_0 \left\{ exp\left[\left(\frac{c_{Red}(0,t)}{c_{Red}} \right) exp\left[+ \frac{(1-\beta)nF \cdot \eta}{RT} \right] \right. \right. \\ \left. \left. - \left(\frac{c_{Ox}(0,t)}{c_{Ox}} \right) exp\left[- \frac{\beta nF \cdot \eta}{RT} \right] \right] \right\} \tag{2.53}$$

2.4.1.3 Tafel equation, overpotential and limiting current density

Several fundamental concepts related to this work, i.e. Tafel equation, overpotential, and limiting current density, are introduced based on the Butler-Volmer equation.

When there is no mass transfer effect, the overpotential can be written based on Butler-Volmer equation (**Equation (2.51)**):

Cathodic reactions:
$$\eta_{el} = \frac{RT}{\beta nF} ln\, j_0 - \frac{RT}{\beta nF} ln|j| \tag{2.54}$$

Anodic reactions:
$$\eta_{el} = -\frac{RT}{(1-\beta)nF} ln\, j_0 + \frac{RT}{(1-\beta)nF} ln|j| \tag{2.55}$$

Therefore, the overpotential has the following form:

$$\eta = A + B\, ln|j| \tag{2.56}$$

This semi-logarithmic equation is the so-called ***Tafel equation***, and B is the ***Tafel slope***. This overpotential is mainly determined by the charge transfer, and thus termed as ***transfer overpotential***, η_{el}.

Under the mass transfer-influenced conditions, the overpotential can be written based on the more general expression of the Butler-Volmer equation (**Equation (2.53)**):

Cathodic reactions:
$$\eta = -\frac{RT}{\beta nF} ln \frac{|j|}{j_0} - \frac{RT}{\beta nF} ln \frac{c_{Ox}^0}{c_{Ox}^s} \tag{2.57}$$

Anodic reactions:
$$\eta = +\frac{RT}{(1-\beta)nF} ln \frac{|j|}{j_0} + \frac{RT}{(1-\beta)nF} ln \frac{c_{Red}^0}{c_{Red}^s} \tag{2.58}$$

where c^s is the concentration of oxidised/reduced species near to the electrode surface, and c^0 the corresponding concentration in bulk. Obviously, the first parts of **Equations (2.57)** and **(2.58)** are the transfer overpotential η_{el}. Therefore, the second

parts are defined as the ***diffusion overpotential***, η_{diff}.

Cathodic reactions:
$$\eta_{diff} = -\frac{RT}{\beta nF} ln \frac{c_{Ox}^0}{c_{Ox}^s} \quad (2.59)$$

Anodic reactions:
$$\eta_{diff} = +\frac{RT}{(1-\beta)nF} ln \frac{c_{Red}^0}{c_{Red}^s} \quad (2.60)$$

This diffusion overpotential is clearly caused by the difference in species concentration between the near-electrode-surface and the bulk. The total overpotential, η_{tot}, is then

$$\eta_{tot} = \eta_{el} + \eta_{diff} \quad (2.61)$$

If continuing to increase the overpotential (at very high current density), the current is not determined by the charge transfer but totally by diffusion. To simplify the discussion, the one dimentional case is only considered. According to Fick's first law, the following equation can be written

$$J_i = -D \frac{\partial c_i}{\partial x} \quad (2.62)$$

where J_i is the diffusion flux of electroactive species *i*, c_i is the concentration of electroactive species *i*, and D is the diffusion constant. If this equation is combined with **Equation (2.36)**, the current density then can be written as:

$$j = \sum_i nFJ_i = \sum_i -nFD(\frac{\partial c_i}{\partial x})_{x=0} = nFD \frac{c^0 - c^s}{\delta N} \quad (2.63)$$

where δN is referred to as Nernst diffusion layer thickness, c^0 is the concertation in bulk, and c^s is the concertation at the electrode surface. If assuming that the reaction on the electrode is fast enough to make c^s approach zero, the current density then becomes a limiting time-independent value, which is known as ***limiting current density***, j_{lim}:

$$j_{lim} = nFD \frac{c^0}{\delta N} \quad (2.64)$$

The corresponding potential range is referred to as the limiting current range.

The corresponding diffusion overpotential is also changed. The potential drop caused

by the charge transfer is so small that η_{el} can be neglected. Thereby, η_{diff} can be seen as the potential drop from the bulk of electrolytes to the surface of electrodes at equilibrium. According to the Nernst equation, η_{diff} can be given as:

$$\eta_{diff} = \frac{RT}{nF} ln \frac{c^s}{c^0} \tag{2.65}$$

If dividing **Equation (2.63)** by **Equation (2.64)**, the following equation will be obtained:

$$\frac{j}{j_{lim}} = 1 - \frac{c^s}{c^0} \tag{2.66}$$

Combined with **Equation (2.66)**, **Equation (2.65)** becomes

$$\eta_{diff} = \frac{RT}{nF} ln(1 - \frac{j}{j_{lim}}) \tag{2.67}$$

In a word, at a low overpotential, the reaction kinetics are mainly controlled by the charge transfer; at a medium overpotential, the influence from both the charge transfer and the diffusion should be considered; at a very high overpotential, the reaction is presumably controlled by the diffusion.

2.4.2 Water electrolysis

Water electrolysis is the process of decomposition of water into oxygen and hydrogen by applying an electric current. Oxygen and hydrogen can be separately collected at the anode and cathode, where the volume ratio of oxygen to hydrogen is 1:2.

The invention of water electrolysers commenced in the 18th century.[83] In 1789, Deiman and Troostwijk[84] discovered that gas evolves 'if a gold wire is discharged in water'. In 1800, water electrolysis was conducted by Nicholson and Carlisle using a voltaic pile, namely the first electrical battery.[85] Following decades of development, thanks to Gramme and Lachinov[86], the cost of water electrolysis was significantly reduced, and water electrolysis was instituted for the industrial production of hydrogen. The first large-scale commercial electrolyser was built in Canada in the 1920s.[87] To date, numerous researchers are still attempting to reduce the cost, especially constituted by the substantial demand for electricity.

The overall reaction of water electrolysis (**Figure 2.6**) is

$$2\ H_2O(l) \rightarrow 2\ H_2(g) + O_2(g)$$

At standard atmospheric pressure and temperature, the equilibrium cell potential is 1.23 V. According to the Nernst equation, this theoretical cell potential is independent of the pH of the electrolyte. Although the theoretical value is just 1.23 V, the typical working potential of commercial electrolysers is significantly higher, typically 1.8 V to 2 V, due to the unavoidable overpotential[34].

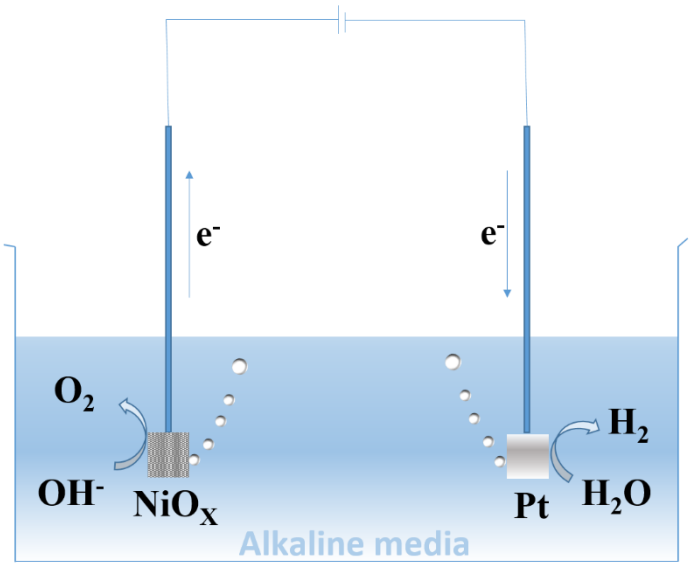

Figure 2.6. A scheme of water electrolysis in basic media. During water electrolysis, OER takes place at the anode whilst HER occurs at the cathode.

Using proper catalysts is an effective way to reduce the overpotential in water electrolysis, as they can reduce the activation energy for the reaction. The choice of the catalyst determines the cell potential of electrolysers and the conversion efficiency. Therefore, the research focus is set upon the designing new electrocatalysts.[88,89]

Nevertheless, due to the high energy density of hydrogen and its environmentally-friendly characteristics, water electrolysis has already been applied in the industry for almost a century. At present, there are primarily two distinct types of industrial electrolysers. One is an alkaline electrolyser[90], in which anodes, cathodes, and electrolytes typically use Ni/Co/Fe composites, Ni-based materials, and highly concentrated KOH or NaOH solutions. The optimal temperature is from 60 to 80 ℃, the typical current density is 0.2-0.4 A cm^{-2} and the hydrogen production is less than

760 N m^3 h^{-1}. The advantage of this electrolyser is that the electrode materials, normally non-noble metal composites, are relatively cheap, but the low conversion efficiency severely limits its application. Another one is the polymer electrolyte membrane (PEM) electrolyser. It typically uses Ir, Pt, and solid polymer electrolytes as anodes, cathodes, and electrolytes, respectively.[91] The optimal temperature is from 50 to 80 ℃, the operational current density is from 0.6 to 2 $A\,cm^{-2}$ and the hydrogen production is less than 30 N m^3 h^{-1}. This electrolyser has a good conversion efficiency, a high current density and a compact design, but the expensive electrode materials and membranes limit wider application of PEM-electrolysers.

2.4.2.1 Hydrogen evolution reaction

During water electrolysis, hydrogen generates at the cathode side of the cell. The reaction taking place at this electrode is referred to as HER. The mechanism of this considerably simple reaction has been widely investigated in the literature, especially in the case of Pt.[92]

In acidic media, the reaction equation at the cathode is

$$2\,H^+ + 2\,e^- \rightarrow H_2$$

The corresponding mechanism involves a two-electron transfer and either follows so-called Volmer-Tafel step or the Volmer-Heyrovsky step[93,94], as shown in the following equations (* corresponds to an adsorption site)

$$H^+ + e^- + * \rightarrow *H \qquad \text{Volmer step}$$

$$2\,*H \rightarrow H_2 + 2\,* \qquad \text{Tafel step}$$

$$H^+ + e^- + *H \rightarrow H_2 + * \qquad \text{Heyrovsky step}$$

Recently, it has been observed that both types of electron transfer are present in acidic HER, especially at high overpotentials.[95] The Tafel step is often recognised as the rate-determining step at least for the acidic HER on Pt-based electrodes[96].

In alkaline media, the HER reaction follows the below scheme

$$2\,H_2O + 2\,e^- \rightarrow 2\,OH^- + H_2$$

resembling that in acidic media, the mechanism is comprised of a two-electron transfer

and follows either the Volmer-Tafel step or the Volmer-Heyrovsky step, as shown below. An additional water dissociation step is added to the Volmer step.[97]

$$H_2O + e^- + * \rightarrow *H + OH^-$$ Volmer step

$$2\ *H \rightarrow H_2 + 2\ *$$ Tafel step

$$H_2O + e^- + *H \rightarrow H_2 + OH^- + *$$ Heyrovsky step

In contrast to the mechanism in acidic media, the Volmer step becomes the rate-determining step for Pt-based electrodes in alkaline electrolytes resulting in their lower overall HER perfomance.[98]

According to the Sabatier principle, the highest activity should be observed on catalysts with an optimal hydrogen binding energy, as the adsorbed hydrogen is the only intermediate in both acidic and basic solutions. Relation of theoretical hydrogen binding energies with experimental HER activities of different materials leads to the HER volcano plot shown in **Figure 2.1**. To date, the highest HER performance in both acidic and alkaline solution has been achieved using Pt-based electrocatalysts. Recently, however, almost comparable alkaline HER activities have been reported for several non-noble metal-based materials, such as NiN_3[99] and CoP[100].

Although the HER has undergone decades of investigation and solely involves one intermediate species, there are still several unsolved problems. For instance, improving the alkaline HER activity of Pt to a similar level as its performance in acidic media is crucial in order to improve the low conversion efficiency of alkaline electrolysers. Moreover, the design of new non-noble metal catalysts for the acidic HER would be highly beneficial to reduce the cost of the devices.

2.4.2.2 Oxygen evolution reaction

At the anode side of a water electrolyser, oxygen is produced during so-called OER. Typically, it occurs on oxidised metal surfaces at relatively high overpotentials.[101,102]

In acidic media, the reaction equation is

$$2\ H_2O \rightarrow O_2 + 4\ e^- + 4\ H^+$$

The corresponding mechanism is much more complex than that of the HER. It involves a four-electron transfer and has at least three reaction intermediates, being *OOH, *OH,

*O. Though there are several possible reaction pathways, those shown in the following equations are widely accepted in the literature[103]:

$$H_2O + * \rightarrow *OH + H^+ + e^-$$

$$*OH \rightarrow *O + H^+ + e^-$$

$$*O + H_2O \rightarrow *OOH + H^+ + e^-$$

$$*OOH \rightarrow O_2 + H^+ + * + e^-$$

In alkaline solutions, the reaction equation is

$$4\ OH^- \rightarrow 2\ H_2O + O_2 + 4\ e^-$$

Similar to that in acidic media, the mechanism in alkaline solutions is also based on the four-electron transfer, which includes the same three different reaction intermediates. The most recognised reaction pathway is shown as follows[104]:

$$OH^- + * \rightarrow *OH + e^-$$

$$*OH + OH^- \rightarrow *O + H_2O + e^-$$

$$*O + H_2O + OH^- \rightarrow *OOH + H_2O + e^-$$

$$*OOH + OH^- \rightarrow O_2 + H_2O + * + e^-$$

However, regardless of the electrolyte, the reaction rate of the OER is very low as compared to the HER. Although considerable efforts have been made to improve the OER performance, the poor stability of the oxide electrodes and the so-called 'scaling relations' are the critical bottlenecks of the OER, as explained below.[105] The surface structure of the electrode materials used for the OER changes over time due to an inevitable 'oxidation process' that occurs during the reaction. This process results in poor long-term stability[106] and is difficult to study *in-situ*. Moreover, it is probable that some components of the oxide electrodes are directly involved in the OER. Shao-Horn *et al.*[107] recently provided direct experimental evidence that lattice oxygen, i.e., oxygen incorporated in the bulk structure of the electrode material, is also involved in the OER. Besides, based on thermodynamic calculations, the OER activity indeed depends on the binding energies of the reaction intermediates (i.e., *OOH, *OH, *O). Optimal adsorption energies of these critical intermediates should affirm a superior activity

according to the Sabatier principle. However, Norskov et al[108] and Rossmeisl et al[109] discovered that the adsorption energies of *OOH, *OH, and *O are linearly related, also referred to as the 'scaling relations' (**Figure 2.7**). For example, RuO_x, the most active electrocatalyst for OER, binds *OOH too strongly and *O too weakly. The *O binding has to be strengthened in order to promote OER kinetics, which will essentially lead to the undesirable strengthening of *OOH binding.[105] Therefore, improving the OER performance and understanding its internal mechanism are required to initially address these limiting factors.

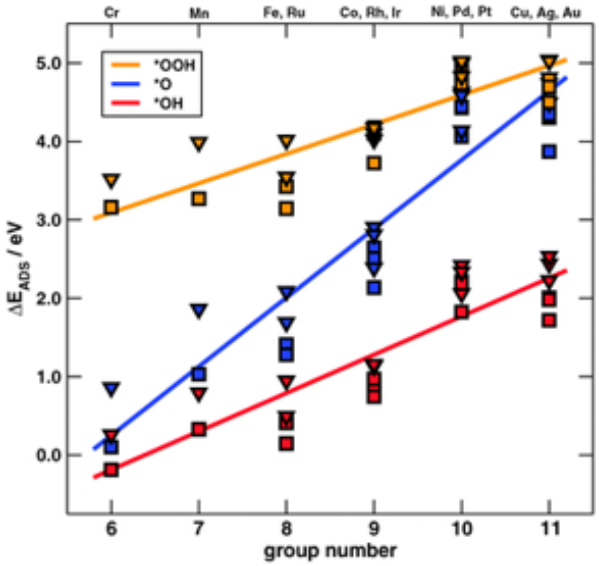

Figure 2.7. Trends in adsorption energies of OER/ORR reaction intermediates. The values were calculated for doped graphite-based materials, in which the active sites are composed of transition metal and nitrogen atoms. The so-called 'scaling relations' indeed exist between the adsorption energies of *OH (red), *OOH (yellow) and *O (blue). There is a constant separation of ~3.10 eV between the adsorption levels of *OH and *OOH; *O is located in-between. The triangle and square symbols are values obtained from two different unit cells. The lines are a guide to the eye. The graph is taken from ref.109. Copyright 2011, The Royal Society of Chemistry.

2.4.3 Fuel cells

A fuel cell is an electrochemical device that converts the chemical energy stored in fuels into electricity. The theoretical conversion efficiency of fuel cells is exceptionally high, because it uses a pair of electrochemical reactions, directly converting the chemical energy of fuels into electricity, and thus is not limited by the Carnot efficiency. In addition, as it typically uses oxygen and hydrogen without any mechanical transmission component, there is negligible noise pollution and no emission of hazardous gases.

Therefore, fuel cells are one of the most promising power generation technologies for the future.[110,111]

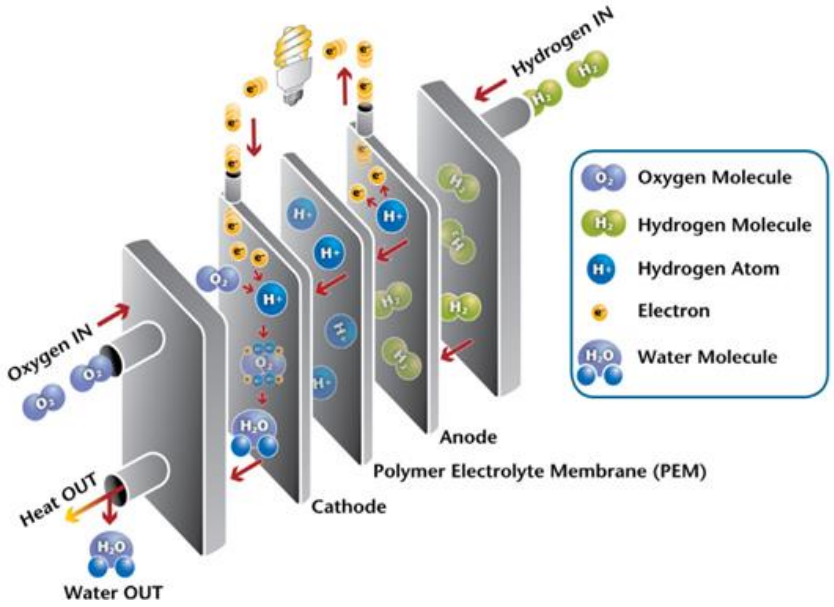

Figure 2.8. Schematic of a hydrogen PEM fuel cell. At the anode, HOR takes place, i.e., the supplied fuel, H_2, decomposes into protons and electrons. The protons then move through the electrolyte to take part in the reaction at the cathode. At the cathode, ORR takes place, i.e., oxygen (normally from air) is reduced, and then together with the hydrogen ions, water is produced. The continuous reactions drive the electrons through the external circuit, resulting in electric power, while only water remains as a waste product. This figure is taken from ref.112.

The first fuel cells were constructed in the 1840s, when Grove[113] and Schönbein[113] discovered that currents were generated from oxygen and hydrogen dissolved in water when Pt electrodes were used. In the 1950s, the so-called 'Grubb-Niedrach fuel cell' was invented[114], with improved fuel cell design; and Pt was deposited onto the membrane to act as a catalyst. In the 1960s, the commercial use of fuel cells was realised in the NASA space programme.[115] In 1991, Billings[116] developed the first hydrogen fuel cell car. At present, various types of fuel cells have been developed, such as the alkaline fuel cell (AFC), the solid oxide fuel cell (SOFC) and the polymer electrolyte membrane fuel cell (PEMFC).[117]

Fuel cells are typically comprised of an anode, a cathode, and an electrolyte. The difference from other energy conversion devices, for example, batteries, is that the electrodes in fuel cells do not contain any reactive substance yet rather serve as catalysts for the corresponding reactions on their surface. In principle, as long as fuel is supplied from the outside, the cells can maintain power generation. Taking an alkaline hydrogen-

oxygen fuel cell as an example, the reactions occurring in the fuel cells are reverse of those in water electrolysis, as follows:

Overall reaction	$½\ O_2 + H_2 \rightarrow H_2O$
Anodic reaction	$H_2 + 2\ OH^- \rightarrow 2\ H_2O + 2\ e^-$
Cathodic reaction	$½\ O_2 + H_2O + 2\ e^- \rightarrow 2\ OH^-$

Furthermore, the occurring reactions depend on the electrolytes used. For instance, the reactions occurring in a phosphoric acid fuel cell (PAFC) and PEMFC are associated with the hydrogen ions in the electrolyte, as follows:

Overall reaction	$½\ O_2 + H_2 \rightarrow H_2O$
Anodic reaction	$H_2 \rightarrow 2\ H^+ + 2\ e^-$
Cathodic reaction	$½\ O_2 + 2\ H^+ + 2\ e^- \rightarrow H_2O$

As shown in **Figure 2.8**, the supplied fuel (H_2) decomposes into protons and electrons at the anode. The protons then move to the cathode side through the electrolyte. Meanwhile, the electrons transition through the external load circuit and participate in the cathodic reaction. Continuous reactions drive the electrons through the external circuit, resulting in harvestable electricity, whilst only water remains as a waste product.

2.4.3.1 Hydrogen oxidation reaction

The anodic reaction in fuel cells is referred to as HOR. The HOR can be considered to be the reverse of the HER, since adsorbed hydrogen is the only reaction intermediate for both reactions. Thus, to a certain extent, an efficient catalyst for HER should also exhibit a considerable activity towards the HOR. As expected, numerous experiments have proven that the volcano plot of the HER can partially be applied to the HOR.[118,119] Therefore, the bottlenecks impairing the HER also affect the kinetics of the HOR.

Conceivably, the most significant obstacle is still the discrepancy of the performance in alkaline media in comparison with acidic solutions. The kinetics of the HOR in alkaline media is almost an order of magnitude slower than in acidic solutions.[120] Although there are various associated hypotheses, the most widely accepted one was proposed by Gasteiger et al.[121]. It suggests that the reactions in alkaline media follow the Heyrovsky-

Volmer mechanism, while the reactions in acidic solutions potentially follow a Nernstian hydrogen diffusion overpotential relationship, resulting in the relatively fast kinetics. Evidently, for the commercial application of alkaline fuel cells, it is vital to enhance the sluggish HOR kinetics. To date, the most practical and feasible solutions are modifying noble metal catalysts, which generally exhibit high acidic HOR activities, for example, $Ni(OH)_2$ ad-islands on Pt(111)[98], Ir-V nanoclusters[122], as well as designing new catalysts such as PdCu[25], PtRu[98] alloys.

Another complication is the limited abundance of the used materials. As is well- known, for fuel cells operating under acidic conditions, Pt-based materials are still the primary catalysts limiting commercial applications.[123] With this in mind, significant effort has been made to design novel catalytic materials[124,125]. Unfortunately, the harsh conditions in the acidic fuel cell appear to be challenging for the vast majority of potential candidates. Consequently, the principal solution is an attempt to decrease the mass loading of noble metal catalysts whilst maintaining a substantial HOR activity.

2.4.3.2 Oxygen reduction reaction

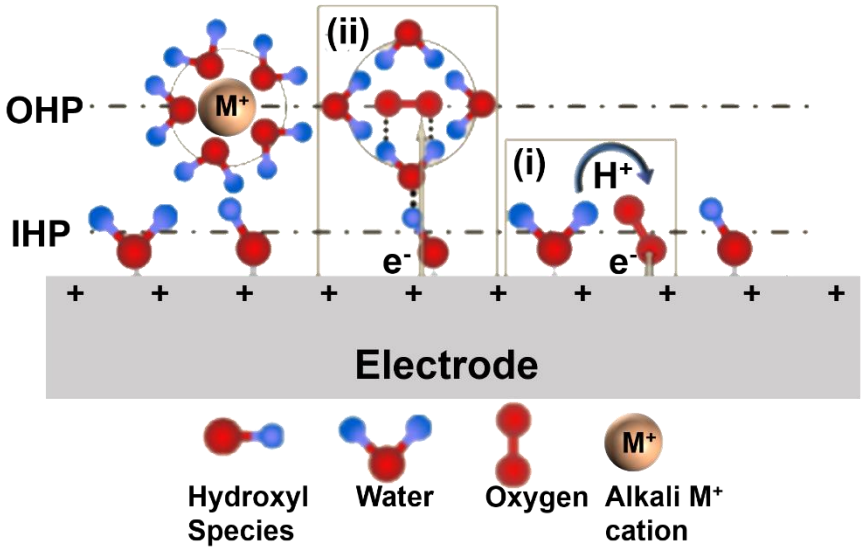

Figure 2.9. Schematic illustration of the ORR mechanisms in alkaline media: inner-sphere (inset i) and outer-sphere (inset ii) electron transfer mechanisms. The inner-sphere electron transfer mechanism is the well-known four-electron transfer process, in which oxygen is directly or serially reduced to hydroxide ions. The outer-sphere electron transfer mechanism is a two-electron reduction promoted by the noncovalent hydrogen bonding forces between solvated oxygen and specifically adsorbed hydroxyl species, in which HO_2^- ions are formed. This graph is taken from ref.126. Copyright 2013, American Chemical Society.

In fuel cells, the oxygen reduction at the cathode side is referred to as the ORR. Over the decades, it has been a prominent topic in the field of electrochemistry due to the high overpotential that is required to drive the reaction, which is analogous to the OER. The mechanism of the ORR is substantially different from the OER, although similar reaction intermediates are involved, namely *OOH, *OH, and *O.

Taking commercial Pt/C (Pt on carbon support) in alkaline electrolytes as an example, the accepted mechanisms are inner- and outer-sphere electron transfers (**Figure 2.9**).[126] With regard to the inner-sphere electron transfer, oxygen, which is dissolved in the electrolyte, adsorbs at the active sites of Pt. Then, the four-electron transfer occurs as follows:

In alkaline media,

Four-electron pathway:

$$O_2 + H_2O + * + e^- \rightarrow *OOH + OH^-$$

$$*OOH + H_2O + e^- \rightarrow *O + H_2O + OH^-$$

$$*O + H_2O + e^- \rightarrow *OH + OH^-$$

$$*OH + e^- \rightarrow OH^- + *$$

Two-electron pathway:

$$O_2 + H_2O + * + e^- \rightarrow *OOH + OH^-$$

$$*OOH + H_2O + e^- \rightarrow HO_2^- + H_2O + *$$ 1st step

$$HO_2^- + H_2O + 2\ e^- \rightarrow 3\ OH^-$$ 2nd step

In the outer-sphere electron transfer, adsorbed OH potentially functions as a bridge site. As such, in the first step of the two-electron pathway, HO_2^- is primarily produced from dissolved oxygen near the Pt-OH sites. This outer-sphere electron transfer explains the oxidation peak of ring electrodes appearing near 0.8 V_{RHE} in RRDE measurements of the ORR.[126] Similar to alkaline media, the aforementioned four- and two-electron pathways also both exist in acidic media. The apparent difference is that during the so-called two-electron pathway, H_2O_2 can be produced, as it is rather stable in acidic media.[127] However, it is worth acknowledging that an in-depth understanding of the ORR mechanism is still not achieved.

As stated in **Section 2.4.2.2**, similar poor stability of the electrodes and so-called 'scaling relations' also severely hinder the improvement of the ORR electrocatalysts. Although Pt/C is the state-of-the-art material used in commercial fuel cells for the ORR, Pt is rare and expensive, and the achieved activity in industrial applications rarely coincides with (scientific) experimental results.[128,129] Moreover, the long-term cycling stability of Pt/C is quite limited. For instance, after 30,000 cycles, the ORR activity of Pt/C was reported to decrease dramatically.[130] The Pt-based electrode undergoes several degradation mechanisms, such as platinum dissolution, Ostwald ripening, coalescence, particle detachment, and carbon corrosion, and consequently loses activity.[131,132,133]

3. Experimental part

3.1 Experimental set-ups

3.1.1 Electrochemical cells

In this thesis, three types of electrochemical cells were used: one cell for single crystal electrochemistry, one cell for electrochemical experiments using polycrystalline electrode materials and a U-shaped cell for water electrolysis. The first two cells utilised the three-electrode configuration; the U-shaped cell adopted the two-electrode measurement scheme.

The cell for single crystal electrochemistry experiments consisted of the preconditioning compartment and the main compartment (compartment (1) and (2) in **Figure 3.1A**). The preconditioning compartment was used to prepare the electrolytes used in the main cell, e.g. to saturate the electrolyte with the targeted inert or electroactive gas. As shown in the cell schematic (**Figure 3.1A**), the working electrode is placed vertically by a moveable shaft and works using so-called hanging meniscus configuration. To maintain the sealing of the cell, a Thermogreen LB-1 (Supelco, Munich, Germany) insert was used. Near to the working electrode, a dummy electrode, a Pt wire (99.99 %, Goodfellow, Germany), was connected in series with the shaft. The reference and counter electrodes were connected to the cell both through ports, as shown in **Figure 3.1**. In the central cell, an additional compartment made for bubbling the electrolyte is connected by an independent gas inlet and outlet. Its principal function is to maintain saturation of the electrolyte with the gas required during the reactions, e.g., for the HER and ORR. A protective inner glass wall was integrated into the compartment to reduce the interference of the constant gas flow on the electrolyte. When the cell is in use, the working atmosphere is controlled by continuous gas flushing, i.e., Ar-CO, O_2, Ar, or H_2 gas. Electrochemical measurements were carried out by a VSP-300 potentiostat (Bio-Logic, France). In this thesis, the cell was mainly used to prepare and characterise Pt(111), Pt(221), Pt(331), Pt(775), Pt(12 10 5), Ir(111), and Au(111) single crystals and to evaluate their HER and ORR activities.

A

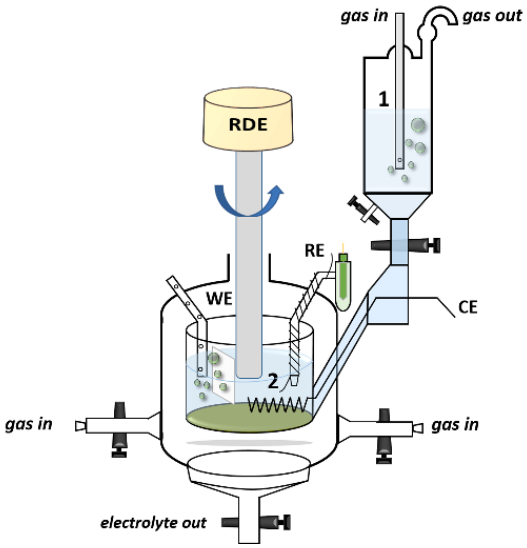

B

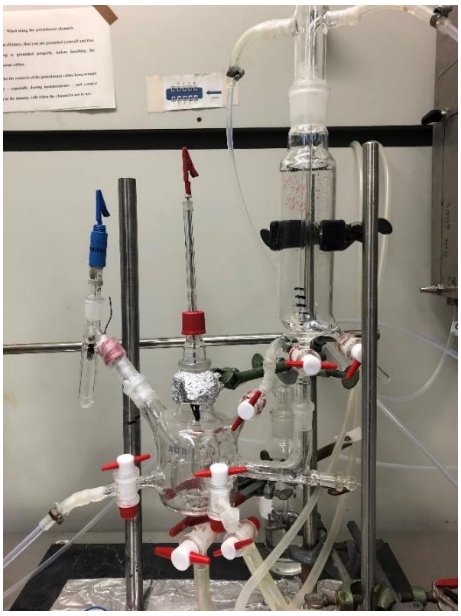

Figure 3.1. Electrochemical cell used for single crystal electrochemistry experiments. (A) Schematic and (B) photograph of the cell, which can be devided into (1) a preconditioning compartment and (2) a central compartment. RDE, WE, RE and CE labels correspond to rotating disk electrode, working electrode, reference electrode, and counter electrode, respectively. This cell was used for the preparation and characterisation of Pt(111), Pt(221), Pt(331), Pt(775), Pt(12 10 5), Ir(111), and Au(111) single crystals and the related activity measurements.

The cell for electrochemical experiments with polycrystalline electrodes consisted of a single compartment (**Figure 3.2**). The working electrode was a traditional RDE, which was operated using the hanging meniscus configuration. The reference and counter electrodes were also connected to the cell through the ports. The cell contained a gas inlet to saturate the electrolyte with the gas, i.e. O_2 or Ar. Moreover, compared with the

cell for single crystal electrochemistry, the temperature of electrolyte could be controlled by a thermostat, as shown in **Figure 3.2**.

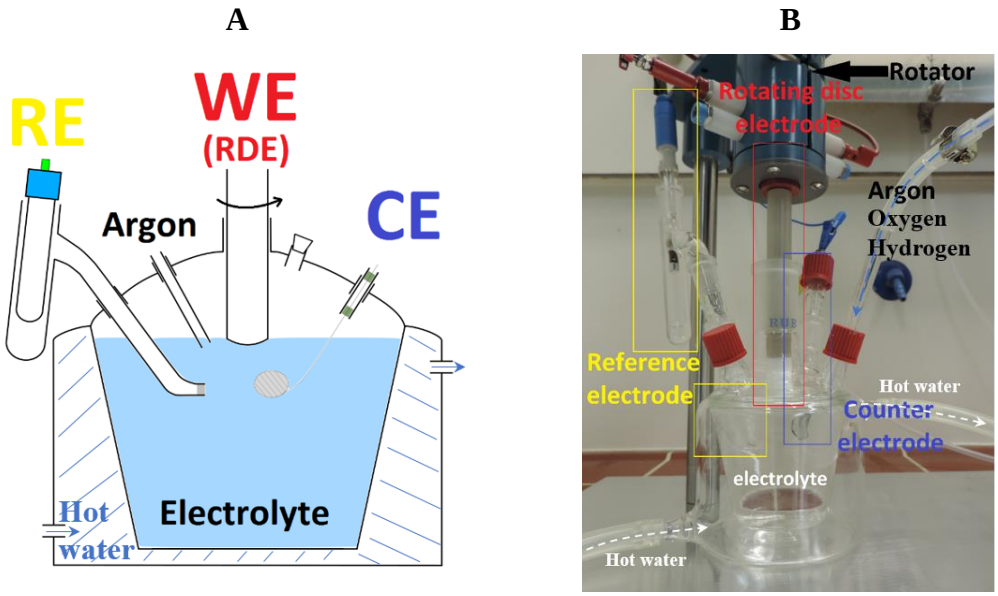

Figure 3.2. Electrochemical cell for the experiments with polycrystalline electrodes. (A) A schematic and (B) photo of the cell. WE, RE, and CE are working, reference, and counter electrodes, respectively. Arrows show the flow directions of hot water and gas. The electrolyte temperature in the cell can be regulated. This cell was mainly used for the deposition of metal oxide thin-films, the preparation of polycrystalline Pt, and corresponding activity measurements.

The U-shaped cell was made from a commercial U-shaped tube (**Figure 3.3**) and two electrode holders with gas outlets added.

Before each measurement, a so-called piranha solution, prepared by mixing H_2O_2 and H_2SO_4 (both Suprapur, Merck, Germany) with a volume rate of 1:3, was used to clean all glassware thoroughly. After rinsing with ultra-pure water several times, the cells were treated with boiling water (Evoqua, Germany) at least ten times, and the other glassware was kept in boiling water for 5 hours to remove any adsorbed ions on the glassware.

As a reference electrode, a commercial MMS electrode (SI Analytics, Germany) was used, which was connected to the electrolyte through ionically conducting glass. As a counter electrode, a Pt wire (99.99 %, Goodfellow, Germany) was used. All potentials shown in this work are referred to the RHE scale.

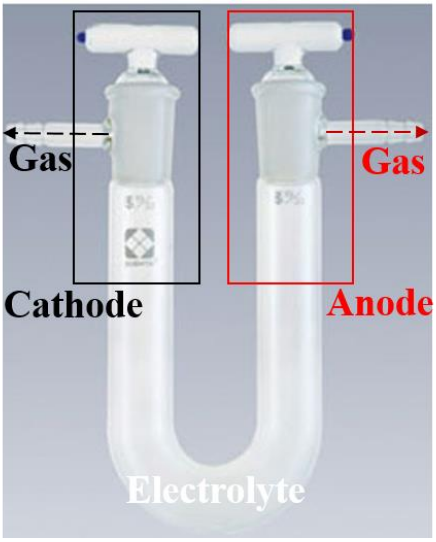

Figure 3.3. Photograph of the U-shaped tube for water electrolysis. Arrows show the gas flow directions. The produced gases are collected through the gas outlets. The picture is adapted from ref.134.

3.1.2 Single crystal electrochemistry

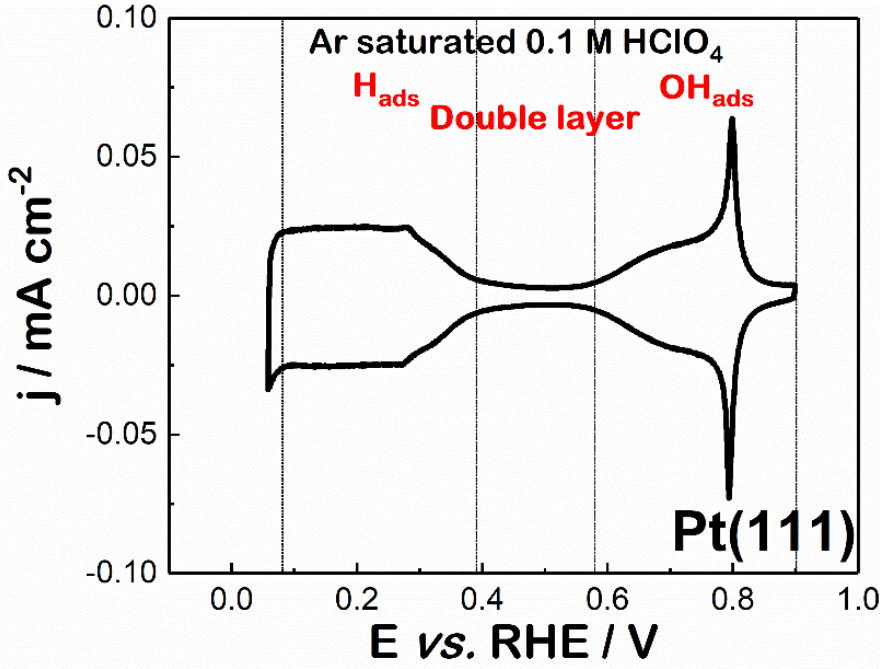

Figure 3.4. A typical CV of Pt(111) electrodes in Ar-saturated 0.1 M $HClO_4$. The CV has a 'butterfly' shape, with three different electrochemical regions: hydrogen adsorption/desorption ($H_{ads/des}$) region, double layer region, and hydroxyl adsorption/desorption ($OH_{ads/des}$) region.

Both bead-type (99.99%, 0.049 cm^2, Icryst, Jülich Germany) and disk-type (99.99%, 0.196 cm^2, Mateck, Germany) Pt(111) crystals were used in this work. The single

crystals were flame-annealed in an isobutene flame, followed by cooling in a mixture of 1000 ppm CO (4.7, Air Liquide, Germany) and Ar (5.0, Air Liquide, Germany). In case impurities could be detected, an additional CV cleaning was needed prior to the annealing. The surface quality was evaluated by CV experiments in Ar-saturated 0.1 M $HClO_4$ (Suprapur, Merck Germany). The CV measurements of Pt(111) were conducted in a potential range from 0.05 to 0.9 V_{RHE}. The CV shape was compared with those published in the literature to ensure the surface quality.

Figure 3.4 shows a typical CV of the well-defined Pt(111) surface, measured in Ar-saturated 0.1 M $HClO_4$. The CV shows a typical 'butterfly' shape, consisting of three different regions: in the potential range from approximately 0.05 to 0.4 V_{RHE}, it is a hydrogen adsorption/desorption ($H_{ads/des}$) region; in the range from approximately 0.4 to 0.6 V_{RHE}, it is usually referred to as a double layer region; in the range from approximately 0.6 to 0.9 V_{RHE}, it is a hydroxyl adsorption/desorption ($OH_{ads/des}$) region.

The stepped single crystals used in this research, i.e., Pt(221) (99.99%, 0.031 cm^2, obtained from Prof. J. Feliu), Pt(331) (99.99%, 0.038 cm^2, obtained from Prof. J. Feliu), Pt(775) (99.99%, 0.036 cm^2, obtained from Prof. J. Feliu), and Pt(12 10 5) (99.99%, 0.049 cm^2, Icryst, Jülich Germany) were all bead-type crystals. The preparation procedures were similar to that for the Pt(111) electrodes. Firstly, the stepped single crystals were flame-annealed in an isobutene flame; then, they were cooled in a mixture of 1000 ppm CO and Ar; finally, CV characterisation in Ar-saturated 0.1 M $HClO_4$ was performed to ensure the surface quality. The corresponding CVs are shown in **Figure 3.5**. The CVs also consist of the three regions: $H_{ads/des}$, double layer region, $OH_{ads/des}$, but the shapes of the CVs obviously differ from each other because they are indicative and sensitive to the crystal surface structure.

The bead-type Au(111) crystal used in this work was purchased from Icryst (Jülich Germany), with a surface area ~0.049 cm^2, orientation better than 0.1°, and surface roughness of *ca.* 30 nm. Before each measurement, the crystals were initially cleaned using the CV method in the potential range from 0.6 to 1.8 V_{RHE} for several cycles. After cleaning with pure water several times, the crystal was flame-annealed in an isobutene flame until the crystal became red. Then analogously to the preparation of single Pt crystals, the crystal was cooled down in an Ar-CO mixture, and the following CV characterisation was performed. **Figure 3.6** shows the measured CV in 0.1 M $HClO_4$. The peaks at approximately 1.35 and 1.55 V_{RHE} in the anodic scan are normally

associated with OH-adsorption and oxidation of the surface, while the peaks at approximately 1.15, 1.05, and 0.98 V_{RHE} appearing in the cathodic scan are related to the reduction of the oxidised surface.

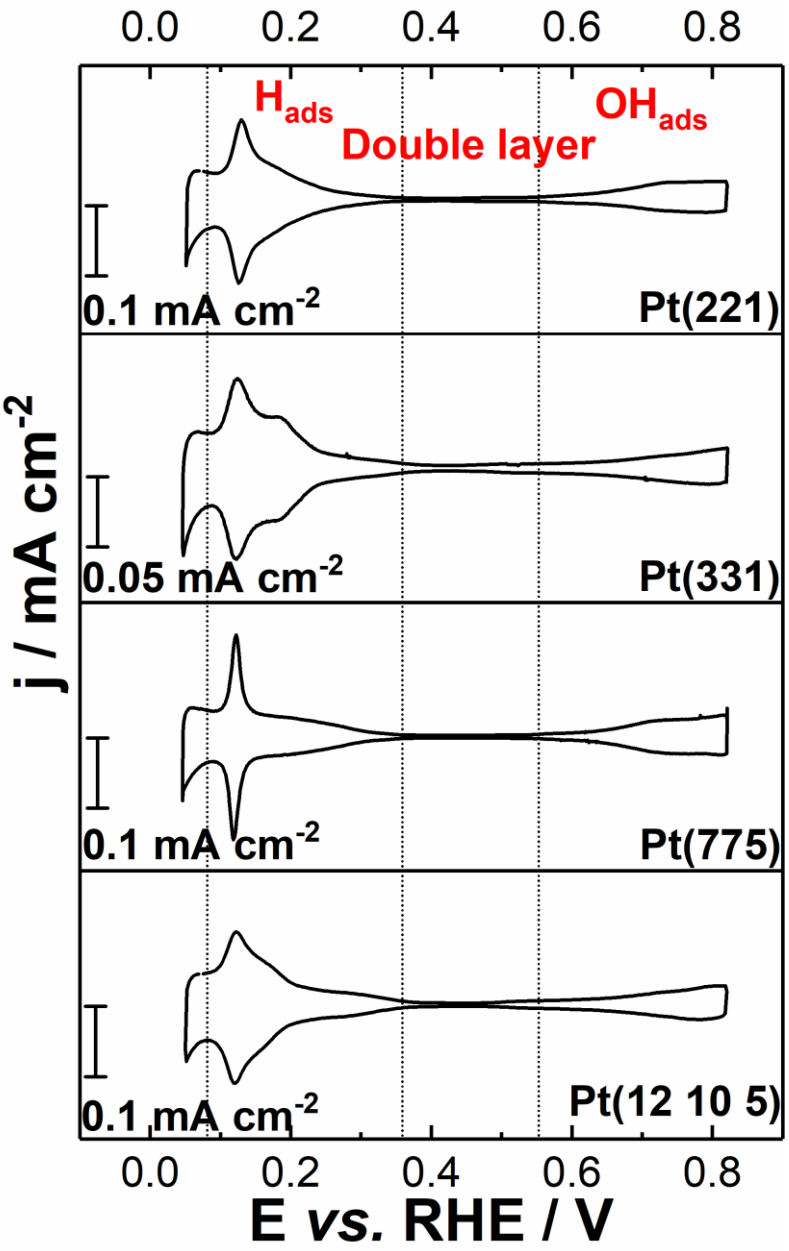

Figure 3.5. Typical CVs of Pt(hkl) single crystals in Ar-saturated 0.1 M $HClO_4$. Similar to the CV of Pt(111), the CVs of stepped single crystals consist of three different regions, namely the $H_{ads/des}$, the double layer region and the $OH_{ads/des}$. However, the respective CV shapes are obviously different from each other, as the shape is indicative and sensitive to the electrode surface structures.

For both Pt and Au single crystals, the surface was cleaned and the atoms at the surface were (re)ordered during the annealing; the followed cooling down in the Ar-CO

atmosphere forms a CO monolayer that protects the (re)ordered surface. During the first cycle of CV measurements, the CO monolayer adsorbed on the surface is oxidised according to the following reaction:

$$*CO + H_2O \rightarrow * + CO_2 + 2\,H^+ + 2\,e^-$$

Since this reaction is sensitive to the surface structure and status, this method was adapted to measure the surface area of Pt crystals. Removal of the CO protective layer creates a clean and well-ordered surface.

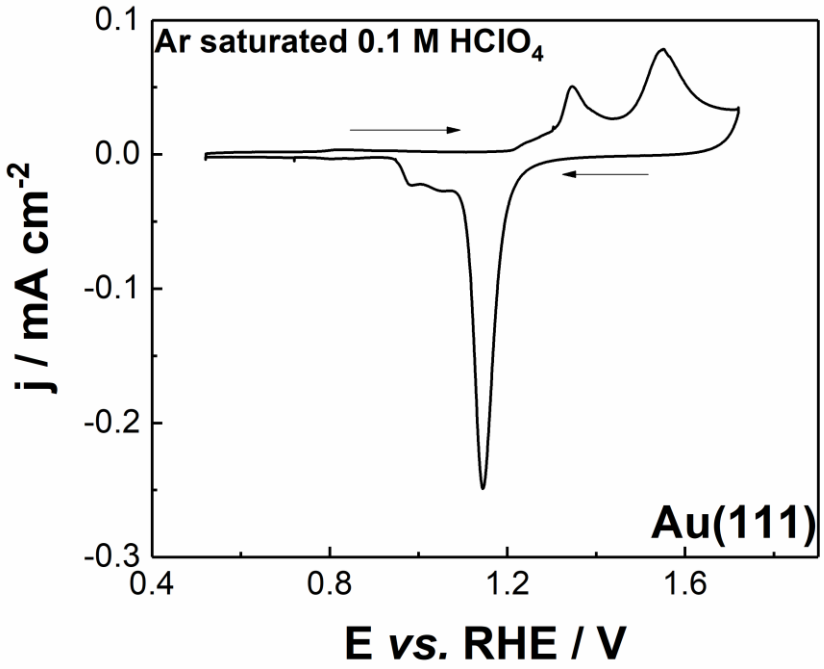

Figure 3.6. A typical CV of Au(111) electrodes in Ar-saturated 0.1 M $HClO_4$. The anodic/cathodic pairs of peaks are associated with the hydroxyl adsorption/desorption.

The preparation of Cu(111) and Cu(100) single crystals was performed in Prof. Kunze-Liebhäuser's group (University of Innsbruck). Physical polishing was performed first. The Cu crystals were successively polished with diamond pastes (ESCIL) of grades 1, 0.5, and 0.25 μm. After a smooth surface was obtained, electrochemical polishing was performed. Under a cell potential of 1.8 V versus a copper counter electrode, the crystals were electropolished in 60% H_3PO_4 (85% EMSURE, Merck) solutions for ~5 min. Finally, the well-polished crystals were moved into a tube furnace and annealed in an H_2 reductive atmosphere for at least 12 hours. Prior to electrochemical measurements, the crystals were constantly protected by the reductive atmosphere.

The Ir(111) single crystal (Mateck, Jülich, Germany) used was of disk-type one with a surface area of 0.196 cm^2, oriented better than 0.1° and with surface roughness less than 30 nm. The surface preparation was performed as the following procedure: the single crystal was firstly annealed in a mixture of 10% H_2 and Ar (both 5.0, Air Liquide, Germany) at around 1200 ℃ for 10 minutes; then it was cooled down and stored in the same atmosphere until the electrochemical experiments needed. The surface quality was ensured by its characteristic CV in Ar-saturated 0.1 M $HClO_4$.

3.1.3 Electrochemical experiments using polycrystalline materials

In industrial production and commercial fuel cell applications, typically a Pt powder mixed with a conductive agent (usually carbon) and an H-conducting polymer (Nafion) is used.[117]

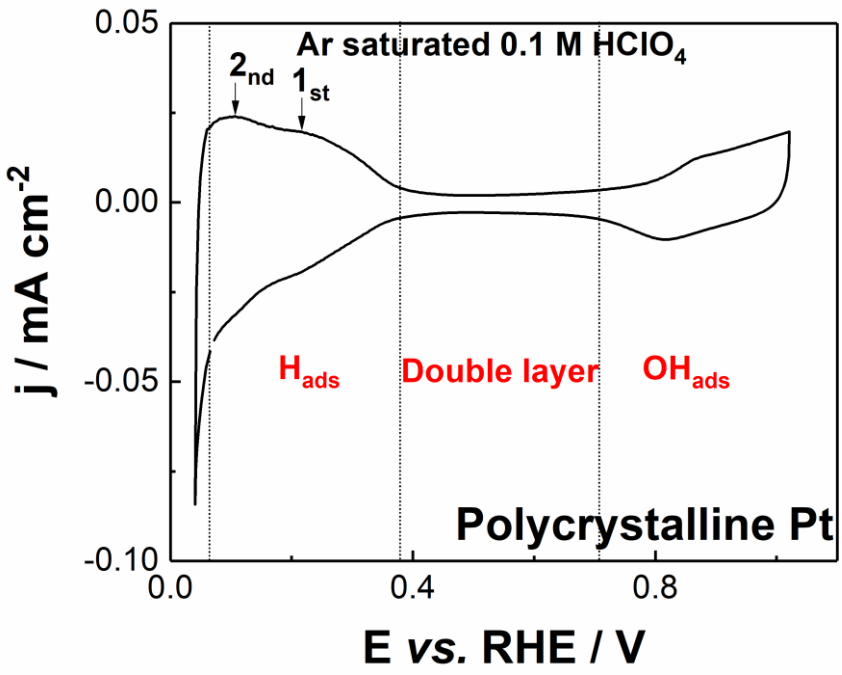

Figure 3.7. Typical CV of a polycrystalline Pt electrode in Ar-saturated 0.1 M $HClO_4$. The CV includes the three regions: $H_{ads/des}$, double layer, and $OH_{ads/des}$.

Polycrystalline materials often resemble the behaviour of nanostructured electrocatalysts. In this work, polycrystalline Pt (99.99%, 0.196 cm^2, Pine, USA) and Ag (99.99%, 0.136 cm^2) electrodes were used. The surface-preparation procedures were similar for both of them, primarily using the CV cleaning method. Accordingly, the polycrystalline electrodes were cycled in 0.1 M $HClO_4$ within a potential range from 0 to 1.7 V_{RHE} for dozens of cycles; then the electrolyte was replaced. After repeating the

previous process three times, the surface quality was checked by a CV characterisation in the potential range from the one close to 0 to 1 V_{RHE}. As shown in **Figure 3.7** for Pt, the CV, similar to that of single crystalline one, included the three regions: $H_{ads/des}$, double layer, and $OH_{ads/des}$, but differs totally in shape. Especially in the region of $H_{ads/des}$, two pairs of peaks were observed at approximately 0.2 and 0.1 V_{RHE}, responding to the hydrogen adsorption/desorption on (110) and (100) steps, respectively. Additional physical polishing was performed in the case of the polycrystalline Ag electrodes prior to the CV cleaning procedure because of the existence of thin oxidation layers on its surface. Moreover, during the electrolyte replacement, the Ag crystal was always kept under potential control to prevent its surface from oxidation.

3.1.4 Electrochemical deposition of oxide electrocatalysts

Before each electrochemical deposition, the substrate, a glassy carbon electrode (0.196 cm^2, Pine, USA), was carefully cleaned. Firstly, the electrode was mechanically polished using Al_2O_3 pastes with grades of 1, 0.3, and 0.05 μm. After complete physical cleaning, the electrode was treated in 0.1 M H_2SO_4 using CV scans in the potential range from -1 to 1 V_{RHE} until a reproducible voltammogram was obtained. The surface quality was then characterised by CV in 1 mM $K_3Fe(CN)_6$ (ACS reagent 99%, Sigma-Aldrich, Germany) and 0.2 M KNO_3 mixture electrolytes in a potential range from -0.1 to 0.6 V_{RHE}.

For the deposition of CoO_X films, a solution composed of 0.1 M $CoSO_4$ (99%, Merck, Germany), 0.1 M CH_3COONa (99%, Sigma-Aldrich, Germany), and 0.1 M Na_2SO_4 (99%, Sigma-Aldrich, Germany) was used. The deposition procedure was conducted using CV scans in the potential range from 1.2 to 1.8 V_{RHE} at 400 rpm.

A similar deposition procedure was also adapted for the preparation of the NiO_X films. Here, a deposition solution consisting of 0.13 M $NiSO_4$ (99%, Merck, Germany), 0.13 M CH_3COONa, and 0.1 M Na_2SO_4 and the potential range from 0.2 to 1.9 V_{RHE} were used.

The preparation of $NiFeO_X$ films was performed using a cathodic deposition. The deposition solution in this case was a mixture of 0.13 M $NiSO_4$, 0.13 M $FeSO_4$ (99%, Merck, Germany), 0.13 M CH_3COONa, and 0.1 M Na_2SO_4. The deposition was performed using a chronopotentiometry method at -50 mA cm^{-2} for 30s with the RDE configuration at a speed of 1200 rpm.

3.1.5 Rotating disk and rotating ring disk electrode experiments

A rotating disk electrode is a high-speed rotating electrode used by researchers to control the mass transport of electroactive species to the electrode surface.

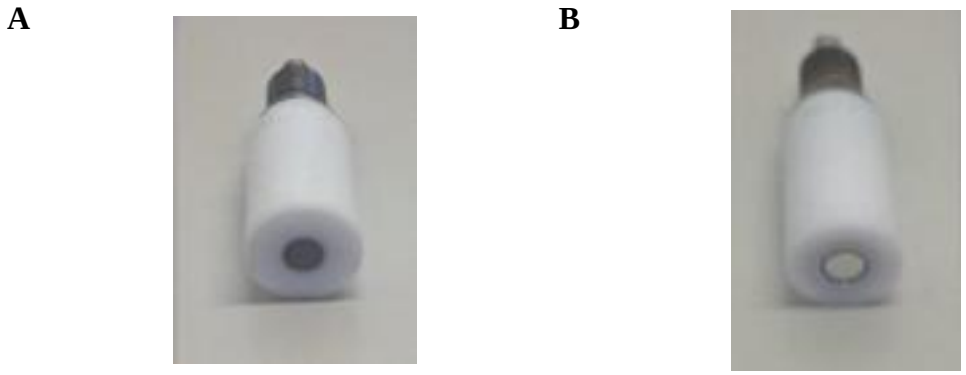

Figure 3.8. Photographs of (A) RDE and (B) RRDE used in this research. The RDE shown here is a glassy carbon disk electrode, while for the RRDE, both the disk and the ring electrode are Pt.

Rotating the electrode in the electrolyte ensures that the analyte quickly reaches the electrode surface along the rotary axis and is then rapidly pulled out along the radial direction of the electrode. The fluid at the surface thus continuously refresh, which reduces mass transfer influence. This idea was proposed by Levich in 1952[135] and realised by Bruckenstein[136]. Nowadays, the electrode is usually a disk of conductive material encapsulated into Teflon (**Figure 3.8A**), and its rotating speed is controlled by a rotary engine.

To further investigate the reaction mechanism and reaction intermediates, an independent ring electrode can be added around the disk electrode separated with insulating material (**Figure 3.8B**). This electrode is known as an RRDE. During a reaction on the disk electrode, more details about the reaction can be collected by simultaneous monitoring of the ring electrode. Two kinds of experiments regularly require RRDE.

One is so-called collection-detection experiment that uses the ring to determine the species generated at the disk. For example, when the reduction potential of H_2O_2 for Pt, namely a constant potential of 1.3 V_{RHE}, is applied at the ring electrode, whether or not H_2O_2 is produced during OER on the disk electrode can be determined by whether a corresponding reduction current can be detected at the ring (**Figure 3.9A**). When the

constant potential is changed to the reduction potential of O_2 for Pt, around 0.7 V_{RHE}, the onset potential of OER on the disk electrode can be accurately obtained by observing the current on the ring (**Figure 3.9B**).

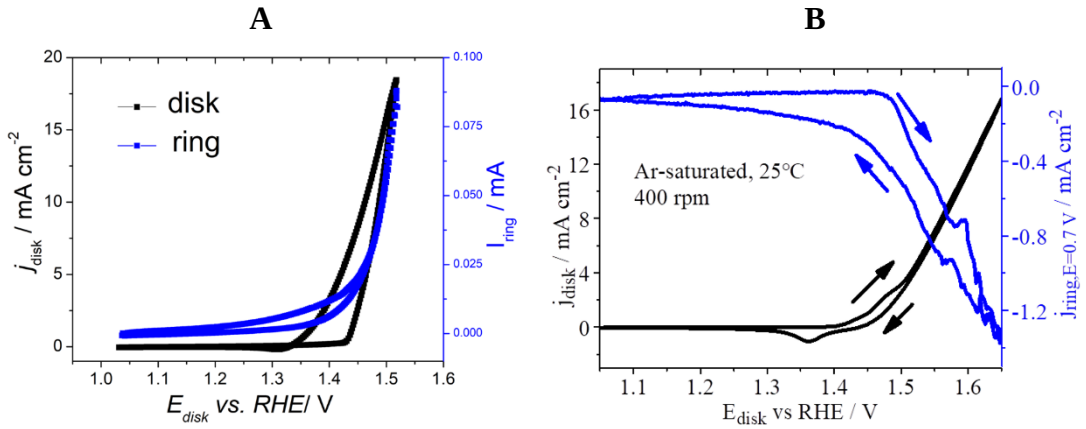

Figure 3.9. RRDE measurements used in OER experiments. (A) Currents at NiO_x disk and Pt ring electrodes in the presence of 0.4 M *n*-butylammonium sulfate. Scan rate for the disk was 50 mV s^{-1} and rotating speed 400 rpm. E_{ring} = 1.3 V_{RHE} (constant). Reprinted with permission from ref.137. Copyright 2017, Wiley. (B) NiFe-based hydroxide disk and Pt ring electrodes measured in 0.1 M KOH. Scan rate for both electrodes was 10 mV s^{-1} and rotating speed 400 rpm. E_{ring} = 0.7 V_{RHE} (constant).

The second kind of experiments is shielding experiments. In such experiments, two consecutive measurements are usually involved. Firstly only the ring is polarised, while the corresponding current is recorded. Then, both the ring and disk are polarised. In this case, the flow of reactive species to the ring is perturbed by the disk reaction. Thus, the shielding can be recorded based on the contest between the electrodes. These experiments are necessary for the exploration of reaction mechanisms, e.g. of the ORR. Therefore, the application of RRDE allows a simple *in-situ* investigation of electrochemical reactions.

3.2 Electrochemical techniques

3.2.1 Cyclic voltammetry

Cyclic voltammogram, CV, is one of the most widely used techniques to acquire quantitative information about electrochemical reactions. In this method, a triangular potential waveform is applied to the electrode one or several times, and the current-potential curves are recorded.

A typical cyclic voltammogram is a plot showing the dependence of the measured current on the applied potential. The CV method has been widely used in the investigation of adsorption processes, heterogeneous electron transfer reactions and redox processes. It can provide information about the properties and mechanisms of electrochemical reactions and kinetic parameters of these reactions. It can be employed to determine reactant concentration, coverages of adsorbates on the electrode surface, the electrochemically active surface area of the electrode and several kinetic parameters such as electrode reaction rate constant, exchange current density and reaction transfer coefficient. Its application can be divided into two main types, as described below:

1. **Reaction reversibility.** The height and symmetry of the oxidation and reduction waves of the obtained CV can often be used to judge about the reaction reversibility.
2. **Reaction mechanism.** Information about electrochemical adsorption phenomena, electrochemical reactions and electrochemical-chemical coupling reactions can be obtained from CV. It is useful for studying the redox mechanism of organic compounds, organometallic compounds and biological materials.

3.2.2 Chronoamperometry and chronopotentiometry

Chronoamperometry (CA) is a basic controlled-potential technique, in which a constant potential is applied, and the response current is then recorded over time. The obtained current-time curve reflects the change in the concentration gradient in the vicinity of the electrode surface. The number of electroactive species involved in the reactions can be also monitored and the diffusion coefficient of electroactive species can be calculated. Several potential steps are often used to polarise the electrode; the double potential-step CA is widely used in this case. In the first step, the potential is applied to start the reaction. After a short period of electrolysis, it jumps back to the original potential or another potential, where the reaction product or intermediate is probably transformed back into its original state. Accordingly, the associated kinetic reaction process is better observed using the CA curve as compared with that of CV. The reaction rate constant can be determined according to the Cottrell equation. Compared with the CV technique, CA has its own unique advantages:

1. **Higher sensitivity.** For example, the peak current obtained from this

method is in many cases much higher than that obtained by the CV method.

2. **Much quicker.** CA is more suitable for rapid detection.
3. **A simple hardware structure** of the required instrument.

Chronopotentiometry (CP) is a basic controlled-current technique, in which a constant current is applied, and the response potential is then recorded as a function of time. This technique is similar to that of CA. However, the applied potential step is replaced by the current step.

In this research, CA and CP are mainly used for electrochemical deposition, such as NiFe hydroxide preparation.

3.2.3 Electrochemical impedance spectroscopy

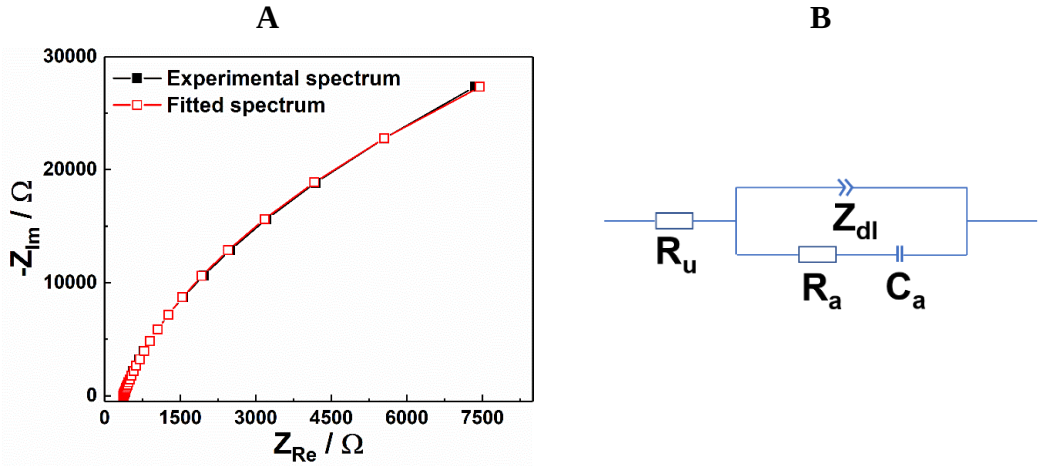

Figure 3.10. (A) A typical EIS spectrum and fitting results. This spectrum was measured within an AC-frequency range from 1 Hz to 30 kHz by immersing a Cu(111) electrode in 0.05 M $NaClO_4$ at pH = 6. The fitted spectrum was obtained using EIS Data Analysis 1.3 software. (B) Equivalent electric circuit used for fitting the EIS spectrum. R_u, Z_{dl}, R_a, and C_a represent the uncompensated resistance, the double layer impedance, an adsorption resistance, and an adsorption capacitance, respectively.

Electrochemical impedance spectroscopy is a technique, which is based on the excitation of an electrochemical system by a sinusoidal signal. This technique is very useful for both the evaluation of the heterogeneous charge transfer parameters and the investigation of the double layer structure.

In EIS, a sinusoidal perturbation around a constant current (or potential) is applied to the electrochemical system as shown in **Equation (3.1)**, but the amplitude of the

perturbation is small enough to assume a linear behaviour of the system.

$$I_{WE} = I + i_a \sin(2\pi f t) \tag{3.1}$$

where I_{WE} is the applied alternating current signal, i_a is the current amplitude, f is the frequency of the applied probing signal and t is time. The potential (or current) responses of the system subjected to the perturbations in the steady-state can be observed:

$$E_{WE} = E + V_a \sin(2\pi f t + \Phi) \tag{3.2}$$

where E_{WE} is the potential measured at time t, V_a is the potential amplitude, Φ is a phase angle between the two phasors (the potential and the current). The obtained response follows at the same frequency, but at a different phase (**Equation (3.2)**). The measured ratio of the perturbing signal and the response is the impedance of the system. The corresponding value depends on the sine wave frequency, f. Effectively, the phase angle, Φ, varies with the probing signal frequency, f. At different angular frequencies, ω ($\omega = 2\pi f$), the overall system impedance, $Z_{Tol}(\omega)$, can be written as:

$$Z_{Tol}(\omega) = Z_{Re}(\omega) + iZ_{Im}(\omega) \tag{3.3}$$

where $Z_{Re}(\omega)$ is the real component of the impedance and $Z_{Im}(\omega)$ is the corresponding imaginary component. Using an equivalent circuit to analyse the EIS data can give a lot of information about the system, such as reaction parameters, interfacial capacitance and mass transport parameters. In EIS, plots of $-Z_{Im}(\omega)$ as a function of the real component, $Z_{Re}(\omega)$, are very often used as shown in **Figure 3.10A**. Equivalent circuits can comprise different elements such as resistors (R), capacitors (C) inductors (L) and specific electrochemical elements, which are connected in series and/or parallel. The actual equivalent circuit and the value of each element of it can be verified by fitting of the EIS data. Accordingly, based on the electrochemical meaning of these elements, the pysico-chemical properties of the electrochemical system can be analysed. Taking an example of the EIS experiment to determine the electric double layer capacitance in Chapter 7, the equivalent electric circuit used for these simulations is given in **Figure 3.10B**, in which R_u represents the uncompensated resistance, Z_{dl} - the double layer impedance, R_a - the additional adsorption resistance and C_a - the adsorption capacitance. In the circuit, R_u and Z_{dl} connected in series are used to

simulate the response of the region from the bulk electrolyte to the interface between the electrode and the electrolyte. Additional R_a and C_a connected in series and parallel to the Z_{dl} account for the impedance response originating from e.g. possible specifically adsorbed species at some electrode potentials. The spectrum obtained from the simulation is well-matched with that obtained directly from EIS measurements, as shown in **Figure 3.10A**, and the corresponding values of circuit parameters are provided in **Table 3.1**. It can be seen that relatively high accuracy as well as excellent modelling of the system's physical properties can be obtained with EIS.

Table 3.1. The value of circuit parameters obtained from fitted results in Figure 3.10

Parameters	Results	Units
R_u	373.79	Ω
R_a	1.6184E05	Ω
C_a	2.0644E-05	F
Preexponential factor	5.9612E-06	Fs^{n-1}
Exponent (n)	0.94918	

It should not be overlooked that certain conditions are required:

1. **Causality.** The output response signal is only caused by the applied perturbation signal.
2. **Linearity.** There should be a linear relationship between the output response signal and the applied perturbation. Although a nonlinear relationship determined by the kinetic law usually exists in a real electrochemical system, an approximately linear relationship can be assumed between the current and the potential when a small-amplitude sine wave signal is used.
3. **Stability.** The perturbation should not cause changes in the properties of the system. In other words, when the perturbation stops, the system should be able to return to the original state. A reversible reaction easily satisfies the stability condition. For an irreversible electrode process, if the system can

recover to a state not far from the original state after the perturbation stops, then as an approximation, the stability condition is still assumed.

4. Influence of the alkali metal cations on the hydrogen evolution reaction

In this chapter, the HER performed in alkaline media was selected as a model reaction to determine the influence of the alkali metal cations (i.e., Li^+, Na^+, K^+, Rb^+ and Cs^+) on the electrocatalytic performance of Pt, Ir, Au and Ag electrodes. Selection of the HER as the model reaction was based on the following considerations: HER is one of the most important reactions for sustainable energy provision[91,138]; it is relatively simple with regard to its mechanism, as only one type of reaction intermediates is involved[92] (detailed description about the importance of the reaction and its mechanism can be found in Chapter 1 and 2, respectively). Additionally, the intention of this study was to ascertain the generally lowered HER activity of Pt in alkaline media compared to the acidic solutions; and it is known to be closely related to the alkali metal cations present in the electrolyte.[139,140]

Based on the volcano plot for the HER (**Figure 2.1** in Chapter 2), the electrode materials with strong hydrogen binding energy relative to the optimum, such as Pt and Ir, as well as electrodes with weak hydrogen binding energy, such as Au and Ag, were investigated in alkaline media containing different alkali metal cations to reveal their role in the hydrogen evolution process. It was observed that HER activity of all investigated electrode materials is not only determined by the affinity of their surface towards the hydrogen adsorbates, but also by the hydration energy of alkali metal cations.

The chapter is divided into three parts. In the first section, the HER activities of electrodes with relatively high hydrogen binding, namely single crystalline Pt(111) and Ir(111), stepped single crystalline Pt(221), Pt(331) and Pt(775) and polycrystalline Pt electrodes, are evaluated in both Ar- and H_2-saturated alkaline electrolytes, i.e., LiOH, NaOH, KOH, RbOH, and CsOH. In the second section, the HER activities of single crystalline Au(111) and polycrystalline Ag electrodes, exhibiting relatively weak hydrogen binding, are investigated under the same experimental conditions. In the third section, the data are compared to deduce the influence of alkali metal cations on the HER through the correlation of the positions of these electrode materials in the HER volcano plot with their specific HER activities in different alkaline media and the

hydration energy of the alkali metal cations.

Parts of this chapter were published in the article '*Influence of alkali metal cations on the hydrogen evolution reaction activity of Pt, Ir, Au and Ag electrodes in alkaline electrolytes*' in *ChemElectroChem 5 (2018) 2326*[141].

4.1 Hydrogen evolution reaction activities of monocrystalline and polycrystalline Pt and Ir electrodes in alkaline media

The HER activities of electrode surfaces exhibiting strong hydrogen binding are presented in this section. Before each measurement, the electrodes were all prepared by the respective procedure introduced in Chapter 3. Besides, there was no *iR*-correction for all measurements in this section to avoid introducing uncertainty factors.

4.1.1 Monocrystalline and polycrystalline Pt electrodes

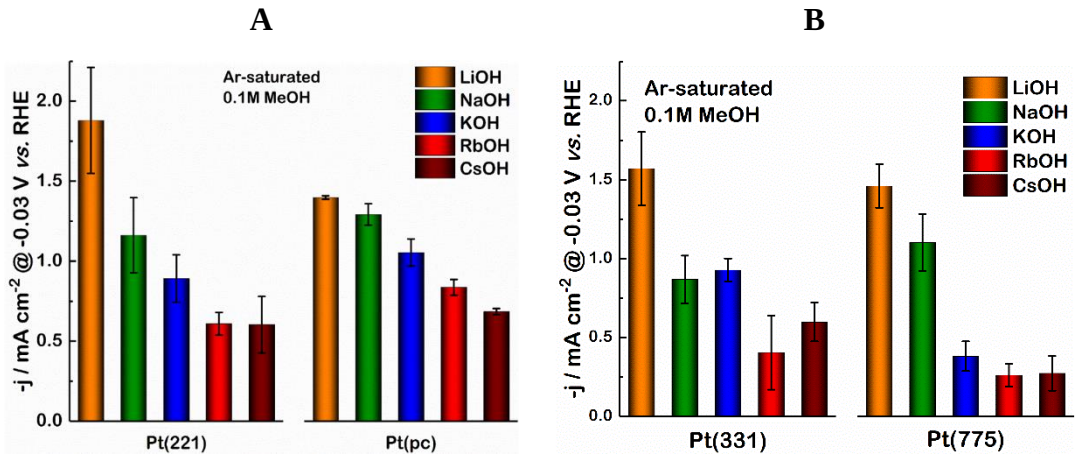

Figure 4.1. Comparison of the HER activities of (A) Pt(221) and Pt(pc), (B) Pt(331) and Pt(775) electrodes at -0.03 V_{RHE}, recorded in Ar-saturated 0.1 M *Me*OH-type electrolyte (Me^+ = Li^+, Na^+, K^+, Rb^+, Cs^+). The error bars are calculated using at least three different measurements.

In **Figure 4.1**, the HER activities of stepped single crystalline Pt(221), Pt(331), Pt(775) and polycrystalline Pt (Pt(pc)) electrodes are summarised. The crystals were measured in Ar-saturated 0.1 M *Me*OH electrolytes (Me^+ = Li^+, Na^+, K^+, Rb^+, and Cs^+). In order to exclude the influence of mass transfer, the current densities were compared at a relatively small overpotentials corresponding to the electrode potential of -0.03 V versus RHE scale.

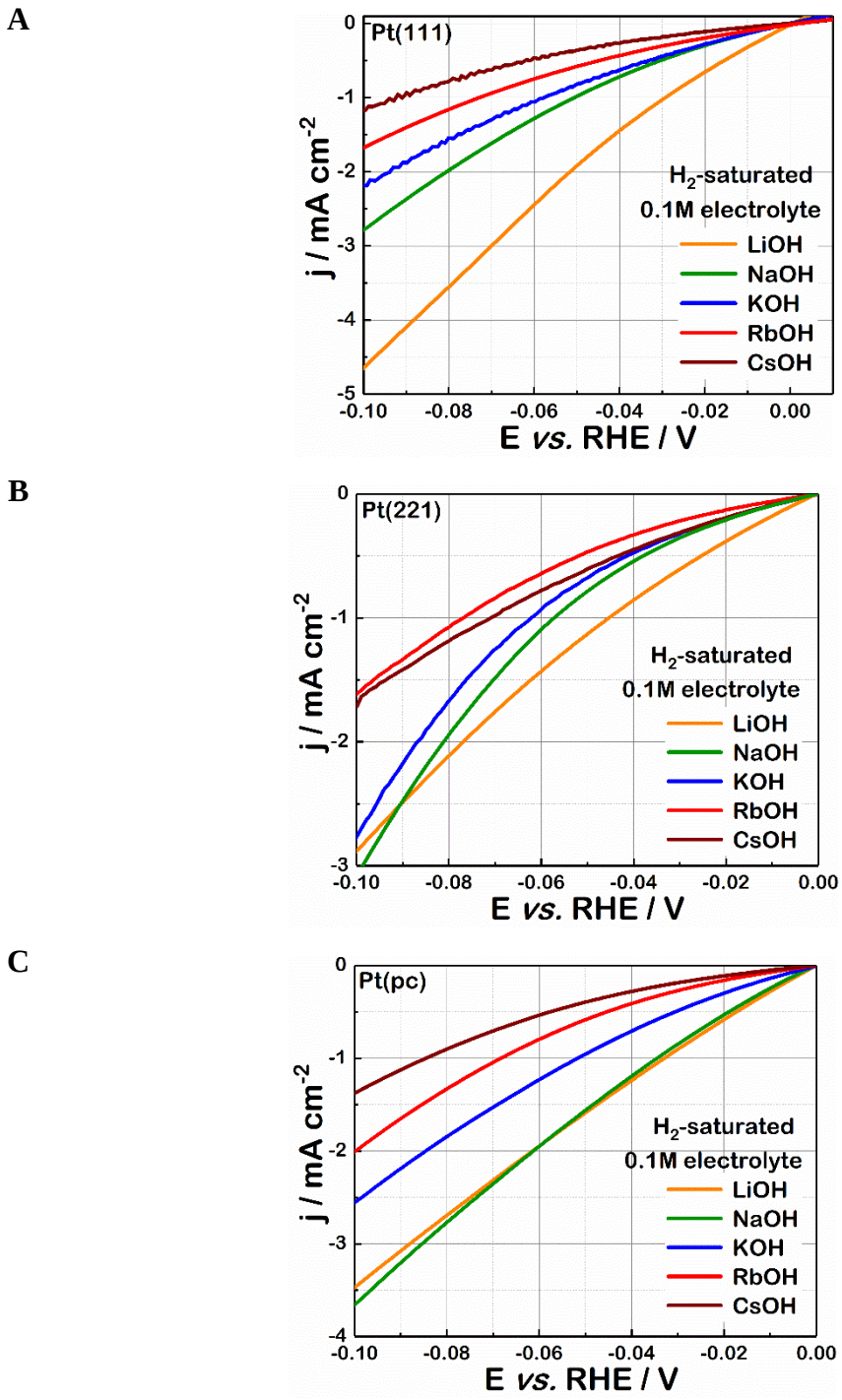

Figure 4.2. Typical HER polarization curves for (A) Pt(111), (B) Pt(221), and (C) Pt(pc) electrodes, recorded in H_2-saturated 0.1 M *Me*OH electrolytes (*Me*$^+$ = Li^+, Na^+, K^+, Rb^+, Cs^+).

In the Ar-saturated electrolytes, almost all investigated electrodes follow the decreasing activity trend $Li^+ > Na^+ > K^+ > Rb^+ > Cs^+$. For Pt(221), the highest current density was observed in LiOH, being almost 1.8 mA cm^{-2}, followed by NaOH and KOH. The lowest one was obtained in RbOH and CsOH, with the current densities close to ~0.6 mA cm $^{-2}$

(**Figure 4.1A**). It can be seen that HER performance can be tuned up to three times by simply exchanging the alkali metal cation present in the electrolyte. For Pt(pc), the highest performance was also obtained in LiOH, showing almost 1.4 mA cm^{-2}, followed by NaOH, KOH, and RbOH, whereas CsOH resulted in the lowest activity of approximately 0.7 mA cm^{-2} (**Figure 4.1A**). One can see that, in the case of Pt(pc), activity changes were observed in different alkaline media; the factor for activity change approached to two. For Pt(775) and Pt(331), a similar activity trend was obtained. The highest activities for both Pt(775) and Pt(331) were recorded in LiOH, which were approximately three times higher than the ones acquired in CsOH for Pt(775) and in RbOH for Pt(331) (**Figure 4.1B**).

Moreover, alkaline HER performance trends appear not only to be closely associated with the surface structure. As shown in **Figure 4.1**, in all these electrolytes, Pt(pc) exhibited the highest activity, apart from one in LiOH. This observation implies that the active sites of Pt electrodes for alkaline HER might vary with the type of alkali metal cation, resulting in a superior activity observed for the Pt(pc).

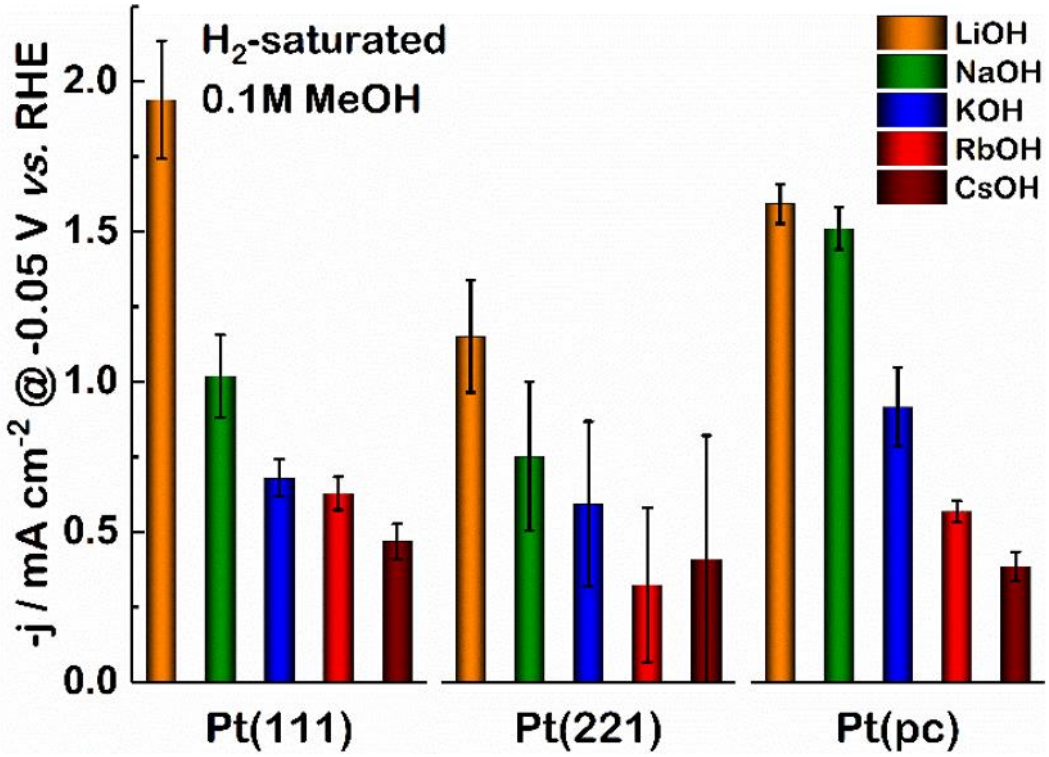

Figure 4.3. Comparison of the HER activities of Pt(111), Pt(221) and Pt(pc) electrodes at -0.05 V_{RHE}, recorded in H_2-saturated 0.1 M *Me*OH electrolytes ($Me^+ = Li^+, Na^+, K^+, Rb^+, Cs^+$).

The above-mentioned results demonstrate that the HER performance is closely related to the nature of alkali metal cations present in the electrolytes. Furthermore, HER activities were recorded and compared in the H_2-saturated electrolytes. Three typical model Pt surfaces, namely Pt(111), Pt(221) and Pt(pc), were investigated. Pt(111) was chosen because of its common use as the simplest model Pt single crystal electrode. The selection of Pt(221) was based on its exceptionally high acidic HER activity[142]. The corresponding HER polarisation curves and current densities at -0.05 V_{RHE} are shown in **Figures 4.2** and **4.3**, respectively.

In the H_2 saturated electrolytes, the same activity trend as in the Ar-saturated ones was observed for all investigated electrodes in corresponding electrolytes, i.e. $Li^+ > Na^+ > K^+ > Rb^+ > Cs^+$. As shown in **Figure 4.2A**, this observed activity trend for the Pt(111) electrode was consistent over the whole investigated potential range from 0.0 to -0.1 V_{RHE}. For both Pt(221) and Pt(pc) electrodes, the activity trends were also stable over almost the whole potential range (**Figure 4.2B** and **C**). Moreover, in the bar chart comparing the HER current density at -0.05 V_{RHE} it is clearly visible that regardless of the surface structure, the activity trend can be observed for all the Pt electrodes (**Figure 4.3**). Furthermore, the current densities obtained in LiOH were almost four times higher than the ones recorded in the CsOH electrolytes for all the studied Pt surfaces.

These observations indicate that the alkali metal cations strongly influence the HER performance of Pt electrodes, irrespective of their surface structure. As noted beforehand, the activity can be tuned up to a factor of four by exchanging the alkali metal cation species. The observed activity trend always follows the sequence: $Li^+ > Na^+ > K^+ > Rb^+ > Cs^+$.

4.1.2 Single-crystalline Ir(111) electrodes

In order to verify if the observed HER activity dependence in the alkali metal cation electrolytes, i.e. $Li^+ > Na^+ > K^+ > Rb^+ > Cs^+$, holds true for other catalysts, the activity of single crystalline Ir(111) electrodes was additionally measured in the same electrolyte solutions, namely Ar- and H_2-saturated 0.1 M *Me*OH ($Me^+ = Li^+$, Na^+, K^+, Rb^+ and Cs^+). The corresponding data recorded under Ar- and H_2-saturation are depicted in **Figures 4.4** and **4.5**, respectively.

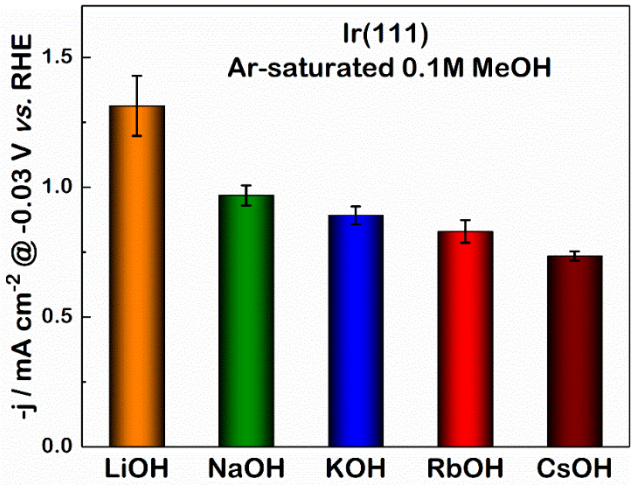

Figure 4.4. Comparison of the HER activities of Ir(111) electrodes at the electrode potential of -0.03 V_{RHE}, recorded in Ar-saturated 0.1 M *Me*OH electrolytes (*Me*$^+$ = Li^+, Na^+, K^+, Rb^+, Cs^+).

Indeed, similar activity trend was obtained for the Ir(111) electrodes under both conditions. As shown in **Figures 4.4** and **4.5A**, in those cases the highest HER current densities were obtained in the LiOH electrolytes followed by NaOH and KOH ones, while the lowest current densities were observed in the RbOH and CsOH solutions. Moreover, the HER current densities measured in LiOH electrolytes were approximately three times higher than those obtained in RbOH or CsOH solutions. Besides, the corresponding HER polarization curves in **Figure 4.5B** demonstrate that this activity trend remained in the whole investigated potential range from 0 to -0.05 V_{RHE}.

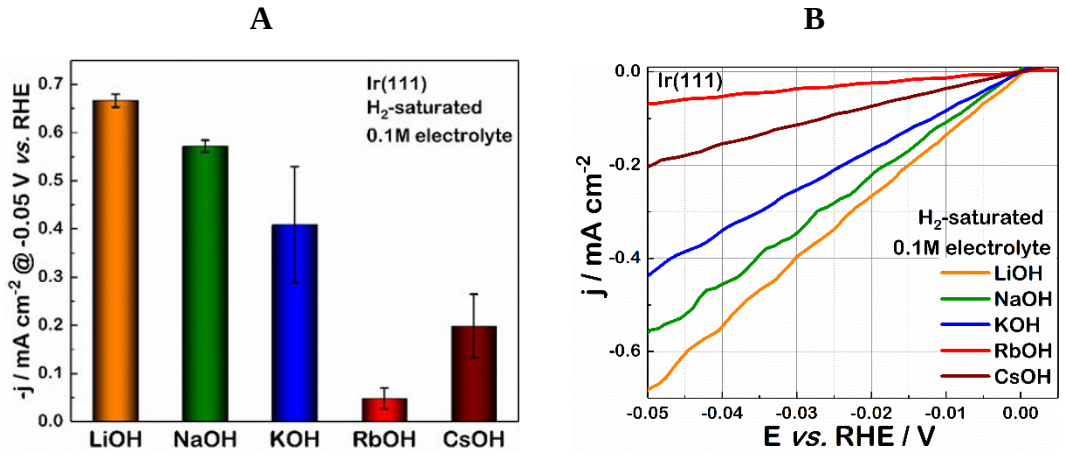

Figure 4.5. Comparison of (A) HER activities at -0.05 V_{RHE} and (B) typical HER polarization curves for the Ir(111) electrodes recorded in H_2-saturated 0.1 M *Me*OH electrolytes (*Me*$^+$ = Li^+, Na^+, K^+, Rb^+, Cs^+).

In summary, the results shown above imply that the HER activity of materials with stronger hydrogen binding is significantly affected by alkali metal cations present in the electrolyte. Depending on the material used, the performance can be tuned up to a factor of four by exchanging the alkali metal cation species in the electrolyte. The activity trend observed always follows the order: $Li^+ > Na^+ > K^+ > Rb^+ > Cs^+$.

4.2 Activities of monocrystalline and polycrystalline Au and Ag electrodes towards hydrogen evolution in alkaline media

In this section, the HER activities of crystals with weak surface-hydrogen binding interactions were investigated. Prior to each measurement, the crystals were prepared according to the preparation procedure described in the experimental section (Chapter 3). The measurements shown here are all displayed without *iR* drop correction.

4.2.1 Single crystalline Au(111) electrodes

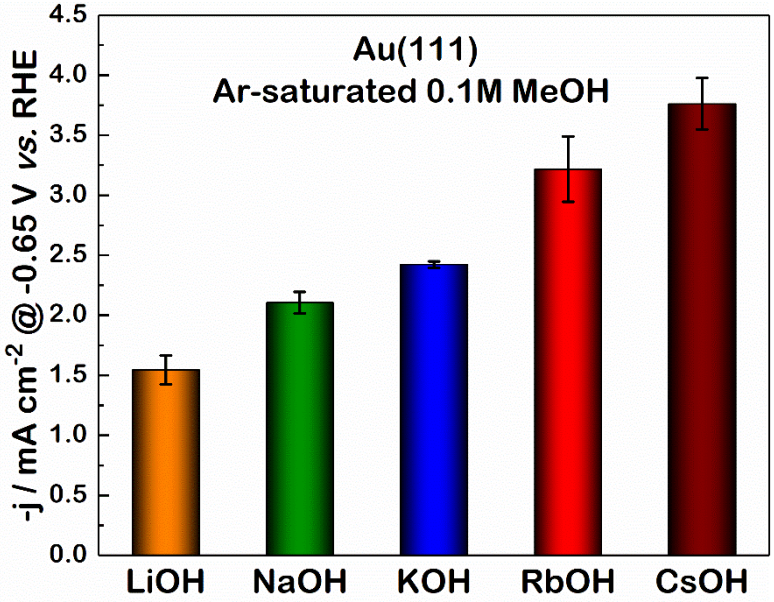

Figure 4.6. Comparison of the HER activities of the Au(111) electrodes at -0.65 V_{RHE}, recorded in Ar-saturated 0.1 M *Me*OH electrolytes ($Me^+ = Li^+, Na^+, K^+, Rb^+, Cs^+$).

Single crystalline Au(111) electrodes were characterised in the Ar-saturated 0.1 M *Me*OH ($Me^+ = Li^+, Na^+, K^+, Rb^+$, and Cs^+) electrolytes. As pure Au is not a good catalyst for the HER, the current densities were compared at a high overpotential of 0.65 V, at which notable HER polarisation currents were observed. The corresponding results are shown in the bar chart of **Figure 4.6**.

The obtained activity trend is surprisingly reversed compared to that observed for the Pt and Ir electrodes, i.e., in the order $Cs^+ > Rb^+ > K^+ > Na^+ > Li^+$. At an overpotential of 0.65 V, the highest current density was observed in the CsOH containing electrolytes, being almost 3.8 mA cm^{-2}, followed by those in RbOH, KOH, and NaOH, whereas the lowest was observed in LiOH, being approximately 1.5 mA cm^{-2} (**Figure 4.6**). Hereby, the HER current density observed in CsOH was about two times higher than the one observed in LiOH.

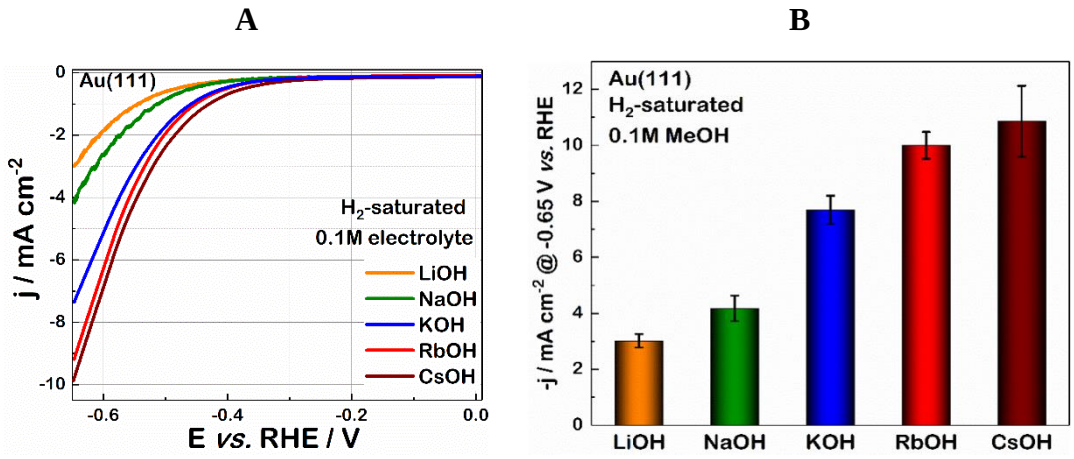

Figure 4.7. (A) Typical HER polarization curves and (B) comparison of the HER activities at -0.65 V_{RHE} for the Au(111) electrodes, recorded in H_2-saturated 0.1 M *Me*OH electrolytes (Me^+ = Li^+, Na^+, K^+, Rb^+, Cs^+).

HER activities of Au(111) in different alkaline media were also measured under H_2 atmosphere. **Figure 4.7A** shows the polarization curves for Au(111) in H_2-saturated *Me*OH (Me^+ = Li^+, Na^+, K^+, Rb^+, and Cs^+) electrolytes. The lowest HER onset potential was obtained in CsOH, followed by RbOH, KOH, and NaOH, whereas the highest one was obtained in LiOH containing electrolytes (comparing absolute values obtained from **Figure 4.7A**). Moreover, the same trend was observed in the whole investigated potential range from the HER onset potential to -0.65 V_{RHE}. **Figure 4.7B** is a bar chart comparing the HER current densities at the overpotential of ~0.65 V. The current density obtained in CsOH, almost 10 mA cm^{-2}, is more than three times higher than the one obtained in LiOH, which is approximately 3 mA cm^{-2}. Obviously, in H_2 atmosphere, the reverse activity trend was observed as well, namely $Cs^+ > Rb^+ > K^+ > Na^+ > Li^+$, and the HER activity can also be easily tailored up to three times by exchanging the alkali metal cation species present in the electrolytes.

Based on these observations, alkali metal cations strongly influence the HER performance of Au(111), but their impact appears to be different from that for Pt and Ir electrodes.

4.2.2 Polycrystalline Ag electrocatalyst

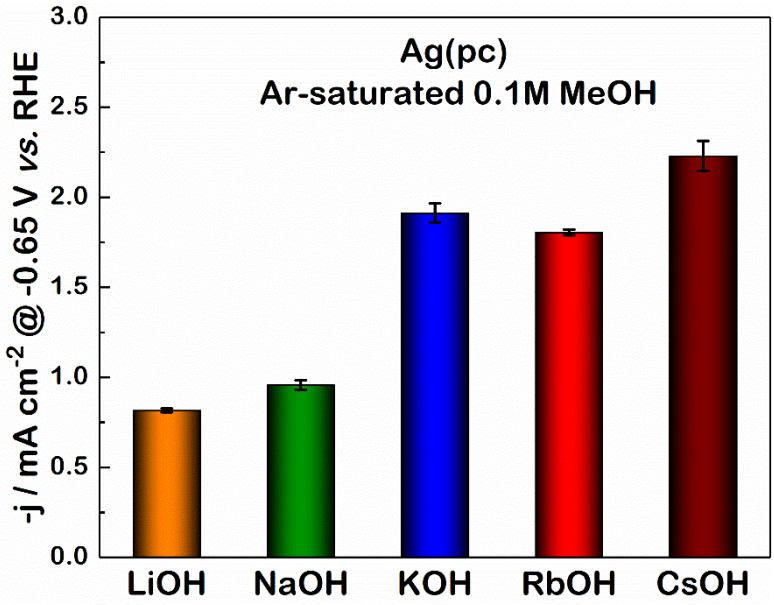

Figure 4.8. Comparison of the HER activities of Ag(pc) electrodes at -0.65 V_{RHE}, recorded in Ar-saturated 0.1 M *Me*OH-type electrolytes (Me^+ = Li^+, Na^+, K^+, Rb^+, Cs^+).

To determine whether this observed reverse activity trend (i.e., $Cs^+ > Rb^+ > K^+ > Na^+ > Li^+$) is also seen for other crystals with weak hydrogen binding, polycrystalline Ag electrodes were examined under similar conditions. The current densities used were compared at an overpotential of 0.65 V. The corresponding results are depicted in **Figure 4.8**.

Polycrystalline Ag indeed demonstrates an almost identical activity trend as Au. As shown in **Figure 4.8**, the highest HER current density was obtained in CsOH, followed by KOH, RbOH, and NaOH solutions whereas the lowest current density was observed in LiOH ones. Moreover, the current density obtained in CsOH was about two times higher than the one observed in the LiOH electrolyte.

These observations suggest that for the materials located on the right side of the volcano plot, alkali metal cations also play a critical role in their HER performance. The activity can be tuned up to a factor of three by simply replacing the alkali metal cation in the solutions. The activity trend always follows an order: $Cs^+ > Rb^+ > K^+ > Na^+ > Li^+$.

4.3 Discussion and summary

Possible explanations of the observations described in the previous sections can be deduced from correlating the affinity of the electrode surfaces towards the hydrogen adsorbates with the hydration energy of alkali metal cations.

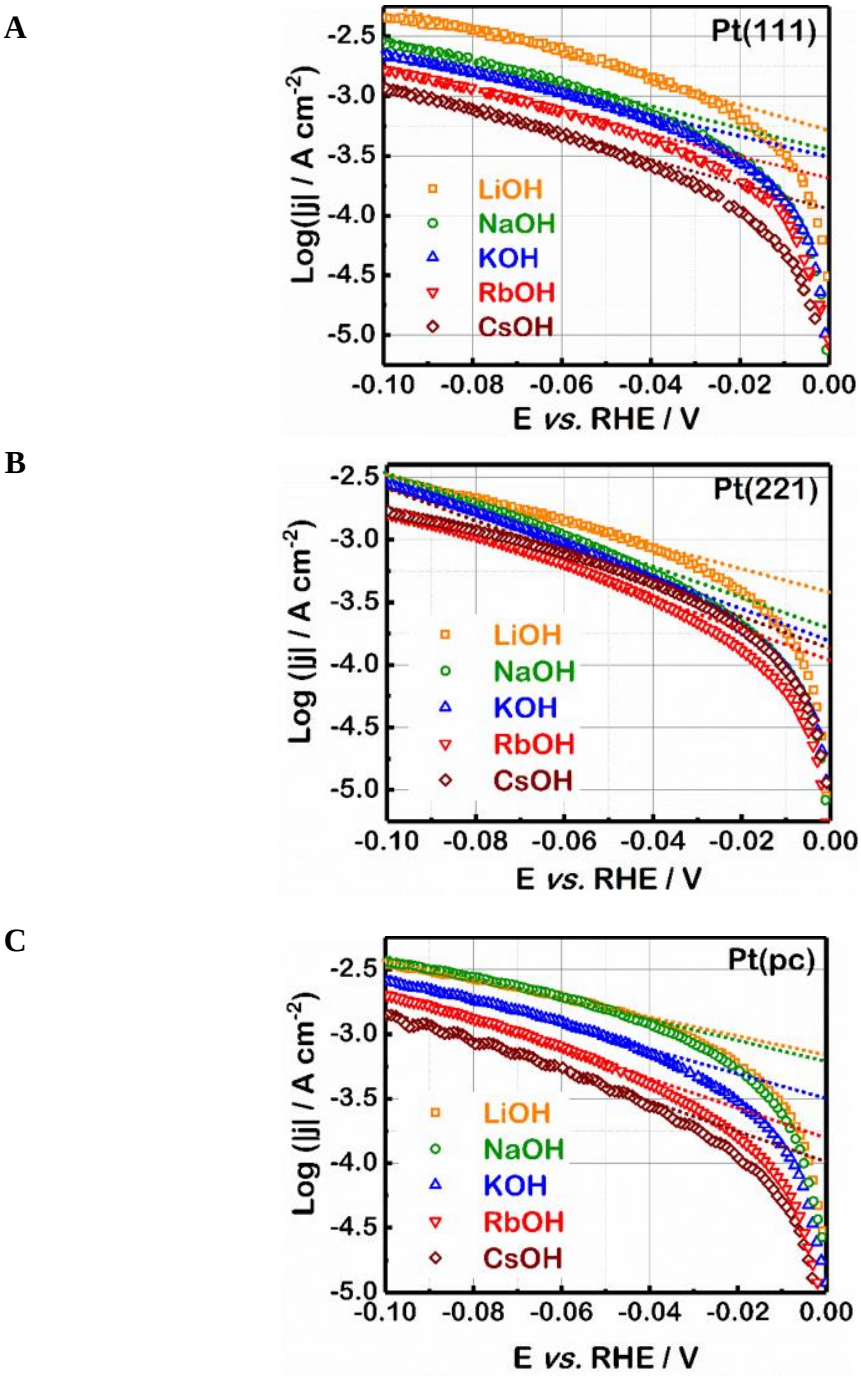

Figure 4.9. Logarithmic plot of the current densities as a function of the applied potential for (A) Pt(111), (B) Pt(221), and (C) Pt(pc) electrodes. The pseudo-exchange current densities were estimated by a 'classical' approach[95], as shown by the dotted line.

Herein, the pseudo-exchange current density was used to represent the observed HER activity. Because of the noticeable Ohmic drop, it is, however, almost impossible to obtain the 'true' exchange current density under current experimental conditions. Accordingly, the pseudo-exchange current density obtained from Tafel plots is typically used to approximate the exchange current density. **Figure 4.9A-C** show the corresponding Tafel plots for Pt(111), Pt(221), and Pt(pc) electrodes, which were estimated from their respective HER polarisation curves in **Figure 4.2**. It can be seen that similar slopes of the curves can be observed for different alkaline electrolytes at each electrode potential: these similar slopes reveal that the HER mechanism has not changed significantly[138]. Thereby, the obtained pseudo-exchange current density can be employed for the comparison, see **Figure 4.10**.

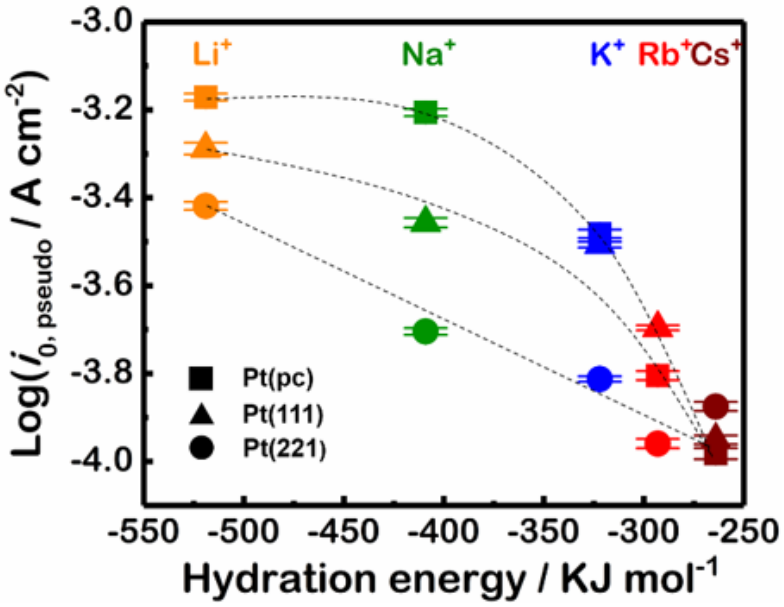

Figure 4.10. Logarithm of the pseudo-exchange current density of Pt(111), Pt(221) and Pt(pc) plotted versus the hydration energy of the corresponding alkali metal cations. The logarithm of the pseudo-exchange current density was taken from Figure 4.9. The dashed lines are added as guides to eyes.

The hydration energy of alkali metal cations is utilised to estimate their ability to influence the electrocatalytic performance, as the hydration energy is a crucial parameter to describe the interactions taking place at the electrode-electrolyte interface, i.e., the trade-off between the interaction within the solid versus the interactions between dissolved ions and water molecules of the solvation shell[143]. Moreover, non-covalent interactions between these water molecules and the reaction intermediates

have increasingly been recognised as an essential factor to determine the electrocatalytic reaction performance.[144,145]

Certainly, there is a correlation between the HER activity and the hydration energy of alkali metal cations. As shown in **Figure 4.10**, with the decrease of the hydration energy, the HER activity increases, irrespective of the Pt surface structure. Combined with the activity trends observed on Ir, Au, and Ag electrodes, it appears that, with the increase of the hydration energy of the used alkali metal cations, i.e., from Cs^+ to Li^+, the HER activities improve for the crystals with strong hydrogen binding but drop for those with weak hydrogen-surface interactions (**Figure 4.11**).

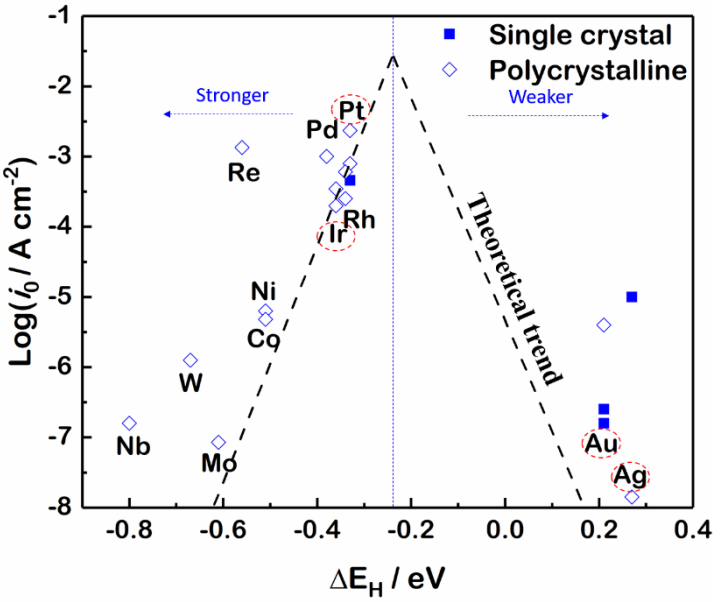

Figure 4.11. 'Volcano plot' ranking the HER activity of different metal surfaces (squares) according to their theoretical binding energies with respect to the hydrogen reaction intermediates. Dotted lines are added as guides to eyes. The theoretical hydrogen binding energies are taken from refs 46,146. Pt, Ir, Au and Ag electrodes used are marked in the plot.

Theoretically, a higher HER activity will be achieved when the hydrogen binding energy of an electrode is tailored to approach the optimum (**Figure 4.11**). Specifically, for Pt and Ir electrodes, as located on the left side of the volcano plot, the HER performance will be improved if their relatively strong hydrogen binding energies become weakened; whereas for Ag and Au electrodes located on the right side, it is reversed. The relatively weak hydrogen binding require strengthening to achieve a better HER performance. Therefore, correlating the observed different activity trends between Pt, Ir and Ag, Au electrodes with the hydration energy of alkali metal cations,

one can assume that increased hydration energy, namely an enhancing interaction of the cation with its water shell, presumably results in weakened hydrogen binding energy. That is, the binding of the HER intermediates depends on the nature of the alkali metal cation present close to them and weakens systematically from Cs^+ to Li^+. This weakened hydrogen binding energy is evidently beneficial for Pt and Ir, yet detrimental for Au and Ag.

The changed hydrogen binding energy is probably caused by so-called non-covalent interactions between the water shell of alkali metal cations/water molecules and the reaction intermediates adsorbed at the catalyst surface. However, it should be noted that the size of different solvated alkali metal cations, the double layer restructured by those cations, and the varied potential of maximum entropy should also be considered.[147,148] Thus, mechanistic details are still unclear and require further research. Regardless of the mechanism, however, the results presented in this thesis unambiguously show that in the case of the HER, the alkali metal cations used in the electrolyte strongly affect the activity.

In summary, the influence of the alkali metal cations on HER activities was primarily investigated in this chapter. Based on the location in the volcano plot, the HER activities of crystals with strong hydrogen binding, including Pt(111), Pt(221), Pt(pc), and Ir(111), as well as crystals with weak hydrogen binding, Au(111) and Ag(pc), were investigated in different alkaline electrolytes. For Pt and Ir electrodes, irrespective of their surface structure, the activities were following the trend: CsOH < RbOH < KOH < NaOH < LiOH. However, for Au and Ag electrodes, the activity order was reversed: LiOH < NaOH < KOH < RbOH < CsOH. These results affirm that the HER activity of the metal electrodes is indeed influenced by alkali metal cations contained in the electrolytes, and the activity can be tuned up to a factor of four by simply switching between Cs^+ and Li^+ based electrolytes. One can conclude that these observations are caused by the altered hydrogen binding to the electrode surfaces. Moreover, this altered hydrogen binding is evidently associated with the alkali metal cation species present close to the active sites of the electrode. However, mechanistic details about how alkali metal cations affect these reaction intermediates still need to be elaborated in further experimental studies.

5. Influence of the alkali metal cations on the activities towards the oxygen reduction reaction

The ORR is one of the key electrocatalytic reactions for fuel cells. However, it has relatively low kinetic efficiency.[149,150] Pt and Pt-group metals are known as good candidates for the ORR catalysis and have been widely studied and applied in commercial devices.[151,152] The activity and selectivity of these metals depend on several factors, including the electrode surface structure[153,154,155,156,157,158], surface composition[159,160,161] and the electrolyte composition[147,162,163,164,165]. The studies on the electrode surface structure and composition have attracted much attention, and several feasible methodologies and approaches, i.e., the coordination-activity relations[22] and Sabatier-type volcano plots[166,167], have been proposed based on the observed trends. They work pretty well in predicting the activity and guiding the catalyst design. However, with regard to the effect of electrolyte composition, there is much less understanding, especially in the case of alkali metal cations that are present in basic electrolytes.

A possible explanation for the role of alkali metal cations in ORR is predominantly based on two concurrent hypotheses. The first one is closely related to the entropy barriers at the electrified interface or structuring in the electrical double layer[148,168,169]. This hypothesis provides a good explanation of the observed ORR activities at various pHs. The second hypothesis is that there are non-covalent interactions between active sites of the electrocatalyst and alkali metal cations present in the electrolyte[147,170]. For instance, in the case of Pt(111) in different basic media, Cs^+ weakens the ORR intermediate, *OH, resulting in a near-optimum *OH binding energy, and thus the highest activity is observed in the Cs^+ based alkaline electrolytes.

In order to analyse these hypotheses and determine the effect of alkali metal cations on stepped single crystalline Pt, high-index model surfaces of Pt(221) and Pt(331) were chosen due to their superior ORR activities in acidic solutions[171]. The influence of the alkali metal cations was investigated in different alkaline media, i.e. LiOH, NaOH, KOH, RbOH, and CsOH. It was discovered that for these high-index surfaces, the observed activities were both systematically lower than those in acidic media, and the

highest ORR activities were obtained in KOH. This is different from the observations for Pt(111) in alkaline solutions. Through the correlation of the observations for high- and low-index Pt electrodes with the corresponding theoretical calculations published recently in the literature, the influence of alkali metal cations on the ORR activity is discussed.

In this chapter, the electrochemical measurements including CVs and ORR activities in acidic and various basic electrolytes are introduced in the first section. The influence of alkali metal cations on the ORR activities is discussed in the second section. The third section provides a summary of this chapter.

The main results of this chapter were published in the article '*Oxygen Electroreduction at High-Index Pt Electrodes in Alkaline Electrolytes: A Decisive Role of the Alkali Metal Cations*' in *ACS Omega 3 (2018) 15325*[172].

5.1 Electrochemical measurements in acidic and various basic solutions

CVs and the results of the ORR activity measurements for Pt(111), Pt(221), and Pt(331) electrodes are introduced in this section. Before each electrochemical measurement, the used crystals were prepared by flame annealing, the detailed description of which can be found in Chapter 3. Besides, all the ORR activities have been corrected for the *iR* drop so that they can be compared to the literature values.

5.1.1 Cyclic voltammograms of Pt(111), Pt(221), and Pt(331)

CVs of single crystalline Pt(221) and Pt(331) were initially recorded in Ar-saturated 0.1 M $HClO_4$ and different 0.1 M alkaline *Me*OH (Me^+ = Li^+, Na^+, K^+, Rb^+, and Cs^+) electrolytes, as shown in **Figure 5.1**. The CVs of Pt(111) in Ar-saturated 0.1 M $HClO_4$ and KOH are also presented for comparison. One can see that as compared to Pt(111), the stepped surfaces exhibit several distinctive features in their CVs, which are normally associated with the distribution of adsorption sites and the structure of the electrode surfaces.[173,174]

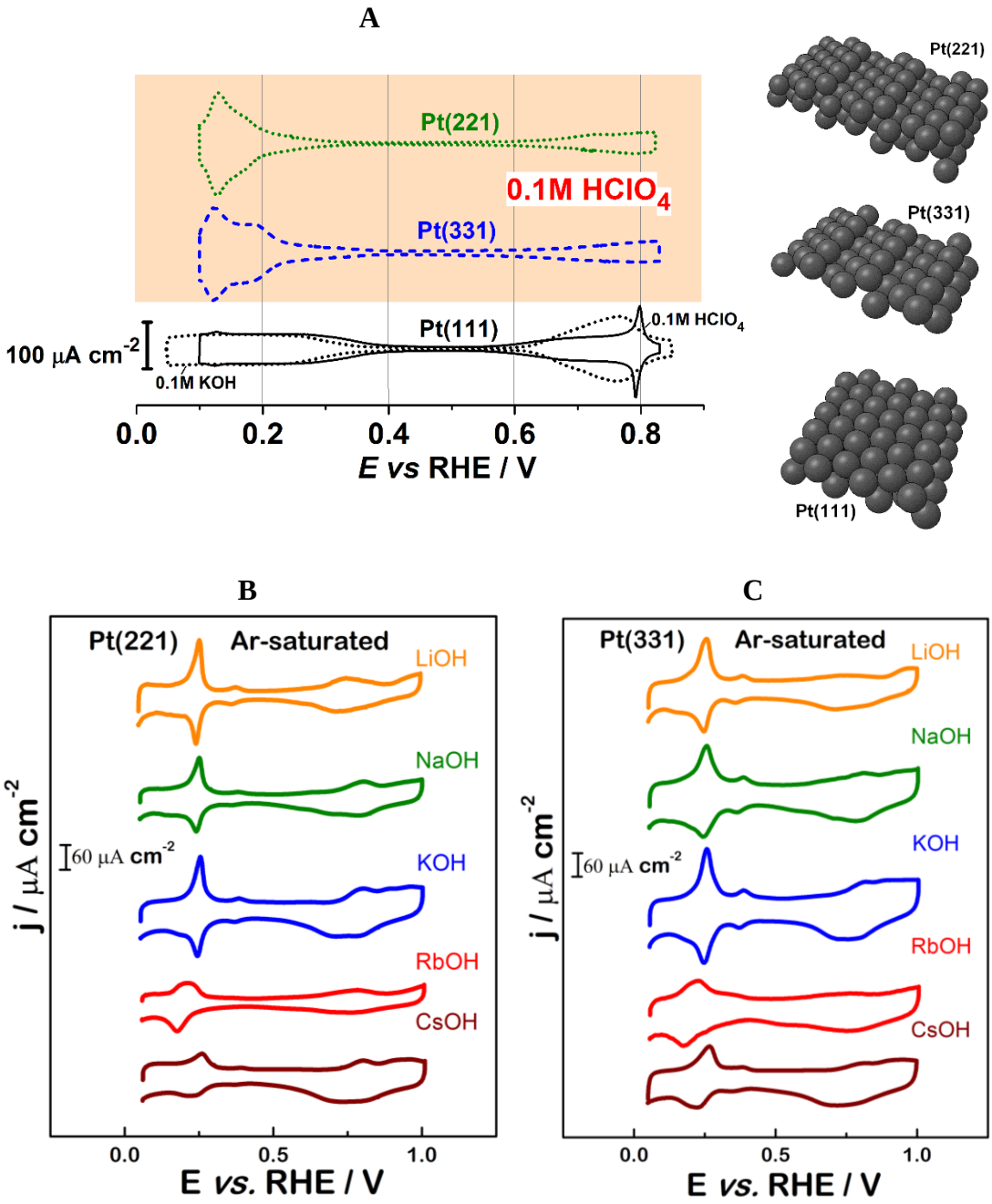

Figure 5.1. (A) CVs of the Pt(221) and Pt(331) electrodes recorded in Ar-saturated 0.1 M $HClO_4$. The voltammograms for Pt(111) in 0.1 M $HClO_4$ and KOH are also shown as the references. The representative single crystal surface structures are presented on the right. Typical CVs of (B) Pt(221) and (C) Pt(331) electrodes in Ar-saturated 0.1 M alkaline electrolytes, i.e., LiOH, NaOH, KOH, RbOH, and CsOH. Scan rate: 50 mV s^{-1}.

Firstly, CVs in the potential range from ~0.1 to ~0.4 V_{RHE}, known for the adsorption and desorption of hydrogen species, were compared between different electrode surfaces and between acidic and alkaline solutions. In 0.1 M $HClO_4$, CV features were

significantly different for these three electrodes (**Figure 5.1A**). Compared to the rather smooth shape observed on the CV of Pt(111), additional peaks at around 0.12 V_{RHE} appeared for the high-index surfaces, which are owing to hydroxyl species adsorbing on undercoordinated sites at steps[139,175]. When changing the electrolyte from acidic to alkaline, the CV shape of Pt(111) remained the same in the H-region (**Figure 5.1A**). However, for the Pt(221) and Pt(331) electrodes, the sharp peaks were shifted toward ~0.25 V_{RHE} (**Figure 5.1B** and **C**). These positive peak shifts are considered to be caused by the presence of the alkali metal cations: the OH-adsorption binding is likely weakened in this case. Recently, the relevant experimental evidence was presented by Koper *et al.*[170], in which they demonstrated that this observed pH dependence of hydrogen adsorption originates from the cations. However, there is still a lack of a conclusive study about the role of these species in these processes in the alkaline electrolytes, as the relevant studies were mostly done under ultra-high vacuum conditions[176].

The so-called double layer region was observed for all investigated surfaces at the potential range from ~0.4 and ~0.6 V_{RHE}, but the width of this region in alkaline media was broader than that in the acidic solutions (**Figure 5.1**). At the potential range between ~0.6 and ~0.9 V_{RHE}, known for the adsorption and desorption of hydroxyl species, several significant changes in the voltammograms can be observed (**Figure 5.1**). In 0.1 M $HClO_4$, characteristic peaks of a 'butterfly' shape were observed for Pt(111), whereas rather broad peaks were observed for Pt(221) and Pt(331). In 0.1 M alkaline electrolytes, these OH adsorption/desorption peaks all became smoother, yet the potentials of these peaks were all shifted, and the shape was different in various alkaline solutions as shown in **Figure 5.1B** and **C**. These findings imply that not only the pH but also the alkali metal cations present in the electrolyte influence the adsorption properties of these low- and high-index Pt electrode surfaces.

5.1.2 Oxygen reduction reaction activities of Pt(111), Pt(221), and Pt(331)

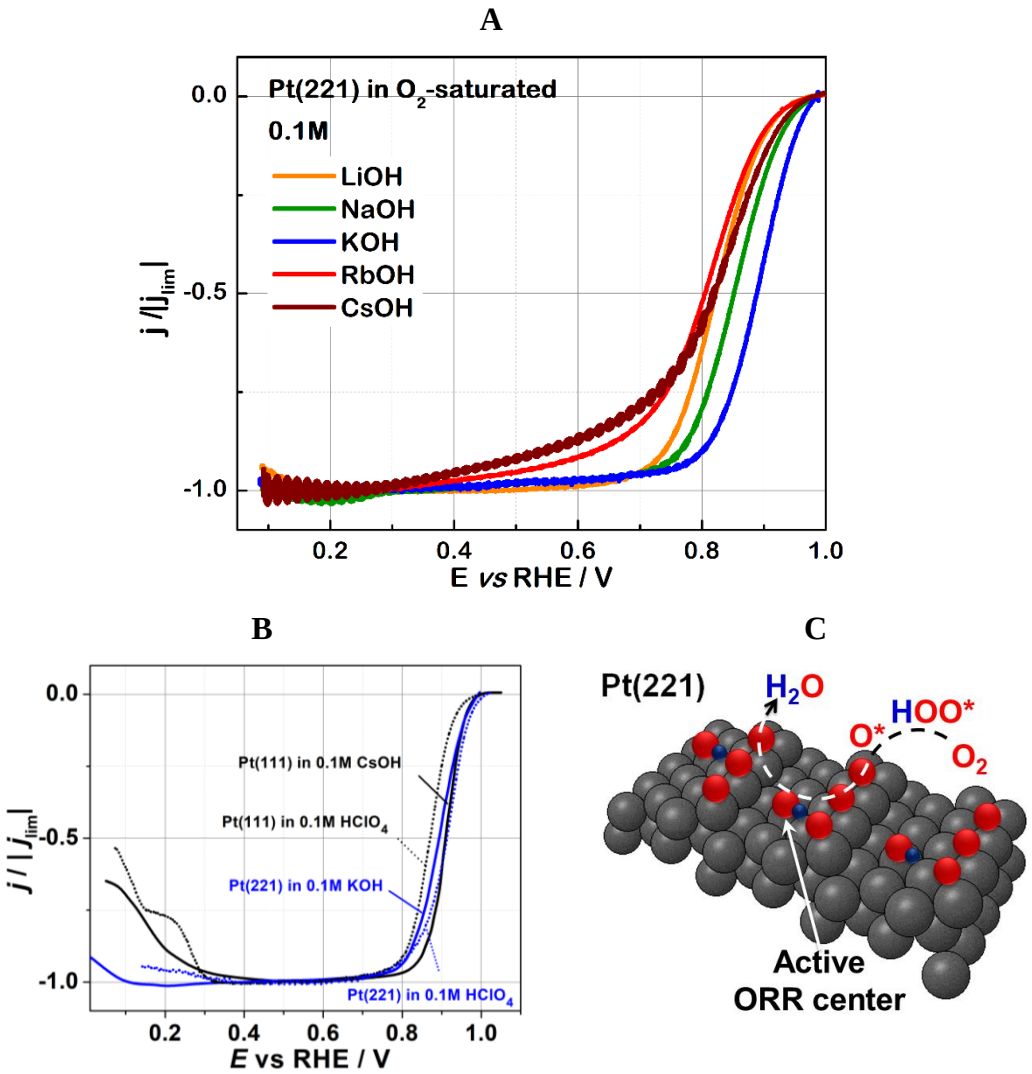

Figure 5.2. (A) *iR*-corrected RDE-voltammograms of stepped single crystalline Pt(221) electrodes in O_2-saturated 0.1 M LiOH, NaOH, KOH, RbOH, and CsOH electrolytes (50 mV s^{-1}, 1600 rpm). (B) Typical anodic branches of the RDE-voltammograms of the Pt(221) electrodes in O_2-saturated 0.1 M $HClO_4$ and KOH, after the *iR*-correction. The RDE-voltammograms of Pt(111) electrodes in $HClO_4$ and CsOH are also shown (taken from ref.147). (C) Model showing the location of the active catalytic centres at the Pt(221) surface for the ORR in $HClO_4$ based on our previous work[171]. These active centres have optimal coordination with regard to the generalised coordination numbers[22]. Note that the under-coordinated sites at Pt(221) surface are permanently blocked by oxygen species represented as red spheres. The platinum and hydrogen atoms are represented by black and blue spheres, respectively.

The pH and electrolyte composition would likely both affect the electrocatalytic performance since they obviously change the adsorption properties of the Pt surfaces as indicated by the changes in the voltammograms above. Thus, the ORR activities of

Pt(221) and Pt(331) were also measured in O_2-saturated 0.1 M $HClO_4$ and different *Me*OH (*Me*$^+$ = Li^+, Na^+, K^+, Rb^+, and Cs^+) electrolytes. The corresponding anodic polarization curves for the Pt(221) are shown in **Figure 5.2A** and **B**. In **Figure 5.2B**, the polarization curves of Pt(111) in 0.1 M $HClO_4$ and CsOH recorded under the same experimental conditions were adapted from the literature for comparison. Moreover, based on our previous work[171], a model illustrating the ORR process on the Pt(221) surface in $HClO_4$ and its corresponding active catalytic centres are proposed (**Figure 5.2C**). Besides, the alkaline ORR kinetic current densities of Pt(221) and Pt(331) at the potential of 0.9 V_{RHE} were summarized in a bar chart for comparison (**Figure 5.3**), in which the kinetic current densities of Pt(111) in 0.1 M $HClO_4$ and KOH, and of Pt(221) in 0.1 M $HClO_4$ were also added.

The Pt(221) electrodes exhibited a higher ORR activity than that of Pt(111) in acidic electrolytes (**Figure 5.2B**). This is consistent with previous observations in 0.1 M $HClO_4$.[171] This high ORR performance of Pt(221) is attributed to the maximal density of active sites, which have optimal coordination (in terms of the generalized coordination number)[177] and consequently, have optimal binding energies for the ORR intermediates. As shown in **Figure 5.2C**, these most active sites were practically those 'on-top' sites located near to the concavities at steps. The values of the generalised coordination numbers and *OH binding energies for the active sites at Pt(111) and Pt(221) surfaces can be found in **Table 5.1**.

However, when measured in alkaline media, the activities of both low- and high- index Pt surfaces were significantly different from those in acidic solutions and evidently depended on the alkali metal cation present in the electrolyte. With regards to Pt(111), the activity trend observed in different alkaline media followed the order: LiOH < NaOH < KOH < RbOH < CsOH and the activity obtained in CsOH was higher than that in $HClO_4$ (**Figure 5.2B**). The reason for this monotonous activity trend given by Markovic *et al.*[147] was that the hydroxyl-binding to (111) terraces of Pt(111) is weaker and these OH-species are destabilised by 'less-solvated' Cs^+ ions as compared with other alkali metal ions, which likely leads to a more optimal *OH binding energy relative to that in acidic solutions. For the high index surfaces, the activities observed in all alkaline electrolytes, however, are worse than those in acidic solutions (**Figures 5.2B** and **5.3**),. This observation is consistent with the results by Rizo *et al.*[164]. Moreover, as shown in **Figure 5.2A** and summarised in **Figure 5.3**, the activity trend in different

alkaline electrolytes was also totally changed compared to that for the Pt(111). For both Pt(221) and Pt(331) electrodes, the highest activities were observed in KOH, followed by NaOH and CsOH, whereas the lowest activities were obtained in LiOH for Pt(221) and in RbOH for Pt(331), respectively. Furthermore, the ORR activities of Pt(221) were higher than those of Pt(331) in almost all the alkaline electrolytes.

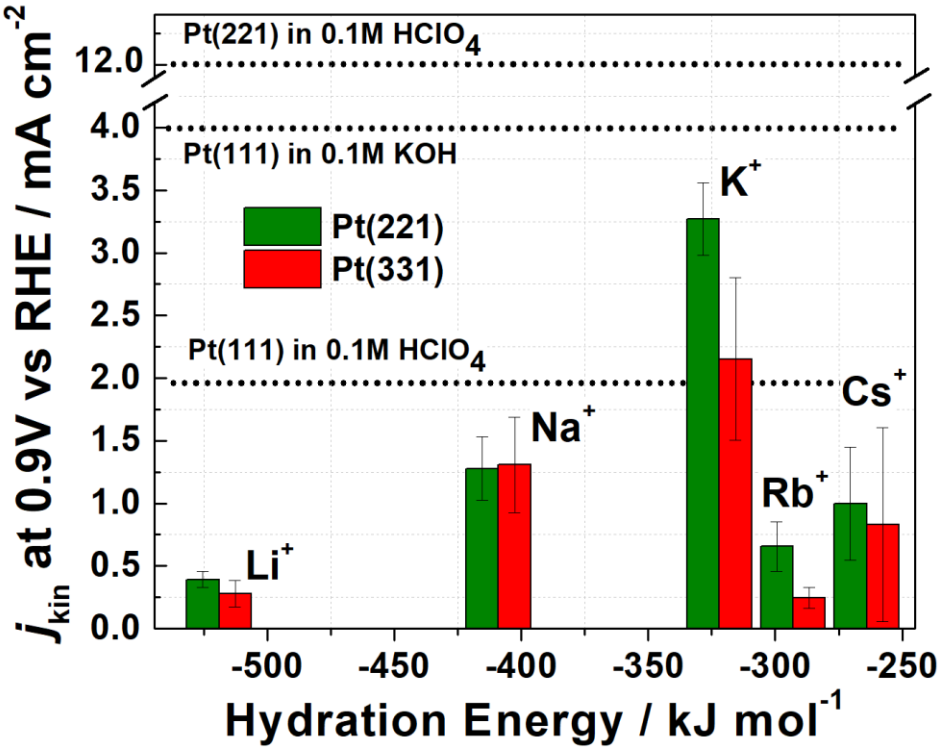

Figure 5.3. Bar chart summarising the ORR kinetic current densities at a potential of 0.9 V_{RHE} for Pt(331) and Pt(221) electrodes in 0.1 M LiOH, NaOH, KOH, RbOH, and CsOH. The activities of Pt(221) in 0.1 M $HClO_4$ and of Pt(111) in 0.1 M $HClO_4$ and 0.1 M KOH are specified by dotted lines for comparison.

5.2 Influence of the alkali metal cations on the oxygen reduction reaction activities of low- and high-index Pt electrodes

The observed ORR activities for the low- and high-index Pt electrodes in different electrolytes raise curiosity about the role of the surface structure and alkali metal cations in the ORR activity. In other words, why the introduction of stepped atoms is beneficial for the ORR performance in acidic media but harmful for that in alkaline media, and why the ORR activity trend obtained in the electrolytes with different alkali metal

cations is totally changed after the introduction of stepped atoms? This is discussed in the next sub-chapter.

5.2.1 Influence of the alkali metal cations on the activity of low-index Pt surfaces

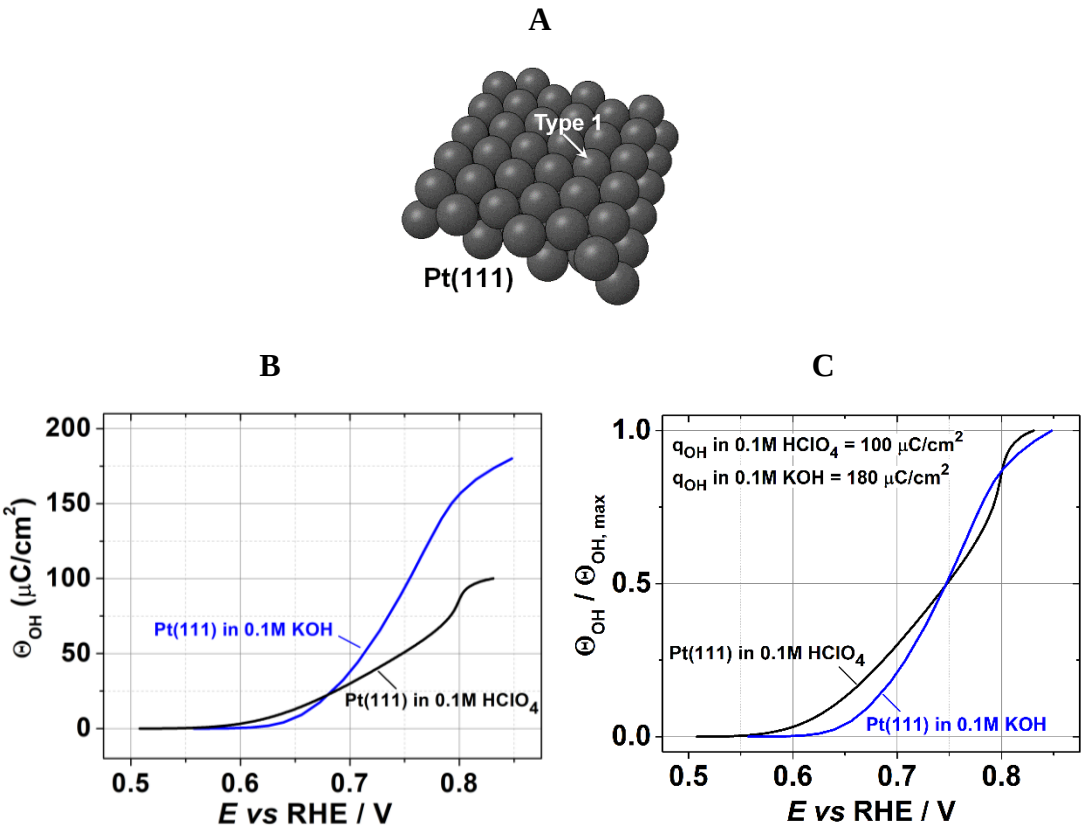

Figure 5.4. The ORR catalytic centres and OH-adsorption isotherms for the Pt(111) surface. (A) Schematic representation of catalytic centres at the surface of Pt(111). Black spheres represent Pt atoms. (B) OH-adsorption isotherms in 0.1 M KOH and $HClO_4$ calculated from the anodic branches of the voltammograms shown in Figure 5.1A. (C) OH-adsorption isotherms normalised by the maximal fractional surface coverages. The inset gives the maximal OH-charges calculated from the CVs.

The *OH-binding to catalytic sites of Pt(111) is supposed to be weakened by the alkali metal cations present in basic media, which is beneficial for their ORR activity as the *OH-binding for Pt(111) in acidic solutions is stronger compared to the optimum. There is only one type of 'on-top' sites present at Pt(111) surface (shown as Type 1 in **Figure 5.4A**). Accordingly, these adsorption sites can be recognised as the probable active centres for Pt(111). Based on the theoretical calculations[171] summarised in **Table 5.1**,

the *OH-binding to the catalytic sites at the Pt(111) surface in acidic solutions is almost 0.1 eV stronger than the optimal one (the value of $\Delta E_{OH} - \Delta E_{OH(optimum)}$ for Type 1). When changing to alkaline media, the alkali metal cation is suggested to weaken the *OH-surface interaction, which is beneficial for the ORR performance of Pt(111).[147] This weakening is determined by the hydration energy of alkali metal cations, in which the Cs^+ ions with the smallest absolute hydration enthalpy result in the least stabilisation, leading to the highest ORR activity. Thus, the alkaline ORR activity trend observed for Pt(111) was as follows: LiOH < NaOH < KOH < RbOH < CsOH.

Table 5.1. Parameters characterising adsorption sites indicated in Figures 5.4A and 5.5C in acidic media.

Adsorption sites (according to Figures 5.4A and 5.5C)	Generalised coordination number (adsorbed O-species and Pt are assumed to contribute equally, according to ref.171)	ΔE_{OH} - $\Delta E_{OH(Pt(111))}$ according to refs 22, 171, and 177	ΔE_{OH} - $\Delta E_{OH(optimum)}$
Type 1	7.5	0.00 eV	-0.1 eV
Type 2	8.0	0.0925 eV	-0.0075 eV
Type 3	9.83	0.43eV	0.33 eV
Type 4	7.5	0.00 eV	-0.1 eV

Another peculiar effect of alkali metal cations is that the amount of OH-adsorbates obviously increases (**Figure 5.4B**), as suggested by the OH-adsorption isotherms for Pt(111) in 0.1 M KOH and $HClO_4$. Their normalisation by the maximum surface coverages are also shown in **Figure 5.4C**. The surface coverage of the adsorbed OH-species was calculated from the area (charge) under the OH-adsorption peaks in the CVs of Pt(111) in KOH and $HClO_4$ at the potential range from ~0.55 to ~0.85 V_{RHE} (**Figure 5.1A**). The maximal surface coverage obtained in KOH, around 180 $\mu C\ cm^{-2}$, is almost two times higher than in $HClO_4$, around 100 $\mu C\ cm^{-2}$. This observation could be attributed to the alkali metal cations present in the electrolytes which decrease the repulsive forces between the OH-species. In other words, a densely packed layer of

*OH on the Pt(111) surface could not be formed due to the repulsive forces between the same charged adsorbates. However, positively charged metal cations near the electrode surface are likely able to weaken those repulsive forces and thus increase the amount of OH-adsorbates. One can assume that all the adsorbed OH will be able to take part in the ORR as the adsorption of OH species on the Pt(111) surface are all reversible in alkaline media[173]. Therefore, this increasing amount of OH-adsorbates may also contribute to the observed higher alkaline ORR activities of Pt(111), i.e. the alkali metal cations simply also increase the number of available active sites due to non-covalent interactions.

5.2.2 Influence of the alkali metal cations on the activity of high-index Pt surfaces

One can see from the last section that the binding energy of *OH is closely associated with the OH-adsorption peak that can be typically observed in cyclic voltammetry measurements. Thus, CVs of high-index Pt surfaces in 0.1 M LiOH and KOH were compared in **Figure 5.5A** and **B**. Surprisingly, for both Pt(221) and Pt(331), the potentials of the OH-adsorption peak were more positive in KOH compared with that in LiOH. This observation implies that the nature of alkali metal cations indeed has an effect on the strength of *OH binding to catalytic sites at the high-index surface.

In order to elucidate aforementioned influence of alkali metal cations, structural and energetic characteristics of the high-index Pt electrodes should be taken into consideration. With regard to Pt(221), four types of surface sites need to be considered (**Figure 5.5C**). It should be noted for ORR that two types of these surface sites are in principle inactive. The first site is located on the top edges, which are permanently blocked by oxygen species, and the second site is hindered, which is shown as Type 3 in **Figure 5.5C**. The existence of these inactive sites, however, is necessary to create highly active sites, labelled as Type 2 in **Figure 5.5C**. The last type of surface sites is comparable to the Type 1 sites of Pt(111) (**Figure 5.4A**), which are labelled as Type 4 in **Figure 5.5C**. For the Pt(331), the only difference from Pt(221) is that the width of the (111) terrace decreases to three atoms, and thus only three types of surface sites are present at the surface. The missing surface sites are Type 4. The *OH binding energies and generalised coordination numbers for these sites in acidic media are summarised in **Table 5.1**. It can be seen that Type 2 demonstrates the most optimal *OH-binding

energy which is only approximately 0.0075 eV stronger than the optimal value, and an almost optimal generalized coordination number. That is the reason why Pt(221) and Pt(331) both exhibit higher acidic ORR activities than Pt(111).

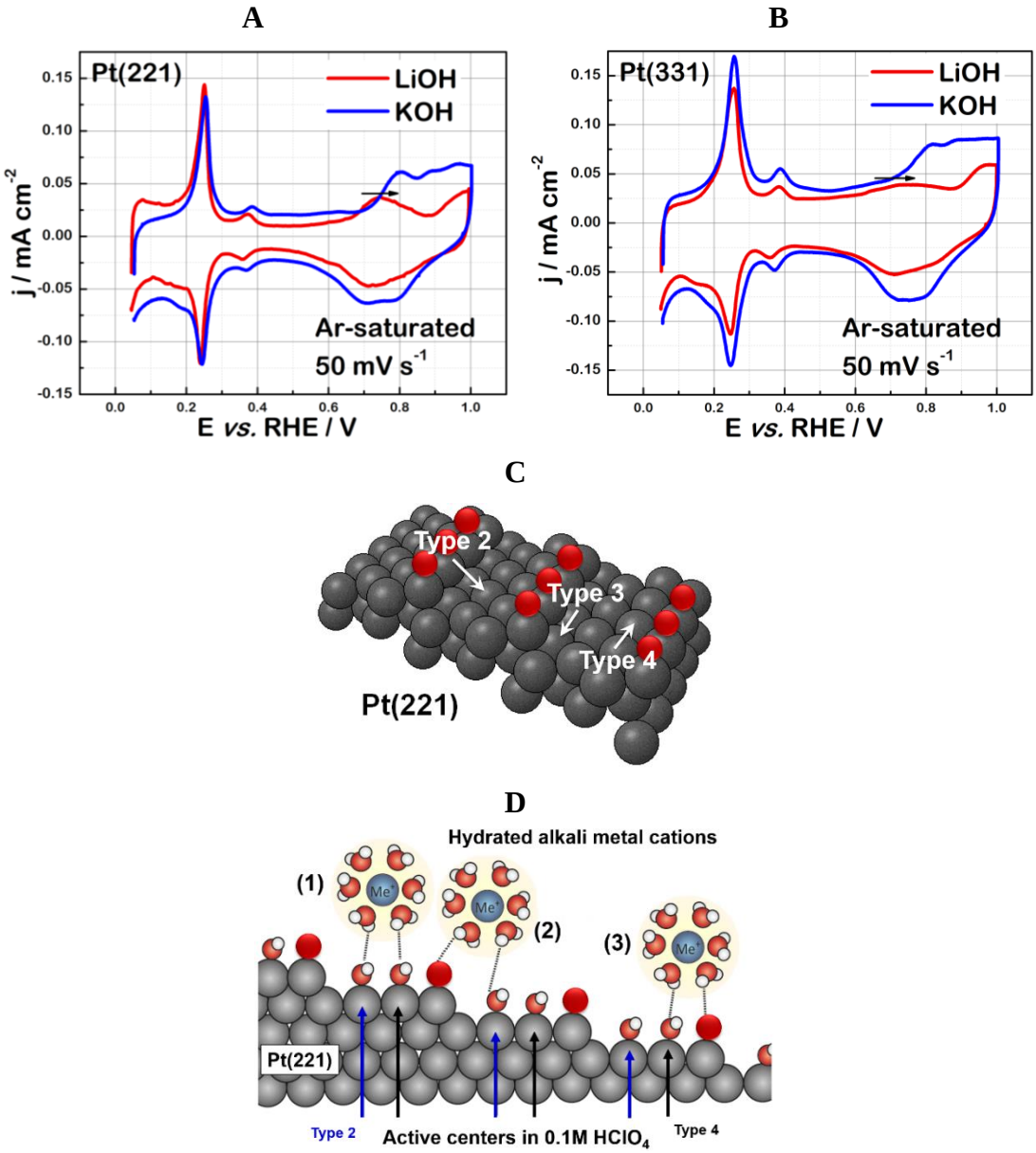

Figure 5.5. CVs and ORR catalytic centres of high-index surfaces. CVs of (A) Pt(221) and (B) Pt(331) electrodes in Ar-saturated 0.1 M LiOH and KOH electrolytes. As indicated by the arrows, the potential of OH-species adsorption peak shifts towards more positive potentials in the KOH electrolytes. (C) Schematic representation of 'on-top' ORR catalytic centres at the surface of Pt(221) at 0.9 V_{RHE}. (D) Schematic description of how alkali metal cations interact with the steps and terraces of Pt(221) surfaces. Note that the under-coordinated sites at Pt(221) surface are permanently blocked by oxygen species, represented as red spheres. Grey, dark blue, and white spheres represent the platinum atoms, the alkali metal cations near to the surface, and the hydrogen atoms, respectively.

In alkaline media, the *OH binding energy of these catalytic sites present at the high-index surface is likely changed by the non-covalent interactions, similar to what happened for Type 1 on Pt(111). However, these noncovalent interactions between Type 2 and the alkali metal cations located nearby are significantly detrimental for its ORR catalytic activity, as these interactions apparently divert its *OH binding energy from the near-optimal values. This hypothesis explains why the ORR activities of Pt(221) and Pt(331) are both worse than Pt(111) in alkaline media. Moreover, since the additional Type 4 present at Pt(221) performs similar to Type 1 in Pt(111), which is beneficial from the interactions of the alkali metal cations, Pt(221) has better ORR activity in alkaline media than Pt(331).

Based on the above considerations, the Pt(221) surface was taken as an example to derive a model describing how the catalytic sites are influenced by the alkali metal cations (**Figure 5.5D**). There are two assumptions in this model. One is that the binding of *OH to the catalytic sites is weakened by the hydrated alkali metal cations through hydrogen bonds, and the other is that there are no alkali metal cations specifically adsorbed on the surface, that is, these alkali metal cations close to the electrode surface keep their integral solvation shell. Correlated with the types of catalytic sites present at the Pt(221) surface, three possible kinds of interactions between the solvated alkali metal cations and these active centres are depicted. These interactions generally are beneficial for Type 4, yet are detrimental for Type 2.

However, quantification of these interactions still seems to be impossible due to the limited fundamental knowledge and methodology. Therefore, the alkaline ORR activity trend for these high-index surfaces can only be explained qualitatively. As mentioned before, these interactions are inversely related to the hydration energy of alkali metal cations. In other words, the electrolyte containing the Cs^+ ions (CsOH) will exhibit the strongest interactions, as Cs^+ ions own the smallest absolute hydration enthalpy. With regard to Type 4, which exhibits a relatively strong *OH binding energy, these interactions are beneficial to catalyse ORR. The strongest interactions show the best activity, based on the observed ORR trend in different alkaline media for Pt(111). However, in terms of Type 2 (site on the Pt(221) and Pt(331)), which exhibits an almost optimal *OH binding energy (only approximately 0.0075 eV stronger), these interactions are harmful for their ORR activity, as the binding of *OH likely becomes too weak. What is more, the size of the solvated metal cations should also be taken into

consideration for these high-index surfaces. For the planar Pt(111) surface, the cations can interact unimpeded with the entire first water layer, whereas, for stepped surfaces, the terrace may be shielded by the step edges. That is, for the stepped surfaces, the interaction between the cations and adsorbed species is not equal for all surface sites, and especially weakened for those 'under' a step. This 'shielding' effect then depends on the size of the solvated metal cations. Therefore, the active sites present at Pt(221) and Pt(331) surfaces, primarily Type 2, become more 'unpredictable' in alkaline media.

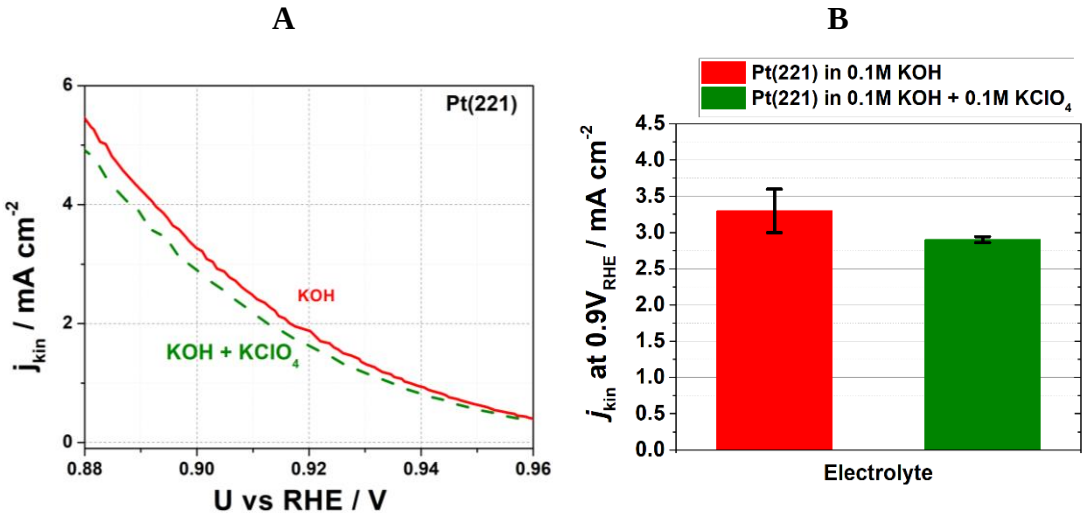

Figure 5.6. (A) Typical kinetic current density for Pt(221) electrodes recorded in 0.1 M KOH + 0.1 M $KClO_4$ and 0.1 M KOH electrolytes. (B) A bar chart showing the corresponding kinetic current densities at 0.9 V_{RHE}. Both electrolytes used here were O_2-saturated. The 0.1 M KOH + 0.1 M $KClO_4$ electrolyte was prepared by mixing KOH and $HClO_4$ solutions. The error bars are from five different measurements.

Besides, additional experiments were performed to demonstrate the role of alkali metal cations on the ORR activities of high-index surfaces. In these separate experiments, the Pt(221) electrodes in K^+ containing electrolytes were investigated, as Pt(221) exhibited the highest ORR activities in KOH compared to in all other alkaline solutions. The influence of K^+ concentration on the ORR activity of Pt(221) was studied. For that, $KClO_4$ solutions were prepared by mixing $HClO_4$ and KOH to increase the K^+ concentration without changing the pH. The reason for choosing perchlorate anions is that they are considered to be inert. The ORR activities of Pt(221) were measured in O_2-saturated 0.1 M KOH + 0.1 M $KClO_4$ under the same experimental condition as that in KOH. The corresponding polarization curve is indicated in **Figure 5.6A**, in which

the polarization curve in 0.1 M KOH is also shown for comparison. The kinetic current density in the mixed solution was lower than that in the pure KOH solution. A bar chart of their kinetic current densities at 0.9 V_{RHE} in **Figure 5.6B** is also used to compare their activity. One can see at the potential of 0.9 V_{RHE} that the kinetic current density dropped by almost 15% when increasing the concentration of K^+ species. Although effects from the additional perchlorate anions cannot be excluded, this observation confirms the negative influence of alkali metal cations on the ORR activities of high-index surfaces.

5.3 Summary

In this chapter, the influence of alkali metal cations on the ORR activities of low- and high-index Pt surfaces has been discussed.

Firstly, CVs of Pt(111), Pt(221) and Pt(331) were recorded in Ar-saturated acidic solution, namely $HClO_4$, and different alkaline electrolytes (LiOH, NaOH, KOH, RbOH, and CsOH). It was observed that not only pH but also the nature of alkali metal cations present in the electrolyte affect the voltammetric features of the Pt electrodes, particularly in the OH_{ads} region. These observations imply that alkali metal cations have a significant influence on the ORR activity.

Then, the ORR activities of Pt(111), Pt(221), and Pt(331) electrodes were measured in the O_2-saturated $HClO_4$ and five different alkaline electrolytes. For Pt(111), the activity became better in alkaline media compared to that in acidic media, and the corresponding activity trend in different basic media was as follows: LiOH < NaOH < KOH < RbOH < CsOH. However, for Pt(221) and Pt(331), when the acidic media was substituted with different basic media, the activities significantly dropped, and the activity trend was also changed, i.e., KOH ≫ NaOH > CsOH > RbOH ≈ LiOH. These results demonstrate that the ORR activities for both low- and high-index surfaces depend not only on the pH but also on the nature of the metal cation present in the electrolyte.

The specific types of active centres present at low-and high-index Pt single crystals are taken into consideration to explain these observations. For Pt(111), the only type of active sites is benefiting from interactions with the alkali metal cations. The binding of reaction intermediates to the active sites is weakened by the alkali metal cations, and this effect is strictly dependent on the solvation energy for the alkali metal cations. For

Pt(221) and Pt(331), the alkali metal cations result in the adverse effects due to the existence of different types of active sites and the shielding effect from the step edges. While it becomes too complex to quantify the specific influence of each sort of alkali metal cations, these results confirmed that alkali metal cations play a critical role in the ORR performance of various Pt surfaces.

6. The role of *n*-butylamine in water electrolysis

Due to its low efficiency, the anode reaction generating gaseous O_2 severely limits the application of water electrolysis in the production of hydrogen fuels. Although the equilibrium potential is merely 0 V_{RHE} for HER and 1.23 V_{RHE} for OER, the real onset potential for the OER is approximately 1.6-1.7 V_{RHE} for the most of the commercial electrodes.[41,178] That is why OER has been increasingly recognized as the bottleneck of the electrochemical water splitting. Additionally, O_2 gas, the product of the OER, is not used in further applications. Therefore, producing more valuable products instead of O_2 would be highly beneficial in these systems. Several important reactions have been suggested to have the potential to replace the OER or proceed simultaneously. Among them are electro-oxidation of some organic compounds, chlorine evolution[179] and production of hydrogen peroxide[180] just to name a few. However, note that these potential alternative reactions should also have high selectivity and stability to satisfy the industry requirements.

Recently, introduction of new spectator species into the aqueous electrolyte, namely *n*-butylamine, as reported by MacFarlane *et al.*[180], can dramatically increase the anodic activity of Mn-oxide electrodes and result in a very low net overpotential. They found that anodic hydrogen peroxide production dominated over the OER for certain MnO_X-type electrocatalysts when *n*-butylammonium sulphate (BAS), one of the 'ionic liquids' (ILs), was added into the aqueous electrolytes at pH=10. It was shown that BAS didn't participate directly in the anodic oxidation reaction. In fact, there are many kinds of ionic liquids that have demonstrated their promising prospects in electrochemical field.[181,182,183,184,185] For example, superoxide, one of the primary ORR products on cathodes of Li-air batteries, can slowly convert itself into Li_2O_2, when using ionic liquids comprised of group 15-centered cations and anions as electrolytes.[186]

Herein, industrially relevant catalysts based on Co-, Ni- and Fe-oxides were tested in aqueous electrolytes containing *n*-butylamine. Different pHs of the electrolytes were also used to find the best water electrolysis system according to the well-known pH effects in typical aqueous solutions. Significant drops in the anodic overpotential (relative to the equilibrium potential of the OER) were observed for almost all measured

catalysts, and the extent of the effect was apparently dependent on the nature of the used catalysts. A pH effect was indeed observed, and the best performance was found at pH 12. Besides, the presence of BAS also increased the catalyst stability of these systems. To further clarify the role of BAS, RRDE measurements were performed, and it was found that some amount of H_2O_2 was indeed produced. With the help of ^{1}H NMR spectroscopy, however, it was found that the primary reaction occurring at the anodes was selective oxidation of BAS to *n*-butyronitrile, a valuable organic chemical, which is widely used in many industrial synthetic schemes[66,187,188,189] as well as in dye-sensitised solar cells[190]. The Faradaic efficiency of this oxidation reaction was found to be as high as 95%. Butyronitrile is only slightly soluble in water and can be easily separated from the electrolyte.

The chapter is divided into six parts: the first section is a simple introduction to the function of ILs. In the second section, the electrochemical activities of nickel, cobalt, and nickel-iron oxy-hydroxide based electrodes (denoted as NiO_X, CoO_X, and $NiFeO_X$, respectively) at the presence and absence of BAS are demonstrated. In the third section, the results related to the pH effect are discussed. The fourth section is mainly about the stability tests. In the fifth section, the RRDE and ^{1}H NMR results are provided followed by a summary.

Parts of this chapter were published in the article '*Reconsidering Water Electrolysis: Producing Hydrogen at Cathodes Together with Selective Oxidation of n-Butylamine at Anodes*' in *ChemSusChem 10 (2017) 4812-4816*[137].

6.1 The role of ionic liquids

Ionic liquids are salts, which are normally liquids at room temperature. They demonstrated a great potential in numerous energy applications, as they are able to offer a range of unique properties in a variety of contexts.[180] A great number of ionic liquids provide high electrochemical and chemical stability, low flammability/volatility, and relatively high intrinsic ionic conductivity;[191,192,193] These advantages make them good electrolytes.

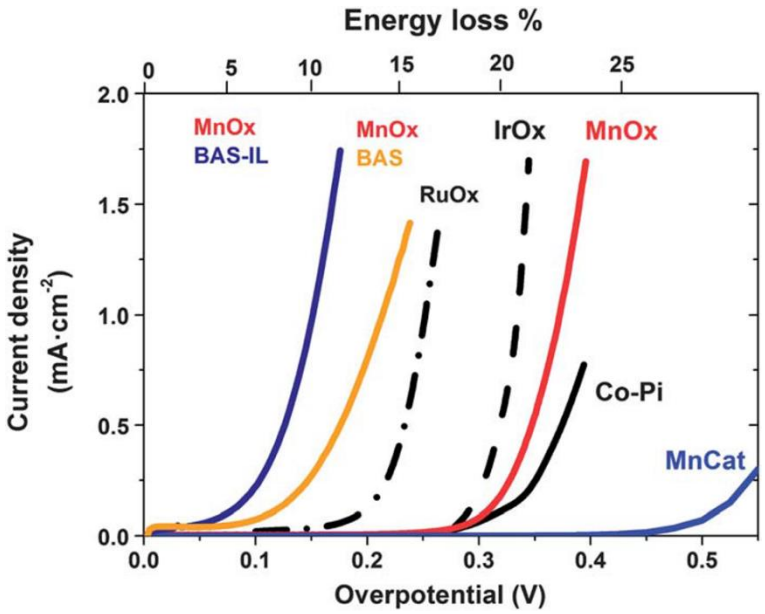

Figure 6.1. Anodic branches of voltammograms for MnO_X electrodes recorded in 1 M NaOH, BAS = 0.4 M di(butylammonium) sulfate at pH=10, and BAS-IL = 2 M di(butylammonium) sulphate at pH=10, in which MnO_X electrodes were prepared by the electrodeposition method using ethyl ammonium nitrate electrolytes. The performances of MnCat, Co-Pi, IrO_X and RuO_X electrodes for the water oxidation reaction in 1 M NaOH are shown for comparison. Graphics is adapted from ref.180. Copyright 2014, Royal Society of Chemistry.

ILs have exhibited superior properties in various electrochemical technologies, including advanced batteries, dye sensitised solar cells, supercapacitors, actuators, as well as in water splitting. In lithium-ion and sodium-ion batteries, cycling stability is dramatically improved when ILs are employed as electrolytes.[194] For instance, pyrrolidinium and piperidinium ILs were reported to improve cycling stabitity.[195,196,197,198] With regard to solar cells, the application of ILs not only improves the conversion efficiency[199] but also makes it possible to develop flexible dye sensitised solar cells on plastic substrates[200]. For the application in supercapacitors, cell voltage can be dramatically increased.[201,202] In terms of actuators, the applied ILs can offer significant advantages in the durability and simplicity of actuator structure.[203,204]

In this chapter, the focus is set on the effect of ILs on water splitting. There are two distinct aspects of current research concerns. One is that ILs are used in the electrosynthesis of catalysts for water splitting.[205,206] For example, MnO_X layer, produced by the electrodeposition method, in which ethyl ammonium nitrate ionic liquids were used as electrolytes, demonstrated an outstanding water oxidation

performance as compared to normal MnCat (**Figure 6.1**). The catalytic materials synthesised in the presence of ILs have fascinating abilities to split water, as ILs can offer several unique advantages for chemical synthesis, such as a reasonably high synthesis temperature without changing the pressure vessel. The other aspect is that (hydrated) ILs are used directly as the electrolytes for water electrolysis.[33,207] As shown in **Figure 6.1**, the water oxidation reaction on MnO_X was dramatically improved in the presence of BAS.

In a word, ILs can help in addressing some of the most challenging problems in energy conversion and storage. However, extensive research is still required. In the following sections, the role of ILs in water electrolysis will be further determined by taking BAS as the research object.

6.2 Anodic oxidation reactions at the industrially relevant metal oxide electrocatalystss

In this section, oxidation reaction at NiO_X, CoO_X, and $NiFeO_X$ anodes, which are frequently used for industrial applications, was performed in the absence and presence of BAS. These thin-film metal oxide electrodes were prepared by electrodeposition, as described in Chapter 3. The BAS-containing electrolytes were prepared by mixing *n*-butylamine and acid aqueous sulfate solutions. The pHs of these electrolytes were then adjusted by adding *n*-butylamine or sulfuric acid. It should be noted that the addition of KOH was necessary to achieve pH $\geq$ 12. An aqueous 0.4 M potassium sulfate solution without BAS served as the reference electrolyte. This electrolyte was prepared by diluting potassium sulfate in pure water to reduce interference factors such as anion influence, and the pH was then adjusted to the desired value by adding KOH. Besides, the activity curves shown in **Figure 6.2** were corrected for the solution resistance in order to be able to compare with literature, but the current densities, shown in **Figure 6.3** for comparing activity between these investigated catalysts, were not corrected for the *iR* drop to avoid introducing extra uncertainty factors.

The anodic reaction is dramatically improved in the BAS-containing electrolytes for all the investigated metal oxide catalysts, as compared to that in reference electrolytes. For the NiO_X electrodes (**Figure 6.2A**), the onset potential for the anodic currents was ~1.4 V_{RHE} in the presence of BAS at pH=10, which is much lower than that measured for the

K_2SO_4 electrolyte. With regard to CoO_X electrodes (**Figure 6.2B**), a similar lower onest potential was observed in the BAS-containing electrolyte, which was around 1.5 V_{RHE}. Correlated with the results for the MnO_X electrodes shown in **Figure 6.1**, the extent of the improvement caused by the presence of BAS seems to depend on the nature of the used electrodes. The highest activity was observed for NiO_X, followed by the one measured for MnO_X, whereas the lowest was obtained for CoO_X.

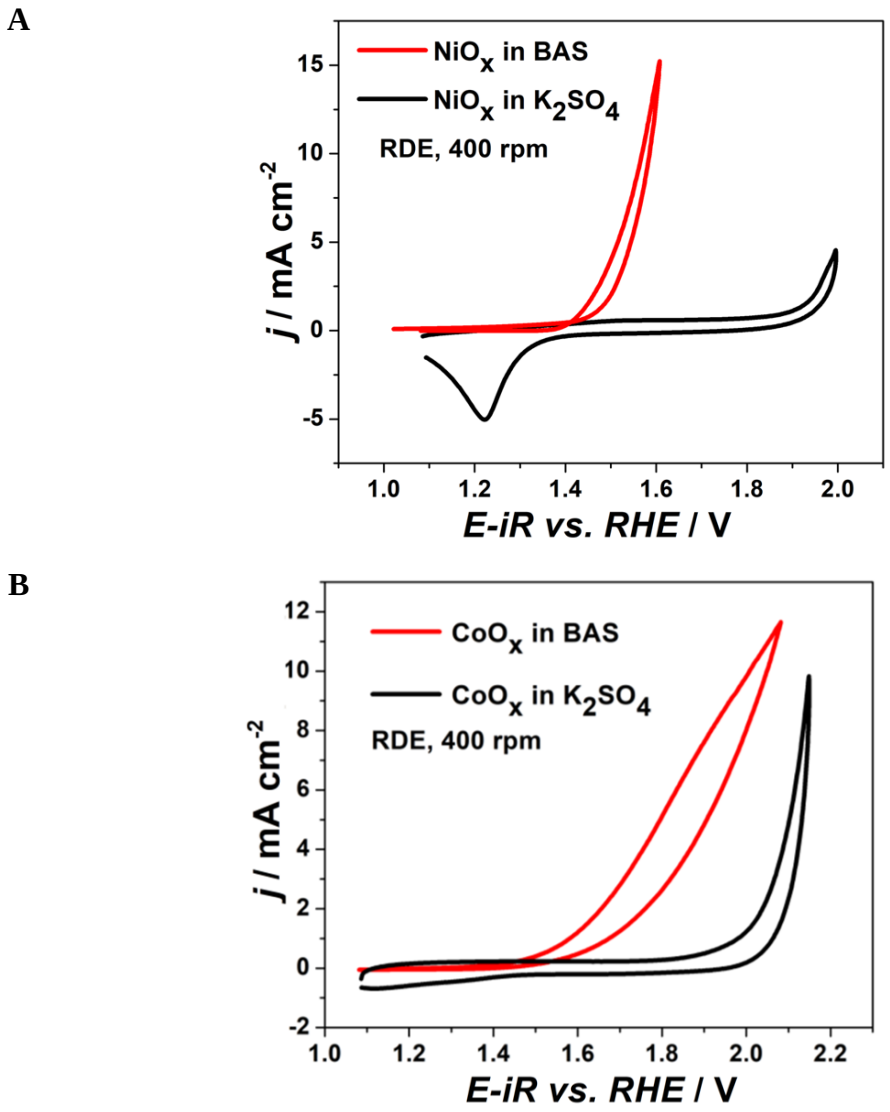

Figure 6.2. Typical cyclic voltammograms of (A) NiO_X and (B) CoO_X thin-film electrodes in 0.4 M BAS-containing electrolytes (red curves) and in 0.4 M K_2SO_4 aqueous reference solutions (black curves). All electrolytes had pH=10, and the potentials were *iR* corrected.

Therefore, to further determine whether the magnitude of the effect from BAS depends on the nature of the electrocatalysts, the activity of various catalysts, i.e., PtO_X, NiO_X, CoO_X, and $NiFeO_X$, was measured in 0.4 M BAS-containing electrolytes and K_2SO_4

electrolytes at pH=12.

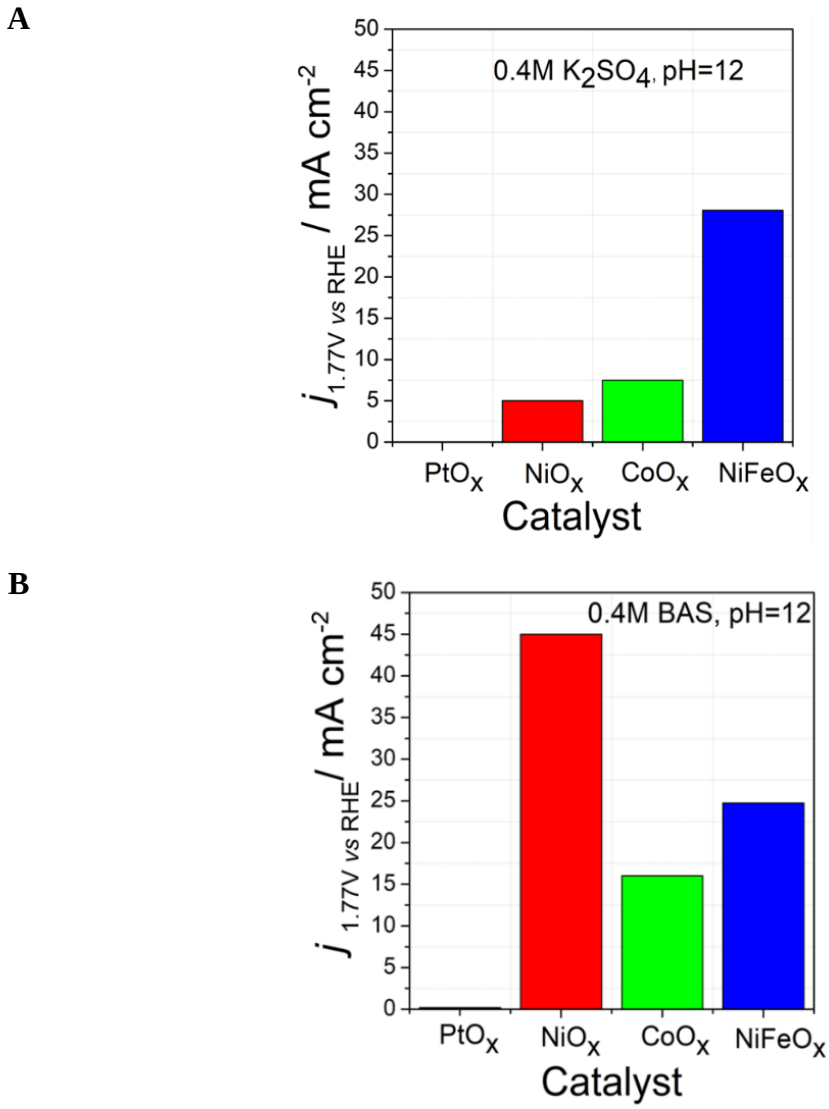

Figure 6.3. Comparison of current densities at 1.77 V_{RHE} for various metal oxide-type electrodes, i.e., PtO_X, NiO_X, CoO_X, and $NiFeO_X$, recorded in (A) 0.4 M K_2SO_4 and (B) 0.4 M BAS-containing electrolytes. The pH values of both solutions were adjusted to 12. The rotational speed of RDE was set to 400 rpm. No *iR* drop compensation was applied.

Figure 6.3A and **B** are bar charts summarising the average current densities of these catalysts at a potential of 1.77 V_{RHE} in aqueous K_2SO_4 and BAS-containing electrolytes, respectively. In the 'purely aqueous' electrolyte, the observed anodic current densities increased in the order: PtO_X < NiO_X < CoO_X < $NiFeO_X$. However, when BAS-containing electrolyte was used, the order of the anodic current densities totally changed, i.e., PtO_X < CoO_X < $NiFeO_X$ < NiO_X. Noteworthy, the anodic currents observed on Pt electrodes can be likely attributed to oxidation of bulk metallic platinum which is

present below the platinum oxide layer rather than the oxidation of the electrolyte components. The highest current density was obtained for the NiO_X electrode, being about 9 times as high as the one measured in aqueous K_2SO_4 electrolyte. With regard to the CoO_X electrode, the current density also increased in the presence of BAS but just by a factor of two compared to the one measured in the aqueous K_2SO_4 electrolyte. However, for the $NiFeO_X$ electrode, the current density remained unchanged. Thereby, BAS did not affect the anodic oxidation process at the $NiFeO_X$ anode. These observations confirmed that there is a certain interplay between the properties of the catalyst and the electrolyte that leads to the variation of the magnitude of the observed effect.

6.3 The pH effect

The existence of pH-effects has been observed in most electrocatalytic systems.[115,208,209] In the case of non-noble metal oxide catalysts utilized to catalyse the OER, higher pH values are typically used, as the corresponding OER activities are generally better and the oxide catalysts are relatively more stable. The alkaline electrolytes used in current industrial applications have relatively high pHs, usually 30 wt. % KOH solutions.[210] Therefore, in order to investigate the pH-effect, different pH values of BAS-containing electrolytes were measured utilizing the most active thin films (NiO_X) as the working electrodes.

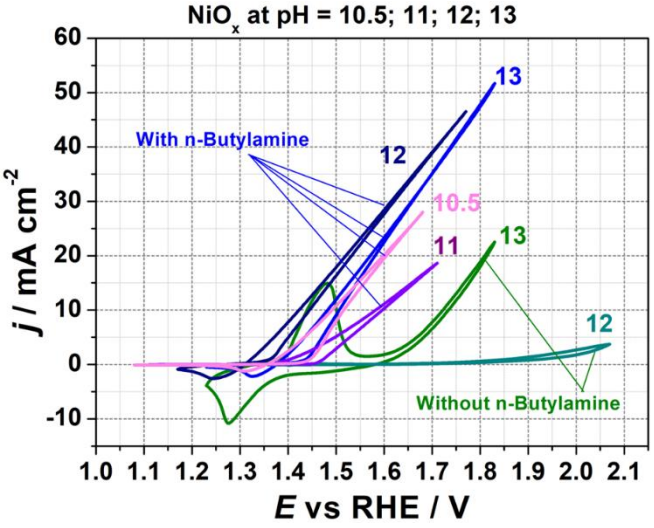

Figure 6.4. Typical cyclic voltammograms of NiO_X thin-film electrodes in pH-corrected 0.4 M BAS-containing electrolytes at pHs of 10.5, 11, 12 and 13, and in pH-corrected 0.4 M K_2SO_4 electrolytes at pHs of 12 and 13. Note that the potentials are shown without *iR* corrections.

It seems that the anodic oxidation activities indeed depend on the pH of BAS-containing electrolytes. **Figure 6.4** compares the corresponding cyclic voltammograms recorded in BAS electrolytes with pHs of 10.5, 11, 12, and 13, and aqueous K_2SO_4 electrolytes at pHs of 12 and 13. Consistent with previous reports[211], the OER activities of NiO_X increased in K_2SO_4 electrolytes when the pH value was changed from 12 to 13. However, converse to the observation in typical aqueous electrolytes, one can see that the activity in the presence of BAS dropped when pH value increased from 12 to 13 and from 10.5 to 11, but only raising pH from 11 to 12 led to a dramatical improvement in the performance. Thus, the pH dependence of the activities in the presence of BAS is not trivial, which is in accordance with previous observations[212]. Here, the best activities obtained in BAS-containing electrolyte were at pH=12. However, it should be noted that the specific mechanism of this pH dependence still requires extensive research.

6.4 Stability measurements

As long-term stability is another critical factor determining whether this system can be used in industrial applications, the stability was investigated using the galvanostatic mode. In these long-term stability experiments, a two-electrode configuration (**Figure 6.5**), i.e., NiO_X anodes and Pt cathodes, was used for two equivalent cells, one filled with 0.4 M BAS and the other one with K_2SO_4 aqueous electrolytes. A constant current of 40 mA was applied for 48 h. The corresponding results are shown in **Figure 6.6**.

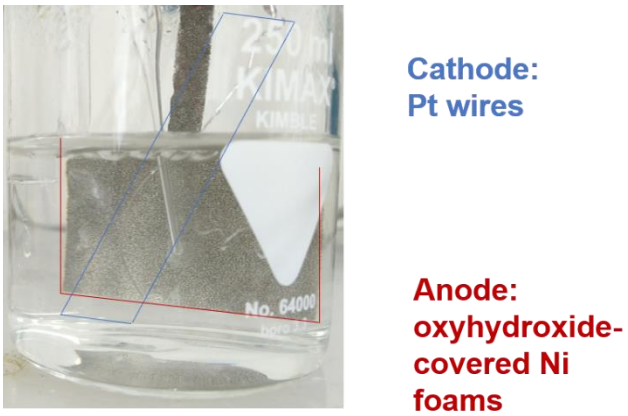

Figure 6.5. Optical photograph of the two-electrode configuration used for long-term stability experiment, in which NiO_X foams were taken as anodes, Pt wires as cathodes, and BAS or K_2SO_4 aqueous solutions as electrolytes.

This new BAS-containing system demonstrates superior stability. After 48 h of running the experiment, the overall cell voltage remained at the initial value in the case of BAS, whereas in the case of K_2SO_4 aqueous electrolyte, the anodes were completely corroded and the cell voltage dramatically increased after just 20 h.

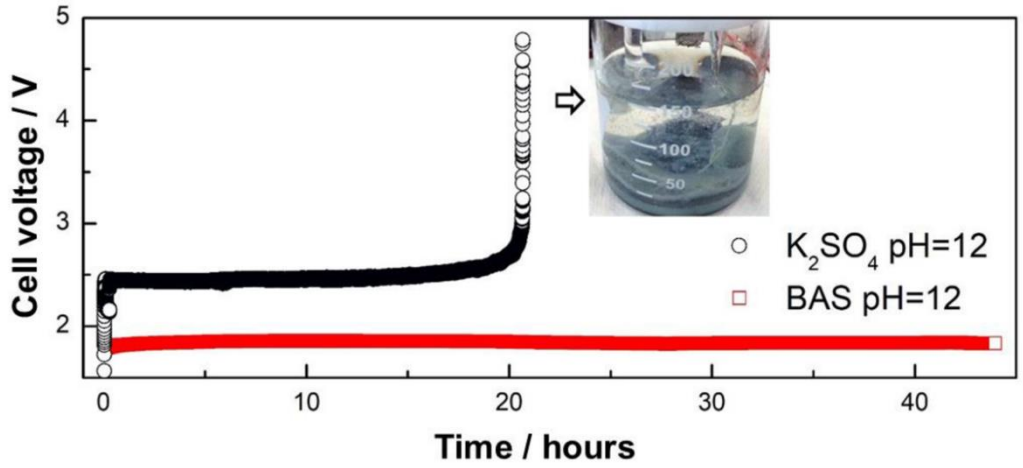

Figure 6.6. Long-term stability experiments in 0.4 M K_2SO_4 and 0.4 M BAS-containing electrolytes at pH=12. A constant current of 40 mA was applied for 48h between the anode (NiOx) and the cathode (Pt wires). In the cell containing K_2SO_4, the NiOx foam corroded within 20 h entirely, resulting in an increase of measured potential before the measurement stopped.

These results indicate that system stability is much better in the presence of BAS than in K_2SO_4 solutions. This superior stability of this new BAS-containing system can be partly attributed to a slight BAS-buffering influence. It, however, cannot completely explain the stabilising effect, which requires further studies.

6.5 The ^{1}H NMR and rotating ring-disk electrode measurements

To determine the role of BAS in the electrolysis system, ^{1}H NMR and RRDE measurements were used. ^{1}H NMR spectroscopy was performed for a freshly prepared 0.4 M BAS electrolyte as well as for the BAS, which had been utilized for the electrolysis for 48 h (see **Section 6.4**). The corresponding results are shown in **Figure 6.7**.

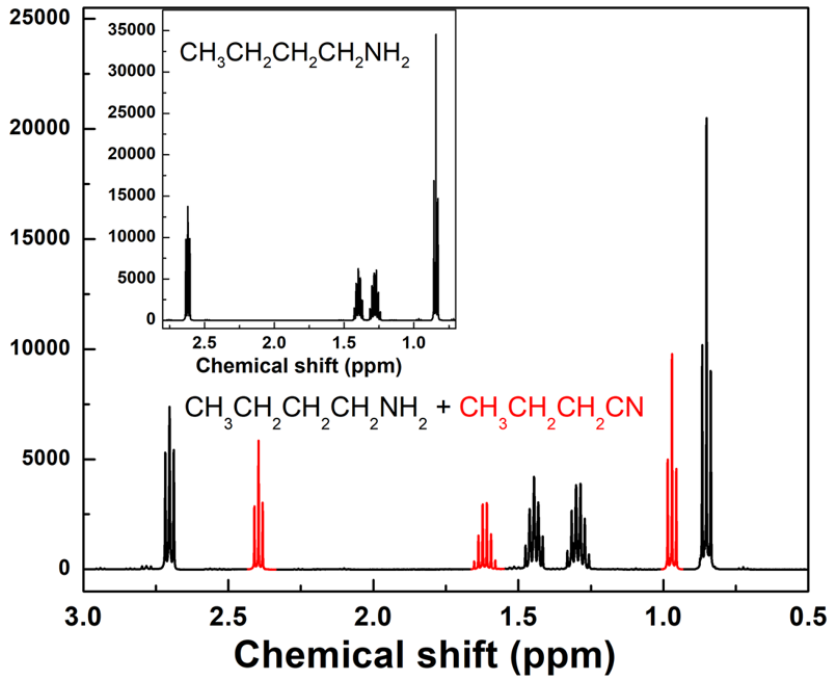

Figure 6.7. ^{1}H NMR spectra of the BAS solution at pH=12 before (inset) and after applying an anodic current of 40 mA for 48 h. The new appearing peaks, marked as red, are consistent well with those of *n*-butyronitrile.

It was found that *n*-butylamine was selectively oxidized into *n*-butyronitrile, and the Faradaic efficiency of this reaction is as high as 95%. The inset graph in **Figure 6.7** gives the ^{1}H NMR spectrum of fresh BAS solutions. The peak positions and relative intensities obtained in this spectrum are well consistent with those reported for *n*-butylamine[213]. After applying 40 mA for 48 h, several new peaks appeared, as shown in the spectrum of **Figure 6.7**. When compared to the literature values, these new peaks are attributed to the *n*-butyronitrile[213], a valuable chemical used as an electrolyte in solar cells as well as an intermediate in synthesis of various organic chemicals. Therefore, by comparing ^{1}H NMR spectra before and after the electrocatalysis, one can see that the reaction occurring at anodes are exclusively selective oxidation of *n*-butylamine to produce *n*-butyronitrile. Note that this remarkable selectivity and highest activity are only obtained at pH=12, as it was reported for NiO_X anodes that at higher pHs almost 15% of *n*-butylamine was converted into several other organic compounds that may complicate the separation process of the products[214].

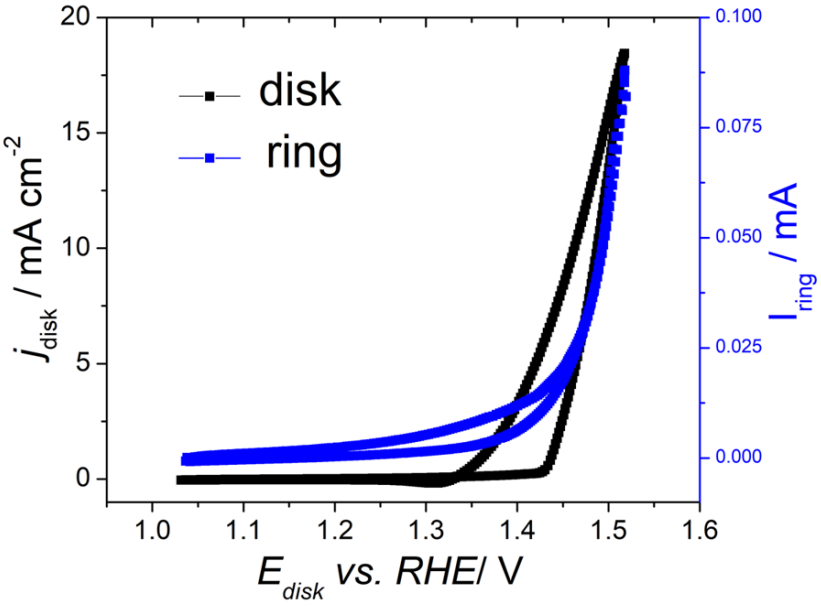

Figure 6.8. Results of the RRDE measurements in BAS-containing electrolytes at pH 12. The disk electrode was NiO_X thin-film electrodes, and the ring electrode was Pt. The potential of the disk was cycled between 1.05 to 1.55 V_{RHE}, whereas the potential of the ring was kept at 1.3 V_{RHE} to investigate whether there is the oxidation of H_2O_2 occurs at the Pt ring. The scan rate and the rotational speed for the disk were 50 mV s^{-1} and 400 rpm, respectively.

To further investigate the processes which occur in the BAS-containing electrolytes, the RRDE measurements were used to *in-situ* check if there are oxygen or hydrogen peroxide produced while running the electrolysis. The RRDE experiments were performed by cycling the potential of the NiO_X disk electrode in the range from 1.05 to 1.55 V_{RHE} while keeping the potential of the Pt ring at 1.3 V_{RHE}. The selected potential for the disk was the standard potential range used for measuring anodic activities in **Figure 6.2**. For the ring electrode, the potential was kept at 1.3 V_{RHE} where only H_2O_2 oxidation can take place (under the conditions of this experiment), as the onset potential for the oxidation of *n*-butylamine on Pt is much higher (as shown for PtO_X in **Figure 6.3**) while for reduction of oxygen it is much lower at around 1 V_{RHE}.

It was demonstrated by RRDE measurements that H_2O_2 was also generated during the anodic oxidation reaction in BAS-containing electrolyte. As shown in **Figure 6.8**, the onset current obtained on the ring appeared almost simultaneously with the emergence of the anodic current on the disk. This observed current on the ring indicates that this species generated at the disk is electroactive at 1.3 V_{RHE}. Thereby, hydrogen peroxide, which solely can be oxidized at this potential on Pt, is most likely a side product of the

anodic reaction in this case. Moreover, a hysteresis of the disk currents in the anodic and cathodic scans was also observed, in which the currents at the anodic scan were much lower than at the cathodic scan (e.g., j_{disk} = 1 mA cm^{-2} at the anodic scan and j_{disk} = 9 mA cm^{-2} at the cathodic scan, when E_{disk} =1.45 V_{RHE}). This hysteresis further demonstrates that H_2O_2 is also produced during the oxidation reaction of BAS, as the hydrogen peroxide generated in the anodic scan may decompose during the cathodic scan, resulting in additional currents. However, note that the onset potential here for producing H_2O_2, around 1.45 V_{RHE}, is much lower than the commonly predicted around 1.76 V_{RHE}. One can assume that this dramatically decreasing onset potential might be attributed to the rather low thermodynamic potential for the formation of H_2O_2, which is as low as 1 V_{RHE}, when there is no pre-existing H_2O_2 in the electrolyte.[215] In the case of BAS-containing electrolyte, H_2O_2 is not stable in alkaline condition, which keeps the concentration of H_2O_2 near the electrode surface very low. Another possibility causing this rather low near-surface concentration of H_2O_2 could be that the BAS, organic matter contained in the electrolyte, helps to stabilise the hydrogen peroxide through the solvation effects[180]. For example, the stabilisation of H_2O_2 by ethylamine molecules has been certified, in which the hydrogen peroxide-ethylamine complexes are approximately 24 kJ mol^{-1} more stable than hydrated hydrogen peroxide, which leads to a negative potential shift for generating H_2O_2 (almost 0.4 V).[180] Combining these observations with the ^{1}H NMR results, one can think that the 5% loss in the Faradaic efficiency could be partially due to the formation of H_2O_2. However, hydrogen peroxide would spontaneously decompose into water and oxygen in alkaline media, and thus *n*-butyronitrile is the only final product. Namely, this anodic oxidation reaction in BAS-containing electrolyte has relatively high selectivity.

These results imply that BAS does not work as a 'spectator species' by influencing the hydrogen bonds of water molecules but takes part in the anodic reaction itself, in contrast to the literature data. The BAS contained in the electrolyte was found to be selectively oxidized into *n*-butyronitrile with a rather high Faradaic efficiency. H_2O_2 was certified to be also generated during this anodic oxidation reaction.

6.6 Summary

Firstly, various industrially relevant catalysts, i.e. NiO_X, CoO_X, and $NiFeO_X$, were used

to test the universality of the reported BAS effect. Apparent improvements of the anodic oxidation reaction were observed on most of these investigated electrodes in the presence of BAS. Utilizing BAS solution increased the activity of NiO_X by a factor of nine, whereas for CoO_X it just increased by a factor of two and for $NiFeO_X$ the activity was comparable to that measured in the K_2SO_4 aqueous solutions. Therefore, it seems that the magnitude of the effect depends on the nature of the catalyst.

Subsequently, the pH effect was investigated. It was observed that the activity dropped when the pH increased from 10.5 to 11 and from 12 to 13 but increased when the pH increased from 11 to 12. The highest anodic activity was obtained at pH=12. These results indicate that there is a non-trivial pH dependency of the apparent activity in the BAS-containing electrolytes.

Additionally, the long-term stability was also measured. After applying 40 mA for 48 h, the overall cell voltage remained at the initial value in the case of BAS. The catalytic sites at the electrode surfaces are not poisoned during the operation.

Last but not least, ^{1}H NMR and RRDE measurements were used to explore the role of BAS in this novel system. It was found that BAS does not work as a 'spectator species' but directly participates in the reaction, in which BAS was selectively oxidized into *n*-butyronitrile with a rather high Faradaic efficiency. H_2O_2 was certified by the conducted RRDE measurements to be also generated during this anodic oxidation reaction. The most selective and active system was found to be NiO_X in the presence of 0.4 M BAS at pH=12.

These observations can pave a novel way to increase the stability and overall cost efficiency of the system for generating H_2 fuel, in which anode reaction OER can be replaced by the production of other valuable chemicals. Moreover, this novel proposed system can be further improved by simultaneously tailoring the electrode surface composition, the electrode surface structure, and the electrolyte composition.

7. Influence of the alkali metal cations on the electric double layer capacitance

It is widely accepted that the electric double layer (EDL) has a significant influence on the functionality of numerous systems applied in energy conversion and storage[216,217,218,219,220,221], ranging from water electrolysis to fuel cells and from batteries to supercapacitors as it determines the interfacial charge and mass transport.[222,223,224] The structure of the EDL is closely connected with the electrode surface structure, electrode surface composition, and electrolyte composition. In other words, measuring the EDL capacitance and its variation can provide a good way of establishing how the properties of the electrode or electrolyte affect the electrocatalytic performance of the systems.

As discussed in Chapter 2 in detail, the electric double layer consists of two regions, namely the Helmholtz region and the diffuse layer. The EDL in the whole region can be seen as the Helmholtz region and the diffuse layer connected in series. If the EDL capacitance is taken into consideration in the whole double layer region, C_D, the following equations are applied:

$$\frac{1}{C_D} = \frac{1}{\mathrm{C}_H} + \frac{1}{\mathrm{C}_{diff}}$$

.

$$\frac{1}{C_H} = \frac{a_{H_2O}}{\varepsilon_{dipole}\varepsilon_0} + \frac{a_{ion}}{2\varepsilon_{IHP-OHP}\varepsilon_0}$$

$$C_{diff} = k\varepsilon_r\varepsilon_0$$

in which

$$k \propto \sqrt{c_s}$$

where c_s is the ion concentration in the diffuse layer. The EIS method was used to estimate the influence of the alkali metal cations on the EDL capacitance C_D. Rather dilute solutions were used as electrolytes. EIS measurements were performed at the potentials close to the potentials of zero charge. The Faradaic processes such as specific adsorption of ions at these potentials are suppressed.[225,226,227] In other words, at these potentials the structure of the double layer is relatively stable, and the EDL capacitance C_D is proportional to:

$$C_D \propto \varepsilon_r \varepsilon_0 \cdot \sqrt{c_s}$$

Here, the values of C'_{DL} are derived from so-called constant phase element (CPE) describing the impedance of the electric double layer (assuming $C'_{DL} = C_D$). The measurements were performed in 0.05 M *Me*ClO_4 (*Me*$^+$ = Li^+, Na^+, K^+, Rb^+, and Cs^+) solutions at pH=6. Different working electrodes, namely Pt(111), Au(111), Cu(111), Cu(100), Pt(775) and Pt(12 10 5), were used. Pt(111) and Au(111) were selected because they are the most commonly used model single crystalline electrodes. The choice of single crystalline Cu is due to the fact that copper electrodes are the most promising catalysts for the carbon dioxide reduction reaction. The selection of stepped crystalline Pt(775) and Pt(12 10 5) is because of their high ORR activities and specific surface defect structures.

The chapter is divided into five parts. The first section introduces the equivalent electric circuit used and the examples of fitted curves. Then, the obtained double layer capacitances of Pt(111) and Au(111) are discussed. The third and fourth sections discuss the corresponding results of Cu(111), Cu(100), Pt(775), and Pt(12 10 5), respectively. The last section is a summary.

Parts of this chapter were published in the article '*Influence of the Nature of the Alkali Metal Cations on the Electric Double-Layer Capacitance of Model Pt(111) and Au(111) Electrodes*' in *The Journal of Physical Chemistry Letters 9 (2018) 1927-1930*[169].

7.1 The equivalent electric circuit

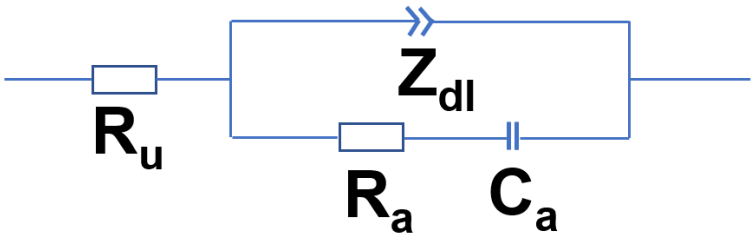

Figure 7.1. The equivalent electric circuit used for fitting of the obtained impedance spectra. R_u represents the uncompensated resistance; Z_{dl} - the double layer capacitance; R_a is an additional adsorption resistance; and C_a - additional adsorption capacitance.

The equivalent electric circuit used for the analysis of the impedance data is shown in **Figure 7.1**. R_u, Z_{dl}, R_a, and C_a represent the uncompensated resistance, the double layer capacitance, additional adsorption resistance, and additional adsorption capacitance, respectively. In addition, R_a and C_a are connected in parallel with Z_{dl} representing the impedance response originating from possible specifically adsorbed species. Note that the element Z_{dl} is not a simple capacitor but a CPE, where $Z_{CPE} = {C'_{DL}}^{-1}(j\omega)^{-n}$. In this case, the exponent n was measured to be higher than 0.95. Therefore, one can assume that the values of C'_{DL} obtained from the CPE are close to the real double layer capacitance, C_D.

For all EIS measurements, the ac-frequency range used was from 30 kHz to 1 Hz. The obtained EIS curves were fitted using the software EIS Data Analysis 1.3. The quality of the fitting and modelling was controlled by individual parameter uncertainties and the root-mean-square deviations.

The EIS experimental and fitted results for the Pt(775) in 0.05 M *Me*ClO$_4$ (Me^+ = Li^+, Na^+, K^+, Rb^+, and Cs^+) are used as examples to demonstrate the quality of the fitting (**Figure 7.2**). For these five electrolytes, the fitted curves all almost overlapped with the obtained experimental curves. The value of the parameter n was higher than 0.95 for all these fitted curves. These observations indicate that the fitted results are acceptable and accurately represent its physical origin; and the physical model is accurate.

7. Influence of the alkali metal cations on the electric double layer capacitance

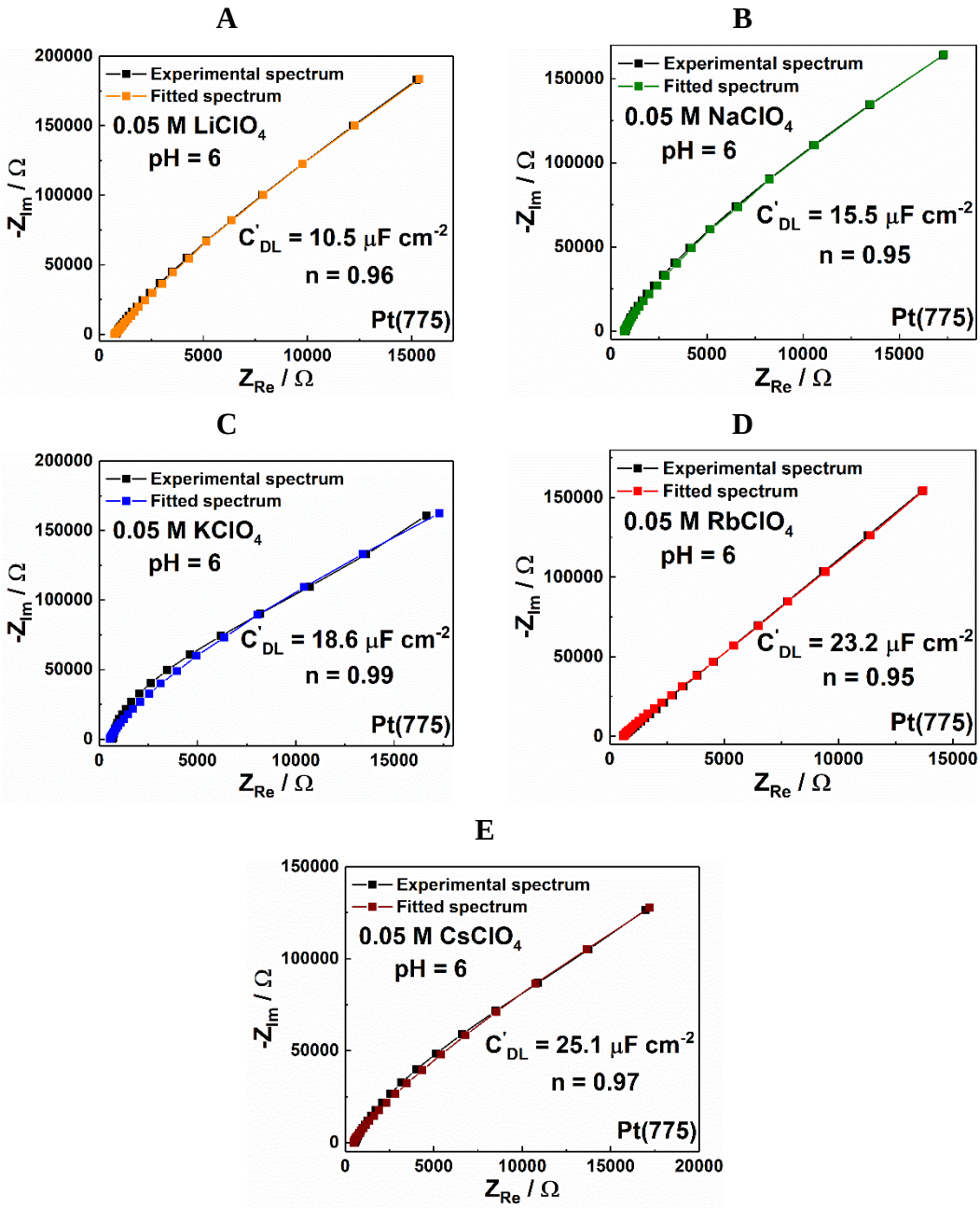

Figure 7.2. Fitted and experimental spectra for Pt(775) in 0.05 M (A) $LiClO_4$, (B) $NaClO_4$, (C) $KClO_4$, (D) $RbClO_4$, and (E) $CsClO_4$ at pH 6. The obtained parameters of CPE, such as the double layer capacitance, C'_{DL}, and the exponent, n, are also indicated.

7.2 The double layer capacitances of Pt(111) and Au(111) electrodes

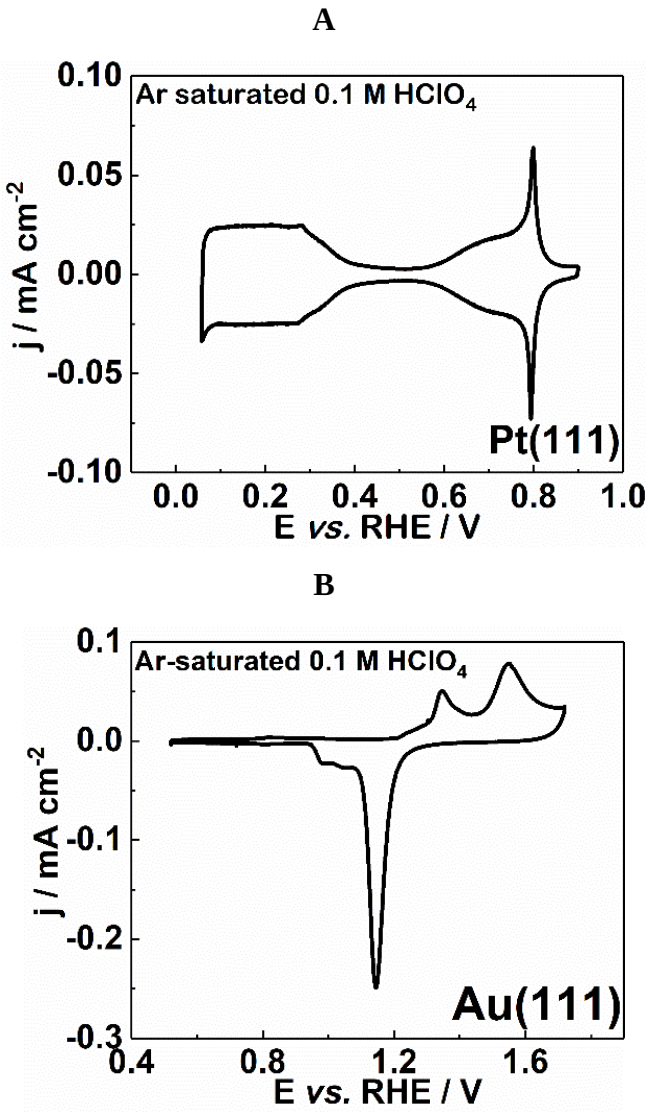

Figure 7.3. Typical cyclic voltammograms of (A) Pt(111) and (B) Au(111) electrodes in Ar-saturated 0.1 M $HClO_4$

Prior to EIS measurements, Pt(111) and Au(111) electrodes were prepared and their CVs then measured in Ar-saturated 0.1 M $HClO_4$ and 0.05 M *Me*ClO_4 (Me^+ = Li^+, Na^+, K^+, Rb^+, and Cs^+) as shown in **Figures 7.3** and **7.4**. With regard to the CVs of Pt(111), the typical three regions, namely hydrogen adsorption/desorption, double layer, and hydroxyl adsorption/desorption, can be observed in *Me*ClO_4, but the shapes of the three regions were quite different from those in $HClO_4$ and appeared to depend on the alkali metal cations present in the electrolytes. In terms of the CVs of Au(111), the shape changed totally when the electrolyte was changed from $HClO_4$ to *Me*ClO_4, but the

shapes were similar to each other in the various *Me*ClO4 electrolytes. Note that, as has already mentioned in Chapter 2, the voltammetric experiments are typically far less accurate in distinguishing different process constituents at the electrochemical interface when compared to impedance spectroscopy. Thus, CV measurements normally cannot be directly correlated with impedance measurements.

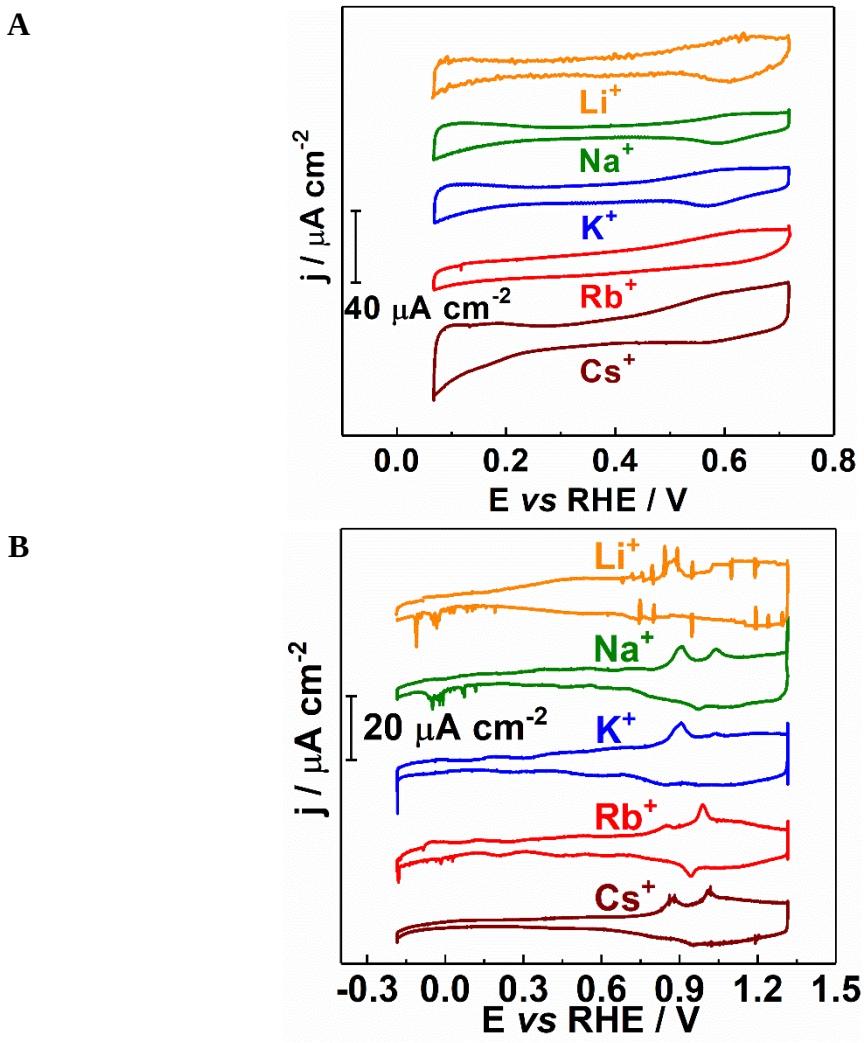

Figure 7.4. Examples of cyclic voltammograms for (A) Pt(111) and (B) Au(111) electrodes in Ar-saturated 0.05 M *Me*ClO4 (*Me*$^+$ = Li$^+$, Na$^+$, K$^+$, Rb$^+$, and Cs$^+$). The potential scan rates were 50 mV s^{-1}.

The electric double layer capacitances of Pt(111) and Au(111) in various *Me*ClO4 electrolytes were plotted against the applied potentials, as shown in **Figure 7.5A** and **B**, respectively. Well-pronounced minima can be observed for all of the curves. It is approximated that there are no significant Faradaic processes occurring at the potentials of these minimal EDL capacitances, $C'_{DL,MIN}$, because these potentials are very close

to the potentials of zero charge [226,227].

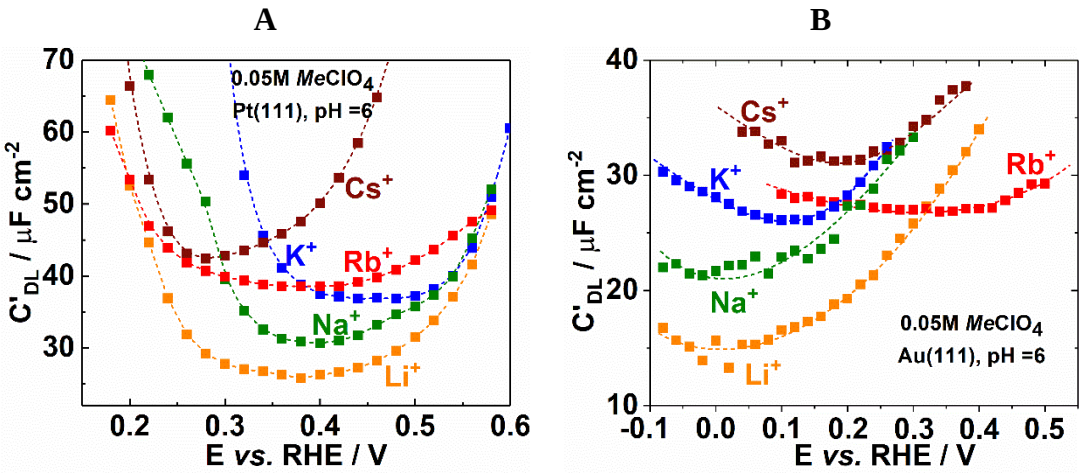

Figure 7.5. The double layer capacitances as functions of the electrode potential for (A) Pt(111) and (B) Au(111) electrodes in Ar-saturated 0.05 M *Me*ClO$_4$ (*Me*$^+$ = Li$^+$, Na$^+$, K$^+$, Rb$^+$, and Cs$^+$). The dashed lines are added as a guide to eye.

The values of $C'_{DL,MIN}$ obtained in the above-mentioned five electrolytes were plotted as a function of the hydration energy of the alkali metal cations in **Figure 7.6**. For both Pt(111) and Au(111) electrodes, linear relationships were observed between the value of $C'_{DL,MIN}$ and the cation hydration energy. The lower the cation hydration energy, the higher the value of $C'_{DL,MIN}$. This phenomenon cannot be simply attributed to the specific adsorption of cations since there are no specific adsorptions at these minima, and the trends, i.e., increasing from Li$^+$ to Cs$^+$ in both cases, are the inverses of that caused by the cation radii. In addition, the slopes obtained were about 0.06 for both the Pt(111) and Au(111) electrodes. The values of $C'_{DL,MIN}$ for Pt(111) in all investigated electrolytes were, however, all slightly higher than those of Au(111). This observation is in accordance with the higher double layer capacitances observed in all CVs of Pt(111) in *Me*ClO$_4$ solutions compared to Au(111) (**Figure 7.4**), which might result from the different work functions of metal electrodes[216].

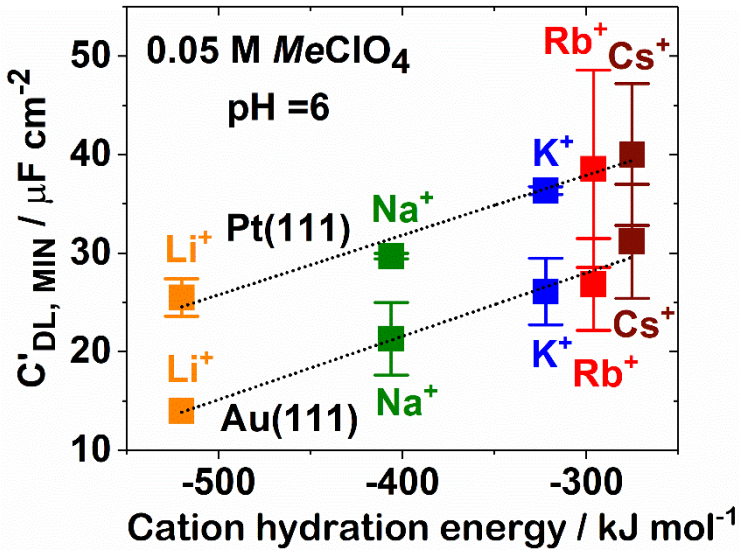

Figure 7.6. Minimum double layer capacitances derived from Figure 7.5 and plotted against the hydration energy of the alkali metal cations. The slopes are about 0.06 for both Pt(111) and Au(111). The error bars are calculated from at least three different independent measurements.

To determine the reason for the observed trends in **Figure 7.6**, the relationships between $C'_{DL,MIN}$ and relative permittivity and between the relative permittivity and the type of ions have been analysed. Since the electrolyte concentration (c_s) is constant in all the cases, the obtained C'_{DL}, especially $C'_{DL,MIN}$, is expected to be roughly proportional to the relative permittivity (ε_r). Thus, these trends in $C'_{DL,MIN}$ should be closely associated with the changed relative permittivity in different *Me*ClO$_4$ solutions. Based on this idea, the dependence of the relative permittivity on the nature of alkali metal cations and their concentrations in aqueous electrolytes are summarised in **Figure 7.7** and derived from the literature[228]. The linear trend of ε_r observed as a function of the hydration energy of alkali metal cations, similar to that for the $C'_{DL,MIN}$. Moreover, the slopes of these linear trends likely depend on the concentration of cations, as shown in **Figure 7.7**. In other words, at relatively low concentrations the type of metal cation does not influence ε_r as much as at relatively high concentrations. When monovalent anions are considered, ε_r does not depend on the type of anions, such as ClO_4^-, SCN^-, NO_3^-, I^-, and Br^-, but rather depends on their concentrations.[229] The values of ε_r remain constant for different monovalent anions with the same concentration, but decrease significantly as the anion concentration increases (**Figure 7.8**). Thus, similar effects of e.g. Cl^- and ClO_4^- on the relative permittivity can be expected.

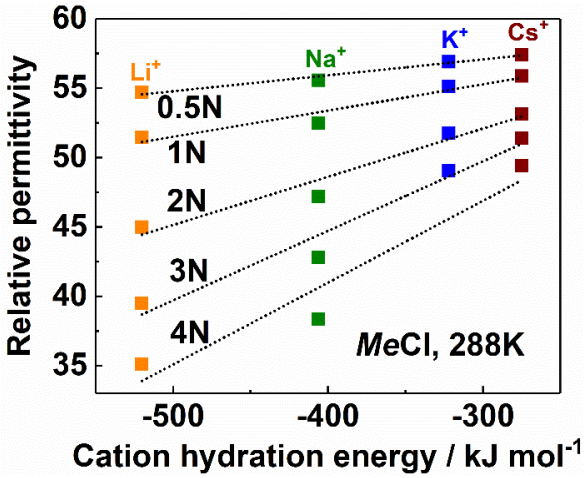

Figure 7.7. Relative permittivity as a function of the hydration energy of alkali metal cations. The relative permittivity was measured in the electrolytes with various concentrations of alkali metal cations, which are adapted from ref.228.

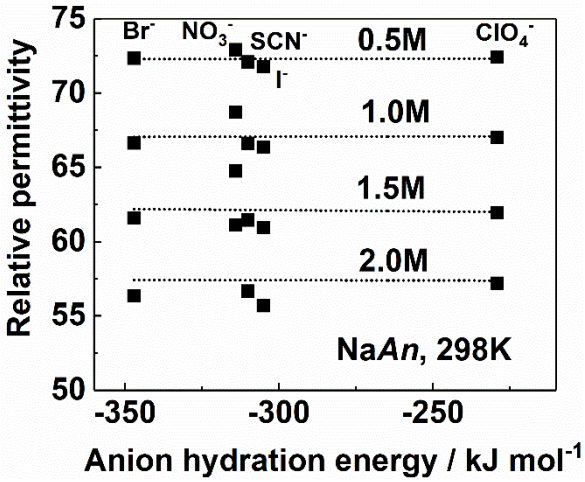

Figure 7.8. Relative permittivity as a function of anion hydration energy. The relative permittivity was measured in the electrolytes with different concentrations of anions, which were taken from ref.229.

To explain the observed identical slopes in **Figure 7.6**, the slopes obtained from **Figures 7.7** and **7.8** were plotted against the corresponding concentrations of the anions and cations as shown in **Figure 7.9**, in which the slopes at different temperatures were also added. One can see from **Figure 7.9** that the slopes depend linearly on the concentration of alkali metal cations, irrespective of the temperature (between 278, 288 and 313 K) and concentration of anions (from 0.5 to 2 M). Therefore, it can be concluded that ε_r is affected by the nature of the alkali metal cations, and that the degree of the effect is determined by the concentration of the alkali metal cation. When comparing $C'_{DL,MIN}$

with the slope values of ε_r in **Figure 7.9**, this identical slope value for $C'_{DL,MIN}$, both almost 0.06 in this case, corresponds to the local effective concentration of alkali metal cations of 4 M. As the concentration of the alkali metal cations in the bulk electrolyte used was just 0.05 M, it can be expected that the effective concentration of the alkali metal cations near the surface could be up to 80 times higher than the bulk concentration.

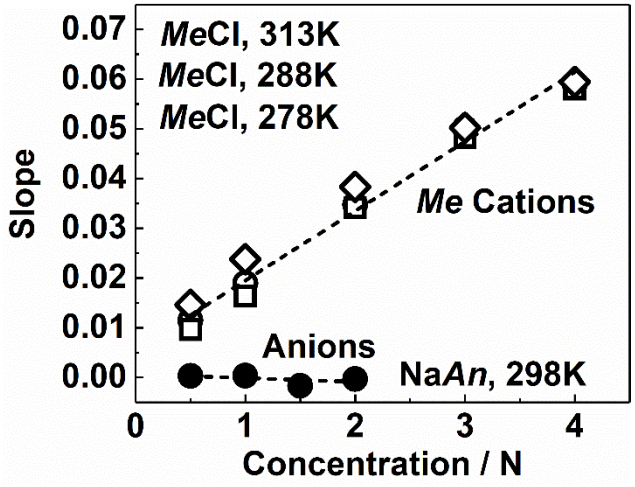

Figure 7.9. Slopes adapted from Figure 7.7 and 7.8 as functions of the concentrations of alkali metal cations and anions. Three different temperatures are also shown for the cations.

This assumption sheds light on the quantification of the electric double layer structure. Combined with the electric double layer theory, the effective concentrations of Me^+ and ClO_4^- in the double layer region are both 4 M. If the approximate 55 M concentration of H_2O is taken into account, each alkali metal cation and anion will effectively be surrounded by *ca.* 7 water molecules in the double layer structure (**Figure 7.10**). This quantification should be very useful in modelling the EDL for future functional electrodes. More importantly, such a high local concentration of alkali metal cations near the electrode surface also addresses the question of why these 'spectator species' can significantly influence the electrochemical activities of electrodes even in dilute electrolytes. To visualise this effect, a representation of the electrode/electrolyte interface, here taking Pt(111) in *Me*ClO_4 solutions as an example, is schematised in **Figure 7.10**.

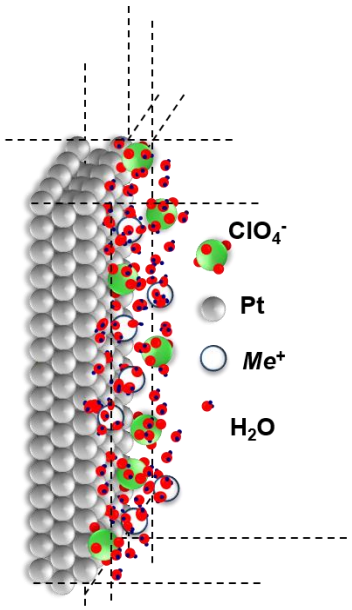

Figure 7.10. A schematics of the ions at the electric double layer of Pt(111) or Au(111) electrodes in 0.05 M *Me*ClO4 electrolytes, in which effective concentrations of anions and cations close to the surface are shown. According to the findings of this study, each ion is surrounded by almost seven water molecules at the electrode surface, and their surface concentrations are nearly two orders of magnitude higher than the bulk concentrations. As these charged ions will largely influence the catalytic centres, the functionality of the surface should indeed be influenced by the alkali metal cations.

7.3 The double layer capacitances of Cu(111) and Cu(100) electrodes

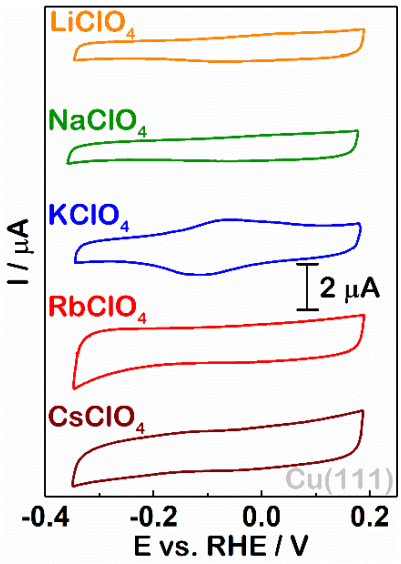

Figure 7.11. Cyclic voltammograms for Cu(111) electrodes recorded in Ar-saturated 0.05 M *Me*ClO4 (Me^+ = Li^+, Na^+, K^+, Rb^+, and Cs^+). Potential scan rates were 50 mV s^{-1}.

To clarify whether this high near-surface concentration of cations is universal for different functional electrodes, similar experiments were conducted on single crystalline copper crystals. Preparation of Cu(111) and Cu(100) followed the procedure introduced in Chapter 3. Then, CV and EIS measurements were performed in succession in Ar-saturated 0.05 M $MeClO_4$ (Me^+ = Li^+, Na^+, K^+, Rb^+, and Cs^+) at pH=6.

The voltammetric results of Cu(111) and Cu(100) are shown in **Figures 7.11** and **7.12**, respectively. For both Cu(111) and Cu(100) electrodes, it can be seen that there are no pronounced peaks in the investigated potential range. This observation is in accordance with the literature data.[230]. Therefore, according to these CVs, there are no significant Faradic processes occurring in this potential range; and consequently, the EIS measurements were performed in this selected potential range.

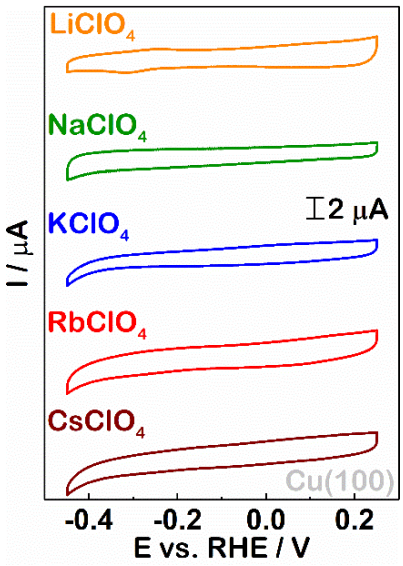

Figure 7.12. Cyclic voltammograms for Cu(100) electrodes in Ar-saturated 0.05 M $MeClO_4$ (Me^+ = Li^+, Na^+, K^+, Rb^+, and Cs^+). The potential scan rates were 50 mV s^{-1}.

The obtained EDL capacitances of Cu(111) and Cu(100) are then plotted as the functions of the applied potentials in **Figures 7.13** and **7.14**, respectively. Well-pronounced minima can be observed in all of the curves.

It seems that the near-surface effective concentration of alkali metal cations for both Cu(111) and Cu(100) electrodes is again much higher than in the bulk electrolyte. The $C'_{DL,MIN}$ for Cu(111) and Cu(100) (taken from **Figures 7.13** and **7.14**) were plotted versus the hydration energy of alkali metal cation as shown in **Figure 7.15**. The values of $C'_{DL,MIN}$ depend linearly on the hydration energy of alkali metal cations and increase

in the same order: $Li^+ < Na^+ < K^+ < Rb^+ < Cs^+$. The slopes were found to be 0.052 and 0.060 for Cu(111) and Cu(100), respectively. As $C'_{DL,MIN}$ is proportional to the relative permittivity; and the relative permittivity is closely associated with the nature of alkali metal cations and their local concentrations (see detailed discussion in **Section 7.2**), the local effective concentration of alkali metal cations was estimated to be *ca.* 3 to 4 M, although the bulk concentration is only 0.05 M. In other words, the near-surface concentration of alkali metal cations is 60 to 80 times higher than the bulk concentration. This result is in agreement with the observation for Au(111) and Pt(111).

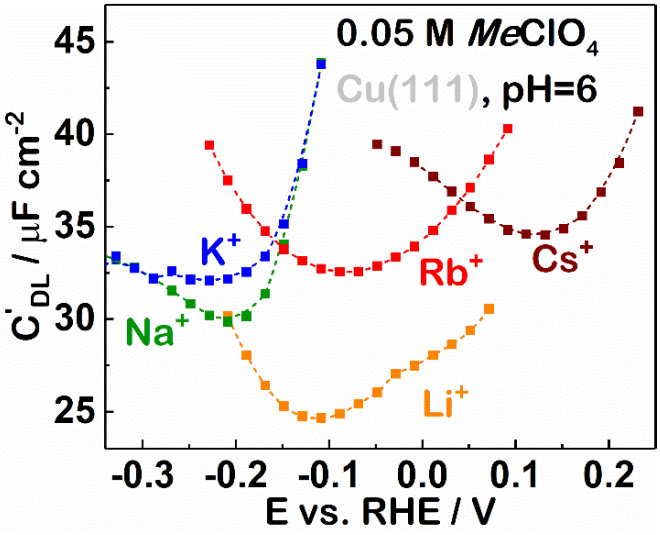

Figure 7.13. Double layer capacitances as functions of the electrode potential for Cu(111) electrodes in Ar-saturated 0.05 M *Me*ClO4 (Me^+ = Li^+, Na^+, K^+, Rb^+, and Cs^+). The dashed lines are added to as a gude to eye.

The double layer capacitance should be sensitive not only to the surface composition but also to the surface structure. As described in **Section 7.2**, higher values of $C'_{DL,MIN}$ in all *Me*ClO4 electrolytes were always observed on Pt(111) electrodes compared to Au(111). As shown in **Figure 7.15**, the different surface structures also dramatically change the values of $C'_{DL,MIN}$. With the same electrolyte, Cu(100) electrodes exhibited higher values of $C'_{DL,MIN}$ than Cu(111) electrodes.

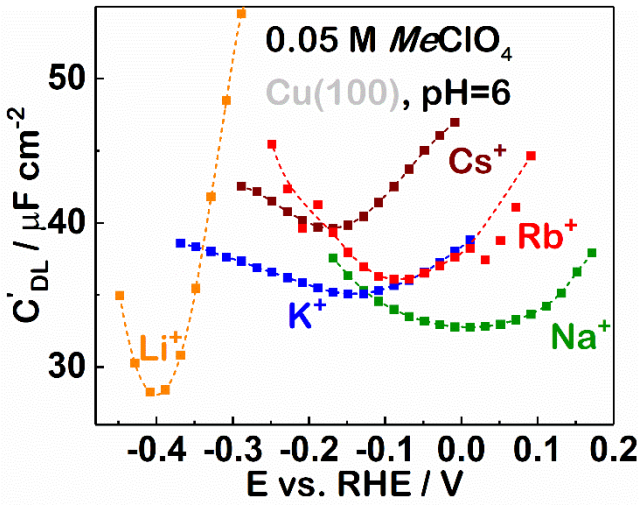

Figure 7.14. EDL capacitances as a function of the electrode potential for Cu(100) electrodes in Ar-saturated 0.05 M $MeClO_4$ (Me^+ = Li^+, Na^+, K^+, Rb^+, and Cs^+). The dashed lines are added as a guide to eye.

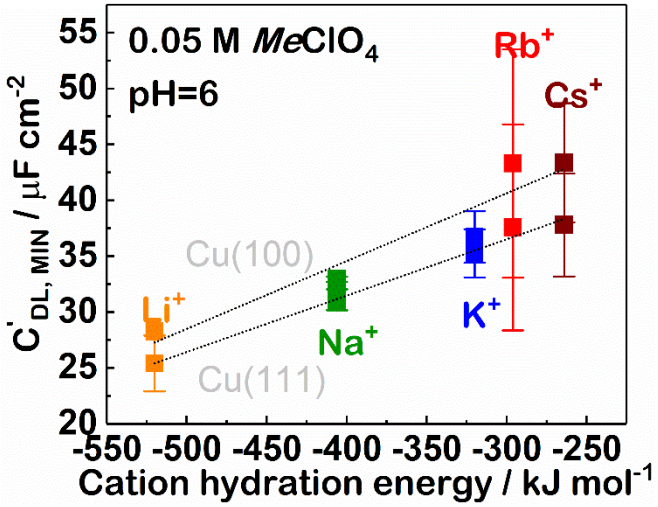

Figure 7.15. Minimum EDL capacitances extracted from Figures 7.13 and 7.14, plotted against the hydration energy of alkali metal cations. The slopes are about 0.052 and 0.060 for Cu(111) and Cu(100), respectively. The error bars are calculated from at least three different independent measurements.

7.4 The double layer capacitances of Pt(775) and Pt(12 10 5) electrodes

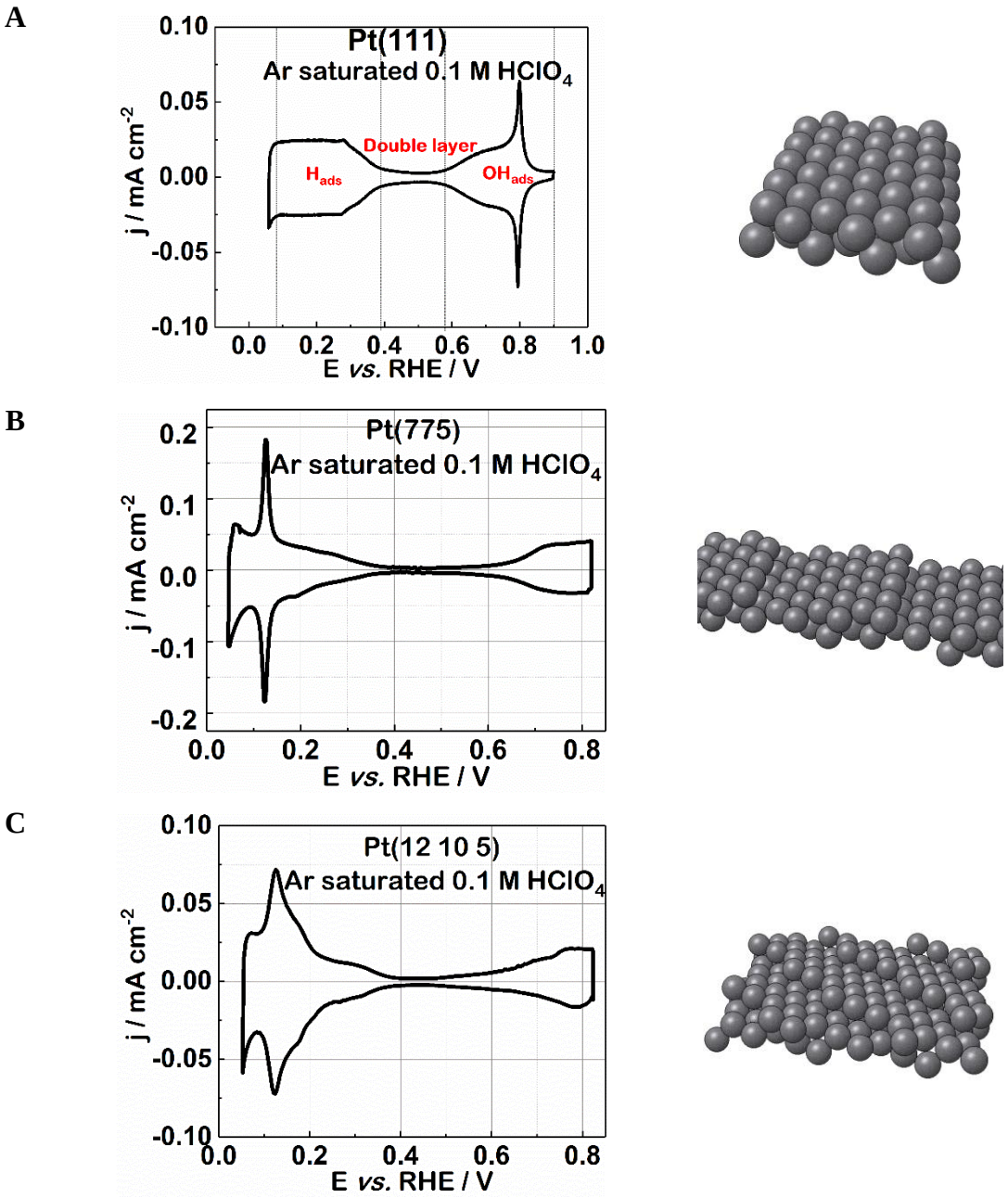

Figure 7.16. Characteristic cyclic voltammograms of (A) Pt(111), (B) Pt(775), and (C) Pt(12 10 5) in Ar-saturated 0.1 M $HClO_4$ under hanging meniscus configuration (scan rate: 50 mV s^{-1}). The corresponding surfaces are schematized on the right side of each CV.

To determine the relations between the double layer capacitance and the electrode surface structure, two different high-index Pt model surfaces (Pt(775) and Pt(12 10 5)) were additionally selected for the investigation. CVs of Pt(775) and Pt(12 10 5) were

first measured in Ar-saturated 0.1 M $HClO_4$ and 0.05 M *Me*ClO_4 (*Me*$^+$ = Li^+, Na^+, K^+, Rb^+, and Cs^+) electrolytes. Then, EIS measurements were conducted in Ar-saturated 0.05 M *Me*ClO_4 (*Me*$^+$ = Li^+, Na^+, K^+, Rb^+, and Cs^+) at pH=6.

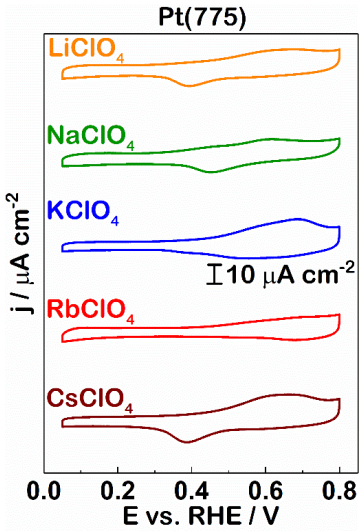

Figure 7.17. Cyclic voltammograms for Pt(775) electrodes in Ar-saturated 0.05 M *Me*ClO_4 (*Me*$^+$ = Li^+, Na^+, K^+, Rb^+, and Cs^+). The potential scan rates were 50 mV s^{-1}.

Figure 7.16 shows CVs of Pt(775) and Pt(12 10 5) in Ar-saturated 0.1 M $HClO_4$ and schematic images of their surface structures, to which corresponding results of Pt(111) are added for comparison. With regard to Pt(111), a typical 'butterfly- shape' CV and a rather planar surface can be observed in **Figure 7.16A**. In **Figure 7.16B**, the 'fingerprint' CV of stepped crystalline Pt(775) is seen. When kinked single crystalline Pt(12 10 5) is considered, the characteristic CV was similar to that of stepped Pt surfaces but with small differences in the potential range from 0.1 to 0.2 V_{RHE} (**Figure 7.16C**). The atomic width of the terrace can be seen as four atoms. Therefore, for these three single crystals, the surface disorder degree increases in the following trend: Pt(111) < Pt(775) < Pt(12 10 5).

The voltammetric results for the Pt(775) and Pt(12 10 5) in *Me*ClO_4 are shown in **Figures 7.17** and **7.18**, respectively. As for the Pt(111) in **Figure 7.3**, the CVs of the Pt(775) and Pt(12 10 5) electrodes in all *Me*ClO_4 electrolytes exhibit the typical three regions, namely hydrogen adsorption/desorption, double layer, hydroxyl adsorption/desorption, but the shapes are influenced by the alkali metal cations present in the electrolytes.

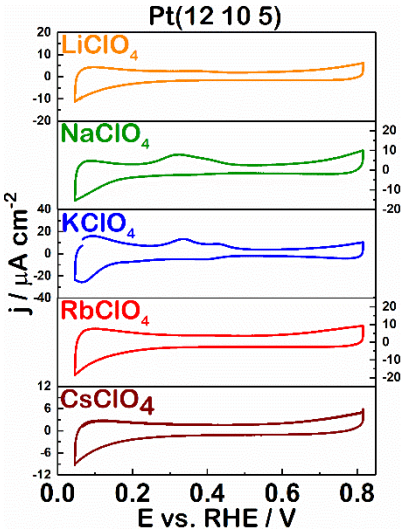

Figure 7.18. Cyclic voltammograms for Pt(12 10 5) electrodes in Ar-saturated 0.05 M *Me*ClO4 (Me^+ = Li^+, Na^+, K^+, Rb^+, and Cs^+). The potential scan rate was 50 mV s^{-1}.

The EDL capacitances of Pt(775) and Pt(12 10 5) were plotted versus the applied potential, as shown in **Figures 7.19** and **7.20**, respectively. Similarly to other investigated crystals, apparent minima of C'_{DL} were observed for both Pt(775) and Pt(12 10 5). The obtained $C'_{DL,MIN}$ values are thus shown in **Figure 7.21** as a function of the hydration energy of alkali metal cations. It can be seen that the linear dependence between $C'_{DL,MIN}$ and the hydration energy of alkali metal cations is observed for both Pt(775) and Pt(12 10 5), and the $C'_{DL,MIN}$ increases in the following order: $Li^+ < Na^+ < K^+ < Rb^+ < Cs^+$. The slopes were almost identical for both electrodes, *ca.* 0.053. Based on the mentioned correlation between the $C'_{DL,MIN}$ and the relative permittivity, the effective concentration of alkali metal cations near these stepped surfaces is likewise estimated to be also about 3 to 4 M. The near-surface concentration of alkali metal cations is also 60 to 80 times higher than the bulk concentration. This result once again demonstrates that the higher near-surface concentration of alkali metal cations is universal for most functional electrodes regardless of the surface structure.

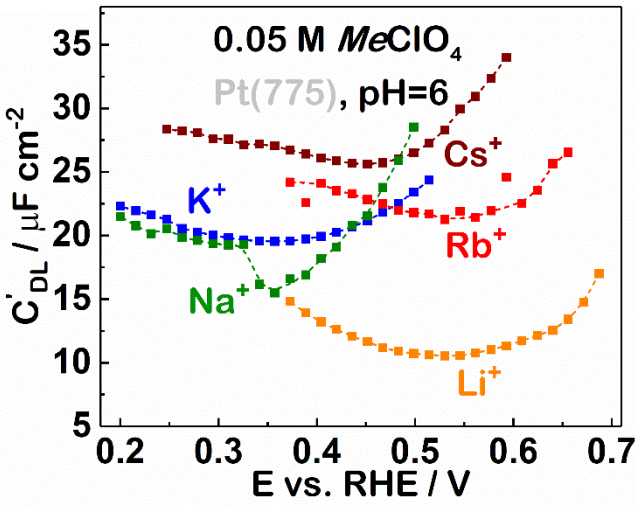

Figure 7.19. EDL capacitances as functions of the electrode potential for Pt(775) electrodes in Ar-saturated 0.05 M *Me*ClO$_4$ (*Me*$^+$ = Li$^+$, Na$^+$, K$^+$, Rb$^+$, and Cs$^+$). The dashed lines are added as a gude to eye.

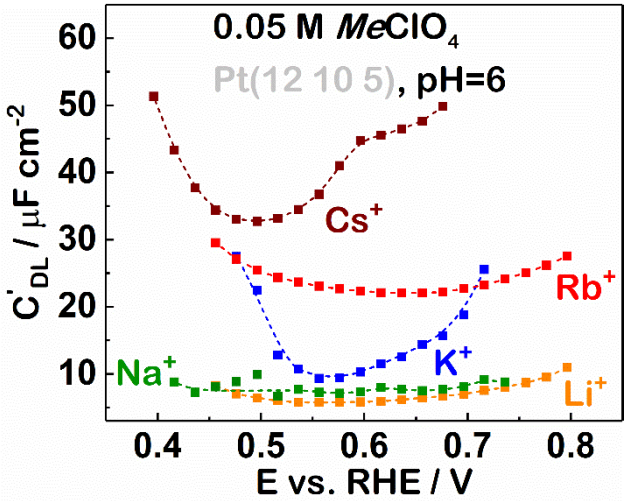

Figure 7.20. EDL capacitances as functions of the electrode potential for Pt(12 10 5) electrodes in Ar-saturated 0.05 M *Me*ClO$_4$ (*Me*$^+$ = Li$^+$, Na$^+$, K$^+$, Rb$^+$, and Cs$^+$). The dashed lines are added as a guide to eye.

The surface structure however has a significant influence on the double layer capacitance values. As shown in **Figure 7.21**, for all investigated *Me*ClO$_4$ electrolytes, the lowest values of $C'_{DL,MIN}$ were always found on Pt(12 10 5), followed by Pt(775), whereas the rather planar Pt(111) surface demonstrated the highest values. Thereby, the values of $C'_{DL,MIN}$ for these Pt surfaces were plotted against the inverse of the number of atoms at their terraces, as shown in **Figure 7.22**. Note that the reciprocal number for

Pt(111) was taken as zero because the ideal Pt(111) surface does not have any steps. The higher the reciprocal number, the lower the value of $C'_{DL,MIN}$. In other words, the more disordered the surface is, the lower the double layer capacitance. Therefore, it can be qualitatively concluded that the EDL capacitance is sensitive to the surface structure. At least for Pt electrodes, the double layer capacitance decreases with the increasing the degree of disorder.

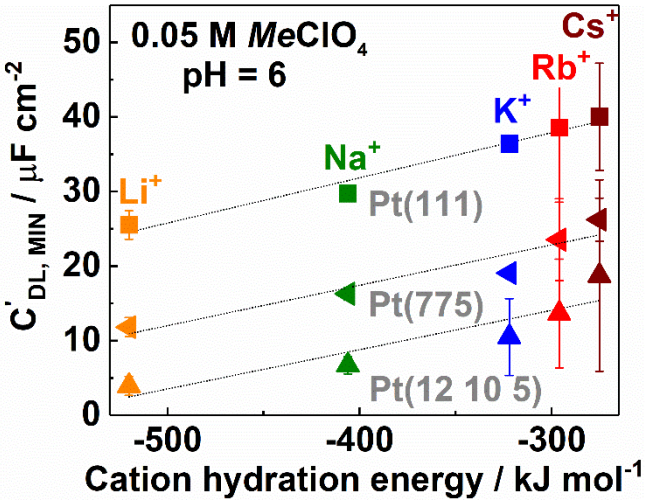

Figure 7.21. Minimum double layer capacitances extracted from Figures 7.19 and 7.20, plotted against the hydration energy of the alkali metal cations, to which the data of Pt(111) is also added for comparison. The slopes are about 0.060, 0.054, and 0.053 for Pt(111), Pt(775), and Pt(12 10 5) electrodes, respectively. The error bars are calculated from at least three different independent measurements.

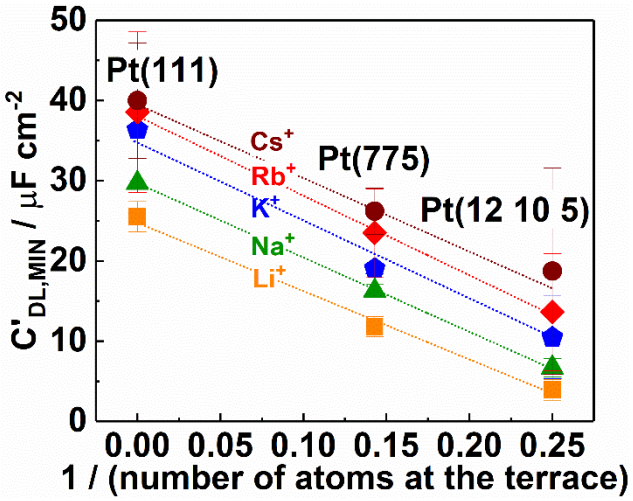

Figure 7.22. Minimum double layer capacitances for different Pt surfaces extracted from Figures 7.19 and 7.20, plotted against the inverse of the number of atoms at their terraces.

7.5 Summary

The double layer capacitances of various electrodes, namely Pt(111), Au(111), Cu(111), Cu(100), Pt(775) and Pt(12 10 5) were measured in 0.05 M *Me*ClO_4 (Me^+ = Li^+, Na^+, K^+, Rb^+, and Cs^+) electrolytes using the EIS method. The minimum EDL capacitances of all investigated electrodes are linearly dependent on the hydration energy of alkali metal cations, increasing in the following order: $Li^+ < Na^+ < K^+ < Rb^+ < Cs^+$, and the obtained slopes are all in the range from 0.05 to 0.06. Based on the correlation between the double layer capacitance and the relative permittivity, the effective concentration of alkali metal cations near the electrode surface is found to be much higher than that in the bulk electrolyte by a factor of 80. It is also shown that this observation can be made for functional electrodes of this study irrespective of the electrode surface composition and structure.

Moreover, by comparing the values of the minimal EDL capacitances between Pt(111), Pt(775), and Pt(12 10 5) in various *Me*ClO_4 electrolytes, these minima are found to increase for all investigated electrolytes in the order: Pt(12 10 5) < Pt(775) < Pt(111). These observations imply that the double layer capacitance is evidently sensitive to the surface structure.

These findings clarify why the spectator species can contribute to the observed significant changes of the electrocatalytic activities. These findings in conjunction with advanced theoretical models are assumed to pave a new way to determining the mechanism of the electrode surface functionalities caused by the spectator species.

8. Conclusions and an outlook

In this thesis, the influence of spectator species that are not directly involved in the electrocatalytic reactions was investigated. The influence of the alkali metal cations, typical spectator species, and *n*-butylammonium sulfate, a newly discovered spectator species, was selected as the research focus. Specific influence of these species on the activity towards HER, ORR, and OER, was investigated. The reason why these spectator species can determine the electrocatalytic performance was suggested.

The HER activities of various electrodes in alkaline media can be tailored by merely varying alkaline metal cations present in the electrolytes. The HER activities in diverse alkaline electrolytes were measured for the electrodes with strong hydrogen binding energy, such as Pt and Ir electrodes, as well as electrodes with weak hydrogen binding energy, such as Ag and Au electrodes, respectively. The HER activities of all electrodes were evidently dependent on the alkali metal cations present in the electrolytes and could be adjusted by a factor of less than or equal to four by exchanging cations present in the electrolytes. Moreover, for Pt and Ir electrodes exhibiting strong hydrogen binding energy, regardless of their surface structure, the activity increased in the following order: CsOH < RbOH < KOH < NaOH < LiOH. In contrast, for Ag and Au electrodes, exhibiting weak hydrogen binding energy, the activity order was reversed: LiOH < NaOH < KOH < RbOH < CsOH. These observations could be attributed to an association between hydrogen binding of the electrode surface and the alkali metal cations near the surface, in which these cations tailor the hydrogen binding by supposed non-covalent interactions.

ORR activities of low- and high-index Pt surfaces closely correlate with the nature of the alkali metal cations present in the solutions. ORR activities of Pt(111), Pt(221), and Pt(331) electrodes were measured in an acidic solutions ($HClO_4$) as well as in various alkaline electrolytes (LiOH, NaOH, KOH, RbOH, and CsOH). For the Pt(111), the ORR activities were enhanced when acidic media was substituted with alkaline media. The corresponding activity trend in different basic media was as follows: LiOH < NaOH < KOH < RbOH < CsOH. However, for Pt(221) and Pt(331), the activity diminished dramatically when changing to basic media. The activity trend in alkaline

media was also changed, producing KOH ≫ NaOH > CsOH > RbOH ≈ LiOH. These different ORR activities between low- and high-index Pt surfaces are attributed to the interactions between their specific active centres and the alkali metal cations near these centres. With regard to the ORR at the Pt(111) surfaces, the only active sites at the terraces are beneficial from interacting with the nearby alkali metal cations: the reaction intermediates are destabilised by the alkali metal cations. For the ORR activities on the Pt(221) and Pt(331) electrodes, the alkali metal cations appear to have mostly negative effects. Due to the existence of different types of active sites and the shielding effect from the step edges, it becomes too complex to distinguish the specific influence of the alkali metal cations. These results indicate that the ORR activity for both low- and high-index surfaces depends on the type of alkali metal cation contained in the electrolyte in addition to the pH of the electrolyte.

The water splitting on various industrial-relevant catalysts can be significantly influenced by *n*-butylamine. Various industrially relevant catalysts, such as NiO_X, CoO_X, and $NiFeO_X$, were tested in different BAS-containing electrolytes of different pHs. With regard to different catalysts, the activity for NiO_X was increased by nine times, whereas for CoO_X it was just two times and for $NiFeO_X$ it remained the same, as compared with the activity in K_2SO_4 aqueous solution. For BAS-containing electrolytes with different pH levels, it was observed that the activity increased when the pH increased from 11 to 12 yet dropped when the pH increased both from 10.5 to 11 and from 12 to 13. The optimal performance was obtained at pH 12. The BAS-containing system exhibits good stability during electrolysis. ^{1}H NMR and RRDE measurements were taken to clarify the role of BAS in this new system. It was found that BAS directly participates in the reaction rather than solely as a spectator species. According to the ^{1}H NMR results, BAS was almost 100% selectively oxidised into *n*-butyronitrile with a notably high Faradaic efficiency, whilst H_2O_2 was also detected by the RRDE measurements.

To ascertain why the catalytic activity is affected by the spectator species, even in considerably dilute electrolytes, the influence of alkali metal cations on the properties of the electric double layer was investigated. The double layer capacitances of various electrodes such as Pt(111), Au(111), Cu(111), Cu(100), Pt(775) and Pt(12 10 5) were measured in the electrolytes containing different alkali metal cations at near-neutral pH using electrochemical impedance spectroscopy. It was observed for all investigated

electrodes that there were linear trends between the minimum double layer capacitances and the hydration energy of the alkali metal cations. The respective capacitances show the following trend: $Li^+ < Na^+ < K^+ < Rb^+ < Cs^+$. According to the correlation between the double layer capacitance and the relative permittivity, the near-surface effective concentration of alkali metal cations could be as much as 80 times higher than the bulk concentration (0.05 M bulk concentrations were used). This unexpected high near-surface concentration of cations can be observed for many electrodes, regardless of their surface composition and surface structure. However, the double layer capacitance depends on the electrode surface structure as well as on the electrode surface composition.

The above mentioned findings indicate that spectator species are of particular importance for improving the efficiency of electrocatalytic systems for sustainable energy provision schemes. Nevertheless, a deeper understanding of these phenomena is still required. Accordingly, future experiments could explore the following aspects:

- The alkali metal cations may not affect the ORR and HER activities at very low pH values ($pH \leq 1$). As it was reported for stepped single crystalline Pt, the voltammetric characteristics remain the same at pH 1 in the absence or presence of alkali metal cations.[170] This would clarify the relations between the pH and the alkali metal cations effect.
- The altered concentrations of these spectator species may also influence HER and ORR activities.
- The relations between the influence of alkali metal cations on the double layer capacitance and the electrode surface composition and structure is needed to be further clarified.
- *In situ* experiments are required to determine whether the presence of the spectator species would change the nature of active sites of the electrodes for a given specific reaction.
- Novel advanced measurements are required in order to acquire the direct experimental evidence for the interaction between spectator species in electrolytes and active sites at electrode surfaces.

Appendix A. List of materials, chemicals, and equipment.

A.1 Chemicals and materials

The chemicals used in this work are listed in **Table A.1**.

Table A.1 All chemicals used in this work

Chemical	Formula	Quality	Provider
Perchloric acid	$HClO_4$	70%, Suprapur	Merck
Sulfuric acid	H_2SO_4	96%, Suprapur	Merck
Phosphoric acid	H_3PO_4	85%, EMSURE	Merck
Hydrogen peroxide	H_2O_2	30%, Suprapur	Merck
Cobalt sulfate heptahydrate	$CoSO_4 \cdot 7H_2O$	≥99%	Merck
Ferric sulfate heptahydrate	$FeSO_4 \cdot 7H_2O$	≥99%	Merck
Nickel sulfate hexahydrate	$NiSO_4 \cdot 6H_2O$	≥99%	Merck
Sodium sulfate	Na_2SO_4	≥99%	Sigma Aldrich
Potassium sulfate	K_2SO_4	≥99%	Sigma Aldrich
Potassium ferricyanide	$K_3Fe(CN)_6$	≥99%	Sigma Aldrich
Sodium acetate	CH_3COONa	≥99%	Sigma Aldrich
Lithium hydroxide	LiOH	99.998%, Trace Select	Sigma Aldrich

Sodium hydroxide	NaOH	99.99%, Semiconductor Grade	Sigma Aldrich
Potassium hydroxide	KOH	99.99 %, Trace Metal Basis	Sigma Aldrich
Rubidium hydroxide	RbOH	99.9%, 50 wt-% solution	Sigma Aldrich
Caesium hydroxide	CsOH	99.9%, 50 wt-% solution	Sigma Aldrich
Butylamine	$C_4H_{11}N$	99.5%	Sigma Aldrich

The crystals and gases used in this work are listed in **Tables A.2** and **A.3**, respectively.

Table A.2 Crystals used in this work

Crystals	Quality	Surface area / cm^2	Provider
Pt(pc)	99.99%, oriented better than 0.1°	0.196	Mateck, Germany
Pt(111)	99.99%, oriented better than 0.1°	0.196	Mateck, Germany
Pt(111)	99.99%, oriented better than 0.5°	0.049	Icryst, Germany
Pt(221)	99.99%	0.031	Prof. J. Feliu, Alicante
Pt(331)	99.99%	0.038	Prof. J. Feliu, Alicante
Pt(775)	99.99%	0.036	Prof. J. Feliu, Alicante
Pt(12 10 5)	99.99%, oriented better than 0.5°	0.049	Icryst, Germany
Au(pc)	99.99%	0.196	Mateck, Germany

Au(111)	99.99%, oriented better than 0.5°	0.049	Icryst, Germany
Ir(111)	99.99%, oriented better than 0.1°	0.196	Mateck, Germany
Ag(pc)	≥99%	0.136	Homemade
Cu(111)	≥99%	0.196	Homemade
Cu(100)	≥99%	0.196	Homemade

Table A.3 Gas used in this work

Gas	Quality	Provider
Ar	5.0	Air Liquide, Germany
O_2	5.0	Air Liquide, Germany
H_2	5.0	Air Liquide, Germany
1000 ppm CO and Ar mixture	4.7 and 5.0	Westfalen, Germany

A.2 Equipment and software

Equipments used in this work are given in **Table A.4**.

Table A.4 Equipment

Equipment	Type	Provider
RDE/RRDE	Pine RDE 710 RDE with MSR electrode rotator with CE and ETL marks	Pine, USA

Reference electrode	MMS	SI Analytics, Germany
Glassy carbon electrode	Diameter: 5mm	Pine, USA
Portable pH meter	PHH222	Omega, Germany
Potentiostat	VSP-300	Bio-logic, France
NMR spectrometer	-	Bruker
Water purification systems	Evoqua Ultra Clear 10 TWF 30 UV	Westfalen, Germany

The used software:

The control over the potentiostat and the followed acquisition of the data were proceeded using the EC-LAB, *Version 11.30* software. The impedance data were fitted by the EIS Data Analysis *1.3*. OriginPro *2017G* was used for analysis of the data and drawing figures.

Appendix B. Symbols and abbreviations.

a	activity
AFC	alkaline fuel cell
BAS	butylammonium sulfate
C	capacitance/capacitor
C_a	adsorption capacitance
C'_{DL}	parameter proportional to the double layer capacitance
$C'_{DL,MIN}$	minimum value related to the double layer capacitance
CA	chronoamperometry
CE	counter electrode
cn	coordination number
CPE	constant phase element
CV	cyclic voltammetry
DFT	density functional theory
e	elementary charge
E	potential
E_0	standard electrode potential
E_D	decomposition potential
E_d	disk electrode potential

E_r	ring electrode potential
EIS	electrochemical impedance spectroscopy
EDL	electrical (or electric) double layer
F	Faraday constant
f	frequency
G	Gibbs free energy
GC	glassy carbon
g	gas
h	Planck constant
$H_{ads/des}$	hydrogen adsorption/desorption
HM	hanging meniscus
HER	hydrogen evolution reaction
HOR	hydrogen oxidation reaction
I	electric current
IHP	inner Helmholtz plane
IL	ionic liquid
$Im[Z]$	imaginary part of the complex number Z
j	current density
l	liquid
L	inductor
m	mass

M	molar mass
MMS	mercury-mercurous sulfate reference electrode
N_A	Avogadro's number
NASA	National Aeronautics and Space Agency (USA)
OCP	open circuit potential
$OH_{ads/des}$	hydroxyl adsorption/desorption
OHP	outer Helmholtz plane
OER	oxygen evolution reaction
ORR	oxygen reduction reaction
pc	polycrystalline
PAFC	phosphoric acid fuel cell
PEMFC	polymer electrolyte membrane fuel cell
q	electric charge
Q	electric charge
R	gas constant
R	resistance/resistor
R_a	additional adsorption resistance
R_{CT}	charge transfer resistance
R_e	external resistance
R_i	internal cell resistance
R_u	uncompensated resistance

RDE	rotating disk electrode
RE	reference electrode
Re[Z]	real part of the complex number Z
rpm	rotations per minute
RHE	reversible hydrogen electrode
RRDE	rotating ring disk electrode
SHE	standard hydrogen electrode
SOFC	solid oxide fuel cell
T	temperature
t	time
UPD	underpotential deposition
WE	working electrode
z	valence number
Z	impedance
Z_{DL}	impedance of the double layer
Z_{CPE}	impedance of the constant phase element
ε	gas phase fraction
η	overpotential
φ	Galvani potential
φ_0	standard Galvani potential
ϕ	Work function

μ	chemical potential
ρ	density
ω	angular frequency

Appendix C. Publications.

1. Sebastian Watzele, Pascal Hauenstein, Yunchang Liang, **Song Xue**, Johannes Fichtner, Batyr Garlyyev, Daniel Scieszka, Fabien Claudel, Frédéric Maillard, Aliaksandr S. Bandarenka: *Determination of Electroactive Surface Area of Ni-, Co-, Fe-, and Ir-based Oxide Electrocatalysts*. ACS Catalysis 9 (2019) 9222-9230. DOI:10.1021/acscatal.9b02006.

2. Batyr Garlyyev, **Song Xue**, Marcus D. Pohl, David Reinisch, Aliaksandr S. Bandarenka: *Oxygen Electroreduction at High-Index Pt Electrodes in Alkaline Electrolytes: A Decisive Role of the Alkali Metal Cations*. ACS Omega 3 (2018) 15325-15331. DOI:10.1021/acsomega.8b00298.

3. Batyr Garlyyev, Yunchang Liang, **Song Xue**, Sebastian Watzele, Johannes Fichtner, Wei-Jin Li, Xing Ding, Aliaksandr S. Bandarenka: *Theoretical and experimental identification of active electrocatalytic surface sites*. Current Opinion in Electrochemistry 14 (2019) 206-213. DOI:10.1016/j.coelec.2018.09.002.

4. **Song Xue**, Batyr Garlyyev, Sebastian Watzele, Yunchang Liang, Johannes Fichtner, Marcus D Pohl, Aliaksandr S. Bandarenka: *Influence of Alkali Metal Cations on the Hydrogen Evolution Reaction Activity of Pt, Ir, Au, and Ag Electrodes in Alkaline Electrolytes*. ChemElectroChem 5 (2018) 2326-2329. DOI:10.1002/celc.201800690.

5. Batyr Garlyyev, **Song Xue**, Sebastian Watzele, Daniel Scieszka, Aliaksandr S. Bandarenka: *Influence of the Nature of the Alkali Metal Cations on the Electrical Double Layer Capacitance of Model Pt(111) and Au(111) Electrodes*. Journal of Physical Chemistry Letters 9 (2018) 1927-1930. DOI:10.1021/acs.jpclett.8b00610.

6. **Song Xue**, Sebastian Watzele, Viktor Čolić, Kurt Brandl, Batyr Garlyyev, Aliaksandr S. Bandarenka: *Reconsidering Water Electrolysis: Producing Hydrogen at Cathodes Together with Selective Oxidation of n-Butylamine at Anodes*. ChemSusChem 10 (2017) 4812-4816. DOI:10.1002/cssc.201702308.

Key publications:

ChemPubSoc Europe

DOI: 10.1002/celc.201800690

CHEMELECTROCHEM Communications

Influence of Alkali Metal Cations on the Hydrogen Evolution Reaction Activity of Pt, Ir, Au, and Ag Electrodes in Alkaline Electrolytes

Song Xue,[a] Batyr Garlyyev,*[a] Sebastian Watzele,[a] Yunchang Liang,[a] Johannes Fichtner,[a] Marcus D. Pohl,[a] and Aliaksandr S. Bandarenka*[a, b, c]

Fundamental understanding of the influence of so-called spectator electrolyte species on the catalytic activity of electrodes is considered as a relatively novel direction in electrocatalysis. Numerous recent examples show that seemingly inert electrolyte components drastically influence the performance of catalytic centers. Even alkali metal cations in aqueous electrolytes at high pH values can change the reaction turnover frequency by orders of magnitude, depending on their nature, from Li^+ to Cs^+. Here, we use several electrodes, namely Pt(polycrystalline), Pt(111), Pt(221), Ir(111), Au(111), and Ag(polycrystalline), in different alkali metal cation-containing electrolytes to reveal their role in the hydrogen evolution reaction (HER). The HER activity trends of various Pt electrodes, irrespective of their surface structure, correlate with the hydration energy of the corresponding alkali metal cations present in the electrolyte ($Li^+ > Na^+ > K^+ > Rb^+ > Cs^+$). The trend remains the same for the Ir(111), however, it is reversed for Au(111) and Ag(pc) electrocatalysts.

While understanding that electrolyte components play a critical role in electrocatalytic reactions can be traced back to 1930s,[1] until very recently these electrolyte-related phenomena were not in the main focus of electrocatalytic science. However, now it is understood that both the reaction rate[2] and selectivity[3] of numerous electrocatalytic processes largely depend on the nature of "spectator species", i.e. electrolyte components, which are not directly involved into the reaction mechanisms.[4,5,6,7,8] According to the current understanding, these species do not form classical chemical bonds with active centers at the electrode surface.[9,10,11,12] Among these "spectator species", alkali metal cations have attracted much scientific attention recently[13,14] due to their wide applications in laboratory and industrial fields:[15] for instance it is difficult to prepare aqueous electrolytes with high pH values without them. However, the influence of the alkali metal cations on the performance of different electrocatalytic systems is not yet well understood. In this work, we focus on revealing the influence of Li^+, Na^+, K^+, Rb^+ and Cs^+ on the hydrogen evolution reaction (HER) in alkaline electrolytes. The choice of HER as the model electrocatalytic reaction is based on two considerations. From one side, HER is crucial for the development of so-called "hydrogen economy".[16,17] On the other hand, HER is relatively simple in terms of mechanisms compared with e.g. the oxygen evolution or oxygen reduction reactions.[18] The reason for performing HER in alkaline media is based on the fact that in the alkaline media, the alkali metal cations can in principle adsorb on electrode surfaces,[19] which means that it might be easier to interpret their role in the electrocatalytic process.

Here, we demonstrate that HER activity of all investigated electrodes, namely monocrystalline and polycrystalline Pt, Ir, Au and Ag, fairly correlates with the hydration energy of the alkali metal cations and the affinity of the surfaces to the H-adsorbates.

Figure 1 shows a bar chart comparing the HER current densities at −0.05 V *vs.* reversible hydrogen electrode (RHE) for the Pt electrodes: single crystalline Pt(111), stepped single crystalline Pt(221), and polycrystalline Pt (Pt(pc)) electrodes measured in H_2-saturated metal hydroxide electrolytes MeOH ($Me^+ = Li^+$, Na^+, K^+, Rb^+, Cs^+). We selected Pt(111) because it is the most commonly used model single crystal Pt electrode. The particular choice of Pt(221) electrode for this study is due to its

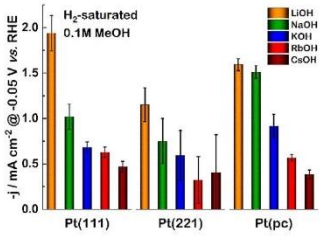

Figure 1. Comparison of the HER activities at −0.05 V (vs. RHE), for the Pt(111), Pt(221), and Pt(pc) electrodes in 0.1 M H_2-saturated alkaline solutions, MeOH ($Me = Li^+$, Na^+, K^+, Rb^+, Cs^+).

[a] S. Xue, Dr. B. Garlyyev, S. Watzele, Y. Liang, J. Fichtner, Dr. M. D. Pohl, Prof. Dr. A. S. Bandarenka
Physics of Energy Conversion and Storage
Physik-Department, Technische Universität München
James-Franck-Str. 1, 85748 Garching, Germany
E-mail: batyr.garlyyev@tum.de
bandarenka@ph.tum.de
[b] Prof. Dr. A. S. Bandarenka
Nanosystems Initiative Munich (NIM)
Schellingstraße 4, 80799 Munich, Germany
[c] Prof. Dr. A. S. Bandarenka
Catalysis Research Center TUM
Ernst-Otto-Fischer-Straße 1, 85748 Garching, Germany

Supporting information for this article is available on the WWW under https://doi.org/10.1002/celc.201800690

ChemPubSoc Europe
CHEMELECTROCHEM Communications

exceptionally high HER-activity in $HClO_4$ media.[20] In Figure 1, it can be seen that the highest HER current densities for the Pt-electrodes are always observed in LiOH, followed by NaOH, KOH, whereas the lowest current densities are obtained in RbOH and CsOH electrolytes. Furthermore, the HER current densities in LiOH are up to ~4 times higher than those measured in CsOH solutions for all Pt electrodes, irrespective of the electrode surface structure. As shown in Figure S1, the comparable trend for the HER current densities was also recorded in Ar-saturated electrolytes. These correlations demonstrate that the HER activity of different Pt electrodes is strongly influenced by the alkali metal cations regardless of their surface structure.

To further clarify the relationship between the HER activity of Pt electrodes and the alkali metal cations, the pseudo-exchange current densities were correlated with the hydration energies of the alkali metal cations. It should be noted, however, that the "true" exchange current density is difficult to obtain due to the inevitable Ohmic drop and noticeable non-linear behavior of the current-potential dependencies in the logarithmic scale. In Figure 2a–c, the Tafel plots are shown for the Pt electrodes. Rather similar slopes of the curves for different alkaline electrolytes at each electrode potential reveal that there are no significant changes in the HER mechanism for Pt(111), Pt(221) and Pt(pc) electrodes among different alkaline electrolytes.[17] Moreover, the logarithm of the pseudo-exchange current densities ($\log(i_{0,\,pseudo})$) in different alkaline electrolytes is plotted in Figure 2d *versus* the hydration energy of corresponding alkali metal cations. The values of $i_{0,\,pseudo}$ were estimated using the "classical" approach, as shown in Figure 2a–c. This observed behavior of these platinum surfaces strongly suggests that there are trends between the nature (hydration energy) of the alkali metal cations and the HER activity of the Pt electrodes, and those observed trends seem to be not influenced by the electrode structure.

A Sabatier-type "volcano" plot, shown in Figure 2e, links the observable HER activities with the surface adsorption energies for the H-intermediates (H-binding energies) for the pure metal electrodes as reported in the literature.[21,22] From this plot, it can be observed that the H-binding at the Pt and Ir electrodes is stronger, while at the Au and Ag electrodes it is weaker than the optimum. If the alkali metal cations influence the H-binding energy at the electrode surfaces always in the same way (as observed for the Pt electrodes above), the activity trends should remain similar for the metals on the left-side of the "volcano" plot (stronger H-binding energy). Furthermore, if the aforementioned statement is valid, then the activity trend should be reversed for the metals on the right-side of the "volcano" plot (weaker H-binding energy). Therefore, it would be interesting to explore how the activity trends change for metals with H-binding energy even stronger than Pt, for instance, Ir, and for those with weaker H-binding energies, such as Au and Ag.

Thus, the HER activities of Ir, Au and Ag electrodes have been studied in different alkaline electrolytes. The HER activity trend for Ir(111) (shown in Figure 3a) was comparable to the results obtained for the Pt electrodes with the exception of

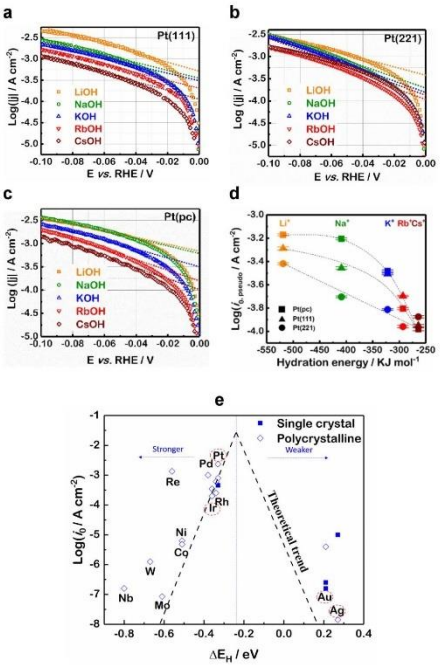

Figure 2. a–c) Logarithmic plot of the current densities versus the applied potential for a) Pt(111), b) Pt(221), and c) Pt(pc). d) Logarithm of the pseudo-exchange current density of Pt(111), Pt(221), and Pt(pc) plotted versus the hydration energy of the corresponding alkali metal cations. The pseudo-exchange current densities were estimated by a "classical" approach. e) The "Volcano" plot ranks the activity of different metal surfaces for the HER (squares) by their theoretical binding energies of the hydrogen reaction intermediates (dotted line, the theoretical H-binding energies and the experimental activity data are taken from Refs. 21,22). Pt, Ir, Au, and Ag are marked in the plot.

RbOH. Figure 3b shows the HER current densities (normalized to the geometric surface area of the electrode) of Au(111) and Ag(pc) in Ar-saturated electrolytes at −0.65 V *vs.* RHE. For both electrodes, the HER current densities increased from Li^+ to Cs^+, opposite to the trends observed for the Pt electrodes. Additionally, the voltammograms of the Au(111) and Ag(pc) electrodes are presented in Figure S2 and S3, respectively. A comparable activity trend was observed for Au(111) in the H_2-saturated electrolytes (Figure 3c), in which the HER current densities in CsOH were ~4-fold higher than those in LiOH. In a word, the results confirm a decreasing HER activity for Au and Ag and an increasing HER activity for Pt and Ir with increasing of the hydration energy of the alkali metal cations ($Li^+ > Na^+ > K^+ > Rb^+ > Cs^+$).

Our results confirm the existence of the influence of the alkali metal cations; and this influence strongly correlates with the type of the alkali metal. This influence might indicate the

ChemPubSoc Europe

CHEMELECTROCHEM Communications

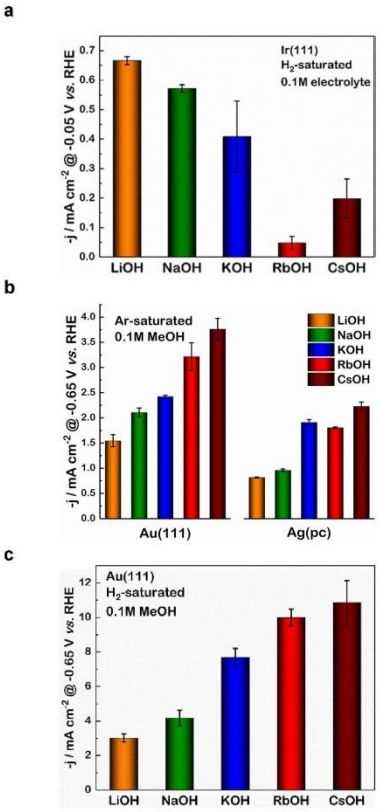

Figure 3. a) The HER current densities of Ir(111) in H_2-saturated alkaline solutions at −0.05 V *vs.* RHE. The HER activity decreases from LiOH to CsOH, similar to that of Pt. b) The HER current densities of Au(111) and Ag(pc) in Ar-saturated alkaline solutions at −0.65 V *vs.* RHE. The activity trend is reversed in comparison with Pt and Ir. c) The HER current density of Au(111) in H_2-saturated alkaline solutions at −0.65 V *vs.* RHE. All measurements were performed under similar conditions to those of Pt electrodes.

presence of non-covalent interactions[10,23] between alkali metal cations and the adsorbed reaction intermediates at the electrode surface, or it could be due to co-adsorption of metal cations onto the electrode surface.[24] However, more detailed experiments are needed to fully confirm the exact origin of this phenomenon. Recently, we have demonstrated that the alkali metal cations accumulate at the electrode surface, where their effective concentration appears to be ~80 times higher than their bulk concentrations.[25] This likely leads to the restructuring of the double layer resulting in a different catalytic activity. Consequently, regardless of the mechanism, the adsorption energy of H-intermediates is influenced by the presence of alkali metal cations. The binding of the HER intermediates to the active centers weakens systematically from Cs^+ to Li^+ depending on the type of alkali metal cation present close to them: $Cs^+ > Rb^+ > K^+ > Na^+ > Li^+$. This phenomenon is beneficial for HER on Pt and Ir but detrimental for HER on Au and Ag electrodes.

In summary, HER activities of Pt(111), Pt(221), Pt(pc), Ir(111), Au(111) and Ag(pc) were measured in different alkaline electrolytes. For Ir(111) and all of the Pt electrodes, irrespective of their surface structure, the activities decrease in the following order: LiOH > NaOH > KOH > RbOH > CsOH, while the order of the activities for Au and Ag electrodes is reversed: CsOH > RbOH > KOH > NaOH > LiOH. These results confirm that alkali metal cations indeed affect the HER performance of the metal electrodes, and there is an influence up to a factor of ~4 between Li^+ and Cs^+ containing electrolytes. We suggest that these observed phenomena might be due to a change in the H-binding energy of the electrode material, which is caused by the interaction between the alkali metal cations present close to the catalytic centers with the reaction intermediates on the electrode surface. However, further detailed experiments are required to confirm how the alkali metal cations change the H-binding energy of the electrode material.

Acknowledgements

Financial supports from the cluster of excellence Nanosystems Initiative Munich (NIM) and TUM-IGSSE project 11.01 are gratefully acknowledged. S.X. acknowledges a financial support from the China Scholarship Council (CSC, award number 201606180040).

Conflict of Interest

The authors declare no conflict of interest.

[1] P. Herasymenko, I. Z. Slendyk, *Physik. Chem. A* **1930**, *149*, 230.
[2] M. Nesselberger, S. Ashton, J. C. Meier, I. Katsounaros, K. J. Mayrhofer, M. Arenz, *J. Am. Chem. Soc.* **2011**, *133*, 17428–17433.
[3] A. Izgorodin, E. Izgorodina, D. R. MacFarlane, *Energy Environ. Sci.* **2012**, *5*, 9496–9501.
[4] J. Suntivich, E. E. Perry, H. A. Gasteiger, Y. Shao-Horn, *Electrocatalysis* **2013**, *4*, 49–55.
[5] Y. X. Chen, M. Heinen, Z. Jusys, R. J. Behm, *Langmuir*, **2006**, *22*, 10399–10408.
[6] V. R. Stamenkovic, B. S. Mun, K. J. Mayrhofer, P. N. Ross, N. M. Markovic, *J. Am. Chem. Soc.* **2006**, *128*, 8813–8819.
[7] E. S. Rountree, B. D. McCarthy, T. T. Eisenhart, J. L. Dempsey, *Inorg. Chem.* **2014**, *53*, 9983–10002.
[8] S. Xue, S. Watzele, V. Čolić, K. Brandl, B. Garlyyev, A. S. Bandarenka, *ChemSusChem* **2017**, *10*, 4812–4816.
[9] M. Mavrikakis, *Nat. Mater.* **2006**, *5*, 847–848.
[10] J. Tymoczko, V. Colic, A. Ganassin, W. Schuhmann, A. S. Bandarenka, *Catal. Today* **2015**, *244*, 96–102.
[11] D. Strmcnik, K. Kodama, D. Van der Vliet, J. Greeley, V. R. Stamenkovic, N. M. Marković, *Nat. Chem.* **2009**, *1*, 466–472.
[12] V. Colic, M. D. Pohl, D. Scieszka, A. S. Bandarenka, *Catal. Today* **2016**, *262*, 24–35.
[13] C. Stoffelsma, P. Rodriguez, G. Garcia, N. , Garcia-Araez, D. Strmcnik, N. M. Marković, M. T. Koper, *J. Am. Chem. Soc.* **2010**, *132*, 16127–16133.
[14] M. Nakamura, N. Sato, N. Hoshi, O. Sakata, *ChemPhysChem* **2011**, *12*, 1430–1434.
[15] O. Bičáková, P. Straka, *Int. J. Hydrogen Energy* **2012**, *37*, 11563–11578.

ChemPubSoc Europe

CHEMELECTROCHEM Communications

[16] M. Carmo, D. L. Fritz, J. Mergel, D. Stolten, *Int. J. Hydrogen Energy* **2013**, *38*, 4901–4934.
[17] J. Tymoczko, F. Calle-Vallejo, W. Schuhmann, A. S. Bandarenka, *Nat. Commun.* **2016**, *7*, 10990.
[18] A. Lasia, *Handbook of fuel cells*, Wiley-VCH, Weinheim, **2010**.
[19] I. T. McCrum, M. J. Janik, *J. Phys. Chem. C* **2015**, *120*, 457–471.
[20] M. D. Pohl, S. Watzele, F. Calle-Vallejo, A. S. Bandarenka, *ACS Omega* **2017**, *11*, 8141–8147.
[21] J. K. Nørskov, T. Bligaard, A. Logadottir, J. R. Kitchin, J. G. Chen, S. Pandelov, U. Stimming, *J. Electrochem. Soc.* **2005**, *152*, 23–26.
[22] J. Greeley, T. F. Jaramillo, J. Bonde, I. B. Chorkendorff, J. K. Nørskov, *Nat. Mater.* **2006**, *5*, 909–913.
[23] E. Skúlason, V. Tripkovic, M. E. Björketun, S. Gudmundsdottir, G. Karlberg, J. Rossmeisl, T. Bligaard, H. Jónsson, J. K. Nørskov, *J. Phys. Chem. C* **2010**, *114*, 18182–18197.
[24] X. Chen, I. T. McCrum, K. A. Schwarz, M. J. Janik, M. Koper , *Angew. Chem. Int. Ed.* **2017**, *56*, 15025–15029.
[25] B. Garlyyev, S. Xue, S. Watzele, D. Scieszka, A. S. Bandarenka, *J. Phys. Chem. Lett.* **2018**, *9*, 1927–1930.

Manuscript received: May 24, 2018
Version of record online: June 19, 2018

ACS OMEGA

Article

Cite This: *ACS Omega* 2018, 3, 15325−15331

http://pubs.acs.org/journal/acsodf

Oxygen Electroreduction at High-Index Pt Electrodes in Alkaline Electrolytes: A Decisive Role of the Alkali Metal Cations

Batyr Garlyyev,[†,∥] Song Xue,[†,∥] Marcus D. Pohl,[†] David Reinisch,[†] and Aliaksandr S. Bandarenka*[,†,‡,§]

[†]Physik-Department ECS, Technische Universität München, James-Franck-Str. 1, D-85748 Garching, Germany

[‡]Nanosystems Initiative Munich (NIM), Schellingstraße 4, 80799 Munich, Germany

[§]Catalysis Research Center TUM, Ernst-Otto-Fischer-Straße 1, 85748 Garching, Germany

ABSTRACT: Currently, platinum group metals play a central role in the electrocatalysis of the oxygen reduction reaction (ORR). Successful design and synthesis of new highly active materials for this process mainly rely on understanding of the so-called electrified electrode/electrolyte interface. It is widely accepted that the catalytic properties of this interface are only dependent on the electrode surface composition and structure. Therefore, there are limited studies about the effects of the electrolyte components on electrocatalytic activity. By now, however, several key points related to the electrolyte composition have become important for many electrocatalytic reactions, including the ORR. It is essential to understand how certain "spectator ions" (e.g., alkali metal cations) influence the electrocatalytic activity and what is the contribution of the electrode surface structure when, for instance, changing the pH of the electrolyte. In this work, the ORR activity of model stepped Pt [n(111) × (111)] surfaces (where n is equal to either 3 or 4 and denotes the atomic width of the (111) terraces of the Pt electrodes) was explored in various alkali metal (Li^+, Na^+, K^+, Rb^+, and Cs^+) hydroxide solutions. The activity of these electrodes was unexpectedly strongly dependent not only on the surface structure but also on the type of the alkali metal cation in the solutions with the same pH, being the highest in potassium hydroxide solutions (i.e., $K^+ \gg Na^+ > Cs^+ > Rb^+ \approx Li^+$). A possible reason for the observed ORR activity of Pt [n(111) × (111)] electrodes is discussed as an interplay between structural effects and noncovalent interactions between alkali metal cations and reaction intermediates adsorbed at active catalytic sites.

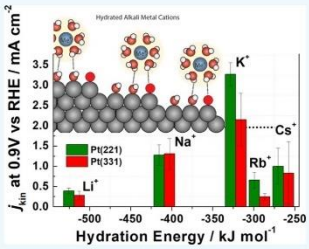

1. INTRODUCTION

The successful development of electrocatalysts strongly correlates with a detailed understanding of processes happening at the electrode/electrolyte interface.[1−5] Platinum and platinum group metals play a crucial role in catalyzing numerous reactions, and one of the electrocatalytic reactions of great importance, particularly for energy conversion and storage systems, is the oxygen reduction reaction (ORR).[6,7] Several factors determine the overall activity and selectivity of Pt and platinum group metals toward the ORR: the electrode surface composition,[8−10] electrode surface structure,[11−16] and the electrolyte composition. Certain approaches and methodologies such as Sabatier-type volcano plots[3,17−19] or so-called coordination−activity relations[20] can in many cases provide a good explanation of the observed catalytic activity trends for various electrode materials. There have also been studies regarding the influence of electrolyte components,[21−29] which is less understood. For example, in sulfuric acid, sulfate anions form strongly adsorbed layers on Pt electrodes, hamper the adsorption of ORR intermediates, and decrease the electrode activity toward oxygen electroreduction in comparison with $HClO_4$ electrolytes.[30,31] On the other hand, in $HClO_4$ media, it has been recently shown that perchlorate anions can interact with OH species adsorbed at the platinum surface and likely influence the ORR active sites.[32,33] However, there is much less understanding of how certain cation "spectator species" (such as Na^+ or K^+), which are widely used as components of supporting electrolytes, affect the ORR activity at different pHs and how they interact with the electrocatalytic surface sites.

There are at least two concurrent hypotheses proposed to explain changes in the electrocatalytic activity of metal electrodes, for example, if one switches the electrolyte pH from acidic to alkaline. The first hypothesis is that the activity of an electrocatalyst simply depends on the pH of the electrolyte because of entropy barriers at the electrified interface[34] or due to structuring in the electrical double layer[35,36] and/or different solvation effects.[37] The second hypothesis is based on a big role of noncovalent interactions between the electrocatalyst active sites and spectator species, for instance, the alkali metal cations.[25,27] In the case of the ORR activity at Pt(111) electrodes in different alkaline solutions, the highest activity was observed in 0.1 M Cs^+-containing solutions, and it was suggested that Cs^+ exhibits the

Received: February 19, 2018
Accepted: September 13, 2018
Published: November 12, 2018

DOI: 10.1021/acsomega.8b00298
ACS Omega 2018, 3, 15325−15331

weakest stabilization of the ORR intermediate, OH*,[25] leading to a near-optimal OH-binding energy for Pt(111) surfaces.

Herein, we demonstrate that the ORR activity of well-defined high-index model surfaces of Pt[n(111) × (111)] [where n = 3 for Pt(331), or n = 4 for Pt(221), and denotes the atomic width of the (111) terraces of the Pt electrodes with (111) step types] is significantly influenced by different alkali metal cations, namely, Li^+, Na^+, K^+, Rb^+, and Cs^+. The particular choice of these electrodes for this study is due to their exceptionally high ORR activities in $HClO_4$ media.[21,38] We compared the results obtained for the above-mentioned stepped single-crystal surfaces with the similar ones for Pt(111) electrodes known from the literature. The highest activity for the Pt(331) and Pt(221) electrodes was observed in K^+-containing electrolytes. However, the activities of the high-index Pt surfaces appeared to be systematically lower in alkaline than in acidic media, which is opposite to what is observed for Pt(111) electrodes. The influence of the alkali metal cations on the active sites located at the steps and terraces of Pt(331) and Pt(221) electrodes is discussed.

2. RESULTS AND DISCUSSION

2.1. Electrochemical Measurements in Acidic and Various Basic Solutions. Cyclic voltammograms (CVs) of stepped Pt(221) and Pt(331) single crystals were recorded in Ar-saturated acidic and alkaline electrolytes. The resulting CVs in perchloric acid solutions are shown in Figure 1A; CVs of Pt(111) single-crystal electrodes in 0.1 M $HClO_4$ and 0.1 M KOH are also presented as a reference. The voltammograms of stepped surfaces demonstrate distinctive features, which are

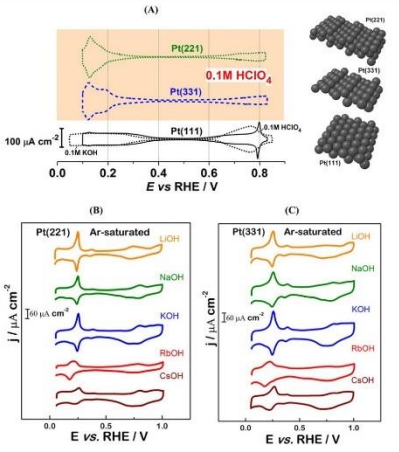

Figure 1. (A) Typical CVs of Pt(221) and Pt(331) electrodes obtained in Ar-saturated 0.1 M $HClO_4$ together with the reference voltammogram for Pt(111) in 0.1 M $HClO_4$ and 0.1 M KOH as indicated in the figure. Representative single-crystal surface structures are also shown for clarity. Typical CVs of (B) Pt(221) and (C) Pt(331) electrodes in Ar-saturated 0.1 M AM−OH (AM = Li^+, Na^+, K^+, Rb^+, and Cs^+) electrolytes. The scan rate is 50 mV/s.

associated with different surface structures and the distribution of adsorption sites as compared to Pt(111).[21−23,43−45]

For all three electrodes, CVs obtained in 0.1 M $HClO_4$ consist of clearly distinguishable regions with pairs of reversible peaks (Figure 1A). In the case of Pt(111), adsorption/desorption of the underpotentially deposited hydrogen species can be revealed between ∼0.1 and ∼0.4 V versus reversible hydrogen electrode (RHE). Within the same potential range, CV features in 0.1 M $HClO_4$ are significantly different for the Pt(221) and Pt(331) electrodes as compared to that for Pt(111). Additional peaks appear at ca. 0.12 V versus RHE, which are attributed to the adsorption of OH species on undercoordinated sites at steps.[39,40] Notably, in 0.1 M alkaline electrolytes (Figure 1B,C), the CVs in the potential region between ∼0.1 and ∼0.4 V versus RHE for Pt(221) and Pt(331) are also considerably different: the sharp peaks are shifted toward ∼0.25 V versus RHE. These peaks can in principle be attributed to the adsorption/desorption of the hydroxide species. However, there is no conclusive experimental study confirming the nature of the adsorption species involved in these processes in alkaline media. Most of the relevant studies were carried out under ultrahigh vacuum conditions and did not consider the influence of metal cations and other ions present in actual experimental solutions (see ref 41). Recently, Koper et al. suggested that coadsorption of cations is the origin of the apparent pH dependence of hydrogen adsorption on stepped Pt single-crystal electrodes.[27]

At the potential range between ∼0.35 and ∼0.65 V versus RHE, the so-called double-layer region is observed (Figure 1), the width of which is, however, noticeably different for Pt electrodes in acidic and alkaline media. At the potential region more positive than ∼0.65 V versus RHE, even more drastic changes in the voltammetric behavior are observed. Whereas for Pt(111), the reversible peaks related to the OH adsorption at terraces are clearly observed between ∼0.6 and ∼0.9 V versus RHE, the hydroxyl anions adsorb significantly weaker at similar sites of Pt(221) and Pt(331) electrodes. Notably, the positive OH shift is more pronounced in the alkaline electrolyte. Summarizing this part, it is important to admit that changes in the electrolyte pH and composition drastically alter the adsorption properties of Pt electrodes and would also likely influence the electrocatalytic activity of these systems.

The ORR activities of stepped Pt(221) and Pt(331) single crystals were studied under the hanging meniscus rotating-disk electrode (HM-RDE) configuration in O_2-saturated 0.1 M $HClO_4$ and 0.1 M AM−OH (AM = Li^+, Na^+, K^+, Rb^+, and Cs^+) electrolytes. Typical anodic polarization curves for Pt(221) are shown in Figure 2A. In Figure 2B, we show the activities of the Pt(221) electrodes in O_2-saturated 0.1 M $HClO_4$ and 0.1 M KOH and for Pt(111) electrodes in O_2-saturated 0.1 M $HClO_4$ and 0.1 M CsOH electrolytes taken from the study of Marković et al.[25] for benchmarking.

It was reported that Pt(221) electrodes demonstrated the highest oxygen reduction activity among Pt single crystals in the 0.1 M $HClO_4$ electrolyte.[21,38] In accordance with those results, stepped Pt(221) crystals indeed show higher activity compared to Pt(111) in acid (Figure 2B). The reason for the increased ORR activity of Pt(221) is the maximal density of surface catalytic sites with optimal coordination (in terms of generalized coordination numbers)[20,42] and consequently the optimal binding toward the most important ORR intermediate, OH*, as discussed in detail in ref 38. The most active ORR catalytic sites are "on-top" sites located close to the concavities

DOI: 10.1021/acsomega.8b00298
ACS Omega 2018, 3, 15325−15331

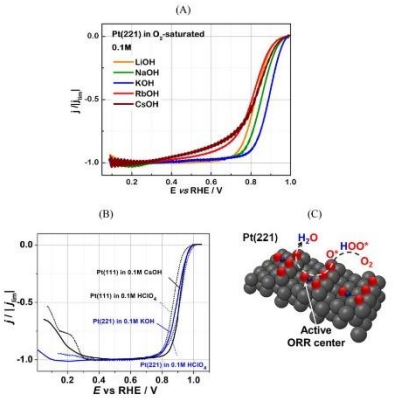

Figure 2. (A) Typical anodic scans of the RDE voltammograms (*iR*-corrected) of the stepped Pt(221) electrodes in O_2-saturated 0.1 M AM−OH (AM = Li^+, Na^+, K^+, Rb^+, and Cs^+) electrolytes. The scan speed was set to 50 mV/s, and the electrode was rotated at 1600 rpm. (B) *iR*-corrected RDE voltammograms of the Pt(221) electrodes in O_2-saturated 0.1 M $HClO_4$ and 0.1 M KOH and for Pt(111) electrodes in O_2-saturated 0.1 M $HClO_4$ and 0.1 M CsOH electrolytes (shown for comparison, adapted from ref 25). (C) Model illustrating the location of the most active catalytic ORR centers at the surface of Pt(221) in perchloric acid according to our previous work (see ref 38). These centers have an optimal coordination in terms of so-called generalized coordination numbers[20] and are consequently close to optimal binding toward the most important ORR intermediate, OH*. Oxygen atoms, which permanently block the undercoordinated sites at Pt(221), are represented as red spheres. Blue and black spheres represent the hydrogen and platinum atoms, respectively.

at steps, where the binding to OH intermediates is ca. 0.093 eV weaker than that of the "on-top" sites located at extended Pt(111) surfaces (Figure 2C).

For pristine Pt(111), the ORR activity increases when the electrolyte is switched from the acidic to some alkaline 0.1 M AM−OH (AM = K^+ and Cs^+) electrolytes. It increases monotonously from Li^+- to Cs^+-containing solutions, and the activity of Pt(111) electrodes is significantly higher in 0.1 M CsOH than that in 0.1 M $HClO_4$ (Figure 2B).[25] Marković et al. suggested that the monotonous increase in the activity from Li^+ to Cs^+ is a direct consequence of less OH stabilization at (111) terraces of Pt(111) electrodes by "less-solvated" Cs^+ (and K^+) ions compared to Li^+.[25] Interestingly, in contrast to Pt(111), the opposite is observed for Pt(221) and Pt(331) electrodes: the ORR activity is systematically higher for the stepped surfaces in the acidic electrolyte compared to the basic ones, as summarized in Figure 3. Our data are also consistent with the study by Rizo et al.[23] where the ORR activities of stepped single crystals were lower in 0.1 M NaOH compared to that in the acidic solutions. In general, the Pt(221) electrodes demonstrated higher ORR activities than Pt(331) in all the basic electrolytes. The highest ORR activity for both stepped single-crystal electrodes was observed in KOH in the following order: $K^+ \gg Na^+ > Cs^+ > Rb^+ \approx Li^+$.

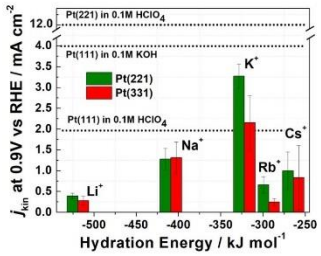

Figure 3. Bar chart showing the ORR kinetic current densities for Pt(331) and Pt(221) electrodes in 0.1 M AM−OH (AM = Li^+, Na^+, K^+, Rb^+, and Cs^+) electrolytes at the reference electrode potential 0.9 V versus RHE. Dotted lines specify the activity of Pt(111) in 0.1 M $HClO_4$, 0.1 M KOH, and Pt(221) in 0.1 M $HClO_4$ for comparison.

Furthermore, Figure 4A shows the comparison of the CVs of Pt(221) in 0.1 M LiOH and KOH electrolytes. In the K^+-containing solution, compared to Li^+-containing electrolytes, the adsorption of OH species and oxide formation are observed at more positive potentials, and the shape of the peak observed is slightly different, possibly because of the different coverages of OH/O* species. Similar trends are observed for the Pt(331) electrodes (Figure 4B). Because the OH species are also important ORR intermediates, clearly not only pH but also the nature of the alkali metal cations influence the properties of the adsorption sites (catalytic centers) at the surfaces of high-index Pt single crystals, similar to the case of Pt(111).[25] Summarizing the observations from Figures 1−4, one can assume that the observed activity of different Pt electrodes in alkaline media is a result of the interplay between structural effects and noncovalent interactions between alkali metal cations and reaction intermediates adsorbed at active catalytic centers.

2.2. Influence of Alkali Metal Cations on the ORR Activity of High- and Low-Index Pt Electrodes. Activity measurements for high-index Pt electrodes raise curiosity about the role of alkali metal cations on the electrocatalyst active sites and what is the role of the surface structure in the resulting ORR activity in alkaline media. In other words, why introduction of steps increases the activity in acidic media and decreases it when in basic solutions in the presence of the alkali metal cations? We address this query in this section by considering varying influences of alkali metal cations on different active sites present at the surface of Pt electrodes in question.

There are nonequivalent OH-adsorption sites at the surface of Pt(111) electrodes and the stepped single-crystal Pt surfaces, as schematically shown in Figure 5A,B. The OH-binding energies for these types of adsorption sites for Pt(111) and Pt(221) surfaces are summarized in Table 1. These adsorption sites can also be considered as the most probable catalytic centers for the oxygen electroreduction. Taking a closer look at Figure 5A, one can see that for the Pt(111) surface, only one type of "on-top" sites is possible (designated as type 1 in Figure 5A). For the "on-top" centers at the Pt(111) surfaces in acidic media, the corresponding OH-binding energy is ca. 0.1 eV stronger than the optimal one ($\Delta E_{OH} - \Delta E_{OH(optimum)}$ value for type 1 in Table 1).

DOI: 10.1021/acsomega.8b00298
ACS Omega 2018, 3, 15325−15331

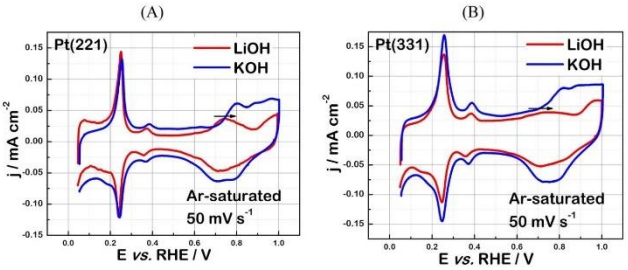

Figure 4. Typical CVs of (A) Pt(221) and (B) Pt(331) electrodes in Ar-saturated 0.1 M LiOH and KOH electrolytes. The adsorption of OH species and surface oxide formation are shifted toward more positive potentials in the K^+-containing electrolytes relative to the Li^+-containing solution, as indicated by the arrows.

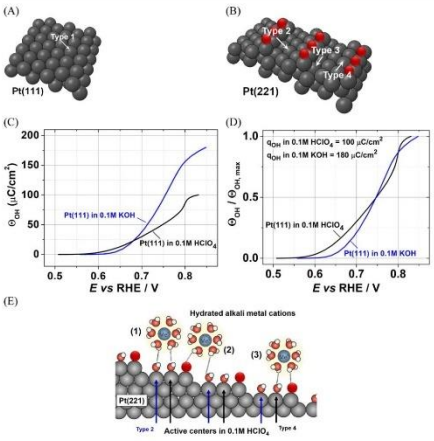

Figure 5. Schematic representation of "on-top" ORR catalytic centers at the surface of (A) Pt(111) and (B) Pt(221) at 0.9 V vs RHE. Oxygen atoms, which are represented by red spheres, permanently block the undercoordinated sites at Pt(221). (C) OH-adsorption isotherm for Pt(111) electrodes in 0.1 M $HClO_4$ and 0.1 M KOH obtained from the anodic parts of the voltammograms shown in Figure 1A. (D) OH-adsorption isotherms in (C) normalized by maximal surface coverages. The maximal OH charges obtained from the CVs are given in the inset. (E) Schematic description of how alkali metal cations interact with the steps and terraces of Pt(221) surfaces. White, red, black, and dark blue spheres represent hydrogen, oxygen, platinum atoms, and the alkali metal cations in the electrolyte, respectively.

Alkali metal cations seem to have another peculiar effect on the amount of the OH adsorbed on the Pt(111) surface; the amount of OH adsorbates seems to increase in the presence of alkali metal cations, namely, K^+ (Figure 5C,D). OH-adsorption isotherms for Pt(111) electrodes in 0.1 M $HClO_4$ and 0.1 M KOH are shown in Figure 5C. Additionally, the OH-adsorption isotherms normalized by maximal surface coverages are shown in Figure 5D. The surface coverages in respective electrolytes were obtained by calculating the area (charge) under the peaks (anodic parts) at the potentials between ∼0.55 and ∼0.85 V versus RHE from the CVs of Pt(111) in $HClO_4$ and KOH shown in Figure 1A. In KOH solution, the obtained maximum coverage OH charges are ∼2-fold higher than that in $HClO_4$. This observation could be explained by considering repulsive and attractive forces between the same and oppositely charged molecules. Because hydroxide molecules have repulsive forces between each other, they cannot form a densely packed layer on the Pt(111) surface. However, the presence of positively charged metal cations seems to alleviate those repulsive forces. Because only reversible OH adsorption occurs on the Pt(111) surfaces in alkaline media,[43] one can assume that all adsorbed OH will participate in the reaction. That is why the increased amount of adsorbed intermediates would directly result in higher ORR activity, as observed for Pt(111) in alkaline solutions.

Moreover, for the Pt(221) electrodes, there are more nonequivalent "on-top" locations as represented in Figure 5B; that is why the same above-mentioned behavior in alkaline solutions is not observed for the high-index stepped Pt surfaces. It seems that the nonuniform surface of Pt(221), Pt(331) (steps and terraces as shown in Figure 5B,E) and the presence of several "on-top" active sites inhibit/hinder the occurrence of the similar phenomena in alkaline solutions. In order to clarify this, we should consider structural and energetic characteristics of stepped Pt(221) and Pt(331) surfaces. For the sake of simplicity, let us consider four types of

Table 1. Parameters Characterizing Adsorption Sites Indicated in Figure 5 in Acidic Media

adsorption sites (according to Figure 5)	generalized coordination number (adsorbed O species and Pt are assumed to contribute equally[38])	$\Delta E_{OH} - \Delta E_{OH(Pt(111))}$ according to refs 20, 38, 42 (eV)	$\Delta E_{OH} - \Delta E_{OH(optimum)}$ (eV)
type 1	7.5	0.00	−0.1
type 2	8.0	0.0925	−0.0075
type 3	9.83	0.43	0.33
type 4	7.5	0.00	−0.1

DOI: 10.1021/acsomega.8b00298
ACS Omega 2018, 3, 15325−15331

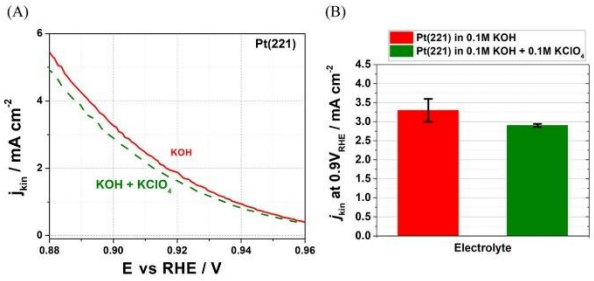

Figure 6. (A) Typical kinetic current density and (B) bar chart showing the kinetic current densities at 0.9 V vs RHE for Pt(221) electrodes in 0.1 M KOH and in 0.1 M KOH + 0.1 M $KClO_4$ electrolytes. The latter electrolyte was prepared by mixing $HClO_4$ (where the highest activity in acidic media is observed) and KOH (where the highest activity in alkaline media is observed). The error bars are from five different measurements.

surface sites on Pt(221) (each corresponding to one of the four atoms on the width of the (111) terraces of the Pt electrodes).

There are two sacrificial surface sites: the first are permanently blocked undercoordinated sites located on the top edges (Figure 5B) and the second are hindered sites labeled as type 3 in Figure 5B. The existence of these sacrificial sites is necessary for creating the highly active sites, shown as type 2 (Figure 5B). In acidic media, the type 2 sites of Pt(221), as mentioned earlier, demonstrate the most optimal OH-binding energy for the intermediates and are responsible for the high ORR activity.

In other words, when there is only relatively moderate influence from the electrolyte components (like in perchloric acid media), the site with an optimum binding energy is type 2 site on the Pt(221) surface, which binds the OH intermediates only ca. 0.0075 eV stronger than the optimum (see Table 1).

In the presence of alkali metal cations (in alkaline solutions), their prominent effects on the type 2 sites divert their OH-binding energy from the near-optimal values. As a result, one always observes lower ORR activity of the stepped Pt electrodes in basic electrolytes compared to that in the acidic ones. Additionally, the reason why Pt(331) shows lower activity compared to Pt(221) in the basic electrolytes could be due to the absence of type 4 sites on Pt(331). The type 4 sites on the Pt(221) surface are similar to the type 1 sites of Pt(111) (see Figure 5A,B), and a comparable behavior (discussed above) in alkaline solutions can be assumed.

There is another peculiarity, which distinguishes the high-index single-crystal Pt surfaces from Pt(111) in alkaline media, apart from the fact that the ORR activity of Pt(221) and Pt(331) is systematically lower than that in $HClO_4$. The ORR activities of Pt(221) and Pt(331) are nonlinear functions of the hydration energy of the alkali metal cations (Figure 3), in contrast to almost a linear relation between these parameters for Pt(111). According to the model proposed in ref 25, the hydrated alkali metal cations should interact with the hydroxide ions adsorbed on the surface via hydrogen bonds. The model assumes that alkali metal cations do not lose their solvation shell and stay intact. Our findings on the influence of different alkali metals on stepped Pt surfaces are mostly consistent with that proposed model[25] for Pt(111). A schematic description of how the alkali metal cations can interact with different adsorption sites at the Pt(221) surface is shown in Figure 5E, where possible three interactions of solvated alkali metal cations with the Pt(221) active sites are depicted. Furthermore, in contrast to the planar Pt(111) surface, where the cations can interact with the whole first water layer unhindered, for stepped surfaces the step edges can shield the terrace depending on the size of the solvated metal cations. This shielding occurs because of the steric hindrance resulting from the neighboring Pt atoms at the steps on the platinum surface, which prevents the hydrated alkali cation to noncovalently interact with some of the atoms at the surface. As a result, active sites on the Pt(221) and Pt(331), especially type 2, will be affected differently depending on the type of the metal cations. One can assume the presence of an optimum metal cation hydration energy/shell size, which correlates with the ORR activity of the electrocatalyst. For instance, Li^+ and Na^+ might have too high hydration energy and small hydration shell radii, whereas Rb^+ and Cs^+ might have too low hydration energy and large hydration shell radii, which results in lowering of the ORR activity. Therefore, it can be concluded that the reason why the electrolytes containing K^+ result in a higher ORR activity compared to other metal cations could be due to the hydration energy/shell size and/or due to the divergent effect of each alkali metal on the OH*-binding energies on the active sites of the high-index Pt surface.

In addition, to demonstrate the possible negative activity role of, namely, alkali metal cations, not only the pH effect the following experiments were performed. It is mostly assumed that perchlorate anions do not adsorb on the electrode surface and do not interact with the reactants/intermediates. Taking this as a working hypothesis, in a separate experiment we explored the effect of K^+ concentration on the activity of Pt(221) (Figure 6). The ORR kinetic current density of Pt(221) in 0.1 M KOH and in 0.1 M KOH + 0.1 M $KClO_4$ electrolytes was measured and shown in Figure 6A, and we also show the kinetic current densities at 0.9 V versus RHE as a bar chart in Figure 6B. The activity of the electrocatalyst significantly decreased with the increasing amount of K^+ at the same pH further explaining the difference in the activities between alkaline and acidic media shown in Figure 3. However, additional influence of ClO_4^- anions cannot be excluded.

DOI: 10.1021/acsomega.8b00298
ACS Omega 2018, 3, 15325−15331

3. CONCLUSIONS

In summary, the influence of metal cations on the ORR activities of the Pt(221) and Pt(331) surfaces was investigated in five different AM−OH alkaline electrolytes (AM = Li^+, Na^+, K^+, Rb^+, and Cs^+). We observed that the influence of the nature of the alkali metal cations on the ORR at Pt(221) and Pt(331) is different when compared to that of Pt(111). For Pt(111), the activity increases when the solution is switched from acidic to basic media. However, for Pt(221) and Pt(331), it is noticeably decreased. The presence of several types of active sites on high-index Pt single crystals interacting with the alkali metal cations seems to have a key role in decreased ORR activity in alkaline solutions. The ORR activity of the stepped Pt electrodes was strongly dependent on the type of the metal cation in alkaline solution and the trend was as follows: $K^+ \gg Na^+ > Cs^+ > Rb^+ \approx Li^+$. The Pt(221) electrodes showed higher ORR activity than Pt(331) in all alkaline solutions. In combination of the divergent effect of each alkali metal cation on the OH-binding energies on the active sites of the high-index Pt surface and the hydration energy/shell size of solvated metal cations, our results confirmed that not only the pH but alkali metal cations also play a decisive role in changes of the ORR activity of complex Pt surfaces. Further research can be carried out on stepped Pt surfaces with various terrace widths in order to endorse the proposed mechanism of the alkali metal cation influence.

4. EXPERIMENTAL METHODS

Single crystals of bead type: Pt(331) (Icryst, Jülich, Germany) and Pt(221) (provided by Prof. Juan Feliu, Alicante, Spain) were used in all of the experiments. For the preparation of the electrode surface crystal structure, the single crystals were flame-annealed with an isobutene gas flame and then cooled down in the mixture of CO (4.7, Air Liquide, Germany) and Ar (5.0, Air Liquide, Germany). The electrode surface structure quality was investigated by taking CVs in Ar-saturated 0.1 M $HClO_4$ solution, which are proven to be extremely sensitive to both miniscule electrolyte contaminations and surface imperfections.[44−46] Afterward, CVs of the Pt electrodes were recorded in Ar-saturated 0.1 M solutions of alkali metal hydroxides (Li^+, Na^+, K^+, Rb^+, and Cs^+). Then, the electrode activities toward ORR were measured under the HM-RDE configuration (see refs 47 and 48) in O_2-saturated (5.0, Air Liquide, Germany) electrolytes. The electrodes were rotated at 1600 rpm for all measurements. The similar experiments were performed in a solution containing 0.1 M KOH and 0.1 M $KClO_4$.

All glassware and experimental cells were cleaned with a 7:3 ratio mixture of H_2SO_4 and H_2O_2 (both Suprapur and purchased from Merck, Germany). Afterward, they were cleaned and rinsed several times with boiling ultrapure water (Evoqua, Germany). A VSP-300 potentiostat (Bio-Logic, France) was used for all of the electrochemical measurements. For an initial cycle of each measurement, the working electrodes were introduced into the solution under potential control at 0.05 V versus RHE.

A polycrystalline platinum wire and a mercury−mercury sulfate electrode (SI Analytics, Germany) were used as a counter and a reference electrode, respectively. All of the reported potentials in this study are referred to the RHE scale.

The solutions of perchloric acid were prepared by diluting the 70% $HClO_4$ (Suprapur, Merck, Germany) with ultrapure water (Evoqua, Germany). The alkali metal hydroxide solutions were prepared from $LiOH{\cdot}H_2O$ (99.998%, Trace-SELECT, Sigma-Aldrich), NaOH (99.99%, semiconductor grade, Sigma-Aldrich), KOH (99.99%, trace metal basis, Sigma-Aldrich), RbOH (99.9%, 50 wt % solution, Sigma-Aldrich), and CsOH (99.9%, 50 wt % solution, Sigma-Aldrich). For the preparation of the mixture solution of $KClO_4$ + KOH, first, a 0.4 M KOH solution and a 0.2 M $HClO_4$ solution were prepared from previously mentioned respective chemicals and subsequently mixed in a 1:1 ratio.

AUTHOR INFORMATION

Corresponding Author

*E-mail: bandarenka@ph.tum.de (A.S.B.).

ORCID

Aliaksandr S. Bandarenka: 0000-0002-5970-4315

Author Contributions

‖B.G. and S.X. contributed equally.

Notes

The authors declare no competing financial interest.

ACKNOWLEDGMENTS

Financial support from the cluster of excellence Nanosystems Initiative Munich (NIM) and DFG project BA 5795/4-1 is gratefully acknowledged. This work was supported by the German Research Foundation (DFG) and the Technical University of Munich within the Open Access Publishing Funding Programme.

REFERENCES

(1) Koper, M. T. M. Structure sensitivity and nanoscale effects in electrocatalysis. *Nanoscale* **2011**, *3*, 2054−2073.

(2) Marković, N.; Ross, P. N. Surface science studies of model fuel cell electrocatalysts. *Surf. Sci. Rep.* **2002**, *45*, 117−229.

(3) Bandarenka, A. S.; Koper, M. T. M. Structural and electronic effects in heterogeneous electrocatalysis: Toward a rational design of electrocatalysts. *J. Catal.* **2013**, *308*, 11−24.

(4) Gasteiger, H. A.; Kocha, S. S.; Sompalli, B.; Wagner, F. T. Activity benchmarks and requirements for Pt, Pt-alloy, and non-Pt oxygen reduction catalysts for PEMFCs. *Appl. Catal., B* **2005**, *56*, 9−35.

(5) Mahmoud, M. A.; Garlyyev, B.; El-Sayed, M. A. Determining the mechanism of solution metallic nanocatalysis with solid and hollow nanoparticles: homogeneous or heterogeneous. *J. Phys. Chem. C* **2013**, *117*, 21886−21893.

(6) Calle-Vallejo, F.; Koper, M. T. M.; Bandarenka, A. S. Tailoring the catalytic activity of electrodes with monolayer amounts of foreign metals. *Chem. Soc. Rev.* **2013**, *42*, 5210−5230.

(7) Stamenkovic, V. R.; Mun, B. S.; Arenz, M.; Mayrhofer, K. J. J.; Lucas, C. A.; Wang, G.; Ross, P. N.; Markovic, N. M. Trends in electrocatalysis on extended and nanoscale Pt-bimetallic alloy surfaces. *Nat. Mater.* **2007**, *6*, 241−247.

(8) Chou, S.-W.; Lai, Y.-R.; Yang, Y. Y.; Tang, C.-Y.; Hayashi, M.; Chen, H.-C.; Chen, H.-L.; Chou, P.-T. Uniform size and composition tuning of PtNi octahedra for systematic studies of oxygen reduction reactions. *J. Catal.* **2014**, *309*, 343−350.

(9) Greeley, J.; Stephens, I. E. L.; Bondarenko, A. S.; Johansson, T. P.; Hansen, H. A.; Jaramillo, T. F.; Rossmeisl, J.; Chorkendorff, I.; Nørskov, J. K. Alloys of platinum and early transition metals as oxygen reduction electrocatalysts. *Nat. Chem.* **2009**, *1*, 552−556.

(10) Coleman, E. J.; Co, A. C. Galvanic displacement of Pt on nanoporous copper: An alternative synthetic route for obtaining robust and reliable oxygen reduction activity. *J. Catal.* **2014**, *316*, 191−200.

DOI: 10.1021/acsomega.8b00298
ACS Omega 2018, 3, 15325−15331

(11) Mukerjee, S.; Srinivasan, S.; Soriaga, M. P.; McBreen, J. Role of Structural and Electronic Properties of Pt and Pt Alloys on Electrocatalysis of Oxygen Reduction. *J. Electrochem. Soc.* **1995**, *142*, 1409−1422.
(12) Stamenkovic, V.; Mun, B. S.; Mayrhofer, K. J. J.; Ross, P. N.; Markovic, N. M.; Rossmeisl, J.; Greeley, J.; Nørskov, J. K. Changing the activity of electrocatalysts for oxygen reduction by tuning the surface electronic structure. *Angew. Chem.* **2006**, *118*, 2963−2967.
(13) Pfisterer, J. H. K.; Liang, Y.; Schneider, O.; Bandarenka, A. S. Direct instrumental identification of catalytically active surface sites. *Nature* **2017**, *549*, 74−77.
(14) Kodama, K.; Jinnouchi, R.; Takahashi, N.; Murata, H.; Morimoto, Y. Activities and stabilities of Au-modified stepped-Pt single-crystal electrodes as model cathode catalysts in polymer electrolyte fuel cells. *J. Am. Chem. Soc.* **2016**, *138*, 4194−4200.
(15) Ueno, T.; Tanaka, H.; Sugawara, S.; Shinohara, K.; Ohma, A.; Hoshi, N.; Nakamura, M. Infrared spectroscopy of adsorbed OH on n (111)-(100) and n (111)-(111) series of Pt electrode. *J. Electroanal. Chem.* **2017**, *800*, 162−166.
(16) Stoffelsma, C.; Rodriguez, P.; Garcia, G.; Garcia-Araez, N.; Strmcnik, D.; Marković, N. M.; Koper, M. T. M. Promotion of the oxidation of carbon monoxide at stepped platinum single-crystal electrodes in alkaline media by lithium and beryllium cations. *J. Am. Chem. Soc.* **2010**, *132*, 16127−16133.
(17) Stephens, I. E. L.; Bondarenko, A. S.; Grønbjerg, U.; Rossmeisl, J.; Chorkendorff, I. Understanding the electrocatalysis of oxygen reduction on platinum and its alloys. *Energy Environ. Sci.* **2012**, *5*, 6744−6762.
(18) Čolić, V.; Bandarenka, A. S. Pt alloy electrocatalysts for the oxygen reduction reaction: from model surfaces to nanostructured systems. *ACS Catal.* **2016**, *6*, 5378−5385.
(19) Bandarenka, A. S.; Ventosa, E.; Maljusch, A.; Masa, J.; Schuhmann, W. Techniques and methodologies in modern electrocatalysis: evaluation of activity, selectivity and stability of catalytic materials. *Analyst* **2014**, *139*, 1274−1291.
(20) Calle-Vallejo, F.; Tymoczko, J.; Colic, V.; Vu, Q. H.; Pohl, M. D.; Morgenstern, K.; Loffreda, D.; Sautet, P.; Schuhmann, W.; Bandarenka, A. S. Finding optimal surface sites on heterogeneous catalysts by counting nearest neighbors. *Science* **2015**, *350*, 185−189.
(21) Kuzume, A.; Herrero, E.; Feliu, J. M. Oxygen reduction on stepped platinum surfaces in acidic media. *J. Electroanal. Chem.* **2007**, *599*, 333−343.
(22) Maciá, M. D.; Campiña, J. M.; Herrero, E.; Feliu, J. M. On the kinetics of oxygen reduction on platinum stepped surfaces in acidic media. *J. Electroanal. Chem.* **2004**, *564*, 141−150.
(23) Rizo, R.; Herrero, E.; Feliu, J. M. Oxygen reduction reaction on stepped platinum surfaces in alkaline media. *Phys. Chem. Chem. Phys.* **2013**, *15*, 15416−15425.
(24) Wang, C.; Markovic, N. M.; Stamenkovic, V. R. Advanced platinum alloy electrocatalysts for the oxygen reduction reaction. *ACS Catal.* **2012**, *2*, 891−898.
(25) Strmcnik, D.; Kodama, K.; van der Vliet, D.; Greeley, J.; Stamenkovic, V. R.; Marković, N. M. The role of non-covalent interactions in electrocatalytic fuel-cell reactions on platinum. *Nat. Chem.* **2009**, *1*, 466−472.
(26) Colic, V.; Pohl, M. D.; Scieszka, D.; Bandarenka, A. S. Influence of the electrolyte composition on the activity and selectivity of electrocatalytic centers. *Catal. Today* **2016**, *262*, 24−35.
(27) Chen, X.; McCrum, I. T.; Schwarz, K. A.; Janik, M. J.; Koper, M. T. M. Co-adsorption of Cations as the Cause of the Apparent pH Dependence of Hydrogen Adsorption on a Stepped Platinum Single-Crystal Electrode. *Angew. Chem., Int. Ed.* **2017**, *56*, 15025−15029.
(28) Xue, S.; Watzele, S.; Čolić, V.; Brandl, K.; Garlyyev, B.; Bandarenka, A. S. Reconsidering Water Electrolysis: Producing Hydrogen at Cathodes Together with Selective Oxidation of n -Butylamine at Anodes. *ChemSusChem* **2017**, *10*, 4812−4816.
(29) Moureaux, F.; Stevens, P.; Chatenet, M. Effect of lithium and potassium cations on the electrocatalytic properties of carbon and manganese oxide electrocatalysts towards the oxygen reduction reaction in concentrated alkaline electrolyte. *Electrocatalysis* **2013**, *4*, 123−133.
(30) Kolics, A.; Wieckowski, A. Adsorption of Bisulfate and Sulfate Anions on a Pt(111) Electrode. *J. Phys. Chem. B* **2001**, *105*, 2588−2595.
(31) Gamboa-Aldeco, M. E.; Herrero, E.; Zelenay, P. S.; Wieckowski, A. Adsorption of bisulfate anion on a Pt(100) electrode: A comparison with Pt(111) and Pt(poly). *J. Electroanal. Chem.* **1993**, *348*, 451−457.
(32) Huang, Y.-F.; Kooyman, P. J.; Koper, M. T. M. Intermediate stages of electrochemical oxidation of single-crystalline platinum revealed by in situ Raman spectroscopy. *Nat. Commun.* **2016**, *7*, 12440.
(33) Attard, G. A.; Brew, A.; Hunter, K.; Sharman, J.; Wright, E. Specific adsorption of perchlorate anions on Pt{hkl} single crystal electrodes. *Phys. Chem. Chem. Phys.* **2014**, *16*, 13689−13698.
(34) Rossmeisl, J.; Chan, K.; Skúlason, E.; Björketun, M. E.; Tripkovic, V. On the pH dependence of electrochemical proton transfer barriers. *Catal. Today* **2016**, *262*, 36−40.
(35) Ledezma-Yanez, I.; Wallace, W. D. Z.; Sebastián-Pascual, P.; Climent, V.; Feliu, J. M.; Koper, M. T. M. Interfacial water reorganization as a pH-dependent descriptor of the hydrogen evolution rate on platinum electrodes. *Nat. Energy* **2017**, *2*, 17031.
(36) Garlyyev, B.; Xue, S.; Watzele, S.; Scieszka, D.; Bandarenka, A. S. Influence of the Nature of the Alkali Metal Cations on the Electrical Double-Layer Capacitance of Model Pt(111) and Au(111) Electrodes. *J. Phys. Chem. Lett.* **2018**, *9*, 1927−1930.
(37) He, Z.-D.; Hanselman, S.; Chen, Y.-X.; Koper, M. T. M.; Calle-Vallejo, F. Importance of solvation for the accurate prediction of oxygen reduction activities of Pt-based electrocatalysts. *J. Phys. Chem. Lett.* **2017**, *8*, 2243−2246.
(38) Calle-Vallejo, F.; Pohl, M. D.; Reinisch, D.; Loffreda, D.; Sautet, P.; Bandarenka, A. S. Why conclusions from platinum model surfaces do not necessarily lead to enhanced nanoparticle catalysts for the oxygen reduction reaction. *Chem. Sci.* **2017**, *8*, 2283−2289.
(39) van der Niet, M. J. T. C.; Garcia-Araez, N.; Hernández, J.; Feliu, J. M.; Koper, M. T. M. Water dissociation on well-defined platinum surfaces: The electrochemical perspective. *Catal. Today* **2013**, *202*, 105−113.
(40) Pohl, M. D.; Colic, V.; Scieszka, D.; Bandarenka, A. S. Elucidation of adsorption processes at the surface of Pt(331) model electrocatalysts in acidic aqueous media. *Phys. Chem. Chem. Phys.* **2016**, *18*, 10792−10799.
(41) van der Niet, M. J. T. C.; Berg, O. T.; Juurlink, L. B. F.; Koper, M. T. M. The Interaction between H2O and Preadsorbed O on the Stepped Pt(533) Surface. *J. Phys. Chem. C* **2010**, *114*, 18953−18960.
(42) Calle-Vallejo, F.; Martínez, J. I.; García-Lastra, J. M.; Sautet, P.; Loffreda, D. Fast prediction of adsorption properties for platinum nanocatalysts with generalized coordination numbers. *Angew. Chem., Int. Ed.* **2014**, *53*, 8316−8319.
(43) Marković, N. M.; Gasteiger, H. A.; Ross, P. N. Oxygen reduction on platinum low-index single-crystal surfaces in alkaline solution: rotating ring disk Pt(hkl) studies. *J. Phys. Chem.* **1996**, *100*, 6715−6721.
(44) Taguchi, S.; Feliu, J. M. Electrochemical reduction of nitrate on Pt(S)[n(111)×(111)] electrodes in perchloric acid solution. *Electrochim. Acta* **2007**, *52*, 6023−6033.
(45) Climent, V.; Gómez, R.; Feliu, J. M. Effect of increasing amount of steps on the potential of zero total charge of Pt(111) electrodes. *Electrochim. Acta* **1999**, *45*, 629−637.
(46) Scortichini, C. L.; Reilley, C. N. Surface characterization of Pt electrodes using underpotential deposition of H and Cu. *J. Electroanal. Chem. Interfacial Electrochem.* **1982**, *139*, 247−264.
(47) Villullas, H. M.; Teijelo, M. L. The hanging-meniscus rotating disk (HMRD) Part 1. Dependence of hydrodynamic behavior on experimental variables. *J. Electroanal. Chem.* **1995**, *384*, 25−30.
(48) Villullas, H. M.; Teijelo, M. L. The hanging meniscus rotating disk (HMRD) Part 2. Application to simple charge transfer reaction kinetics. *J. Electroanal. Chem.* **1995**, *385*, 39−44.

DOI: 10.1021/acsomega.8b00298
ACS Omega 2018, 3, 15325−15331

ChemPubSoc Europe

DOI: 10.1002/cssc.201701802

CHEMSUSCHEM Communications

Reconsidering Water Electrolysis: Producing Hydrogen at Cathodes Together with Selective Oxidation of *n*-Butylamine at Anodes

Song Xue[+,a] Sebastian Watzele[+,a] Viktor Čolić,[a,d] Kurt Brandl,[a] Batyr Garlyyev,*[a] and Aliaksandr S. Bandarenka*[a,b,c]

Electrocatalysis for the oxygen evolution reaction (OER) is of great interest for improving the effectiveness of water splitting devices. Decreasing the anodic overpotential and simultaneously changing the anodic reaction selectively to produce valuable chemicals instead of O_2 would be a major improvement of the overall cost efficiency. Some amines, when present in aqueous electrolytes, were recently shown to change the selectivity of the anodic process to generate H_2O_2 rather than O_2 on MnO_x at pH 10. This results in unusually high apparent "anodic activities". In this work, industrially relevant OER catalysts, oxyhydroxides of cobalt (CoO_x), nickel–iron ($NiFeO_x$), and nickel (NiO_x) all show more pronounced effects. Moreover, as anodes they also selectively catalyzed the production of *n*-butyronitrile from *n*-butylamine at higher pH as an easily retrievable valuable product. The pH dependence of the activity was investigated at pH values closer those at which alkaline electrolyzers operate. The highest activities were observed for NiO_x thin-film electrodes at pH 12 in the presence of 0.4 M *n*-butylammonium sulfate, without poisoning the active sites of Pt electrocatalysts at the hydrogen evolution electrode. ^{1}H NMR spectroscopy showed that *n*-butylamine is selectively oxidized to *n*-butyronitrile, an organic chemical with numerous applications. However, measurements using rotating ring-disk electrodes indicated that some H_2O_2 is also generated at the surface of the oxide anodes.

In the electrolytic production of hydrogen fuel from H_2O, the majority of energy losses comes from the side of the electrode generating gaseous O_2. Therefore, the corresponding anodic reaction, the oxygen evolution reaction (OER), is considered as the bottleneck of the whole process.[1] The product of the anodic reaction, O_2 gas, is, however, not used in further applications. Therefore, producing more valuable products instead of O_2 would be a benefit to such electrolysis systems. In other words, the system can be optimized by altering the anodic reaction, so that a different reaction proceeds for the production of certain valuable chemicals, without disrupting the overall activity. There are several other important reactions that could potentially replace the OER or proceed simultaneously, such as production of H_2O_2,[2,3] chlorine evolution,[4] or certain electroorganic reactions. However, due to high amounts of hydrogen fuel deemed to be needed in the future, there is a need to elaborate a wider portfolio of reactions to proceed with high selectivity instead of the OER at anodes (e.g., the amount of chlorine that is required for chemical industry corresponds to only about 4% of current hydrogen consumption).

Recently, MacFarlane and co-workers reported that certain MnO_x-type catalysts facilitate anodic H_2O_2 production to an extent that it dominates over the OER in aqueous electrolytes, which contain an "ionic liquid" (IL)—*n*-butylammonium sulfate (BAS).[2,3] This results in unusually high apparent anodic activities, that is, very low net overpotentials for the anodic electrode processes. In fact, a number of ionic liquids can influence the OER, as well as the oxygen reduction reaction (ORR) selectivity towards hydrogen peroxide formation.[5,6] For instance, one of the main ORR products on the cathode in Li-air batteries is superoxide, which slowly converts itself into Li_2O_2 in ionic liquids.[7] Therefore, one can, in principle, expect some similar effects in certain electrocatalytic systems containing H_2O/IL mixtures. For further notice, although the possibilities for application of ILs show many promising prospects,[3,8–12] further elucidation of their behavior in electrochemical systems is necessary.

Herein, we report a drastic decrease in the apparent anodic overpotentials for water electrolysis system in electrolytes containing *n*-butylamine with catalysts more frequently used in current industrial applications. In addition, we selectively produced the valuable organic chemical *n*-butyronitrile.[13–17] Selective conversion of amines to nitriles is an important task in catalysis (for examples, see refs. [18, 19]). Here, we use higher pHs and the best non-precious metal catalysts reported to date for the OER: cobalt, nickel, and nickel–iron oxyhydroxide based electrodes (further denoted as CoO_x, NiO_x, and $NiFeO_x$, respectively), which are known to be chemically stable only within

[a] S. Xue,[+] S. Watzele,[+] Dr. V. Ćolić, K. Brandl, Dr. B. Garlyyev, Prof. Dr. A. S. Bandarenka
Physics of Energy Conversion and Storage, Department of Physics
Technische Universität München
James-Franck-Str. 1, 85748 Garching (Germany)
E-mail: batyr.garlyyev@tum.de
bandarenka@ph.tum.de

[b] Prof. Dr. A. S. Bandarenka
Nanosystems Initiative Munich (NIM)
Schellingstraße 4, 80799 Munich (Germany)

[c] Prof. Dr. A. S. Bandarenka
Catalysis Research Center TUM
Ernst-Otto-Fischer-Straße 1, 85748 Garching (Germany)

[d] Dr. V. Čolić
Present Addresses: Department of Physics
Technical University of Denmark
Fysikvej Building 307, Room 058, 2800 Kgs. Lyngby (Denmark)

[+] These authors contributed equally to this work.

ChemPubSoc Europe

CHEMSUSCHEM Communications

higher pHs. With the new systems, we observe that the presence of *n*-butylamine also increases the catalyst stability. The oxides facilitate the selective production of *n*-butyronitrile, which is only slightly soluble in water and can be separated with relative ease, without poisoning the hydrogen evolution reaction activity of Pt cathodes during water electrolysis. ^{1}H NMR spectroscopy indicated that the only product of *n*-butylamine oxidation was *n*-butyronitrile, which is widely used as a precursor/intermediate in many industrial syntheses of organic chemicals,[14,18] as well as a low-volatility electrolyte in dye-sensitized solar cells.[15] With rotating ring-disk electrode (RRDE) measurements, we observed that the presence of *n*-butylamine seems to also facilitate H_2O_2 production. We believe that this work can be further extended to the production of other valuable chemicals together with H_2 fuel by simultaneously tailoring the electrolyte composition and the electrode surface composition and structure.

In the initial series of experiments, the MnO_x electrocatalysts, used by MacFarlane and co-workers,[2] were replaced by NiO_x and CoO_x thin-film electrode materials. Furthermore, the apparent activity increase in the presence of *n*-butylamine is reproducible with the Ni-based catalyst (Figure 1a): a notable anodic current appears at electrode potentials close to 1.5 V in the presence of *n*-butylamine at pH 10, much earlier than in the pH-corrected BAS-free K_2SO_4 solution. Moreover, the shift in the potential is more pronounced compared to the case of MnO_x-electrodes.[2] Finally, the observed apparent activity pronouncedly depends on the chemical nature of the electrocatalysts. For instance, CoO_x electrodes appear to be less active than NiO_x in the presence of BAS (Figure 1b).

In various alkaline electrolyzers, NiO_x and CoO_x electrocatalysts are usually used at higher pH values, as the OER overpotentials are generally lower under these conditions and the oxide electrocatalysts are more stable. Therefore, it is of particular interest to determine the pH dependence of the observed effect at higher pH values. The influence of the pH on the anodic currents for the most active NiO_x films is illustrated in Figure 2. It should be noted that testing at pH values higher than 13 was not achieved, owing to the instability of the bulk electrolytes. It is clear that the pH dependence of the activities in the presence of BAS is not trivial, in accordance with previous observations.[20] Raising the pH from 10 to 12 initially resulted in an increase in the apparent activity, whereas at higher pH values it dropped; the highest currents were observed in solutions with BAS at pH 12. This could potentially be due to the fact that to reach pH values of 12 and higher, it was necessary to add relatively large amounts of KOH to the IL-containing electrolytes, which might affect the formation and/or stability of the proposed complexes.

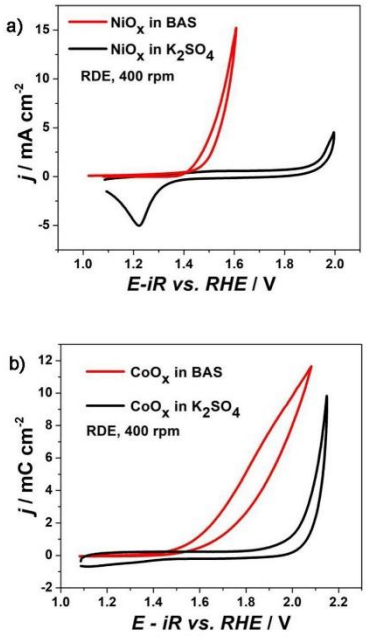

Figure 1. Typical cyclic voltammograms of (a) NiO_x and (b) CoO_x thin-film electrodes in 0.4 M K_2SO_4 aqueous reference solutions (black lines) and in 0.4 M BAS-containing electrolytes (red lines). All solutions had pH 10. The electrode potentials were *iR* corrected.

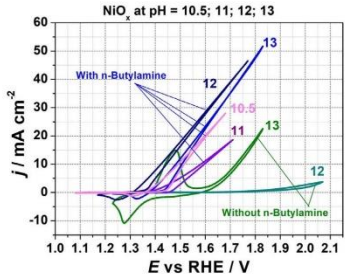

Figure 2. Typical cyclic voltammograms of NiO_x thin-film electrodes in pH-corrected 0.4 M BAS and pH-corrected 0.4 M K_2SO_4 electrolytes at different pH values (10.5, 11, 12 and 13) as indicated. The electrode potentials were not corrected for the *iR* drop in this case, owing to high currents at "lower overpotentials" to minimize possible mistakes.

Although the exact origin of the catalytic effect should be further investigated, it is demonstrated that pH in the presence of the IL has a large influence on the observed activities of metal oxyhydroxide catalysts. The current densities for different metal oxide catalysts at 1.77 V vs. RHE in "purely aqueous" solutions and in the presence of BAS are summarized in Figure 3.

Figure 3a shows that in aqueous 0.4 M K_2SO_4 electrolyte the apparent activities of the metal oxide catalysts towards the OER increase in the order $PtO_x < NiO_x < CoO_x < NiFeO_x$. It

ChemPubSoc Europe

CHEMSUSCHEM Communications

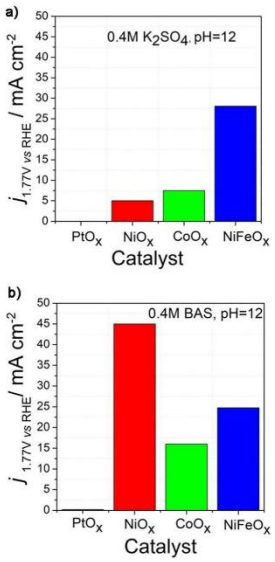

Figure 3. Average current densities at 1.77 V vs. RHE for different metal oxide-type electrodes in (a) 0.4 M K_2SO_4 and (b) 0.4 M BAS-containing electrolytes. The pH values of both solutions were adjusted to 12 with KOH. RDE at 400 r.p.m. All currents are shown without *iR* corrections.

should be noted that the anodic currents in the case of Pt electrodes are likely due to further oxidation of metallic Pt present below the Pt oxide layer, rather than to the oxidation of BAS. However, in the presence of *n*-butylamine (Figure 3b), the order of the apparent activities changes and the largest current density at the potential of 1.77 V is observed at the NiO_x catalyst, being by an order of magnitude larger than that observed in purely aqueous solution at the same potential. The order of the apparent activities in the presence of BAS is thus $PtO_x < CoO_x < NiFeO_x < NiO_x$. It should again be noted that the anodic currents in the case of Pt-electrodes are mainly due to furter oxidation of metallic Pt below the Pt-oxide. Additionally, it is interesting to note that the current densities for CoO_x catalysts also increase, albeit to a smaller extent, whereas for the $NiFeO_x$ catalyst it remains similar in both cases. This indicates that there is likely an interplay between the properties of the electrolyte and the catalyst that results in variation of the magnitude of the observed effect.

To elucidate the processes happening during water electrolysis in the presence of BAS, we explored the system with ^{1}H NMR spectroscopy and RRDE measurements. ^{1}H NMR spectroscopy was applied before and after running the electrolysis for 48 h with the most active catalyst NiO_x at pH 12. The ^{1}H NMR results are shown in Figure 4a. By comparing ^{1}H NMR spectra before and after the reaction, we could clearly see the main reaction happening at the anode: exclusively selective oxidation of *n*-butylamine to form *n*-butyronitrile. The corresponding chemical shifts for *n*-butylamine and *n*-butyronitrile are in good agreement with the reported values.[21] Such a remarkable selectivity, together with the highest activity, is observed only at pH 12. At higher pHs Ni anodes are known to convert up to 15% of *n*-butylamine into a number of other organic compounds,[22] which also complicates separation of the main product.

Although the ^{1}H NMR results clearly indicate that *n*-butylamine was selectively electrocatalytically oxidized to *n*-butyronitrile during anodic polarization, the faradaic efficiency of the reaction, which was assessed by using the ^{1}H NMR data, appeared to be around 95%, possibly due to the fact that some amount of O_2 or H_2O_2 is also formed (see below). However, since H_2O_2 will spontaneously disproporionate in alkaline media, only *n*-butyronitrile is formed as the main product, with very high selectivity as shown by the ^{1}H NMR spectrum (Figure 4a).

To further study the processes taking place in the BAS-containing solutions at higher pH, RRDE measurements were conducted by cycling the potential of the NiO_x disk electrode in the potential range between 1.05 and 1.55 V while keeping the potential of the Pt ring at 1.3 V, where only H_2O_2 oxidation can take place (Figure 4b; neither oxidation of *n*-butyronitrile nor *n*-butylamine occurs at Pt; see Figure 3 and discussion above).

The emergence of the ring current simultaneously with the appearance of the anodic current on the disk electrode indicates that species electroactive at 1.3 V vs. RHE are generated at the disk, in this case indicating that H_2O_2, which undergoes oxidation at this potential, is the most likely side product of the anodic reaction. A hysteresis detected for the disk currents in the cathodic and anodic scans (Figure 4b), where the currents at the cathodic scan are higher (e.g., ca. 1 mA cm^{-2} at 1.36 V vs. RHE, without *iR* correction) than in the anodic scan, can be explained by additional autocatalytic decomposition of the generated H_2O_2 in alkaline media at the Pt disk, further indicating that hydrogen peroxide is generated in the reaction. The reason that H_2O_2 is generated at potentials lower than those commonly predicted (1.76 V vs. RHE) could be that there is no pre-existing H_2O_2 in the solution: the thermodynamic potential for H_2O_2 formation is, therefore, lowered below about 1 V vs. RHE[23] (and in alkaline media, H_2O_2 is not stable, keeping its surface concentration very low). Another possible reason could be that the presence of the ionic liquid stabilizes H_2O_2 through solvation by the IL.[2] For instance, ethylamine molecules have been shown to stabilize H_2O_2 at the electrode surface in aqueous media, given that the H_2O_2–ethylamine complexes are approximately 24 kJ mol^{-1} more stable than hydrated H_2O_2, shifting the potential by roughly 0.4 V towards more negative values.[2]

Long-term stability experiments comparing the performance of NiO_x anodes and Pt cathodes in 0.4 M K_2SO_4 and 0.4 M BAS aqueous electrolytes at pH 12 were performed by using the 2-electrode configuration (galvanostatic regime; Figure 4c). The overall cell voltage at the same constant current was found to be much lower in the case of BAS-containing electrolytes than

ChemPubSoc Europe
CHEMSUSCHEM Communications

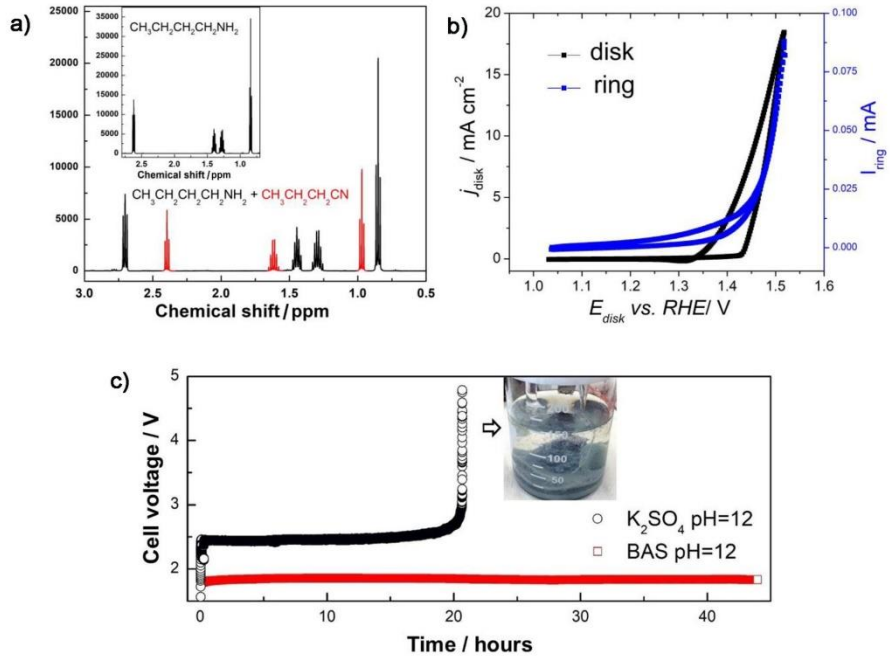

Figure 4. a) Typical ^{1}H NMR spectra after water electrolysis with NiO_x anodes in 0.4 M BAS at pH 12 for 48 h. Inset shows the ^{1}H NMR spectrum before the start of the experiment. Shifts corresponding to the *n*-butyronitrile are shown in red. b) Typical results of the RRDE measurements with NiO_x disk and Pt ring electrodes in presence of 0.4 M BAS. Scan rate for the disk: 50 mV s^{-1}. 400 r.p.m. $E_{ring} = 1.3$ V (constant). c) Stability measurements of NiO_x in 0.4 M K_2SO_4 and 0.4 M BAS-containing electrolytes at pH 12. Galvanostatic mode, $I = 40$ mA. Inset shows the quickly corroded anode when only K_2SO_4 is present in the solution.

that when only K_2SO_4 was present. Moreover, the cell voltage is very stable in the case of BAS solution through 48 h of running the experiment, whereas in the case of K_2SO_4 solutions, the anodes were completely corroded after just 20 h. These results show that the electrochemical stability in the presence of BAS is much better than in K_2SO_4. This can be partly attributed to a slight buffering effect of BAS solutions. However, it cannot completely explain the stabilizing effect.

To summarize, selectively producing a valuable organic chemical, which is relatively easy to separate, at the anode side instead of oxygen during water electrolysis could potentially improve the cost effectiveness of this electrocatalytic process. Additionally, the presence of BAS improves the stability of the system, affecting the performance of neither the metal oxide anodes nor the Pt cathodes, which is significant for its applicability in "real-world" devices.

In conclusion, we have demonstrated that an apparent increase in the anodic electrode activities during H_2O electrolysis occurs in the presence of *n*-butylamine for metal oxyhydroxide catalysts other than MnO_x, namely for industrially relevant metal oxides such as $NiFeO_x$, CoO_x, and NiO_x. In addition to the decrease in anodic overpotential, the electrocatalyst selectively produced *n*-butyronitrile, a valuable chemical used as an intermediate in synthesis of many organic chemicals, and also used as an electrolyte in dye-sensitized solar cells. The dependences of the apparent activity on the pH, particularly at higher pH values, were also investigated. The most active and selective system appeared to be NiO_x in presence of 0.4 M *n*-butylammonium sulfate at pH 12. Furthermore, the apparent activity due to the presence of BAS was found to be different for distinct catalysts and the magnitude of the effect also depended on the nature of the catalyst. The conducted RRDE measurements gave further indication that H_2O_2 is also generated as a result of the electrochemical anodic reaction of water molecules. Long-term electrolysis of water in the presence of *n*-butylammonium sulfate at pH 12 showed that the anode and cathode are stable and the catalytic sites at their surfaces are not poisoned during the process. To further increase the overall cost efficiency and stability of the system, more research needs to be done on producing valuble chemicals at the anode side during water electrolysis.

ChemPubSoc Europe

CHEMSUSCHEM Communications

Experimental Section

Glassy carbon (GC) and Pt electrode supports were pretreated by cycling in 0.5 M H_2SO_4 (96%, Suprapur, Merck, Germany) solutions up to 1.55 V vs. RHE. Cobalt oxyhydroxide thin films (denoted as CoO_x) were deposited according to the procedure described in ref. [24], from a solution containing 0.1 M Na_2SO_4 (99.99%, Sigma Aldrich, Germany), 0.1 M CH_3COONa (≥99%, Sigma Aldrich, Germany), and 0.1 M $CoSO_4$ (≥99%, Merck, Germany) in ultrapure water from an Evoqua Ultra Clear 10 TWF 30 UV system (Evoqua, Germany), by performing cyclic voltammetry scans between 1.23 and 1.83 V (RHE). Nickel oxyhydroxide thin films (denoted as NiO_x) were prepared similarly from a solution containing 0.1 M Na_2SO_4, 0.13 M CH_3COONa, and 0.13 M $NiSO_4$ (≥99%, Merck, Germany) by cycling the electrode in the range between 0.23 V and 2.13 V vs. RHE. The formation of mixed nickel–iron oxyhydroxide (denoted as $NiFeO_x$) electrocatalysts was performed as described in Ref. [25] by cathodic deposition at a constant current (50 mA cm^{-2}) for 50 s from a solution containing 0.09 M $NiSO_4$, 0.009 M $FeSO_4$ (≥99%, Merck, Germany) and 0.022 M $(NH_4)_2SO_4$ (≥99.0%, Sigma Aldrich, Germany). The thickness of CoO_x, NiO_x, and $NiFeO_x$ films necessary to achieve bulk-like properties (i.e., to eliminate substrate effects) was determined according to a procedure described in refs. [24,26]. All experiments in this work were performed with catalyst layers thick enough to eliminate the substrate effect.

BAS-containing solutions were prepared by mixing *n*-butylamine (99.5%, Sigma Aldrich, Germany) and H_2SO_4 aqueous solutions. The pH was adjusted by adding *n*-butylamine or H_2SO_4. To achieve pH ≥ 12, the addition of KOH (85%, Grüssing, Germany) was necessary. The reference K_2SO_4 solutions were prepared by diluting K_2SO_4 (99.99%, Sigma Aldrich, Germany) in ultrapure water and adjusting the pH to the desired value with KOH.

All measurements were performed by using Bio-Logic VSP-300 potentiostats (Bio-Logic, France). The potentials in this work are referred to the RHE scale. When necessary, the *iR* correction was performed according to ref. [27].

Stability of the electrolytes was tested in prolonged electrochemical experiments by using oxyhydroxide-covered Ni foams as anodes in a 2-electrode configuration in galvanostatic mode. An NMR spectrometer (Burkar, Germany) was utilized to analyze the electrolyte (90% D_2O + 10% BAS solution) before and after 24 h and 48 h electrochemical treatment.

Acknowledgements

Financial support from the cluster of excellence Nanosystems Initiative Munich (NIM) is gratefully acknowledged. S.X. acknowledges financial support from the China Scholarship Council (CSC). B.G. is thankful to the Technische Universität München University Foundation Fellowship (TUFF).

Conflict of interest

The authors declare no conflict of interest.

Keywords: electrocatalysis · hydrogen production · nitriles · oxidation · water splitting

[1] H. Dau, C. Limberg, T. Reier, M. Risch, S. Roggan, P. Strasser, *ChemCatChem* **2010**, *2*, 724–761.
[2] A. Izgorodin, E. Izgorodina, D. R. MacFarlane, *Energy Environ. Sci.* **2012**, *5*, 9496–9501.
[3] D. R. MacFarlane, N. Tachikawa, M. Forsyth, J. M. Pringle, P. C. Howlett, G. D. Elliott, J. H. Davis, M. Watanabe, P. Simon, C. A. Angell, *Energy Environ. Sci.* **2014**, *7*, 232–250.
[4] I. Moussallem, J. Jörissen, U. Kunz, S. Pinnow, T. Turek, *J. Appl. Electrochem.* **2008**, *38*, 1177–1194.
[5] H. S. Wroblowa, G. Razumney, *J. Electroanal. Chem. Interfacial Electrochem.* **1976**, *69*, 195–201.
[6] V. Colic, M. D. Pohl, D. Scieszka, A. S. Bandarenka, *Catal. Today* **2016**, *262*, 24–35.
[7] R. G. Evans, O. V. Klymenko, S. A. Saddoughi, C. Hardacre, R. G. Compton, *J. Phys. Chem. B* **2004**, *108*, 7878–7886.
[8] M. V. Fedorov, A. A. Kornyshev, *Chem. Rev.* **2014**, *114*, 2978–3036.
[9] M. Armand, F. Endres, D. R. MacFarlane, H. Ohno, B. Scrosati, *Nat. Mater.* **2009**, *8*, 621–629.
[10] T. Welton, *Coord. Chem. Rev.* **2004**, *248*, 2459–2477.
[11] D. R. MacFarlane, M. Forsyth, P. C. Howlett, J. M. Pringle, J. Sun, G. Annat, W. Neil, E. I. Izgorodina, *Acc. Chem. Res.* **2007**, *40*, 1165–1173.
[12] H. Olivier-Bourbigou, L. Magna, D. Morvan, *Appl. Catal. A* **2010**, *373*, 1–56.
[13] S. Gao, D. Herzig, B. Wang, *Synthesis* **2001**, 0544–0546.
[14] F. E. Chen, Y. Y. Kuang, H. F. Dai, L. Lu, M. Huo, *Synthesis* **2003**, 2629–2631.
[15] F. Sauvage, S. Chhor, A. Marchioro, J. E. Moser, M. Graetzel, *J. Am. Chem. Soc.* **2011**, *133*, 13103–13109.
[16] "Nitriles": P. Pollak, G. Romeder, F. Hagedorn, H.-P. Gelbke in *Ullmann's Encyclopedia of Industrial Chemistry* (Ed.: H.-J. Arpe), Wiley-VCH, Weinheim, **2002**.
[17] B. M. Naasz, I. Böszörményi, G. A. Somorjai, *J. Catal.* **1989**, *115*, 399–409.
[18] K. C. Nicolaou, C. J. N. Mathison, *Angew. Chem. Int. Ed.* **2005**, *44*, 5992–5997; *Angew. Chem.* **2005**, *117*, 6146–6151.
[19] K. Yamaguchi, N. Mizuno, *Angew. Chem. Int. Ed.* **2003**, *42*, 1480–1483; *Angew. Chem.* **2003**, *115*, 1518–1521.
[20] C. McDonnell-Worth, D. R. MacFarlane, *RSC Adv.* **2014**, *4*, 30551–30557.
[21] R. J. Abraham, M. Mobli, *Modelling ^{1}H NMR Spectra of Organic Compounds: Theory, Applications and NMR Prediction Software*, Wiley, Hoboken, **2008**.
[22] K. Fleischmann, K. Korinek, D. Pletcher, *J. Electroanal. Chem. Interfacial Electrochem.* **1971**, *31*, 39–49.
[23] I. Katsounaros, W. B. Schneider, J. C. Meier, U. Benedikt, P. U. Biedermann, A. A. Auer, K. J. Mayrhofer, *Phys. Chem. Chem. Phys.* **2012**, *14*, 7384–7391.
[24] A. Ganassin, A. Maljusch, V. Colic, L. Spanier, K. Brandl, W. Schuhmann, A. S. Bandarenka, *ACS Catal.* **2017**, *6*, 3017–3024.
[25] C. C. McCrory, S. Jung, J. C. Peters, T. F. Jaramillo, *J. Am. Chem. Soc.* **2013**, *135*, 16977–16987.
[26] S. Watzele, A. S. Bandarenka, *Electroanalysis* **2016**, *28*, 2394–2399.
[27] V. Čolić, J. Tymoczko, A. Maljusch, A. Ganassin, W. Schuhmann, A. S. Bandarenka, *ChemElectroChem* **2015**, *2*, 143–149.

Manuscript received: September 21, 2017
Revised manuscript received: October 20, 2017
Accepted manuscript online: October 24, 2017
Version of record online: November 22, 2017

References

1. Bockris, J. M. A hydrogen economy. *Science* **1972,** *176,* 1323.

2. Tuzikov, A. R. *et al*. Global challenges of the 21st century and possible university's answer. *Ekoloji Dergisi* **2018,** *27,* 33-38.

3. Crabtree, G. W. *et al*. The hydrogen economy. *Phys. Today* **2004,** *57,* 39-44.

4. Debe, M. K. Electrocatalyst approaches and challenges for automotive fuel cells. *Nature* **2012,** *486,* 43.

5. Jacobson, M. Z. *et al*. Cleaning the air and improving health with hydrogen fuel-cell vehicles. *Science* **2005,** *308,* 1901-1905.

6. Global Energy Statistical Yearbook (2017): *https://yearbook.enerdata.net/*, (accessed June 2019).

7. Moriarty, P. *et al*. Can renewable energy power the future? *Energy policy* **2016,** *93*, 3-7.

8. Tanaka Y. in *Hydrogen Energy Engineering: Green Energy and Technology,* Sasaki, K. et al. Ed. (Springer, Tokyo, 2016), chap. Development of the MIRAI Fuel Cell Vehicle, p. 461-475.

9. Song, C. *et al*. Fuel processing for low-temperature and high-temperature fuel cells: Challenges, and opportunities for sustainable development in the 21st century. *Catal. Today* **2002,** *77*, 17-49.

10. Gregory D. *et al.* in *Electrochemistry of Cleaner Environments*, Bockris, J. M. Ed. (Plenum Press, New York, 1972), chap. 8, p. 226.

11. Ursua, A. *et al.* Hydrogen production from water electrolysis: Current status and future trends. *Proc. IEEE Inst. Electr. Electron. Eng.* **2011,** *100,* 410-426.

12. Rebouillat, S. *et al.* Paving the way to the integration of smart nanostructures: Part II: Nanostructured microdispersed hydrated metal oxides for electrochemical energy conversion and storage applications. *Int. J. Electrochem. Sci.* **2011,** *6*, 5830-5917.

13. Léger, J. M. *et al.* in *In-situ Spectroscopic Studies of Adsorption at the Electrode and Electrocatalysis,* (Elsevier Science BV. 2007), chap. 3, p. 63-98.

14. Talk of Elbaz L.: *http://inrep.org.il/wp-content/uploads/2017/07/Electrocatalysis-INREP-summer-school.pdf*, (accessed June 2019).

15. Seh, Z. W. *et al.* Combining theory and experiment in electrocatalysis: Insights into materials design. *Science* **2017,** *355,* 4998.

16. Sun, Z. *et al.* Fundamentals and challenges of electrochemical CO_2 reduction using two-dimensional

materials. *Chem* **2017,** *3,* 560-587.

17. Appel, A. M. *et al.* Frontiers, opportunities, and challenges in biochemical and chemical catalysis of CO_2 fixation. *Chem. Rev.* **2013,** *113,* 6621-6658.

18. Tayyebi, E. *et al.* Trends of electrochemical CO_2 reduction reaction on transition metal oxide catalysts. *J. Phys. Chem. C* **2018,** *122,* 10078-10087.

19. Crisostomo, V. M. B. *et al.* New synthetic route, characterization, and electrocatalytic activity of nanosized manganite. *Chem. Mater.* **2007,** *19,* 1832-1839.

20. Zhou, S. *et al.* Engineering electrocatalytic activity in nanosized perovskite cobaltite through surface spin-state transition. *Nat. Commun.* **2016,** *7,* 11510.

21. Hu, Z. *et al.* Oxygen reduction electrocatalysis enhanced by nanosized cubic vanadium carbide. *Electrochem. Commun.* **2011,** *13,* 763-765.

22. Calle-Vallejo, F. *et al.* Finding optimal surface sites on heterogeneous catalysts by counting nearest neighbors. *Science* **2015,** *350,* 185-189.

23. Becknell, N. *et al.* Control of architecture in rhombic dodecahedral Pt-Ni nanoframe electrocatalysts. *J. Am. Chem. Soc.* **2017,** *139,* 11678-11681.

24. Grimaud, A. *et al.* Double perovskites as a family of highly active catalysts for oxygen evolution in alkaline solution. *Nat. Commun.* **2013,** *4,* 2439.

25. Qiu, Y. *et al.* BCC-phased PdCu alloy as a highly active electrocatalyst for hydrogen oxidation in alkaline electrolytes. *J. Am. Chem. Soc.* **2018,** *140*, 16580-16588.

26. Subbaraman, R. *et al.* Trends in activity for the water electrolyser reactions on 3d M (Ni, Co, Fe, Mn) hydr (oxy) oxide catalysts. *Nat. Mater.* **2012,** *11,* 550.

27. Trotochaud, L. *et al.* Nickel-iron oxyhydroxide oxygen-evolution electrocatalysts: The role of intentional and incidental iron incorporation. *J. Am. Chem. Soc.* **2014,** *136,* 6744-6753.

28. Herasymenko, P. *et al.* Wasserstoffüberspannung und Adsorption der Ionen. *Z. Physik. Chem. Abt. A* **1930,** *149,* 123-139.

29. Jung, Y. J. *et al.* An investigation of the formation of chlorate and perchlorate during electrolysis using Pt/Ti electrodes: The effects of pH and reactive oxygen species and the results of kinetic studies. *Water. Res*. **2010,** *44,* 5345-5355.

30. Merrill, M. D. *et al.* Electrolyte effects on hydrogen evolution and solution resistance in microbial electrolysis cells. *J. Power Sources* **2009,** *191,* 203-208.

31. Varela, A. S. *et al.* Controlling the selectivity of CO_2 electroreduction on copper: The effect of the electrolyte concentration and the importance of the local pH. *Catal. Today* **2016,** *260,* 8-13.

32. Nesselberger, M. *et al.* The particle size effect on the oxygen reduction reaction activity of Pt catalysts:

Influence of electrolyte and relation to single crystal models. *J. Am. Chem. Soc.* **2011,** *133,* 17428-17433.

33. Izgorodin, A. *et al.* Low overpotential water oxidation to hydrogen peroxide on a MnO_x catalyst. *Energy Environ. Sci.* **2012,** *5,* 9496-9501.

34. Suntivich, J. *et al.* The influence of the cation on the oxygen reduction and evolution activities of oxide surfaces in alkaline electrolyte. *Electrocatalysis* **2013,** *4,* 49-55.

35. Chen, Y. X. *et al.* Bridge-bonded formate: Active intermediate or spectator species in formic acid oxidation on a Pt film electrode? *Langmuir* **2006,** *22,* 10399-10408.

36. Stamenkovic, V. R. *et al.* Effect of surface composition on electronic structure, stability, and electrocatalytic properties of Pt-transition metal alloys: Pt-skin versus Pt-skeleton surfaces. *J. Am. Chem.* Soc. **2006,** *128,* 8813-8819.

37. Rountree, E. S. *et al.* Evaluation of homogeneous electrocatalysts by cyclic voltammetry. *Inorg. Chem*. **2014,** *53,* 9983-10002.

38. Lopes, P. P. *et al.* Double layer effects in electrocatalysis: The oxygen reduction reaction and ethanol oxidation reaction on Au(111), Pt(111) and Ir(111) in alkaline media containing Na and Li cations. *Catal. Today* **2016,** *262,* 41-47.

39. Strmcnik, D. *et al.* Effects of Li^+, K^+, and Ba^{2+} cations on the ORR at model and high surface area Pt and Au surfaces in alkaline solutions. *J. Phys. Chem. Lett.* **2011,** *2,* 2733-2736.

40. Lamy-Pitara, E. *et al.* Effect of anions on catalytic and electrocatalytic hydrogenations and on the electrocatalytic oxidation and evolution of hydrogen on platinum. *Electrochim. Acta* **2000,** *45,* 4299-4308.

41. Stamenkovic, V. R. *et al.* Energy and fuels from electrochemical interfaces. *Nat. Mater.* **2017,** *16,* 57.

42. Sabatier, P. in *La catalyse en chimie organique,* (Paris et Liège: Librairie Polytechnique, 1920).

43. Trasatti, S. Work function, electronegativity, and electrochemical behaviour of metals: III. Electrolytic hydrogen evolution in acid solutions. *J. Electroanal. Chem. Interfacial Electrochem*. **1972,** *39,* 163-184.

44. Deutschmann, O. *et al.* in *Heterogeneous Catalysis and Solid Catalysts,* (Wiley-VCH, Weinheim, 2009), chap. 1, p. 8-10.

45. Balandin, A. A. Modern state of the multiplet theor of heterogeneous catalysis. *Adv. Catal.* **1969,** *19,* 1.

46. Nørskov, J. K. *et al.* Trends in the exchange current for hydrogen evolution. *J. Electrochem. Soc.* **2005,** *152,* 23-26.

47. Greeley, J. *et al.* in *Materials For Sustainable Energy,* (Nature Publishing Group, 2011), chap. Computational high-throughput screening of electrocatalytic materials for hydrogen evolution, p. 280-

284.

48. Skúlason, E. *et al.* Modeling the electrochemical hydrogen oxidation and evolution reactions on the basis of density functional theory calculations. *J. Phys. Chem. C* **2010,** *114,* 18182-18197.

49. Durst, J. *et al.* New insights into the electrochemical hydrogen oxidation and evolution reaction mechanism. *Energy Environ. Sci.* **2014,** *7,* 2255-2260.

50. Bockris, J. O. M. *et al.* The mechanism of the hydrogen evolution reaction on platinum, silver and tungsten surfaces in acid solutions. *J. Phys. Chem.* **1957,** *61,* 879-886.

51. Bockris, J. O. M. *et al.* The mechanism of the cathodic hydrogen evolution reaction. *J. Electrochem. Soc.* **1952,** *99,* 169-186.

52. Greeley, J. *et al.* Computational high-throughput screening of electrocatalytic materials for hydrogen evolution. *Nat. Mater.* **2006,** *5,* 909-913.

53. Norskov, J. K. *et al.* Towards the computational design of solid catalysts. *Nat. Chem.* **2009,** *1,* 37.

54. Sparnaay, M. J. in *The electrical double laye*r, (Oxford: Pergamon Press,1972), p. 4.

55. Conway, B. E. *et al.* The dielectric constant of the solution in the diffuse and Helmholtz double layers at a charged interface in aqueous solution. *J. Chem. Soc. Faraday Trans.* **1951,** *47,* 756-766.

56. Hamann, C. H. *et al.* in *Electrochemistry,* (Wiley-VCH, Weinheim, 2007).

57. Bard, A. J. *et al.* in *Electrochemical Methods: Fundamentals and Applications,* (Wiley, New York, 1980), chap. 2.

58. Helmholtz, H. Ueber einige Gesetze der Vertheilung elektrischer Ströme in körperlichen Leitern mit Anwendung auf die thierisch-elektrischen Versuche. *Annalen der Physik und Chemie* (in German) **1853,** *165,* 211-233.

59. Ehrenstein, G. *et al.* Evidence for membrane surface from measurement of potassium kinetics as a function of external divalent cation concentration. *Biophys.* **1973,** *13,* 495.

60. Henderson, D. *et al.* Some exact results and the application of the mean spherical approximation to charged hard spheres near a charged hard wall. *J. Chem. Phys.* **1978,** *69,* 5441.

61. Stern, O. Z. Zur Theorie der Elektrolytischen Doppelschicht. *Zeitschrift für Elektrochemie* **1924,** *30,* 508.

62. Srinivasan S. in *Fuel cells from Fundamentals to Applications,* (Springer, 2006), chap. 2.

63. Bockris, J. O'm. *et al.* On the structure of charged interfaces. *Proc. Roy. Soc, Ser. A.* **1963,** *274,* 55.

64. Langmuir I. Chemical reactions at low pressures. *J. Am. Chem. Soc.* **1915,** *37,* 1139.

65. Langmuir I. The mechanism of the catalytic action of platinum in the reactions $2CO + O_2 = 2CO_2$ and $2H_2 + O_2 = 2H_2O$. *Trans. Faraday Soc*. **1922,** *17,* 607.

66. Knözinger, H. *et al.* in *Heterogeneous catalysis and solid catalysts,* (Ullmann's Encyclopedia of Industrial Chemistry, 2002), chap. 2, p. 8-9.

67. Colic, V. *et al.* Pt alloy electrocatalysts for the oxygen reduction reaction: From model surfaces to nanostructured systems. *ACS Catal.* **2016,** *6,* 5378-5385.

68. Taylor, H. S. A theory of the catalytic surface. *Proceedings of the Royal Society of London. Series A, Containing Papers of a Mathematical and Physical Character* **1925,** *108,* 105-111.

69. Che, M. *et al.* The influence of particle size on the catalytic properties of supported metals. *Adv. Catal.* **1989,** *36,* 55.

70. Davis, S. M. *et al.* in *The Chemical Physics of Solid Surfaces and Heterogeneous Catalysis,* (Elsevier, New York, 1982, chap. 4, p. 217.

71. Boudart, M. *et al.* On the specific activity of platinum catalysts. *J. Catal.* **1966,** *6,* 92-99.

72. Somorjai, G. A. Surface reconstruction and catalysis. *Ann. Rev. Phys. Chem.* **1994,** *45,* 721.

73. Ertl, G. *et al.* Dynamics of reactions at surfaces. *Adv. Catal.* **2000,** *45,* 1.

74. Stojić, D. L. *et al.* Hydrogen generation from water electrolysis-possibilities of energy saving. *J. Power Sources* **2003,** *118,* 315-319.

75. Elmer, T. *et al.* Fuel cell technology for domestic built environment applications: State of-the-art review. *Renew. Sustain. Energy Rev.* **2015,** *42,* 913-931.

76. Yan, Y. *et al.* A review on noble-metal-free bifunctional heterogeneous catalysts for overall electrochemical water splitting. *J. Mater. Chem. A* **2016,** *4,* 17587-17603.

77. Kacprzak, A. Hydroxide electrolyte direct carbon fuel cells—Technology review. *Int. J. Energy Res.* **2019,** *43,* 65-85.

78. Blum, W. *et al.* The definition of polarization, overvoltage and decomposition potential. *J. Electrochem. Soc.* **1934,** *66,* 359-367.

79. Stewart, J. V. in *Intermediate electromagnetic theory,* (World Scientific Publishing Company, 2001), p. 389.

80. Bard, A. J. *et al.* in *Electrochemical Methods: Fundametnals and Applications,* (Wiley & Sons, New York, 2001), chap.4.

81. Napporn, T. W. *et al.* in *Fuel Cells and Hydrogen,* (Elsevier, New York, 2018), chap. 9, p. 175-214.

82. Bockris, J. O'm. *et al.* in *Modern Electrochemistry 2A. Fundamentals of Electrodics,* (Kluwer Academic/Plenum Publishers, 2000), p.1083.

83. Trasatti, S. Water electrolysis: Who first? *J. Electroanal. Chem.* **1999,** *476,* 90-91.

84. Levie, R. D. The electrolysis of water. *J. Electroanal. Chem.* **1999,** *476,* 92-93.

85. Lefrou, C. *et al.* in *Electrochemistry: The basics, with examples,* (Springer-Verlag, Heidelberg, 2012), chap. 4, p.169-256.

86. Pauling, L. in *General chemistry,* (W. H. Freeman and Company, San Fransico, 1970), chap.2.

87. LeRoy, R. L. *et al.* Industrial water electrolysis: Present and future. *Int. J. Hydrogen Energy* **1983,** *8,* 401-417.

88. Qiu, Z. *et al.* Direct observation of active catalyst surface phases and the effect of dynamic self-optimization in NiFe-layered double hydroxides for alkaline water splitting. *Energy Environ. Sci*. **2019,** *12,* 572-581.

89. Wang, C. *et al.* Iridium-based catalysts for solid polymer electrolyte electrocatalytic water splitting. *ChemSusChem* **2019,** *12,* 1576-1590.

90. Marini, S. *et al.* Advanced alkaline water electrolysis. *Electrochim. Acta* **2012,** *82,* 384-391.

91. Carmo, M. *et al.* A comprehensive review on PEM water electrolysis. *Int. J. Hydrogen Energy* **2013,** *38,* 4901-4934.

92. Lasia, A. in *Handbook of fuel cells,* (Wiley-VCH, Weinheim, 2010), chap. 2.

93. Vetter, K. J. in *Electrochemical Kinetics: Theoretical and Experimental Aspects,* (Academic Press, New York, 1967), chap. 4.

94. Skúlason, E. *et al.* Density functional theory calculations for the hydrogen evolution reaction in an electrochemical double layer on the Pt (111) electrode. *Phys. Chem. Chem. Phys.* **2007,** *9,* 3241-3250.

95. Watzele, S. *et al.* On the dominating mechanism of the hydrogen evolution reaction at polycrystalline Pt electrodes in acidic media. *ACS Catal.* **2018,** *8,* 9456-9462.

96. Laursen, A. B. *et al.* Electrochemical hydrogen evolution: Sabatier's principle and the volcano plot. *J. Chem. Educ*. **2012,** *89,* 1595-1599.

97. Subbaraman, R. D. *et al.* Enhancing hydrogen evolution activity in water splitting by tailoring Li^+-$Ni(OH)_2$-Pt interfaces. *Science* **2011,** *334,* 1256-1260.

98. Strmcnik, D. *et al.* Improving the hydrogen oxidation reaction rate by promotion of hydroxyl adsorption. *Nat. Chem.* **2013,** *5,* 300.

99. Ni, W. *et al.* Ni_3N as an active hydrogen oxidation reaction catalyst in alkaline medium. *Angew. Chem., Int. Ed. Engl.* **2019,** *58,* 7445-7449.

100. Yang, X. *et al.* CoP nanosheet assembly grown on carbon cloth: A highly efficient electrocatalyst for hydrogen generation. *Nano Energy* **2015,** *15,* 634-641.

101. Stamenkovic, V. R. *et al.* Improved oxygen reduction activity on $Pt_3Ni(111)$ via increased surface site availability. *Science* **2007,** *315,* 493-497.

102. Suntivich, J. K. *et al.* A perovskite oxide optimized for oxygen evolution catalysis from molecular orbital principles. *Science* **2011,** *334,* 1383-1385.

103. Rossmeisl, J. *et al.* Electrolysis of water on oxide surfaces. *J. Electroanal. Chem*. **2007,** *607,* 83.

104. Zeng, K. *et al.* Recent progress in alkaline water electrolysis for hydrogen production and applications. *Prog. Energy Combust. Sci.* **2010,** *36,* 307-326.

105. Zeradjanin, A. R. Is a major breakthrough in the oxygen electrocatalysis possible? *Curr. Opin. Electrochem.* **2018,** *9,* 214-223.

106. Man, I. C. *et al.* Universality in oxygen evolution electrocatalysis on oxide surfaces. *ChemCatChem* **2011,** *3,* 1159-1165.

107. Grimaud, A. *et al.* Activating lattice oxygen redox reactions in metal oxides to catalyse oxygen evolution. *Nat. Chem.* **2017,** *9,* 457.

108. Nørskov, J. K. *et al.* Origin of the overpotential for oxygen reduction at a fuel-cell cathode. *J.*

Phys. Chem. B. **2004,** *108,* 17886-17892.

109. Calle-Vallejo, F. *et al.* Density functional studies of functionalized graphitic materials with late transition metals for oxygen reduction reactions. *Phys. Chem. Chem. Phys.* **2011,** *13,* 15639.

110. Minh, N. Q. Solid oxide fuel cell technology-features and applications. *Solid State Ionics* **2004,** *174,* 271-277.

111. Nelson, D. B. *et al.* Unit sizing and cost analysis of stand-alone hybrid wind/PV/fuel cell power generation systems. *Renew. Energy* **2006,** *31,* 1641-1656.

112. Hydrogen fuel cell: *http://energy.asu.edu.jo/index.php/r-d/hydrogen-fuel-cells*, (accessed June 2019).

113. Grove, W. R. On voltaic series and the combination of gases by platinum. *Philosophical Magazine and Journal of Science* **1839,** *86-87,* 127-130.

114. Fuel cell history: *https://americanhistory.si.edu/fuelcells/intro.htm*, (accessed June 2019).

115. Prater, K. The renaissance of the solid polymer fuel cell. *J. Power Sources* **1990,** *29,* 239-250.

116. Barbir, F. in *Handbook of Transnational Economic Governance Regimes,* (Brill Nijhoff, 2010), chap. 5, p. 915-921.

117. Wang, Y. *et al.* A review of polymer electrolyte membrane fuel cells: Technology, applications, and needs on fundamental research. *Appl. Energy* **2011,** *88,* 981-1007.

118. Sheng, W. *et al.* Correlating the hydrogen evolution reaction activity in alkaline electrolytes with the hydrogen binding energy on monometallic surfaces. *Energy Environ. Sci*. **2013,** *6,* 1509-1512.

119. Durst, J. *et al.* Hydrogen oxidation and evolution reaction (HOR/HER) on Pt electrodes in acid vs.

alkaline electrolytes: Mechanism, activity and particle size effects. *ECS Trans.* **2014,** *64,* 1069-1080.

120. Sheng, W. *et al.* Hydrogen oxidation and evolution reaction kinetics on platinum: Acid vs alkaline electrolytes. *J. Electrochem. Soc.* **2010,** *157,* 1529-1536.

121. Rheinländer, P. J. *et al.* Kinetics of the hydrogen oxidation/evolution reaction on polycrystalline platinum in alkaline electrolyte reaction order with respect to hydrogen pressure. *J. Electrochem. Soc.* **2014,** *161,* 1448-1457.

122. Li, B. *et al.* Synthesis of a highly active carbon-supported Ir-V/C catalyst for the hydrogen oxidation reaction in PEMFC. *Electrochim. Acta* **2009,** *54,* 5614-5620.

123. Bing, Y. *et al.* Nanostructured Pt-alloy electrocatalysts for PEM fuel cell oxygen reduction reaction. *Chem. Soc. Rev.* **2010,** *39,* 2184-2202.

124. Sheng, W. *et al.* Non-precious metal electrocatalysts with high activity for hydrogen oxidation reaction in alkaline electrolytes. *Energy Environ. Sci.* **2014,** *7,* 1719-1724.

125. Shao, M. Palladium-based electrocatalysts for hydrogen oxidation and oxygen reduction reactions. *J. Power Sources* **2011,** *196,* 2433-2444.

126. Ramaswamy, N. *et al.* Activity descriptor identification for oxygen reduction on nonprecious electrocatalysts: Linking surface science to coordination chemistry. *J. Am. Chem. Soc.* **2013,** *135*, 15443.

127. Siahrostami, S. *et al.* Enabling direct H_2O_2 production through rational electrocatalyst design. *Nat. Mat.* **2013,** *12,* 1137.

128. Dong, Q. *et al.* Efficient approach to iron/nitrogen co-doped graphene materials as efficient electrochemical catalysts for the oxygen reduction reaction. *J. Mater. Chem. A* **2015,** *3,* 7767.

129. Barman, B. K. *et al.* Prussian blue as a single precursor for synthesis of Fe/Fe_3C encapsulated N-doped graphitic nanostructures as bi-functional catalysts. *Green Chem*. **2016,** *18,* 427-432.

130. Harzer, G. S. *et al.* Cathode loading impact on voltage cycling induced PEMFC degradation: a voltage loss analysis. *J. Electrochem. Soc.* **2018,** *165,* 3118-3131.

131. Meier, J. C. *et al.* Design criteria for stable Pt/C fuel cell catalysts. *Beilstein J. Nanotechnol.* **2014,** *5,* 44-67.

132. Sasaki, K. *et al.* Core-protected platinum monolayer shell high-stability electrocatalysts for fuel-cell cathodes. *Angew. Chem., Int. Ed.* **2010,** *49,* 8602.

133. Kannan, A. *et al.* Long term testing of start-stop cycles on high temperature PEM fuel cell stack. *J. Power Sources* **2015,** *277,* 312.

134. U-shaped tube: *https://www.monotaro.sg/g/imagewindow/1294717/* (accessed June 2019)

135. Levich, V. G. in *Physicochemical hydrodynamics: VG Levich festschrift* (Advance Publications, 1977), chap. 2.

136. Bruckenstein, S. *et al.* The rotated, mercury-coated platinum electrode. *Anal. Chem.* **1961,** *33,* 1201-1209.

137. Xue, S. *et al.* Reconsidering water electrolysis: Producing hydrogen at cathodes together with selective oxidation of n-butylamine at anodes. *ChemSusChem* **2017,** *10,* 4812-4816.

138. Tymoczko, J. *et al.* Making the hydrogen evolution reaction in polymer electrolyte membrane electrolysers even faster. *Nat. Commun.* **2016,** *7,* 10990.

139. Van Der Niet, M. J. *et al.* Water dissociation on well-defined platinum surfaces: The electrochemical perspective. *Catal. Today* **2013,** *202,* 105-113.

140. Garcia-Araez, N. *et al.* Enthalpic and entropic effects on hydrogen and OH adsorption on Pt (111), Pt (100), and Pt (110) electrodes as evaluated by Gibbs thermodynamics. *J. Phys. Chem. C* **2010,** *115*, 501-510.

141. Xue, S. *et al.* Influence of alkali metal cations on the hydrogen evolution reaction activity of Pt, Ir, Au, and Ag electrodes in alkaline electrolytes. *ChemElectroChem* **2018,** *5,* 2326-2329.

142. Pohl, M. D. *et al.* Nature of highly active electrocatalytic sites for the hydrogen evolution reaction at Pt electrodes in acidic media. *ACS Omega* **2017,** *11,* 8141-8147.

143. Greenwood, N. N. *et al.* in *Chemistry of the Elements,* (Elsevier Earnshaw, Alan, 2012), chap. 4.

144. Tymoczko, J. *et al.* Influence of the alkali metal cations on the activity of Pt (111) towards model electrocatalytic reactions in acidic sulfuric media. *Catal. Today* **2015,** *244,* 96-102.

145. Skúlason, E. *et al.* Modeling the electrochemical hydrogen oxidation and evolution reactions on the basis of density functional theory calculations. *J. Phys. Chem. C* **2010,** *114*, 18182-18197.

146. Greeley, J. *et al.* in *Materials For Sustainable Energy* (Nature Publishing Group, 2011), p. 280-284.

147. Strmcnik, D. *et al.* The role of non-covalent interactions in electrocatalytic fuel-cell reactions on platinum. *Nat. Chem.* **2009,** *1,* 466-472.

148. Ledezma-Yanez, I. *et al.* Interfacial water reorganization as a pH-dependent descriptor of the hydrogen evolution rate on platinum electrodes. *Nat. Energy* **2017,** *2,* 17031

149. Gasteiger, H. A. *et al.* Activity benchmarks and requirements for Pt, Pt-alloy, and non-Pt oxygen reduction catalysts for PEMFCs. *Appl. Catal. B* **2005,** *56,* 9-35.

150. Mahmoud, M. A. *et al.* Determining the mechanism of solution metallic nanocatalysis with solid and hollow nanoparticles: Homogeneous or heterogeneous. *J. Phys. Chem. C* **2013,** *117,* 21886-21893.

151. Calle-Vallejo, F. *et al.* Tailoring the catalytic activity of electrodes with monolayer amounts of foreign metals. *Chem. Soc. Rev.* **2013,** *42,* 5210-5230.

152. Stamenkovic, V. R. *et al.* Trends in electrocatalysis on extended and nanoscale Pt-bimetallic alloy surfaces. *Nat. Mater.* **2007,** *6,* 241-247.

153. Mukerjee, S. *et al.* Role of structural and electronic properties of Pt and Pt alloys on electrocatalysis of oxygen reduction an in situ XANES and EXAFS investigation. *J. Electrochem. Soc.* **1995,** *142,* 1409-1422.

154. Stamenkovic, V. *et al.* Changing the activity of electrocatalysts for oxygen reduction by tuning the surface electronic structure. *Angew. Chem.* **2006,** *118,* 2963-2967.

155. Pfisterer, J. H. *et al.* Direct instrumental identification of catalytically active surface sites. *Nature* **2017,** *549,* 74-77.

156. Kodama, K. *et al.* Activities and stabilities of Au-modified stepped-Pt single-crystal electrodes as model cathode catalysts in polymer electrolyte fuel cells. *J. Am. Chem. Soc.* **2016,** *138,* 4194-4200.

157. Ueno, T. *et al.* Infrared spectroscopy of adsorbed OH on n(111)-(100) and n(111)-(111) series of Pt electrode. *J. Electroanal. Chem.* **2017,** *800,* 162-166.

158. Stoffelsma, C. *et al.* Promotion of the oxidation of carbon monoxide at stepped platinum single-crystal electrodes in alkaline media by lithium and beryllium cations. *J. Am. Chem. Soc.* **2010,** *132,* 16127-16133.

159. Chou, S. W. *et al.* Uniform size and composition tuning of PtNi octahedra for systematic studies of oxygen reduction reactions. *J. Catal.* **2014**, *309*, 343-350.

160. Greeley, J. *et al.* Alloys of platinum and early transition metals as oxygen reduction electrocatalysts. *Nat. Chem.* **2009,** *1,* 552-556.

161. Coleman, E. J. *et al.* Galvanic displacement of Pt on nanoporous copper: An alternative synthetic route for obtaining robust and reliable oxygen reduction activity. *J. Catal.* **2014,** *316,* 191-200.

162. Kuzume, A. *et al.* Oxygen reduction on stepped platinum surfaces in acidic media. *J. Electroanal. Chem.* **2007,** *599,* 333-343.

163. Macia, M. D. *et al.* On the kinetics of oxygen reduction on platinum stepped surfaces in acidic media. *J. Electroanal. Chem.* **2004,** *564,* 141-150.

164. Rizo, R. *et al.* Oxygen reduction reaction on stepped platinum surfaces in alkaline media. *Phys. Chem. Chem. Phys.* **2013,** *15,* 15416-15425.

165. Wang, C. *et al.* Advanced platinum alloy electrocatalysts for the oxygen reduction reaction. *ACS Catal.* **2012,** *2,* 891-898.

166. Stephens, I. E. *et al.* Understanding the electrocatalysis of oxygen reduction on platinum and its alloys. *Energy Environ. Sci.* **2012,** *5,* 6744-6762.

167. Bandarenka, A. S. *et al.* Techniques and methodologies in modern electrocatalysis: Evaluation of activity, selectivity and stability of catalytic materials. *Analyst* **2014,** *139,* 1274-1291.

168. Rossmeisl, J. *et al.* On the pH dependence of electrochemical proton transfer barriers. *Catal. Today*

2016, *262,* 36-40.

169. Garlyyev, B. *et al.* Influence of the nature of the alkali metal cations on the electrical double-layer capacitance of model Pt (111) and Au (111) electrodes. *J. Phys. Chem. Lett.* **2018,** *9,* 1927-1930.

170. Chen, X. *et al.* Co-adsorption of cations as the cause of the apparent pH dependence of hydrogen adsorption on a stepped platinum single-crystal electrode. *Angew. Chem., Int. Ed.* **2017,** *56,* 15025-15029.

171. Calle-Vallejo, F. *et al.* Why conclusions from platinum model surfaces do not necessarily lead to enhanced nanoparticle catalysts for the oxygen reduction reaction. *Chem. Sci.* **2017,** *8,* 2283-2289.

172. Garlyyev, B. *et al.* Oxygen electroreduction at high-index Pt electrodes in alkaline electrolytes: A decisive role of the alkali metal cations. *ACS Omega* **2018,** *3,* 15325-15331.

173. Marković, N. M. *et al.* Oxygen reduction on platinum low-index single-crystal surfaces in alkaline solution: Rotating ring disk Pt(hkl) studies. *J. Phys. Chem.* **1996,** *100,* 6715-6721.

174. Taguchi, S. *et al.* Electrochemical reduction of nitrate on Pt(S)[n(111)×(111)] electrodes in perchloric acid solution. *Electrochim. Acta* **2007,** *52,* 6023-6033.

175. Pohl, M. D. *et al.* Elucidation of adsorption processes at the surface of Pt(331) model electrocatalysts in acidic aqueous media. *Phys. Chem. Chem. Phys.* **2016,** *18,* 10792-10799.

176. van der Niet, M. J. *et al.* The interaction between H_2O and Preadsorbed O on the Stepped Pt(533) Surface. *J. Phys. Chem. C* **2010,** *114,* 18953-18960.

177. Calle-Vallejo, F. *et al.* Fast prediction of adsorption properties for platinum nanocatalysts with generalized coordination numbers. *Angew. Chem., Int. Ed.* **2014,** *53,* 8316-8319.

178. Dau, H. *et al.* The mechanism of water oxidation: From electrolysis via homogeneous to biological catalysis. *ChemCatChem* **2010,** *2,* 724-761.

179. Moussallem, I. *et al.* Chlor-alkali electrolysis with oxygen depolarized cathodes: History, present status and future prospects. *J. Appl. Electrochem.* **2008,** *38,* 1177-1194.

180. MacFarlane, D. R. *et al.* Energy applications of ionic liquids. *Energy Environ. Sci.* **2014,** *7,* 232-250.

181. Fedorov, M. V. *et al.* Ionic liquids at electrified interfaces. *Chem. Rev.* **2014,** *114,* 2978-3036.

182. Armand, M. *et al.* Ionic-liquid materials for the electrochemical challenges of the future. *Nat. Mater.* **2009,** *8,* 621-629.

183. Welton, T. Ionic liquids in catalysis. *Coord. Chem. Rev.* **2004,** *248,* 2459-2477.

184. MacFarlane, D. R. *et al.* Ionic liquids in electrochemical devices and processes: Managing interfacial electrochemistry. *Acc. Chem. Res.* **2007,** *40,* 1165-1173.

185. Olivier-Bourbigou, H. *et al.* Ionic liquids and catalysis: Recent progress from knowledge to applications. *Appl. Catal. A* **2010,** *373,* 1-56.

186. Evans, R. G. *et al.* Electroreduction of oxygen in a series of room temperature ionic liquids composed of group 15-centered cations and anions. *J. Phys. Chem. B* **2004,** *108,* 7878-7886.

187. Naasz, B. M. *et al.* The synthesis of butyronitrile from n-butanol and ammonia over rhodium (111) and (331) single-crystal surfaces. *J. Catal.* **1989,** *115,* 399-409.

188. Gao, S. *et al.* OsO_4-mediated conversion of primary amines to nitriles. *Synthesis* **2001,** *4,* 0544-0546.

189. Chen, F. E. *et al.* A selective and mild oxidation of primary amines to nitriles with trichloroisocyanuric acid. *Synthesis* **2003,** *17,* 2629-2631.

190. Sauvage, F. *et al.* Butyronitrile-based electrolyte for dye-sensitized solar cells. *J. Am. Chem. Soc.* **2011,** *133,* 13103-13109.

191. Watanabe, M. *et al.* High ionic conductivity of new polymer electrolytes consisting of polypyridinium, pyridinium and aluminium chloride. *J. Chem. Soc. Chem. Commun.* **1993,** *11,* 929-931.

192. Goodenough, J. B. *et al.* The Li-ion rechargeable battery: A perspective. *J. Am. Chem. Soc.* **2013,** *135,* 1167-1176.

193. Matsumoto, H. *et al.* Highly conductive room temperature molten salts based on small trimethylalkylammonium cations and bis (trifluoromethylsulfonyl) imide. *Chem. Lett.* **2000,** *29,* 922-923.

194. Nikitina, V. A. *et al.* Properties of sodium tetrafluoroborate solutions in 1-butyl-3-methylimidazolium tetrafluoroborate ionic liquid. *J. Chem. Eng. Data* **2012,** *57,* 3019-3025.

195. Bhatt, A. I. *et al.* Group 15 quaternary alkyl bistriflimides: Ionic liquids with potential application in electropositive metal deposition and as supporting electrolytes. *J. Chem. Soc., Dalton Trans.* **2002,** *24,* 4532-4534.

196. Howlett, P. C. *et al.* High lithium metal cycling efficiency in a room-temperature ionic liquid. *Electrochem. Solid-State Lett.* **2004,** *7,* 97-101.

197. Garcia, B. *et al.* Room temperature molten salts as lithium battery electrolyte. *Electrochim. Acta* **2004,** *49,* 4583-4588.

198. Matsumoto, H. *et al.* Fast cycling of $Li/LiCoO_2$ cell with low-viscosity ionic liquids based on bis (fluorosulfonyl) imide $[FSI]^-$. *J. Power Sources* **2006,** *160,* 1308-1313.

199. Bai, Y. *et al.* Lithium-modulated conduction band edge shifts and charge-transfer dynamics in dye-sensitized solar cells based on a dicyanamide ionic liquid. *Langmuir* **2011,** *27,* 4749-4755.

200. Hashmi, G. *et al.* Review of materials and manufacturing options for large area flexible dye solar cells. *Renewable Sustainable Energy Rev.* **2011,** *15,* 3717-3732.

201. Simon, P. *et al.* Materials for electrochemical capacitors. *Nat. Mater.* **2008,** *7,* 845-854.

202. McEwen, A. B. *et al.* Electrochemical properties of imidazolium salt electrolytes for electrochemical

capacitor applications. *J. Electrochem. Soc.* **1999,** *146,* 1687-1695.

203. Smela, E. Conjugated polymer actuators for biomedical applications. *Adv. Mater.* **2003,** *15,* 481-494.

204. Baughman, R. H. *et al.* Carbon nanotube actuators. *Science* **1999,** *284,* 1340-1344.

205. Zhou, F. L. *et al.* Electrodeposited MnO_x films from ionic liquid for electrocatalytic water oxidation. *Adv. Energy Mater.* **2012,** *2,* 1013-1021.

206. Izgorodin, A. O. *et al.* CdS thin-film electrodeposition from a phosphonium ionic liquid. *Phys. Chem. Chem. Phys.* **2009,** *11,* 8532-8537.

207. MacFarlane, D. R. *et al.* Ionic liquid "buffers"—pH control in ionic liquid systems. *Chem. Commun.* **2010,** *46,* 7703-7705.

208. Blizanac, B. B *et al.* Oxygen electroreduction on Ag (111): The pH effect. *Electrochim. Acta*. **2007,** *52,* 2264-2271.

209. Shi, Q. *et al.* Sulfur and nitrogen co-doped carbon nanotubes for enhancing electrochemical oxygen reduction activity in acidic and alkaline media. *J. Mater. Chem. A* **2013,** *1,* 14853-14857.

210. Speck, F. D. *et al.* On the electrolytic stability of iron-nickel oxides. *Chem* **2017,** *2,* 590-597.

211. Giordano, L. *et al.* pH dependence of OER activity of oxides: Current and future perspectives. *Catal. Today* **2016,** *262,* 2-10.

212. McDonnell-Worth, C. *et al.* Ion effects in water oxidation to hydrogen peroxide. *RSC Adv.* **2014,** *4,* 30551-30557.

213. Abraham, R. J. *et al.* in *Modelling ^{1}H NMR Spectra of Organic Compounds: Theory, Applications and NMR Prediction Software,* (Wiley, Hoboken, 2008).

214. Fleischmann, M. *et al.* The oxidation of organic compounds at a nickel anode in alkaline solution. *J. Electroanal. Chem. Interfacial Electrochem.* **1971,** *31,* 39-49.

215. Katsounaros, I. *et al.* Hydrogen peroxide electrochemistry on platinum: Towards understanding the oxygen reduction reaction mechanism. *Phys. Chem. Chem. Phys.* **2012,** *14,* 7384-7391.

216. Lust, E. in *Encyclopedia of Electrochemistry,* (Wiley-VCH, 2007), chap. Electrical Double Layers. Double Layers at Single-crystal and Polycrystalline Electrodes.

217. Janssen, M. *et al.* Coulometry and Calorimetry of Electric Double Layer Formation in Porous Electrodes. *Phys. Rev. Lett*. **2017,** *119,* 166002.

218. Kornyshev, A. A. Double-Layer in Ionic Liquids: Paradigm Change? *J. Phys. Chem. B* **2007,** *111,* 5545-5557.

219. Merlet, C. *et al.* The electric double layer has a life of its own. *J. Phys. Chem. C* **2014,** *118,* 18291-18298.

220. Bandarenka, A. S. *et al.* Localized electrochemical impedance spectroscopy: Visualization of spatial distributions of the key parameters describing solid/liquid interfaces. *Anal. Chem.* **2013,** *85,* 2443-2448.

221. Parsons, R. *et al.* The electrical double layer: Recent experimental and theoretical developments. *Chem. Rev*. **1990,** *90,* 813-826.

222. Burt, R. A review of molecular modelling of electric double layer capacitors. *Phys. Chem. Chem. Phys*. **2014,** *16,* 6519-38.

223. Choi, N. S. *et al.* Challenges facing lithium batteries and electrical double-layer capacitors. *Angew. Chem., Int. Ed*. **2012,** *51,* 9994-10024.

224. Vatamanu, J. *et al.* Capacitive energy storage: Current and future challenges. *J. Phys. Chem. Lett*. **2015,** *6,* 3594-3609.

225. Scholz, F. *et al.* in *Electroanalytical Methods: Guide to Experiments and Applications,* (Springer Science & Business Media, 2002), p. 331.

226. Gileadi, E. *et al.* The potential of zero charge of platinum and its pH dependence. *J. Phys. Chem*. **1966**, *70,* 2044-2046.

227. Bockris, J.O'm. *et al.* The determination of the potential of zero charge on solid metals. *Electrochim. Acta* **1969,** *14,* 1259-1283.

228. Yastremskii, P. S. Dielectrical constant of aqueous cesium chloride solutions and hydration of alkali metal cations. *J. Structural Chem*. **1962,** *3,* 262-265.

229. Wachter, W. *et al.* Is there an anionic hofmeister effect on water dynamics? Dielectrical spectroscopy of aqueous solutions of NaBr, NaI, $NaNO_3$, $NaClO_4$, and NaSCN. *J. Phys. Chem. A* **2005,** *109,* 8675-8683.

230. Hai, N. T. *et al.* Electrochemical reactions at a porphyrin-copper interface. *Phys. Chem. Chem. Phys.* **2009,** *11,* 5422-5430.